LAYERED DOUBLE HYDROXIDE-BASED CATALYSTS FOR FINE ORGANIC SYNTHESIS

Alexandra-Elisabeta Stamate

UNIVERSITY OF BUCHAREST
FACULTY OF CHEMISTRY
DOCTORAL SCHOOL IN CHEMISTRY

PhD THESIS

PhD student: Stamate Alexandra-Elisabeta

Thesis supervisor: Prof. Dr. Habil. Marcu Ioan-Cezar

Defense date: December 16, 2022

2022

UNIVERSITY OF BUCHAREST
FACULTY OF CHEMISTRY
DOCTORAL SCHOOL IN CHEMISTRY

PhD THESIS

LAYERED DOUBLE HYDROXIDE-BASED CATALYSTS FOR FINE ORGANIC SYNTHESIS

PhD student: Stamate Alexandra-Elisabeta

Thesis supervisor: Prof. Dr. Habil. Marcu Ioan-Cezar

Doctoral committee:

President: Prof. Dr. Bala Camelia

Thesis supervisor: Prof. Dr. Habil. Marcu Ioan-Cezar

Official reviewers:

1. Prof. Dr. Eng. Cârjă Gabriela from „Gheorghe Asachi" Technical University of Iași
2. Assoc. Prof. Dr. Habil. Catrinescu Cezar from „Gheorghe Asachi" Technical University of Iași
3. Assoc. Prof. Dr. Jurca Ciprian Bogdan from University of Bucharest

2022

TABLE OF CONTENTS

THEORETICAL PART

Introduction

Layered double hydroxides (LDH), a class of anionic compounds that can be found in nature as minerals and can also be synthesized, have cached the eye of the scientific community. Due to their particular lamellar structure and their versatility in composition, these synthetic inorganic materials exhibit unique properties that make them suitable for applications in several advanced technological processes. However, their primary applicability is in catalysis, either as precursors, catalyst supports, or actual catalysts. The most known representative of the layered double hydroxide is the one that contains magnesium and aluminum cations and carbonate as compensation anion. The current thesis focuses on developing layered double hydroxides derived from the aforementioned solid having different compositions of the cations or anions to observe the changes induced by these modifications on the structural, textural and catalytic properties.

The solids prepared for the current thesis and their catalytic purpose in fine organic synthesis are the following:

- A part of the trivalent cations, namely aluminum present in the brucite-type layer of the hydrotalcite, is replaced with a cerium lanthanide. Two methods of synthesis are applied, co-precipitation and mechanochemical technique. The resulting layered double hydroxides and their corresponding mixed oxides were catalytically tested in different types of condensation reactions. First, in the self-condensation of cyclohexanone and then in the Claisen-Schmidt condensation, where compounds belonging to the flavonoid class, namely chalcone and flavone, are synthesized. The literature on this topic indicates that various LDH compositions were tested as catalysts for these reactions. Still, no studies referred to the usage of LDH-type compounds modified with cerium.
- The previous solid containing cerium prepared by co-precipitation was modified with graphene oxide, resulting in a sandwich-like compound. The composites bear different concentrations of GO in the range of 5-25 wt. %. The LDH-GO composites were tested as catalysts in two other organo-chemical transformations: i) Knoevenagel condensation reaction and ii) one-pot cascade oxidation-Knoevenagel condensation. Again, there were no studies in the literature about these types of samples used in the reaction aforementioned.
- To observe if there are noticeable differences between the catalytic results of hybrid GO and Mg_3Al layered double hydroxides not only when the brucite-like layers are modified by inserting another cation like cerium, but also when the interlayer space contains other

anions, like molybdate, the neat Mg3Al-LDH was modified with molybdate anions (MoO_4^{2-}) and with graphene oxide in the range of 5-25 wt.%. The solids were tested as in the previous case in one-pot cascade oxidation-Knoevenagel condensation.

- To open up new perspectives in the rational design of efficient bifunctional catalytic systems, several samples were prepared by inserting various metallic cations having different molar ratios. The study involved synthesising MgNi(Cu)Al-layered double hydroxides having different molar ratios using the co-precipitation method. Practically, three series of catalysts were developed, having the following general formulas: $Mg_{1.2}Ni_aCu_bAl(OH)_6(CO_3)_{0.5}$ (a+b=0.8), $Mg_{0.8}Ni_cCu_dAl(OH)_6(CO_3)_{0.5}$ (c+d=1.2), $M2Al(OH)_6(CO_3)_{0.5}$ (where M is Ni or Cu). All three series were tested catalytically in the one-pot cascade oxidation-Knoevenagel condensation reaction. The calcined forms of the $Mg_{1.2}Ni_aCu_bAl(OH)_6(CO_3)_{0.5}$ (a+b=0.8) and $M2Al(OH)_6(CO_3)_{0.5}$ (where M is Ni or Cu) series were also tested in Payne oxidation reaction of cyclohexene.
- To check the importance of the copper inserted in the brucite-type layers, samples containing cobalt instead of copper were created. So, series having the following general formulas $Mg_{1.2}Ni_aCo_bAl(OH)_6(CO_3)_{0.5}$ (a+b=0.8), $Mg_{0.8}Ni_cCo_dAl(OH)_6(CO_3)_{0.5}$ (c+d=1.2), $M_2Al(OH)_6(CO_3)_{0.5}$ (where M is Ni or Co) were created. The samples were also tested as catalysts in the one-pot oxidation-Knoevenagel condensation reaction.

The current thesis brings excellent contributions to the layered double hydroxides and catalysis. There are no references in the literature that any catalyst developed herein was used for the above mentioned fine organic syntheses.

Chapter 1: Layered double hydroxide-based catalytic materials

1.1. Overview

Clay minerals have aroused humanity's interest and curiosity since early stages due to their frequent occurrence in nature and wide range of applications. Depending on their ionic exchange capacity, clay minerals are divided into three large groups: non-ionic (e.g., kaolinite, serpentine, chlorite, illite, pyrophyllite, and talc), cationic (e.g., alumino-silicate clays such as vermiculites, smectites, and swelling micas) and anionic clays represented by layered double hydroxides [1]. The cationic clays are abundant but relatively complex and expensive to synthesize, unlike the anionic ones that are rare and can be readily prepared in the laboratory.

Layered double hydroxides (LDH), known as hydrotalcite compounds, present various physicochemical properties that are similar to those of the cationic clay materials. Still, due to their anion-exchange properties, LDH belong exclusively to the anionic clay group [2]. Their lamellar structure with versatile interlayer zone, rheological properties, colloidal behaviour, variable chemical composition and layer charge density have allowed the LDH to be included in the vast family of mineral clays [2]. The history of layered double hydroxides dates back to 1842, when the natural hydrotalcite was discovered in Sweden and was first reported by Hochstetter [3]. Hydrotalcite (HT) is a white powder similar to talc-containing hydroxycarbonate of magnesium and aluminum found in nature as distorted planar or foliated masses [4].

One hundred years later, W. Feithnecht has successfully created numerous artificial hydrotalcites by combining different diluted metal salt solutions with bases [4]. The German scientist has named these materials “doppelschichtstrukturen” or double-sheet structures, believing that they are mixed hydroxides of different cations divided into layers [4]. Practically, each layer will contain the hydroxide of one cation leading to compounds with the following structure:

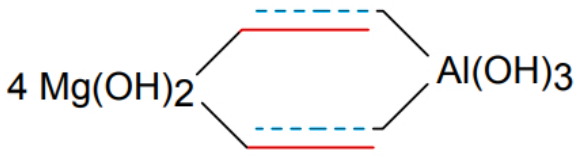

Figure 1. Hypothetically structure of the hydrotalcite. Adapted from [4].

Although the correct stoichiometry of the hydrotalcite, namely, $[Mg_6Al_2(OH)_{16}]CO_3 \cdot 4H_2O$, was first established in 1915 by Professor E. Manasse from Florence University (Italy), the

main structural characteristics of LDHs were fully understood in the 1960s, when Allman [5] and Taylor [6] carried out single-crystal X-ray diffraction (XRD) studies on mineral samples. The XRD analysis revealed that each layer is formed by both cations, while the anions and water molecules are in the interlamellar space, thus destroying the hypothetical structure proposed by W. Feithnecht.

The research regarding layered double hydroxides has always imposed various controversies in the scientific world, mainly referring to their structural composition, the stacking of the layers, the arrangement of metal cations within the lamellar sheets, the composition of the interlayer space and many others [7]. Although there are many studies related to layered double hydroxides, there are still unresolved issues that need to be elucidated. LDH materials have incited the researchers' minds not only due to their disputable structure but also because of their advantageous properties, such as:

- Easy removal from the reaction mixture.
- The possibility of being recycled.
- Reduced corrosive action.
- Memory effect.
- Anion exchange capability.

Layered double hydroxides have a promising future due to their unlimited application potential overthrowing materials such as sepiolite organic resins in what concerns the thermic stability, the variable composition, the distribution, and size of the pores.

1.2. Structure of LDH

There is a strong resemblance between the lamellar structure of layered double hydroxides and brucite, $Mg(OH)_2$. Practically, in brucite, the Mg^{2+} cations are coordinated octahedrally by six OH^- groups, having the hydrogen atoms pointed towards the interlamellar zone. The octahedral units share the edges forming planar, infinite, neutral charge layers joined by hydrogen bonds [8,9]. In the case of LDH, the brucite-type sheets stack on top of one another resulting in a 3D structure [10]. The structure of an idyllic layered double hydroxide can be seen in Figure 2. There are two possibilities to stack the brucite-like layers, either with rhombohedral symmetry (3R) or a hexagonal one (2H). The 3R symmetry is attributed to the hydrotalcite compounds, while the 2H is known as manasseite [11]. Also, the partial isomorphous substitution of the Mg^{2+} cations with trivalent ones with a similar ionic radius leads to positively charged layers. The electroneutrality of the LDH solid is maintained by the

presence of anionic species between the layers. In the interlayer space, besides the anions, there are also water molecules.

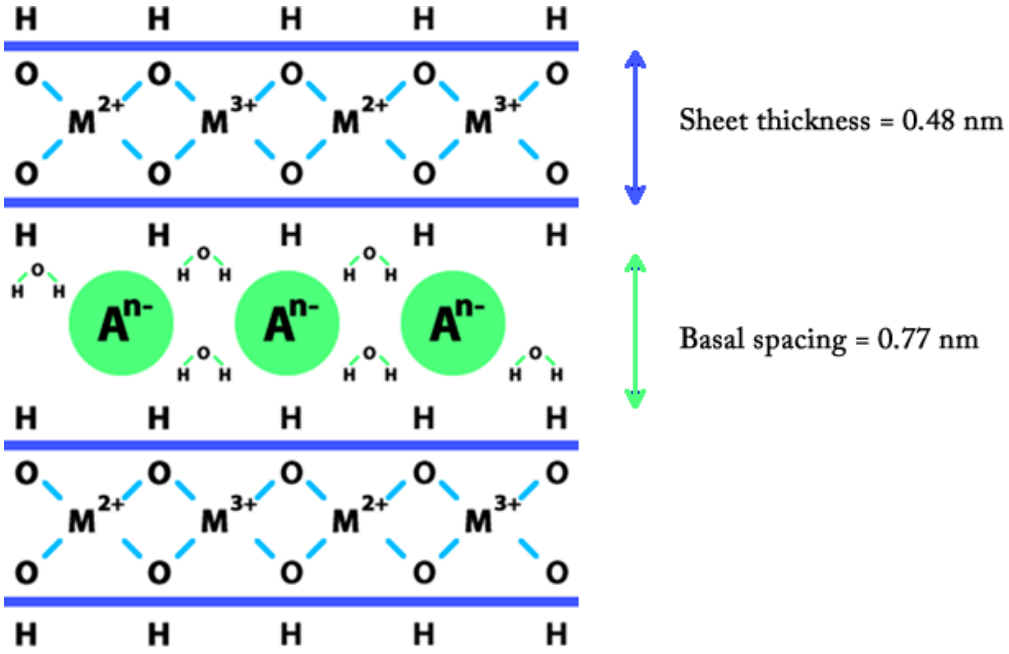

Figure 2. The idyllic structure of layered double hydroxides. Adapted from [10].

The following general molecular formulas can represent layered double hydroxides: $[M(II)_{1-x}M(III)_x(OH)_2][A^{m-}_{x/m} \cdot nH_2O]$ or $[M(I)_{1-x}M(III)_x(OH)_2]^{(2x-1)+}[A^{m-}_{(2x-1)/m} \cdot nH_2O]$ [7], where M^+ (M: Li), M^{2+} (M: Mg, Ni, Co, Zn), M^{3+} (M: Al, Cr, Fe, In) are metallic cations present in the brucite-type layers, linked to each other through the hydroxyl groups, A^{m-} are the anions which along with m molecules of water are forming the interlayer area. Last but not least, x represents the charge density or the anionic exchange capacity, and it can take values between 0.15-0.5 [8].

1.3. Cation substitution in the LDH layers

It is possible to obtain a large variety of synthetic hydrotalcite-like compounds by simply adjusting their chemical composition in what concerns the nature and proportion of the cations. A wide range of M^{2+}/M^{3+} combinations [12] have been used to synthesize the LDH-type solids, as shown in Table 1. The metals that have been reported as constituents of the brucite-like layers, both in articles and patents [13] are shown in Figure 3. A considerable number of experimental studies [2] have tried to establish a general rule meant to asses which metallic ions can lead to the formation of LDH. Most of them revealed that the metal cation intended to be inserted in the brucite-like matrix needs to possess an ionic radius close to that of Mg^{2+}, namely 0.720 Å [2]. However, this assumption is not feasible for all the empirical

findings. Cations such as Ca^{2+} or Cd^{2+} with a larger ionic radius (1.000 Å and 0.950 Å) than that of Mg^{2+} have been successfully incorporated into the brucite-type layers [2]. In comparison, ions like Pd^{2+} and Pt^{2+} with closer ionic radii (0.860 Å and 0.800 Å, respectively) could not be introduced entirely into the layers [2]. The 2D layers of the LDH consist of octahedral units joined via edge-sharing; hence, the coordination preference of the cation has a crucial influence on the formation of the hydrotalcite-type solids.

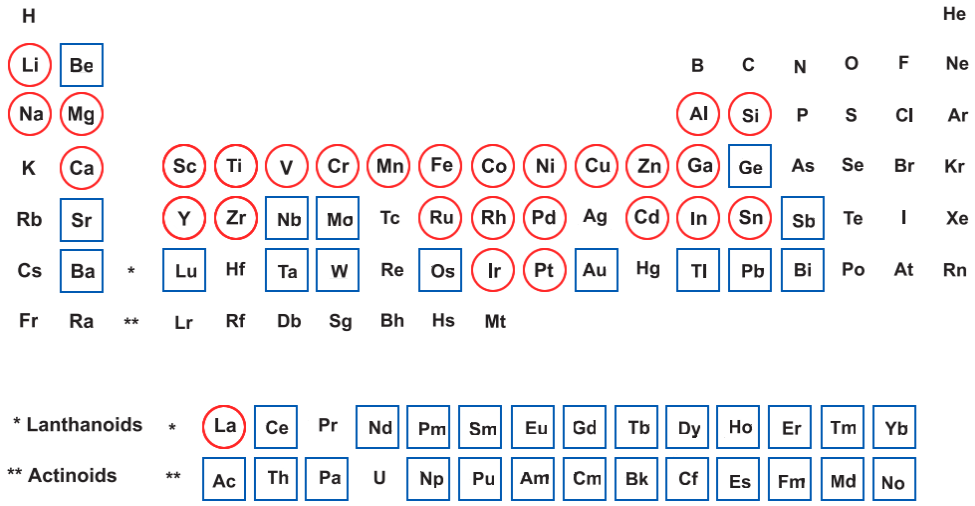

Figure 3. Metals present in the LDH layers, reported in journals ◯ and claimed in patents [13]□

Divalent and trivalent cations located in the third and fourth periods of the Periodic Table are the most frequently found in the brucite-type layers. The divalent cations are often represented by Mg, Ca (Group 2) and Mn, Fe, Co, Ni, Cu, Zn, Cd (late transition period). In contrast, the trivalent ones may come from Group 13 (Al, Ga, In), Group 15 (Bi), and the early transition period (Sc, V, Cr, Mn, Fe, Co, Y) [14]. The low amounts of di- and trivalent cations present in the layers reside in Groups 8, 9 and 10 of the second and third transition periods. There are also some LDH containing monovalent cations, namely Li^{+} and a few having incorporated tetravalent cations belonging to Group 4 (Ti, Zr), Group 7 (Mn) and Group 14 (Sn), respectively [14].Besides the binary systems of metallic cations, the LDH layer architecture may also contain ternary, quaternary and even multi-component ensembles [14]. Pure phases of layered double hydroxides are obtained when x values range from 0.2 to 0.33, depending on the nature of the metallic cations. Hydrotalcite-type materials with x taking values between 0.1-0.5 were also reported, but the X-ray measurement did not reveal the existence of pure phases [14]. Based on the studies completed by Brindley and Kikkawa [15], in the layered double hydroxides having the x value lower than 0.33, the aluminum six-

fold (octahedral) coordination is non-neighboring. If the value of x is higher than 0.33, the possibility of neighboring aluminum octahedral coordinated increases leading to the formation of $Al(OH)_3$. The isomorphic replacement of the metal cations in the brucite-type layers enables the obtaining of a wide variety of layered double hydroxides.

Table 1. Binary systems of metallic cations located in the brucite-like layers of the LDH [12].

		M^{2+}												M^{+}
		Mg	**Fe**	**Co**	**Ni**	**Cu**	**Zn**	**Ca**	**Sr**	**Be**	**Cd**	**Pb**	**Mn**	**Li**
M^{3+}	**Al**													
	Cr													
	Fe													
	Co													
	Ni													
	Bi													
	Sb													
	Ga													
	In													
	V													
	Cr													
	Y													
	La													
M^{4+}	**Ti**													
	Sn													
M^{6+}	**Mo**													

The formation of layered double hydroxides occurs simultaneously with other reactions, namely the obtaining of derivative metal hydroxides, mixed phases or metallic hydrated oxides, as can be seen in the following scheme:

$$(1\text{-}x)M^{2+}_{aq.} + xM^{3+}_{aq.} + yOH^{-}_{aq.} + nH_2O \quad [2]$$

$$\Downarrow$$

$$M^{2+}\text{-}M^{3+}\text{- X LDH} + M(OH)z + MO(OH) + M_xO_y{\cdot}nH_2O + \text{others} \quad [2]$$

The molar ratio between M^{2+}/M^{3+} and the entire chemical composition of the layered double hydroxides is strongly influenced by thermodynamic and structural determinants [2].

1.3.1. Cations replacing magnesium and aluminum in the brucite-type layers

1.3.1.1. Layered double hydroxides with cations that replace magnesium

The most recurrent layered double hydroxide solid consists only of Mg and Al, which can easily be replaced by many metallic cations having the right valence state and ionic radius [16]. The magnesium can be substituted by all the divalent cations from Mg^{2+} to Mn^{2+} with one exception regarding the copper ion, which can produce LDH-type compounds only when it is mixed with other divalent cations such as Mg, Co, Cr, Mn and many others [16]. The literature [17,4,18] sustains that the CuAl-LDHs are difficult to synthesize due to the following reasons: i) at a small pH value (around 5), isolated hydroxide compounds such as $Cu(OH)_2$ or $Al(OH)_3$ may be obtained; ii) the Jahn-Teller effect of the copper cation when is octahedrally surrounded by hydroxyl anions can alter the development of the lamellar structure also reducing the electrostatic interaction between the brucite-type layers and the anions present in the interlayer region; iii) the prepared solids may be impurified with different phases like malachite or gerhardtite, due to the Jahn-Teller effect of the copper cation [16]. As mentioned before, obtaining LDH containing copper cations is possible only when a third divalent cation with a higher concentration will be used, which could overpass the Jahn-Teller effect of the Cu^{2+}. The ratio between the copper cation and the other M^{2+} should be equal to or lower than 1 [4]. After calcination, the copper-based layered double hydroxides are mostly converted in well-dispersed CuO and Cu-spinel phases [16].

When Ni^{2+} species replace the magnesium cations present in the brucite-like layers, the Ni cations are usually evenly distributed in the layered structure and octahedrally coordinated as the literature confirms [19,20]. The Ni/Al ratios influence the stability of the catalysts containing Ni and Al cations. A molar ratio between 0.5-0.85 [21] will enable the formation of stable layered double hydroxide. Neat NiAl-LDHs can be synthesized only when $0.2 \leq x \leq 0.33$ and the Ni/Al atomic ratio varies between 2 and 4 [22]. When the values of x are different from the ones before mentioned, the hydrotalcite-type solids will also contain $Ni(OH)_2$ (bayerite) [22]. The pH value of the preparation method also plays a significant role in the synthesis of Ni-Al hydrotalcites, influencing their morphology but having no effect on the nickel crystallite size [22]. Moreover, lower pH values will generate high amounts of nitrates existing in the structure of the LDH [21]. Different decomposition products are

obtained during the calcination of Ni-Al hydrotalcites depending on the calcination temperature [21,23].

At temperatures around 330 °C, there is an interaction between the components leading to the formation of two mixed oxides: a phase abundant in NiO with a few dispersed aluminum cations and another one containing Al_2O_3 and some dispersed nickel ions [21,23]. The NiO particles can be viewed either as supported by a Ni-aluminate phase [23,24], or decorated by such a phase [23]. The size of these particles is directly proportional to the increase of temperature and is also influenced by the Ni/Al ratio [23]. When the calcination is performed at around 730 °C, nickel oxide (NiO) and nickel aluminate spinel ($NiAl_2O_4$) are obtained [23]. After calcination, an exciting observation is that the aluminum present in the calcined solids exhibits a stabilization effect [22] but not when the atomic Ni/Al ratio is higher than 3 [22].

The literature [25,26] states that the layered double hydroxides containing nickel have higher thermal stability than the copper-based hydrotalcites, which can only operate in reactions to temperatures up to 250 °C because their activity will dramatically decrease due to copper sintering.

In the case of the magnesium cations replacement with cobalt ones, the literature reports are pretty insufficient. The CoAl-layered double hydroxides samples that have been synthesized up until now have the sole purpose of acting as precursors for obtaining oxide-type catalysts, usually denoted as CoO/Al_2O_3 [27]. When cobalt is added to the MgAl-LDH matrix, the newly acquired solid is thermally destabilized because cobalt hydroxide is not as stable in the air as magnesium or aluminum hydroxides, and cobalt cations also present a decreased affinity for the carbonate anions in comparison with Mg^{2+} [28]. When the CoAl-LDHs are calcined different oxide phases result. The obtaining of a mixed phase of different spinels (Co_3O_4, $CoAl_2O_4$, Co_2AlO_4) even at low temperatures (approx. 200 °C) is attributed to the easy oxidability of Co^{2+} and the thermodynamic stability of Co_3O_4 (compared with CoO) in the air [29]. Besides forming different cobalt aluminate mixed spinel phases, a (Co, Mg)O solid solution is also obtained [28]. Cobalt cations adopt an octahedral geometry in the (Co, Mg)O solid solution, while in the spinels based on the aluminum substitution, it may exhibit both octahedral and tetrahedral coordination [28]. The amount of spinel phases obtained is directly proportional to the increase in the calcination temperature [30]. The reduction of Co^{3+} to Co^{2+} present in the spinel phase occurs at smaller temperatures than the reduction of Co^{2+} to Co^0 in the (Co, Mg)O solid solution, suggesting that the catalytically active sites are preponderantly located in the spinel phases [30].

In what concerns the ionic radius of the presented cations (Cu^{2+}, Co^{2+}, Ni^{2+}), the Periodic Table offers the following trendline $Co^{2+}>Ni^{2+}>Cu^{2+}$ [31]. Moreover, due to the Jahn-Teller effect, the copper cations in an octahedral stoichiometry have a smaller CFSE (crystal field splitting energy) value compared to Ni^{2+} [31], which adds more stability to Cu^{2+} and modifies the ordering of the ionic radius as indicated in the Irving-Williams series [32], namely $Co^{2+}<Ni^{2+}<Cu^{2+}$. Both octahedral and tetrahedral crystal field splitting energies are important for the cations as a criterion of inclination towards the octahedral sites or the tetrahedral ones, respectively [31]. Burns [33] considered that Co cations in an octahedral stoichiometry compared to Ni^{2+} and Cu^{2+} have a small CFSE and by default larger ionic radius. So, the final trendline of the ionic radius will be as follows: $Co^{2+}>Cu^{2+}>Ni^{2+}$.

The catalytic activities of layered double hydroxides containing different combinations of Ni, Cu, Co have been usually tested in reactions such as oxidation [19,34], dehydrogenation [35], isomerization [36], steam reforming [36], photocatalysis [37] and many others.

1.3.1.2. Cations that replace aluminum

Rare earth metals are a group of 17 elements (lanthanum and the other 14 elements that follows it, together with scandium and yttrium) often divided into light and heavy rare earth elements [38]. Lanthanides have proved their value to the scientific world due to their remarkable contribution to catalysis and technology [39]. The aluminum cations usually present in the layered double hydroxides can be replaced with different trivalent cations, including ones from the group of lanthanides (Figure 4) [40]. The amount of rare earth metallic cations in the hydrotalcite matrix is influenced mainly by their ionic radius (Table 2) and preparation methods [41]. The Shannon ionic radii of hexacoordinated cations belonging to the lanthanides (Table 2) are larger than those of the usual cations present in the LDH matrix, namely Mg^{2+} (0.72 Å) and Al^{3+} (0.535Å), respectively [42]. Therefore, most of the lanthanides can be partially included or not inserted at all in the brucite-like layers leading to an alteration of the structure and the deposition of different segregated oxihydroxi-carbonate phases on the hydrotalcite surface [40]. A few examples in the literature sustain that the total insertion of cerium cations in the hydrotalcite matrix is possible through the urea hydrolysis method [43,44] or by the sol-gel technique [44, 45]. The hydrotalcite-type solids are usually modified with rare earth cations to increase their basicity in terms of the number of medium/strong sites [40] and thus, leading to improved catalytic activities in reactions such as cyanoethylation [46], transesterifications [47], condensation [48], etc. Apart from their scarcely use in catalysis, the layered double hydroxides containing lanthanide ions and/or

lanthanide complexes have been intensively studied as light-emitting materials, with practical device applications [49].

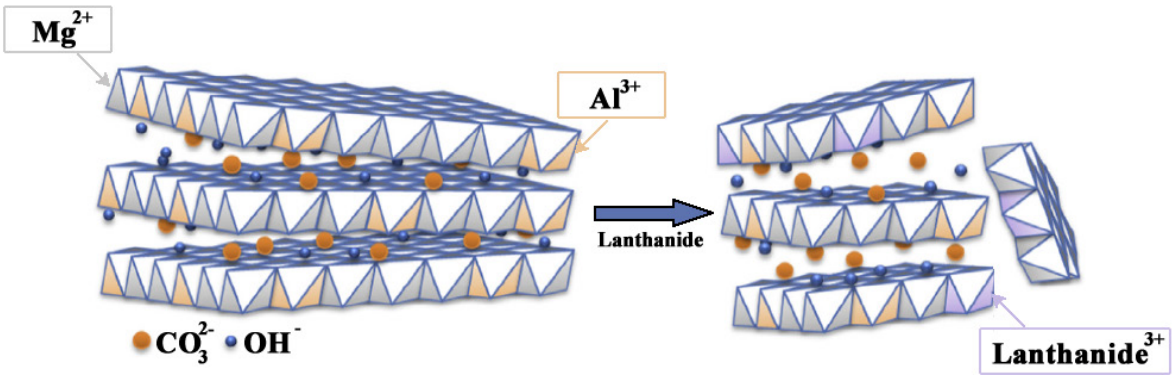

Figure 4. Representation of the structure for MgAl-LDH and the MgAl-LDH modified with rare earth cations [40].

Table 2. Shannon ionic radii of the hexacoordinated cations [42].

Cation	Shannon ionic radii of the hexacoordinated cation (Å)
Mg^{2+}	0.720
Al^{3+}	0.535
La^{3+}	1.032
Ce^{3+}	1.010
Pr^{3+}	0.990
Nd^{3+}	0.983
Pm^{3+}	0.970
Sm^{3+}	0.958
Eu^{3+}	0.947
Gd^{3+}	0.983
Tb^{3+}	0.923
Dy^{3+}	0.912
Ho^{3+}	0.901
Er^{3+}	0.890
Tm^{3+}	0.880
Yb^{3+}	0.868
Lu^{3+}	0.861

The literature sustains that the luminescence properties of hydrotalcites doped with lanthanides depend mostly on the morphology of the host framework [41]. Due to the highly tunable composition regarding the metallic cations and interlamellar anions of the layered double hydroxides, the development of lanthanide-LDH hybrid systems will lead to obtaining new functional materials with both optical and catalytical properties.

1.4. Interlayer structure of layered double hydroxides

The interlayer space can be described as an intricated matrix of hydrogen bonds created between the hydroxyl groups present in the brucite-type layers, anions, and water molecules [4]. Practically, the interlamellar galleries are disorganized, and the hydrogen bonds are in ongoing fluctuation leading to an inaccurate determination of the interlayer composition [14]. The brucite-type layers and interlamellar galleries of the layered double hydroxides are held together by an amalgam of hydrogen bonds and electrostatic interactions. The hydroxyl groups, especially those chained to the trivalent cations present in the layers, are highly polarized and connect with the interlayer anions located between the lamellas [14]. The purpose of each anion is to compensate for the positive charges provided by both cationic layers. There are practically endless possibilities regarding the nature of the anions capable of satisfying the positive charges, considering the anions do not extract the metallic cations from the layers and have proper charge density [14]. By now, many anions have been included in the LDH structure during the formation of the lamellar structure or introduced by anion exchange [50]. These anions can be grouped into the following families of compounds [51]:

- Halide anions (fluoride, chloride, bromide, iodide anions).
- Non-metal oxo-anions (carbonate, sulfate, arsenate, nitrate ions, etc.).
- Oxometallate anions (vanadate, molybdate tungstate, etc.).
- Polyoxometallate anions (decavanadate, decatungstate, etc.).
- Organic anions (acetate, carboxylates, dicarboxylates, alkylsulfates, alkanesulfonates etc.).
- Anionic polymers (poly(sodium styrene sulfonate), poly(vinyl sulfonate), polyacrylate, poly(methyl methacrylate) etc.).
- Biochemical anions (large variety of amino acids in anionic form, enzymes, proteins, DNA with 500-1000 base pairs, ATP, ADP, etc.).

The above-mentioned anionic species should only be superficially maintained in the LDH network, enabling their exchange with other anions with cross-sectional areas smaller than the remaining free space near the steady positively charged sites [51]. The layered double

hydroxide compounds having oxoanions intercalated show confined hydration status due to the increased charge densities and their hydrophilic character, while the LDH containing organic anions display a much better water-swelling performance [51].

Moreover, the amount, the dimensions, the orientation of the anionic species and the stability of the bonds created between them and the hydroxyl groups located in the brucite-type layer impose the thickness of the interlamellar space [51].

1.4.1. Interlamellar anions

1.4.1.1. Polyoxometalates (POMs)

Polyoxometalates (POMs) are a diverse family of compounds obtained from the condensation of metal oxide polyhedra (MO^x, M = W^{VI}, Mo^{VI}, V^V, Nb^V, Ta^V, etc., and x = 4 – 7) with each other through corner-, edge-, or rarely in a face-sharing manner [52]. Their formation is based on the appropriate charge to ionic radius ratio and charge density which: (i) constrains infinite polymerization; (ii) enables the formation of π-bonds with the O^{2-} ligands; (iii) exhibits flexible and various coordination geometries [53]. The metal atoms are addenda atoms because they can change their coordination with oxygen from 4 to 6 while the MO_x polyhedral condenses in solution upon acidification [52]. The nature of the ligand (water, hydroxo or oxo species) dictates the extent of the polymerization. The nature and the number of the ligands depend on the solution pH and on the metal Mn^+ charge value. Although oxygen is the most known ligand capable to coordinate with the addenda atoms, there were some POM clusters reported in the literature [52] which contain other atoms/groups such as sulphur, bromine, nitrosyl and alkoxy. When the POM framework consists of addenda metals (from groups 5 and/or 6) and oxygen, the cluster is called isopolymetalate, and the Lindqvist type anion $[M_6O_{19}]^{2-}$ is an archetypical example (Figure 5). If the POM shows additional elements besides addenda metals and oxygen, it is known as a heteropoly complex, formed by condensation of MOx polyhedra around a central heteroatom while the solution is acidified [52]. A large variety of atoms can be slotted as heteroatoms such as Be, B, Al, Si, Ge, Sn, P, Te and the whole first row of transition elements. The atomic ratio between the surrounding atoms (referred to the addenda atoms) and the central heteroatom (arranged in tetrahedral or octahedral coordination) can be 6, 9, 11 or 12 [54]. These ratios come from the most common heteropoly compound structures. The most well-known and studied structure is the so-called Keggin with the general formula $[X^{n+}M_{12}O_{40}]^{(8\ -\ n)-}$ (atomic ratio M/X = 12) [54]. POM compounds present high Brønsted acidity attributed to their large size which allows the delocalization of the surface charge density throughout the polyanion, leading to a

weak interaction between H^+ and the anion. In addition to their high acidity, POMs display efficient redox behavior allowing fast transformations under soft conditions [54].

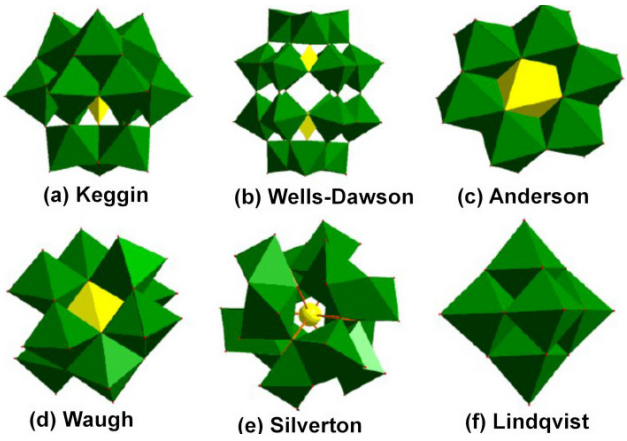

Figure 5. POM structures in polyhedral representations.

This makes of POM highly efficient catalysts in oxidation reactions. More than just creating a large diversity of polyoxometalates compounds, these discrete and well-defined structures offer huge adjustable possibilities for a variety of functional nanoscale systems [53].

1.4.1.2. POM/LDH nanocomposites

The POM/LDH nanocomposites have attracted wide interest as they have great advantages over other LDH compounds, especially as catalytically active materials [53] attributed to the synergetic effects between the hydrotalcite and the polyoxometalates. LDH materials possess relatively weak interlayer interactions and therefore, they offer a remarkable opportunity for the development of different techniques that will allow the modification of their functionality without compromising their structural features. Incorporation of catalytically active species, such as simple inorganic anions, complex ligands or biomolecules into the interlayer region of LDHs, is an effective immobilization method and has been demonstrated to be an effective approach to enhance the catalytic stability and recyclability when compared to their corresponding homogeneous system [53]. A series of intermolecular interactions, including electrostatic and hydrogen bonding can be found between the brucite-like layers of LDHs and the intercalated POM anions [52]. The general structure of the POM-LDH composition is illustrated below in Figure 6. Although POM intercalated LDH exhibits superior application capabilities compared to individual components, the intercalation of POMs into LDH faces several serious complications. First of all, there is the possibility that the M^{2+}/M^{3+} cations will leach out during the anions exchange reactions between LDH precursor and the POM anions which occurs under the neutral to slightly acidic reaction conditions [52]. Secondly, the

M^{2+}:M^{3+} ratio in the POM pillared LDH must be rigorously controlled since it helps to determine the charge density of the LDH layers, affecting also the basal spacing between the brucite-type layers [55,52]. In order to prepare POM/LDH nanocomposites with different pore size distributions, it is necessary to retain, as much as possible, the desired M^{2+}:M^{3+} ratio from the initial step of synthesis through the final product [52].

It should be mentioned that according to IUPAC rules [56], the main characteristic of intercalation compounds is the swelling of layered materials appeared when guest species are inserted in the interlayer region, while the term "pillared" should be applied only to the solids obtained by thermal or chemical transformation of a layered compound, which shows microporosity or mesoporosity and is considered to be stable, both chemically and thermally [57]. This is not often related to POM–LDH hybrids, which are thermally less stable than the compounds obtained starting from cationic clays [57]. Moreover, some POM anions were proven to be unstable at weakly acidic to base pH [52], explaining why the pillaring reactions are usually accompanied by the co-formation of an impurity phase, which is the M^{2+} rich salt of the POM that deposits on the surface of the LDH crystallites [52]. Its deposition can block the micropores of LDH, resulting in low surface areas [52].

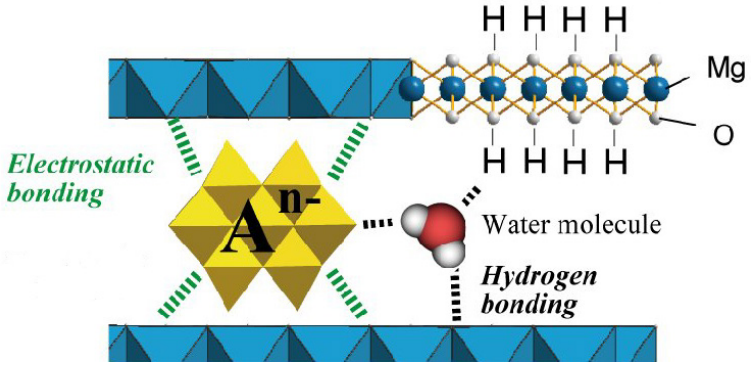

Figure 6. Schematic representation of a POM/LDHs structure.

It is difficult to prepare POM/LDH nanocomposites in a crystalline form mostly because LDH hosts act like a base, while most polyoxometalates present acidic properties. Several synthetic approaches can be used for the preparation of POM-LDH composites. Among the most developed ones are the ion exchange synthetic pathway, co-precipitation and reconstruction [53]. There are also some relatively new preparation techniques that still need improvements such as electrochemical reduction, ultrasound treatment and delamination technology. The variety in what concerns the size and features of polyoxometalate compounds can be effectively used in the structural construction of new composite materials

that display specific gallery height. Also, it is possible to access the gallery region by enlarging the lateral anion spacing if POMs with relatively high-charge density will be used in the construction of the hybrid materials. Therefore, POM can be viewed as ideal functional guest anions for intercalation offering the possibility of enhancing and fine tuning of the composite's properties. Moreover, the synergetic effect between the constituents of the POM intercalated LDH composite material may cause the appearance of new functionalities which will lead to improved performance and will offer the opportunity to expand the areas of application [53]. The POM/LDH nanocomposites have been widely applied in catalytic reactions such as epoxidation of alkenes, molecular oxygen generation, esterification of acetic acid, oxidation of thioether and thiophene, etc [52]. The prepared POM-LDH composites show superior catalytic performance compared to the relevant performance of their parent components. The active components are uniformly dispersed in the 2D confined space defined by the LDH layers. Additionally, the design of the robust confined space in combination with the intermolecular interactions induces further stability to the system, prevents leaching of the POM species into the reaction mixture and increases the catalyst's selectivity [52]. The POM/LDH composite materials have also found a wide range of applications in enhancing the photo-luminescent properties of lanthanide anions and promoting the adsorption of harmful materials like dyes from wastewater [52]. Recently, the delamination of LDH nanosheets before their use in the development of the POM/LDH nanocomposites has been employed to engineer novel materials in this field. This new technology may solve the above stated problems as well as retain the original composition of POMs apart from opening a new field of application as photo-luminescent materials based on the ultra-thin film [53].

Further investigations and expansion of the family of POM-LDH composite materials will bring great opportunities in the development of economical and versatile methods for designing specific structural features that could lead reactions towards the desired path and will offer a better control over electron transfer properties of the POM-LDH intercalated composite [52]. Finally, the exploration of alternative design approaches will enable the construction of POM-LDH materials that present new chemical and physical properties, new types of functionalities as well as a wider view of catalytic applications [52].

1.4.1.3. Molybdates

The intercalation of molybdenum-based anions in the structure of layered double hydroxides is a laborious process and depends mostly on the pH and the Mo(VI) concentration. Moreover, the evolution of Mo(VI) in solutions is enriched due to the existence of polymers which may lead to the obtaining of a variety of anions, the predominant ones being $[MoO_4]^{2-}$, $[HMoO_4]^{-}$, $[Mo_6O_{19}]^{2-}$, $[Mo_7O_{24}]^{6-}$, $[HMo_7O_{24}]^{5-}$, $[H_2Mo_7O_{24}]^{4-}$ and $[Mo_8O_{26}]^{2-}$ [58]. The geometry of smaller anions, such as $[MoO_4]^{2-}$ is tetrahedral, while larger anions like $[Mo_6O_{19}]^{2-}$ and $[Mo_7O_{24}]^{6-}$ possess octahedral or distorted octahedral configuration. The intercalation of vanadates in the interlayer space of layered double hydroxides has been intensively studied, while that of molybdates has been restricted to the heptamolybdate $[Mo_7O_{24}]^{6-}$ ions which can be stabilized at a lower pH and can act as pillars used to expand the distance between the brucite-type sheets. Also, Van Laar et al. [59] discovered that the $[MoO_4]^{2-}$ hydrolysis at a pH value of 10 inhibits intercalation in the LDH structure and polymerization of molybdate does not occur until pH < 7 (Figure 7). The molybdate-containing LDH with slightly different chemical composition could be useful as selective catalysts for different processes. The first studies recorded for the characterization of oxomolybdate species at different acidic pH values were based on potentiometric titrations [58]. The main conclusion was that $[MoO_4]^{2-}$ ions are stable at pH 6.5, while at a pH between 4 and 6.5, the heptamolybdate $[Mo_7O_{24}]^{6-}$ exists in equilibrium with $[MoO_4]^{2-}$. Further acidification, 1.5 < pH < 2.9, enabled the obtaining of octamolybdate anion $[Mo_8O_{44}]^{2-}$. Larger ionic aggregates are expected to appear at lower pH values, but there are no studies related to this statement [60]. Similar to the chromate- and vanadate-containing LDH, the reported methods used to prepare hydrotalcites with intercalated molybdenum-based anions containing different pairs of divalent/trivalent cations in the brucite-like layers are co-precipitation, anion exchange and hydrothermal method. The studies showed that molybdenum can be introduced either as a cation in the brucite-type layers, or as one of its anionic forms in the interlayer. The most used method for molybdate incorporation in MgAl-LDH structure is the anionic exchange. However, Drezdon et al. [61] reported a new technique derived from the classical ionic exchange that involves primarily the synthesis of an organic anion-pillared precursor also called swelling agent which is subsequently exchanged with an adequate polyoxometalate anion under acidic conditions [61]. In this case, the organic anion needs to have slightly larger dimensions than the polyoxometalate to be incorporated. By creating an acidic medium, the organic anion already incorporated in the LDH will be protonated, weakening the electrostatic interaction between the cationic layers

and the intercalated organic species and thus allowing the partial exchange of the organically-pillared hydrotalcite with the polyoxometalate [61]. Moreover, the anion affinity in LDH interlayers depends on the size of the ion and its associated charge [62]. Monovalent anions have lower affinities than divalent anions and are therefore more likely to participate in anion exchange reactions [62]. Based on the XRD results, Davantes et al. [63] were able to create a representative scheme which describes the interlayer exchange of different anions (Figure 8). The affinity series decreases in the order $[Mo_7O_{24}]^{6-} > CO_3^{2-} > [MoO_4]^{2-} > SO_4^{2-}$ [63]. The diffraction patterns of the Mo-intercalated samples obtained by Carriazo et al. [64] are characteristic to hydrotalcite-like structure, indicating a rhombohedral packing of the layers.

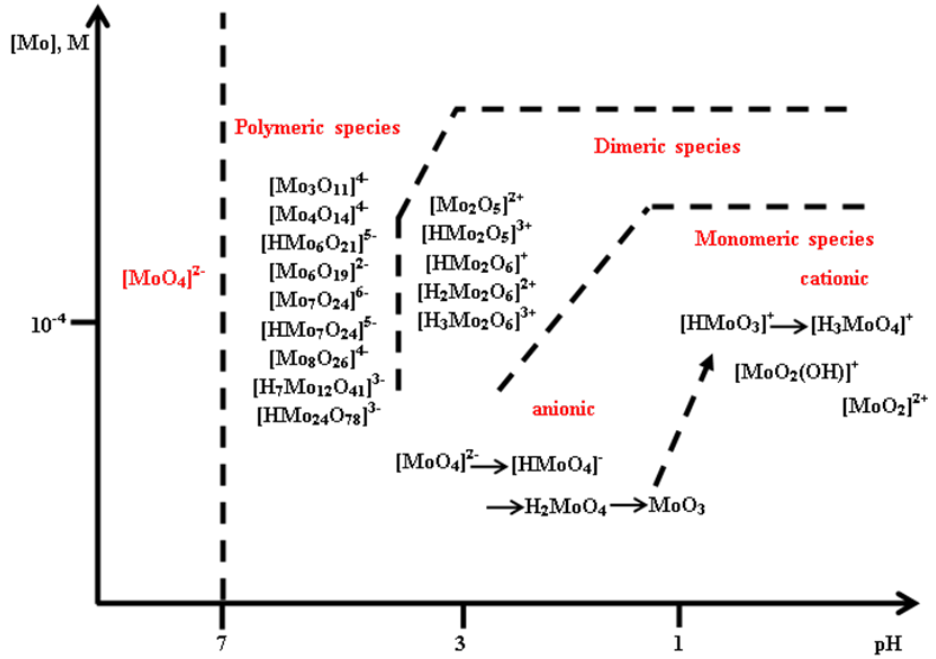

Figure 7. The polymerization degree of oxomolybdate versus pH. Adapted from Ref. [65], Copyright 2004, American Chemical Society.

The powder XRD patterns of layered double hydroxides usually present a decrease in the intensities of the (00l) lines while the value of *l* increases, but in this situation, it was observed that the intensity of the (006) and (009) lines are larger than that of the (003) line.

This abnormal behavior is specific for LDH intercalated with different POM and appears due to the large atomic scattering factor of the interlamellar species [64].

In the Raman spectra recorded for the Mo-LDH samples it was observed that the most important bands are present in the regions 890–950 and 300–360 cm^{-1} and are most likely attributed to the main types of molybdenum-based anions that can appear within the hydrotalcite structure: $[MoO_4]^{2-}$, $[Mo_2O_7]^{2-}$ and $[Mo_7O_{24}]^{6-}$ [66]. At low Mo loading, the

Raman spectra display bands at about 895 and 320 cm^{-1} which clearly belong to the monomer $[MoO_4]^{2-}$ species. In these spectra, there are also some bands at 1050 and 709 cm^{-1} attributed probably to the residual NO_3^- anions [66]. By increasing the Mo loading, the Raman spectra became more complex, suggesting that octahedrally coordinated polymolybdate species (i.e., $[Mo_2O_7]^{2-}$ with band at 920 cm^{-1} and $[Mo_7O_{24}]^{6-}$ with bands at 947 and 358 cm^{-1}) were formed, while the bands characteristic for the nitrate and molybdate ions decreased in intensity until their complete disappearance.

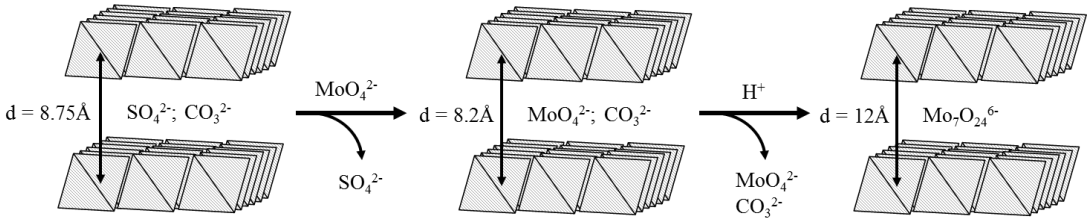

Figure 8. Schematic representation of molybdate exchange in LDH. Adapted from Ref. [63], Copyright 2013, American Chemical Society.

The heptamolybdate anion was the major species in the sample containing the highest Mo concentration [66].

Table 5. Raman frequencies (cm^{-1}) for Mo oxyanions species [67,66,68].

Vibration type*	**Anion species**			
	$[MoO4]^{2-}$	**$[Mo_2O_7]^{2-}$**	**$[Mo_7O_{24}]^{6-}$**	**$[Mo_8O_{26}]^{4-}$**
υ_s (Mo=O)	895-898	920-930	937-945	965
υ_{as} (Mo=O)	837-846		903	925
δ (Mo=O)	300-320	355	355-365	370
υ (Mo-O-Mo)			564	860

* υ_s = symmetric stretching mode attributed to Mo=O bond vibrations; υ_{as} = antisymmetric stretching mode; δ = bending mode.

Yu et al. [69] were able to record the FT-IR spectrum of $[MoO_4]^{2-}$-pillared ZnAl hydrotalcite which consists in bands attributed to hydroxyl stretching vibrations (3430 cm^{-1}) and bending modes of interlayer water (1630 cm^{-1}). There is also a band at 1368 cm^{-1} specific for CO_3^{2-} stretching mode which may indicate the contamination of the material by atmospheric CO_2 [69]. Additionally, the characteristic band assigned to the antisymmetric mode of Mo–O–Mo in $[MoO_4]^{2-}$ is found at 834 cm^{-1}. Moreover, the bands at 620, 559 and 428 cm^{-1} can be related to the vibrations modes of the oxygen atoms at the layer crystal lattice [69].

Polyoxometalates based on molybdenum have been often applied in heterogeneous catalysis because of their interesting redox properties. Layered double hydroxides containing heptamolybdate $[Mo_7O_{24}]^{6-}$ species in the interlayer prepared by ion exchange from suitable precursors proved to be effective catalysts in epoxidation of different substrates.

Zavoianu et al. [70] have studied the effect of the synthesis methods on the physicochemical properties and catalytic performance of MgAl-molybdate-LDH in cyclohexene oxidation with hydrogen peroxide [70]. Five samples have been prepared by (i) ionic exchange procedure as described by Kwon et al. [71], between a hydrotalcite containing carbonate anions previously obtained by co-precipitation at pH = 10 and low supersaturation with aqueous Na_2MoO_4; (ii) competitive ionic exchange at pH 10 using a hydrotalcite containing carbonate anions, aqueous Na_2MoO_4 and p-toluene sulfonic acid (pTOS) as swelling agent, based on Van Laar studies [72]; (iii) exchange of the carbonate precursor LDH with pTOS at pH 4.5 followed by the exchange with molybdate at pH 4.5 under a constant stirring for 24 h and a readjustment of the pH to 10 using NaOH; (iv) direct synthesis at high supersaturation and pH 10 [57]; and (v) direct synthesis at low supersaturation and pH 10 [57,70]. The characterization techniques used (FTIR, Raman and UV–Vis spectroscopies) indicate the presence of $[MoO_4]^{2-}$ and smaller amounts of $[Mo_7O_{24}]^{6-}$ species in all samples. The catalytic activity of the solids is correlated with the basicity which decreases with the increase in Mo loading [57,70].

Van Laar et al. [72] reported on a molybdate-exchanged layered double hydroxide heterogeneous catalyst for the conversion of H_2O_2 into singlet molecular dioxygen ($^1O_2$) [72].

Ciocan et al. [68] have synthesized two series of Mo-containing hydrotalcites by different techniques: one by ion exchange at atmospheric pressure, after complete synthesis of LDH, and another by ion exchange under hydrothermal conditions during the aging step of LDH synthesis. The influence of the anion exchange method on the catalytic properties was investigated for oxidation reactions of dibenzothiophene (DBT) and anthracene by hydrogen peroxide [68]. The catalytic tests performed under moderate conditions (40–70 °C), indicated that both types of catalysts are active, but the samples obtained under hydrothermal conditions are more active due probably to their larger specific surface area which makes easier the access to active sites [68]. The oxidation of dibenzothiophene with H_2O_2 using as catalyst a MgAl-LDH intercalated with heptamolybdate species was also studied by Dobrea et al. [66]. The DBT conversion powerfully increased when the metal amount in the Mo-LDH sample increased [66]. Zavoianu at al. [73] have studied the oxidation of tert-butanethiol (t-BuSH) using as catalysts Mo-LDH samples obtained from two different molybdenum

sources, e.g. Na_2MoO_4 or $(NH_4)_6Mo_7O_{24}$ and prepared by two methods: (i) ionic exchange and (ii) co-precipitation at pH 10 under high supersaturation [73]. When Na_2MoO_4 was used as a molybdenum source, crystalline materials with relatively high basicity and fine dispersion of molybdate species were obtained. These samples showed the best catalytic activities leading to high conversions of t-BuSH of about 80%.

Choudary et al. [74] have reported the use of molybdate-containing MgAl-LDH for the synthesis of β-bromostyrenes in aqueous medium via halodecarboxylation reaction of cinnamic acid. The high catalytic activity exhibited by the LDH may be due to its basic character and the large positive charge of brucite layers which may further lead to the enrichment of bromide ion near the surface [74]. Moreover, the excess of positive charge on the LDH surface shields the negative charge of the peroxomolybdate and bromide reaction partners and therefore ensuring high halide oxidation rates [74].

Klemkaite-Ramanauske et al. [75] have prepared molybdate-containing MgAl layered double hydroxides by using different variations of the co-precipitation method and used them as catalysts for the synthesis of 2-adamantylidene(phenyl)amine Schiff base. All the synthesized molybdate-containing layered double hydroxides presented a similar catalytic activity for the studied reaction; no matter what co-precipitation route was used for preparation [75].

Apart from the crucial role in the conventional catalysis, Mo-containing LDH can be also used as photocatalyst for electrocatalytic water oxidation [76], as adsorbent [77,64,63] or as an anti-corrosion material [69,78].

1.4.1.4. LDH modified with graphene oxide

The history of graphene and graphene oxide (GO) dates back to 1859, when Benjamin Collins Brodie, a professor at the University of Oxford, started investigating graphite's structural and chemical properties [79]. Then, the field of graphene and its derivatives was taken by storm in 2004 when Geim, Novoselov and coll. have sent to publication a paper about the characterization of a single sheet of graphene deposited on films [80]. Their research regarding graphene was rewarded with the Nobel Prize in Physics in 2010. Graphene is a monolayer of carbon atoms organized in a two-dimensional honeycomb framework which presents an increased theoretical surface area of approx. 2600 m^2/g, impressive electrical conductivity, and electron mobility [81,82]. Graphene oxide (GO) is an essential derivative of graphene and can be produced on a large scale and at a low cost by chemical exfoliation of graphite [83]. Although graphene oxide has been the main subject of a consistent number of studies [83,84], its precise chemical structure is still vague and

challenging to determine due to the following reasons: i) it has high hygroscopicity, ii) at a temperature above 60-80 °C, it starts to decompose, iii) the synthesis method dictates its final composition [84]. Hofmann and Holst [85] were the first who propose a structural model of graphene oxide (Figure 9) in which the oxygen forms an epoxy linkage with the carbon atoms [84]. Ruess [86] has created a structural model that includes hydrogen atoms by suggesting that the carbon planes are creased and made of linked trans cyclohexene chair conformation, while in 1,3 position, the carbon atoms are bound to hydroxyl groups and ether oxygens [84].

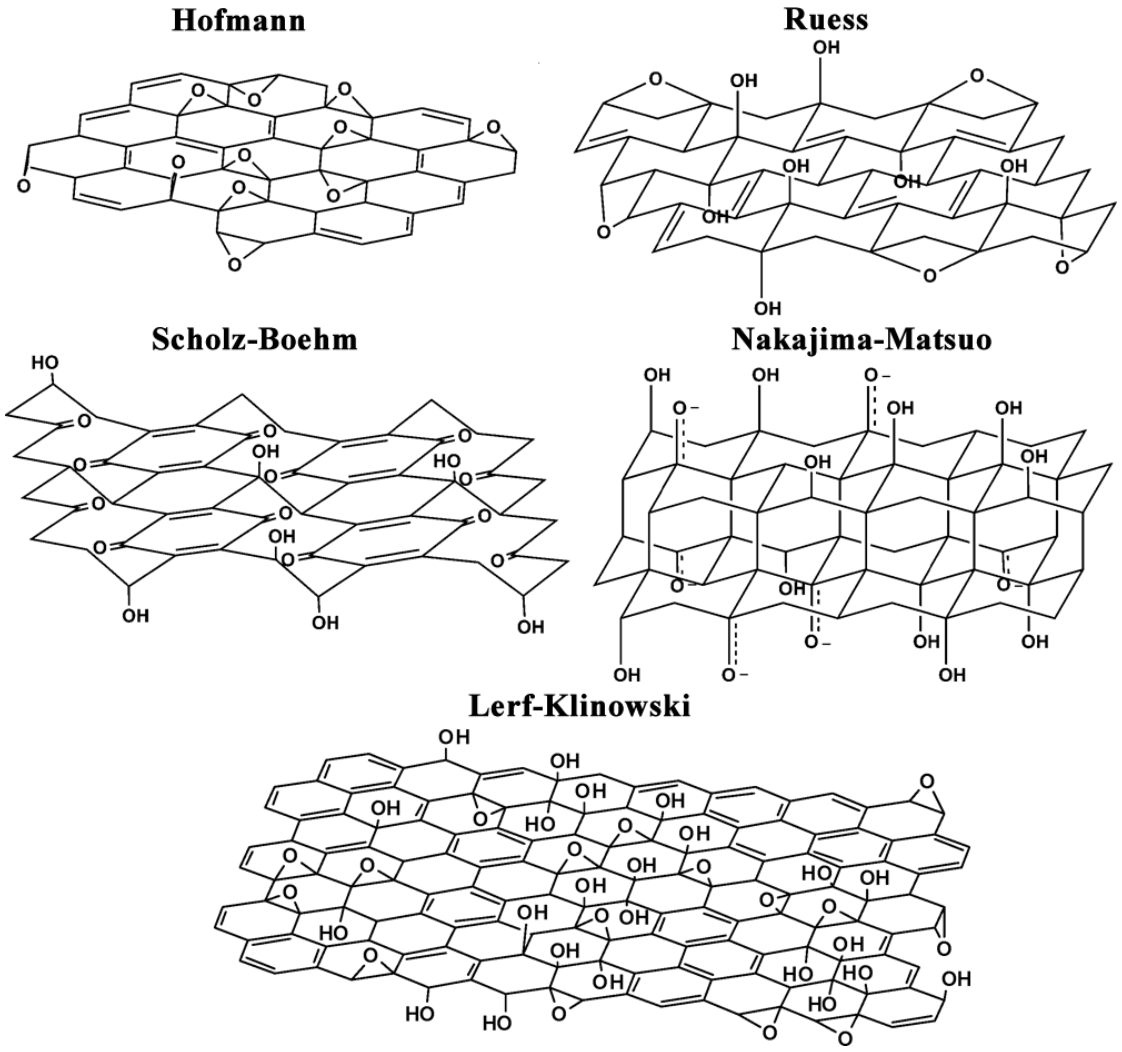

Figure 9. Structural models of graphene oxide (GO). Adapted from Ref. [84].

The model was improved by Clauss and his team [87] by adding C=C double bonds, ketone and enolic groups, and it was stereochemically remastered by Scholz and Boehm [88]. Nakajima [89] observed that the fluorination process of graphene oxide would give a diffraction pattern similar to graphite fluoride $(C_2F)_n$, stage 2. All the proposed models were overthrown by the one created by Lerf and his co-workers [84], which is based on NMR

spectroscopy. Their study indicated that the graphene oxide layer has irregular disposal of sp^2 and sp^3 hybridized carbon atoms and different pendant groups like hydroxyl, epoxy, and carboxylic groups [84].The structural arrangement is not the only difficulty regarding graphene oxide but also its instability in air and water, leading to an unpremeditated shrinkage and gradually converting GO flakes into humic acid-like structures [90-93]. The main synthesis methods of graphene are divided into bottom-up and top-down methods [94]. The bottom-up strategies, including CVD (chemical vapour deposition) and epitaxial growth, have proven expensive, challenging, and time-wasting [94].

So, top-down methods are usually preferred to prepare graphene oxide [94]. Brodie [95], Staudenmaier [96], and Hummers [97] are the scientists who gradually contributed to the development of a safer technique for the synthesis of GO-based on the oxidation of graphite.

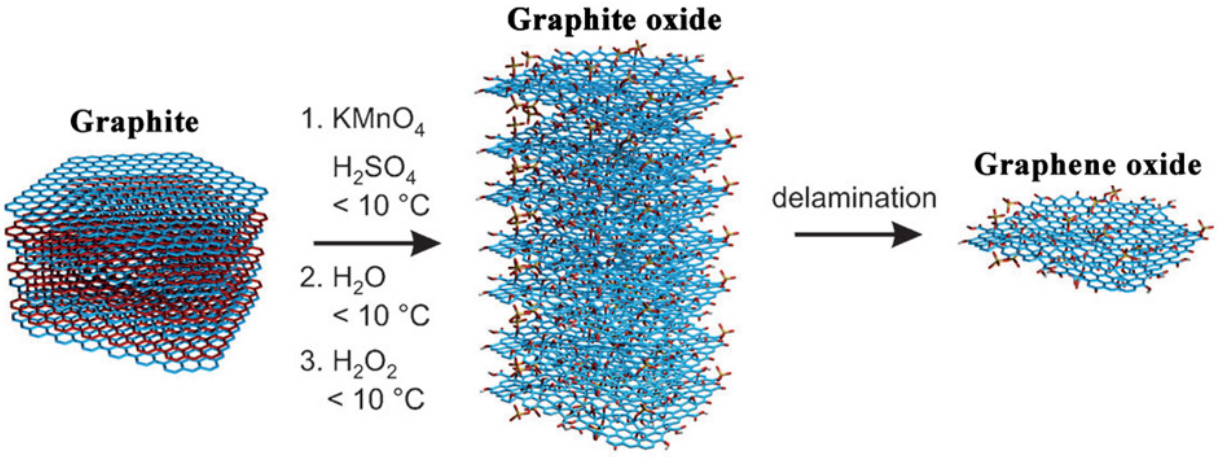

Figure 10. Hummers method for the preparation of graphene oxide (GO). Adapted from Ref. [94]

The method developed by Hummers (Figure 10) is scalable and safer and is the most often used procedure to obtain graphene oxide [98]. In the first step, a carbonaceous source, usually naturally graphite, is dispersed into protonate solvents like sulfuric or phosphoric acid or a mixture, leading to graphite sulfate obtaining [98]. The introduction of sulfate increases the layer distance, activating the graphite [98]. In the obtained mixture, a strong oxidizing agent like KMnO4 is also added, which diffuses through the interlayer space of the graphite sulfate creating manganese esters [94,98]. Water and H2O2 are further inserted into the mixture to hydrolyze the formed esters and dissolve the manganese-oxo species [98].

The resulting solid is then treated with dilute HCl to remove any metallic species remaining in the mixture [94].The resulting graphite oxide is then washed with hot water and

centrifuged. The hot water starts the delamination of the graphite oxide and its conversion into graphene oxide [94,98]. Combining various nanomaterials with different physical and chemical properties can lead to obtaining improved nanocomposites possessing the qualities of the parent building blocks [99]. Recently, such hybrid materials have gained much attention due to their usefulness in various applications [100]. Graphene oxide and layered double hydroxides are among the multiple compounds that can be combined. Despite its advantageous properties, graphene oxide tends to agglomerate and restack [100], so to overcome this problem, it is necessary to embed other materials onto GO, like layered double hydroxides. Graphene oxide and LDH present different reciprocated chemical and physical properties until a certain point [100], offering hybrid materials with a layered structure, large surface area, multiple functional groups coming from GO, and the anionic exchange ability of the hydrotalcites [101]. The synthesis of GO-LDH hybrids will automatically imply two steps. The first step will be the preparation of the graphene oxide-water suspension, using one of the methods discussed previously, usually Hummer's method [97]. The second one will combine the graphene oxide suspension with different metallic ions and an alkali compound by applying one of the following preparation techniques: co-precipitation, in-situ growth, and hydrothermal method [101]. The synthesis process of GO-LDH hybrid materials is schematically represented in Figure 11.

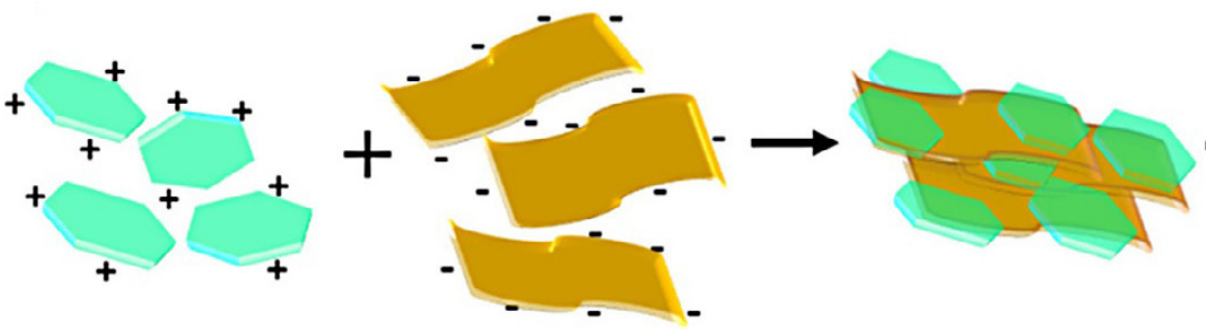

Figure 11. Schematic representation of preparation process of GO-LDH composites. Adapted from Ref. [81].

The literature confirms that there is a synergistic effect between GO and LDH which leads to hybrids having an improved performance when they are utilized in energy storage [102], catalysis [103], adsorbents [104], nanofillers [105] or when they participate in drug delivery [106]. GO-LDH nanocomposites present an excellent performance in many fields of application, so they need to be explored further.

1.5. LDH-derived mixed oxides

The thermal decomposition of layered double hydroxides at certain temperatures can lead to the obtaining of derived mixed metal oxides (MMO) [107]. The thermal decomposition of the LDH precursors usually includes the following steps: dehydration, dehydroxylation, decomposition of anions [108]. This entire process ends with the obtaining of metastable crystalline and amorphous phases, oxides with rock salt phase and mixed oxides with spinel phase [50,108]. The properties of these phases are influenced by [50]:

i) The nature of both anions and cations
ii) The ageing time and the temperature during the precipitation
iii) The presence of impurities, usually acquired during the precipitation step

For instance, the transformation of the natural occurring hydrotalcite, $[Mg_3Al(OH)_8][(CO_3)_{1/2}\cdot 2H_2O]$ starts with the dehydration of the compound at 100-250°C, followed by dehydroxylation (300-450°C) and decarbonation (420-470°C) generating a MgO phase and mixed oxides (rock salt and spinel) [108]. When the layered double hydroxides contain oxidable divalent cations, such as Ni^{2+}, Fe^{2+}, Co^{2+}, the thermal transformation contains an additional step involving a spontaneous oxidation reaction. Also, the dehydroxylation is mitigated and occurs at lower temperatures (250-300°C) [108]. During the decomposition step, there is a high probability that the rock salt oxide phase will not be obtained [108]. The metallic cations are known to be evenly dispersed in the brucite-like layers of the LDH. However, during the calcination step, at temperatures around 500°C, the entire layered network collapses in a topotactic manner [108].

Usually, the LDH undergoes thermal breakdown to metal mixed oxide at moderate calcination temperatures, 400–600°C [109]. When the temperature is below 300°C, the multilayered network will continue to exist, but will have low crystallinity [109]. The unique LDH phase eventually will vanish as the calcination temperature rises to about 600°C [109]. Above 600°C, the formation of the spinel phase and the disappearance of the MMO phase happen simultaneously, and as the temperature rise further, the spinel phase is more crystalline and the surface area decreases [109]. When the calcination temperature used is lower than 600 °C, the mixed-metal oxides obtained can recover their lamellar structure, namely the LDH status by immersing them in an aqueous solution containing the desired anions [109]. This regeneration of the mixed oxides is attributed to the 'memory effect' property of the layered double hydroxides [108,109]. The LDH-derived mixed oxides are well-known for their unique properties which consists in relatively large specific surface

areas, thus high porosity, increased thermal stability, great metal oxide dispersion and improved acid-base properties [109].

The high porosity of the mixed oxides can be caused by several reasons, as seen in the Figure 12. The primary cause of porosity might be attributed to the intraparticle space between M(II)O domains [109]. Second, the calcination process may lead the MMO particles to form agglomerates, which have pores in the interparticle space [109]. By using a nanometer-sized pore developing agent, porogen, during the LDH synthesis, the specific surface area of mixed oxides can be precisely adjusted [109]. The porogen is decomposed by the thermal treatment creating voids in the structure (Figure 12).

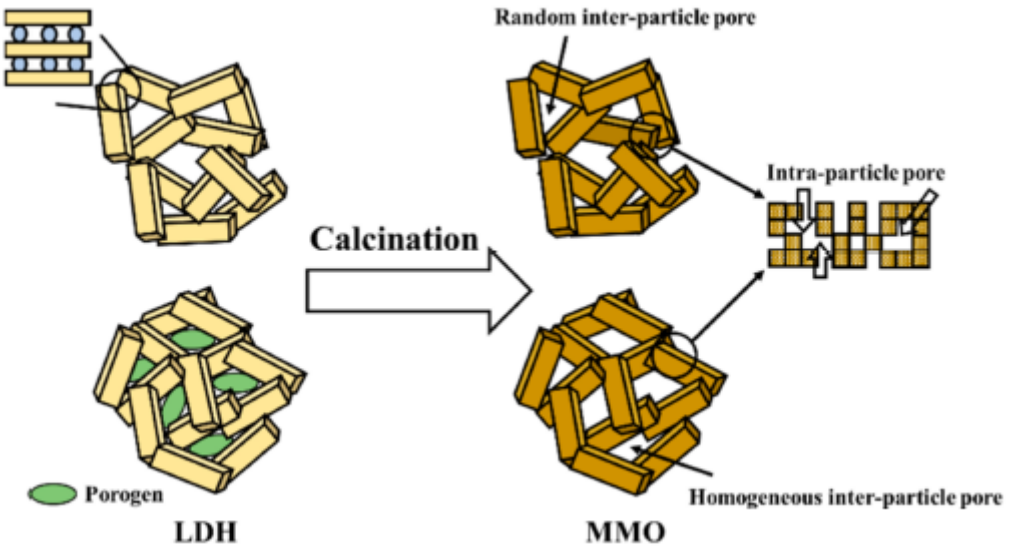

Figure 12. Porosity of the mixed oxides, created with and without the porogen [109].

The calcination of multi-component LDHs lead to mixed oxides which contain numerous acid and base sites attributed to the presence of O^{2-}-M^{n+} acid-base pairs [110]. The nature of the cations, their molar ratio, the preparation technique of the LDH, the calcination temperature, and the types of interlayer anion, all affect the nature, strength, and the relative amounts of the base sites [109,110]. For instance, the Al concentration (Mg/Al = 0.5 to 9.0) has a significant impact on the type, density, and strength of the surface basic sites of Mg-Al mixed oxide produced by the calcination of Mg-Al LDH [110]. Calcined LDH has weak (OH groups), medium (Mg-O pairs), and strong (O_2 anions) basicity surface sites [110]. A high Al concentration can lead to the increase of the weak and medium strength base sites. The density of surface base sites can be significantly reduced when aluminum is added in small proportion to MgO [110]. LDH-derived mixed oxides present various applications in many fields. They can be used as catalysts, adsorbents, electrodes, semiconductors and more [109].

These applications make full use of the inherent properties of the LDH, thus the mixed oxides and will continue their exploration in the near future.

1.6. The synthesis of the hydrotalcites

Depending on the specific requirements and the desired properties, HT catalysts can be synthesized by various methods. The most commonly used is co-precipitation. Other methods applied to prepare the HT include urea hydrolysis, sol-gel method, microwave synthesis, topochemical synthesis.

1.6.1. The co-precipitation method

Co-precipitation is a recurrent method used for the preparation of hydrotalcite-like compounds. It consists in the mixing of the parent materials (divalent and trivalent metal salts solutions, in well-defined proportions) with an alkali solution containing the precipitating agent (Na_2CO_3, NH_4Cl_2, NaOH), which purpose is to maintain a constant pH value to start the co-precipitation process [4]. The co-precipitation mechanism implies the condensation of hexaaqua complexes in solution, which contributes to the formation of the layers having the metallic cations evenly dispersed and solvated interlayer anions [111]. The studies referring to the precipitation process clearly state that the brucite-type layers and the interlamellar regions of the hydrotalcite-like compounds are formed during the early stages [111]. To obtain precipitates containing well organized crystalline phases, it is necessary to keep under control the following parameters [111]:

- the reaction temperature (60-80°C)
- the pH of the reaction medium (7-10)
- a slow flow rate of the two streams of reagents
- the stirring speed
- the ageing time
- the possible occurrence of electrolytes in the reaction medium.
- a low supersaturation level in the reaction mixture
- the metal cations can produce complexes

The experimental protocol for obtaining the layered double hydroxide catalysts is represented in Figure 13. A serious disadvantage of the co-precipitation method is that the resulting material, a gel-like compound, can be difficult to separate by filtration, and it may be poorly crystalized. Also, its purification may require a large amount of water. To improve the crystallinity of the layered double hydroxides, an extra processing step is added during co-

precipitation which consists in long-term ageing in aqueous solutions at temperatures in the range of 60-150°C, often under hydrothermal conditions [111,112]. The additional step adds complexity to the LDH synthesis. So, it is no surprise that considerable effort has been concentrated on searching for other processes that would be easier to implement and more sustainable.

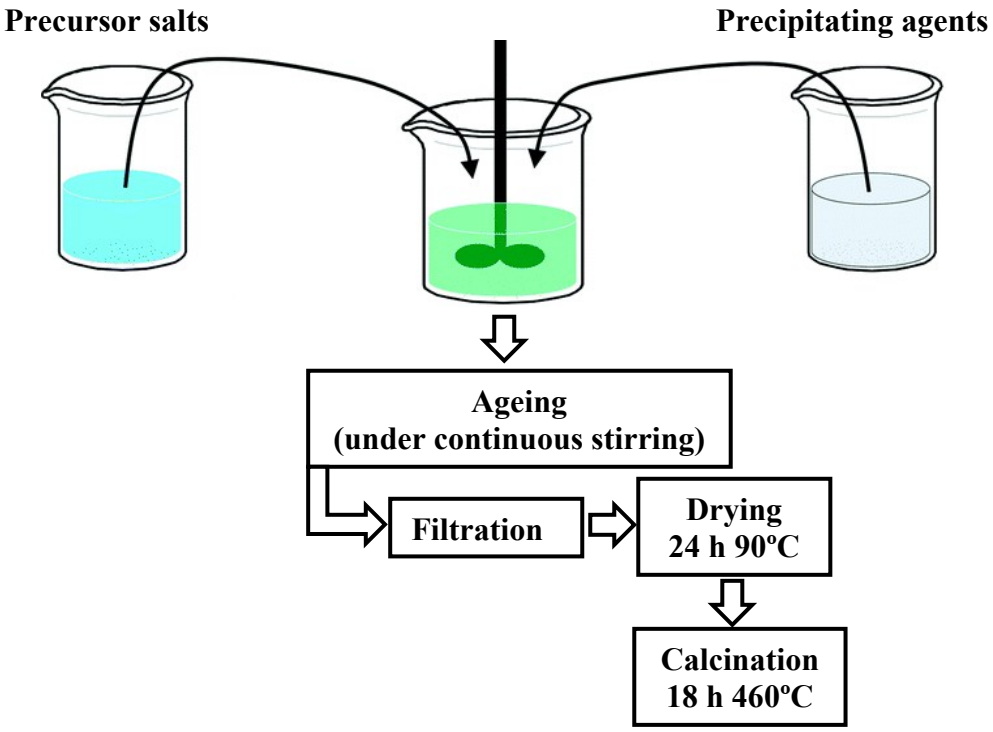

Figure 13. Experimental protocol for obtaining of LDHs by co-precipitation method.

1.6.2. SOL-GEL METHOD

The sol-gel method consists in the reaction, at room temperature, between metallic precursors (organo-metallic compounds, different organic or inorganic salts) and water, aqueous solutions or organic solvents aiming for the formation of a polymeric sol or particles [113]. This hydrolysis process can be performed both in basic and acidic catalysis (with the help of mineral acid, such as HCl) [113]. The reaction products generated using the sol-gel method, usually mixed oxides, are well known for their increased purity and homogeneity at a molecular scale, allowing them to be utilized especially in the pharmaceutical industry [113]. The sol-gel method is considered one of the best ways to synthesize layered double hydroxides because the obtained hydrotalcite-like catalysts have both a 10-25% bigger surface than the ones obtained by co-precipitation and improved basicity [113].

1.6.3. MECHANOCHEMICAL SYNTESIS

The essence of all the above methods applied to prepare HT-like materials is similar, involving the precipitations of different metallic precursors. The experimental protocol with all the required steps for obtaining of the layered double hydroxide catalysts using the mechanochemical method is represented in Figure 14.

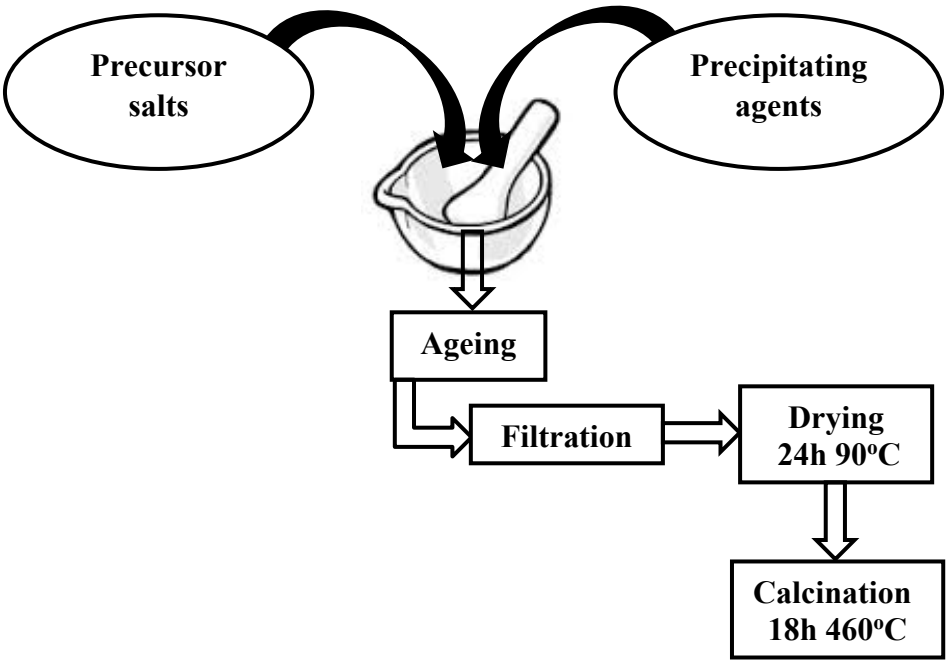

Figure 14. Experimental protocol for obtaining of LDHs by mechanochemical method.

However, the earlier mentioned conventional processes have some severe drawbacks: they are very complicated in what concerns the addition of reagents with controlled flow rate the maintaining of a constant pH and temperature during heating [114]. When multi-components are involved, in ternary or quaternary systems, due to the different precipitation rates of metal ions, the generation of intermediate phases as impurities to the final product may quickly occur [115], which will increase the cost of production. Another significant disadvantage of all the above methods is the time taken to obtain the reaction products. Recently, a new synthesis method, the mechanochemical technique, received considerable attention. It has been widely used to get a large variety of advanced materials, covering almost all aspects of material science.

The main advantages over the synthesis procedures described above include environmentally friendly, simplified process, atom-economical process, low-cost technology and the possibility of making a product in the metastable state, which is difficult to obtain using other conventional methods [112]. Mechanical energy applied on a solid leads, besides its

comminution and the formation of new free surfaces, to its mechanical activation and, with increasing activation, to mechanochemical reactions [112]. Mechanical activation and mechanochemical reactions are the subjects of mechanochemistry, a special branch of chemistry that has been studied intensively since the 19th century [116]. Mechanochemical reaction is a process that involves the destruction of a material using a strong mechanical force (pressure or shear), causing physico-chemical changes and, in the end, the formation of a different structure [116]. The principle of this method is that the precursors under the conditions of the mechanical treatment undergo a chemical reaction resulting in the formation of the LDH.

Given that the formation of the LDH takes place in the solid state, there is no need for filtration, which, in many cases, proves to be quite complex; there is no need for further treatments such as ageing or hydrothermal treatment to increase the crystallinity of the LDH phases. In all cases, the thermodynamic potentials of the treated compounds are changed, and free energy and enthalpy are enhanced. These depend on the size of the starting particles used and the presence of defects in their crystal structure [116]. The mechanochemical syntheses can be successfully carried out if the crystalline forms of the solids to be converted are similar or if, in an acid-base type interaction, one of the reactants is a strong acid or base [116]. Mechanical activation and mechanochemical reactions are carried out predominantly in mills. The milling processes play an essential role in the chemical industry and are responsible for a large proportion of the process costs [116]. They are usually used for the comminution and mechanochemical treatment of a solid. The processes that occur during the comminution are based on different types of stress mechanisms exerted and lead to different grinding results and different structural changes, depending on the material's behavior. According to Rumpf [116], there are three types of exerted stresses:

- stress between two surfaces (Figure 15)
- stress without milling faces:

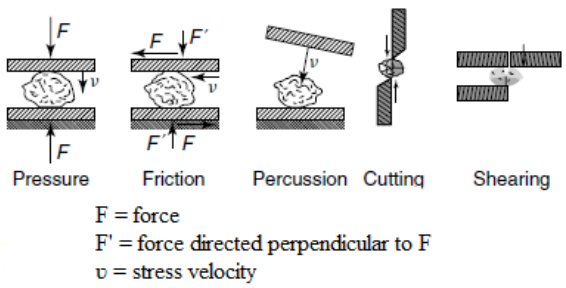

Figure 15. Stress between two surfaces [116].

- stress at a single surface (Figure 16)

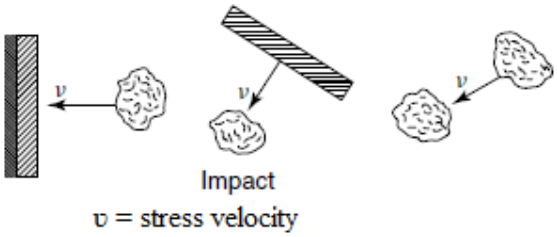

Figure 16. Stress at a single surface [116].

The mechanochemical process is suitable for preparing composite materials producing homogenous hybrid structures. Some syntheses of important composite materials were explored via mechanochemical process, for example, some metal-oxide systems, like Al_2O_3/IMC (intermetallic compound) [117]. Another attractive feature of the mechanochemical method is its easy synthesis process of nanostructured materials. Furthermore, the mechanochemical way is known to induce solid-state reactions, where hydrated and hydroxide samples have been involved [117]. Based on this concept, recently it has been investigated this alternative in the synthesis and intercalation of LDHs [117]. Three different mechanochemical processes have been exploited to obtain layered double hydroxides: single-step grinding, mechano-hydrothermal and two-step grinding (dry and wet grinding), as seen in Figure 17 [115].

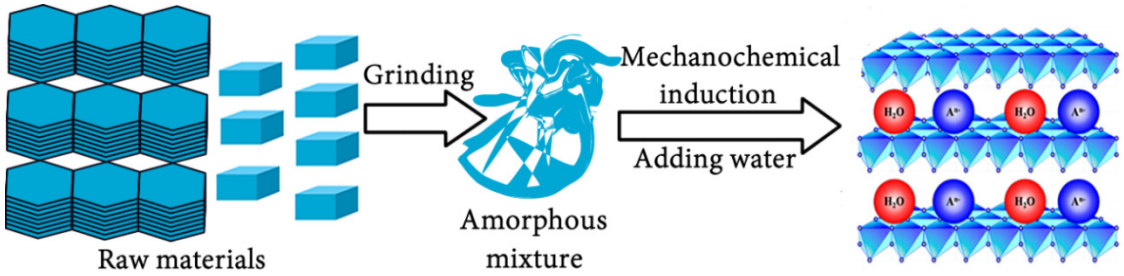

Figure 17. General illustration of two-step grinding [115].

The mechanochemical process enables the obtaining of LDH via a short-term synthesis, avoiding using a large amount of wash water, showing its superiority over the conventional co-precipitation method.

1.6.3.1. COMPARISONS OF DIFFERENT MECHANOCHEMICAL METHODS

The main advantages and drawbacks of the mechanochemical methods analyzed above are listed in Table 6. Nevertheless, the two-step grinding technique should be fully studied among the summarized processes because it has more advantages than disadvantages. Compared to the conventional aqueous solution processes, the mechanochemical ones, particularly the two-step grinding, have noticeable advantageous features of easy operation,

no need for waste solution treatment and so on. Besides, the potential for synthesizing a new type of LDH, containing a metal with valence over 4, which are difficult to achieve by traditional methods, may be exploited only by mechanochemical processes [115].

Table 6. Advantages and disadvantages of mechanochemical processes [115].

Mechanochemical processes		**Advantages**	**Disadvantages**
Mechano-hydrothermal process	Manual grinding hydrothermal	Regular hexagonal shape particles Highly dispersed	Solvent involvement Energy waste Raw materials limited to soluble salts
	Ball-milling hydrothermal	Regular hexagonal shape particles Salts, oxides, hydroxides used as raw materials	Solvent involvement Energy waste
Direct mechanochemical syntheses	Single-step grinding wet	Ease of operation Energy saving	Solvent involvement Energy waste
	Single-step grinding dry	Ease of operation Energy free	Low crystallinity
	Two-step grinding	Ease of operation Solvent-free Salts, oxides, hydroxides used as raw materials	Particle agglomeration

1.7. LDH applications in organic synthesis

Hydrotalcites may be used as such, or they may be calcined to form mixed oxides that are valuable catalysts. The materials are mainly applied as base or redox catalysts in the pharmaceuticals industry, or as supercapacitors and adsorbents [118]. Moreover, in the uncalcined form, hydrotalcites can be used as catalyst supports, and this confers to these materials an even broader spectrum of activities and selectivities. LDHs have been applied in many organic transformations, such as alkylation, isomerization, hydroxylation, transesterification, hydroformylation, redox reactions, condensation and environmentally friendly reactions (Figure 18) [119]. The mixed oxides obtained after calcination of the LDH usually have good catalytic activities. They have been applied to the following reactions: aldol and Knoevenagel condensations, epoxidation of olefins, halide exchanges, phenol hydroxylation, Michael additions [119].

A significant process in organic synthesis is Carbon-Carbon (C-C) bond formation achieved by different methods: alkylation, condensation, and addition reactions [119].

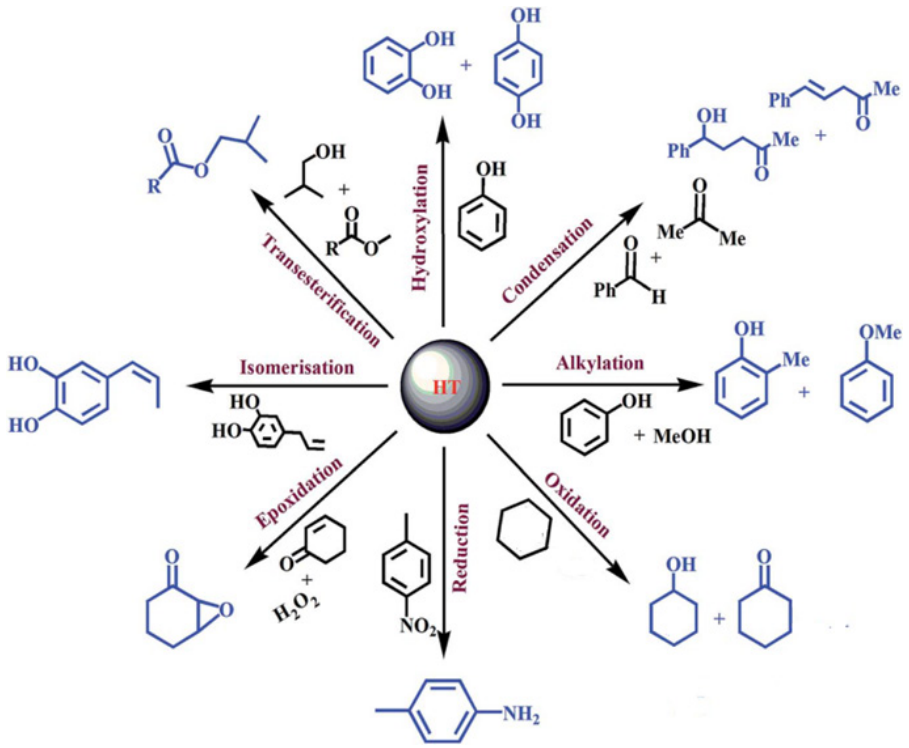

Figure 18. Schematic representation of different organic transformations [119].

Because many of the alkyl phenols are utilized as starting materials in the production of several medicines, agrochemicals, and other significant organic products, the alkylation of phenol with alcohols is a reaction of great importance. The alkylation of phenol with 1- and 2-propanol in the vapor phase over Mg,Al-hydrotalcite (Mg/Al molar ratios of 2, 3, and 4, respectively) was explored by Velu et al. [120]. The phenol conversion increased with the increase of temperature, and have reached a peak of 80% at about 350°C. In comparison to other catalysts like CuAl-HT and NiAl-HT, the MgAl-HT with a Mg/Al atomic ratio of 2 and 3 was shown to be adequate for this type of reaction [120]. Aldol-condensation reactions between two molecules with carbonyl groups (aldehydes or ketones) allow the construction of these bonds under mild conditions but need a base catalyst [121]. During time, large amounts of liquid bases were used as catalysts on an industrial scale [121] for such reactions. Their replacement with environmentally friendly and low-cost base solids with similar catalytic activities and selectivities was a real challenge. However, base oxides, such as MgO, CaO, BaO and their mixtures, meant possible options [121]. The usage of the hydrotalcites in aldol condensation has been the main subject of many studies. The most known examples are the self-condensation of acetaldehyde, butyraldehyde and acetone and the cross-condensation of formaldehyde with butyr- and isobutyraldehyde [122]. Oxidation and reduction can also be considered as key reactions in the synthesis of organic compounds. In the past years, a variety

of HT or supported HT materials have garnered a lot of interest as heterogeneous redox catalysts [50]. By using hydrogen peroxide and several ternary hydrotalcite-like systems containing Cu, Zhu et al. [123] performed liquid phase phenol hydroxylation. The highest phenol conversion (53.5 %) and catechol selectivity (59 %) were obtained when CuAl-HT was used as catalyst [123]. Catechol and hydroquinone conversion from phenol is a significant industrial process, and these compounds have a variety of application. Using various hydrotalcite (HT) materials (as-synthesised and calcined) and H_2O_2 as an oxidant, Antonyraj et al. [124] examined the hydroxylation of phenol. CuZnAl-HT, in both its as-prepared and calcined forms was shown to provide the best phenol conversion among the several HT materials used (CuMgAl-HT, CuNiAl-HT, and CuCoAl-HT), 21.6 and 17.6%, respectively [124]. With the help of MgAl-HT and H_2O_2, Cativiela et al. [125] were able to epoxidize a variety of unsaturated cyclic and acyclic ketones. Open-chain, substituted, and unsaturated compounds demonstrated stereo-selective epoxidation with a maximum yield of 97%. The activity of the substituted cyclic compounds was noticeably decreased [125]. Using Ru-MgAl-HT and molecular oxygen, Kaneda et al. [126] converted allylic and benzylic alcohols into the corresponding aldehydes or ketones. When using the MgAl-HT as catalyst, the conversion and yield were low. Ruthenium-HT effectively catalyzed the oxidation of allylic and benzylic alcohols, producing the corresponding carbonyl molecules [126]. A number of heterogeneous catalysts were created by Choudary et al. [127] for the conversion of 2-pyridine carboxyaldehydes to 2-pyridine carboxyalcohols. When compared to other HT and alternative Ni/Al_2O_3 catalysts, NiAl-HT, which has a Ni/Al molar ratio of 2, demonstrated superior conversion in this type of reaction [127]. Due to its potential economic uses in the synthesis of fine, fragrant compounds and in the pharmaceutical sectors, C-C double bond isomerization is of great interest. Using several hydrotalcite materials as the base catalyst, Kishore et al. [128] examined the isomerization of safrole to the corresponding thermodynamically stable iso-safrole. The conversion and selectivity of iso-safrole decreased in the following order: MgAl-HT ~ MgFe-HT >MgCr-HT [128].New opportunities for heterogeneous catalysis are opened up by the intercalation of different anions into the hydrotalcite structure. The utilization of HT materials for various oxidation and reduction processes is facilitated by their capacity to integrate transition metal ions into the framework's octahedral configuration. These materials also offer a high degree of adaptability for adjusting the active sites via framework cations or interlayer anions, which makes the introduction of multifunctionality easier. Their variable composition and tunable intrinsic properties clarify why catalytic usage belongs to their main field of applications.

References

1. Choy, J.H., Park, M., Cationic and anionic clays for biological applications, Clay Surfaces: Fundamentals and Applications, F. Wypych and K. G. Satyanarayana (editors) 2004 Elsevier Ltd.

2. Forano, C., Costantino, U., Prevota, V., Taviot Gueho, C. Layered Double Hydroxides (LDH) Developments. Clay Science 2013, 5, 745-782.

3. Hochstetter, C. Untersuchung über die Zusammensetzung einiger Mineralien. Journal für praktische Chemie 1842, 27, 375-378.

4. Cavani, F., Trifiro, F., Vaccari, A. Hydrotalcite-type anionic clays: Preparation, Properties, and applications, Catalysis Today 1991, 11, 173-301.

5. Allmann, R. The crystal structure of pyroaurite. Acta Cryst. 1968, B24, 972-977.

6. Taylor, H. F. W. Segregation and cation-ordering in sjgrenite and pyroaurite: Mineral. Mug. 1969, 37, 338-342.

7. Evans, D.G., Slade, R. C. T. Structural Aspects of Layered Double Hydroxides, Struct Bond 2006, 119, 1–87.

8. Newman, S.P, Jones, W. Synthesis, characterization, and applications of layered double hydroxides containing organic guests. New J. Chem., 1998, 105-115.

9. Bini, M., Monteforte, F. Layered Double Hydroxides (LDHs): Versatile and Powerful Hosts for Different Applications. Anal Pharm Res 2018, 7, 00206.

10. Zhang, F., Xiang, X., Li, F., Duan, X. Layered Double Hydroxides as Catalytic Materials: Recent Development. Catal Surv Asia 2008, 12, 253–265.

11. Li, T., Miras, H.N., Song, Y.F. Polyoxometalate (POM)-Layered Double Hydroxides (LDH)Composite Materials: Design and Catalytic Applications. Catalysts 2017, 260.

12. Qu, J., Zhang, Q., Li, X., He, X., Song, S. Mechanochemical approaches to synthesize layered double hydroxides: a review. Appl. Clay Sci. 2016, 185-192.

13. Bravo-Suárez, J.J., Páez-Mozo, E.A., Oyama, S.T. Review of the synthesis of layered double hydroxides: a thermodynamic approach. Quim. Nova, 2004, 601-614.

14. Yan, H., Zhao, X.J., Zhu, Y.Q., Wei, M., Evans, D.G., Duan, X. The Periodic Table as a Guide to the Construction and Properties of Layered Double Hydroxides. The Periodic Table II 2019, 89-120.

15. Brindley, W.G., Kikkawa, S. A crystal-chemical study of Mg,Al and Ni,Al hydroxyl-perchlorates and hydroxyl-carbonates. Am. Miner. 1979, 64, 836-843.

16. Alejandre A., Medina, F., Rodriguez, X. , Salagre, P., Cesteros, Y., Sueiras, J.E. Cu/Ni/Al layered double hydroxides as precursors of catalysts for the wet air oxidation of phenol aqueous solutions. Applied Catalysis B: Environmental 2001, 30, 195–207.
17. Sotiles, A.R., Grassi, M.T., Dos Santos, M.P., Wypych, F. Synthesis, characterization, and exchange reactions of layered double hydroxides of copper and aluminum, intercalated with sulfate. J. Braz.Chem. Soc. 2021, 32, 170-181.
18. Layrac, G., Harrisson, S., Destarac, M., Gérardin, C., Tichit, D. Comprehensive study of the formation of stable colloids of Cu Al layered double hydroxides assisted by double hydrophilic block copolymers. Appl. Clay Sci. 2020, 193, 105673.
19. Kawabata, T., Shinozuka, Y., Ohishi, Y., Shishido, T.,Takaki, K.,Takehira, K. Nickel containing Mg-Al hydrotalcite-type anionic clay catalyst for the oxidation of alcohols with molecular oxygen. Journal of Molecular Catalysis A: Chemical 2005, 236, 206–215.
20. Choudary, B.M., Kantam, L.M., Rahman, A., Reddy, C.V., Rao, K.K. The First Example of Activation of Molecular Oxygen by Nickel in Ni-Al Hydrotalcite: A Novel Protocol for the Selective Oxidation of Alcohols. Angew Chem Int Ed Engl 2001, 40, 763-766.
21. Vos, B., Poels, E., Bliek, A. Impact of calcination conditions on the structure of alumina nickel particles. Journal of Catalysis 2001,198, 77-88.
22. Rathouský, J., Schulz-Ekloff, G., Starek, J., Zukal, A. Supported Nickel Catalyst from Hydroxycarbonate of Nickel and Aluminum Chem. Eng. Technol.,1994, 17, 41-46.
23. Titulaer, M.K., Jansen, J.B.H, Geus, J.W.The Quantity of Reduced Nickel in Synthetic Takovite: Effects of Preparation Conditions and Calcination Temperature. Clays and Clay Minerals 1994, 42, 249–258.
24. Arias, S., Eon, J.G, San Gil, R.A.S., Licea, Y.E., Palacio, L.A., FaroJr. A.C. Synthesis and characterization of terephthalate-intercalated NiAl layered double hydroxides with high Al content. Dalton Trans., 2013, 42, 2084-2093.
25. Newsome, D.S. The Water-Gas Shift Reaction. Catal. Rev. Sci. Eng.1980, 21, 275–318.
26. Fuentes, E.M., Da Costa Faro Júnior, A., De Freitas Silva, T., Assaf, J.M., Do Carmo Rangel, M. A comparison between copper and nickel-based catalysts obtained from hydrotalcite-like precursors for WGSR. Catalysis Today 2011, 171, 290–296.
27. Perez-Ramirez, J., Mul, G., Moulijin, J.A. In situ Fourier transform infrared and laser Raman spectroscopic study of the thermal decomposition of Co-Al and Ni-Al hydrotalcites. Vibrational Spectroscopy 2001, 27, 75-88.

28. Espinal, R., Taboada, E., Molins, E., Chimentao, R.J., Medina, F., Llorca, J. Cobalt hydrotalcite for the steam reforming of ethanol with scarce carbon production. RSC Advances 2012, 2, 22946-2956.
29. Kannan, S., Swamy, C.S. Catalytic decomposition of nitrous oxide over calcined cobalt aluminum hydrotalcites. Catalysis Today 1999, 53, 725-737.
30. Basag, S., Kovanda, F., Piwowarska, Z., Kowalczyk, A., Pamin, K., Chmielarz, L. Hydrotalcite-derived Co-containing mixed metal oxide catalysts for methanol incineration. Role of cobalt content, Mg/Al ratio and calcination temperature. J. Therm. Anal. Calorim. 2017, 129, 1301-1311.
31. Mamat, M., Tagg, T., Khairul, W. M., Abdullah, M.A.A., Tahir, N.M., Jubri, Z., As'ari R.A. Behavior of Layered Double Hydroxides Having Different Divalent Transition Metal Groups. Applied Mechanics and Materials 2014, 563, 94-101.
32. Atkins, P., Overton, T., Rourke, J., Weller, M., Armstrong, F., Shriver and Atkins' Inorganic Chemistry, Fifth ed., Oxford University Press, Italy, 2010.
33. Burns R.G. Mineralogical Applications of Crystal Field Theory, Cambridge University Press, Cambridge, 1993.
34. Alejandre A., Medina, F., Rodriguez, X. , Salagre, P., Sueiras, J.E. Preparation and Activity of Cu–Al Mixed Oxides via Hydrotalcite-like Precursors for the Oxidation of Phenol Aqueous Solutions. Journal of Catalysis 1999, 188, 311-324.
35. Wang, J., Zhang, T., Li. K., Cao, Y., Zeng, Y. Dehydrogenation Catalysts for Synthesis of O-Phenylphenol via Cu/Ni/Mg/Al Hydrotalcite-Like Compounds as Precursors. Catalysts 2018, 8, 186-200.
36. Fan, G., Li, F., Evans, D.G., Duan, X. Catalytic applications of layered double hydroxides: recent advances and perspectives. Chem. Soc. Rev. 2014, 43,7040-7066.
37. Li, J., Zhang, S., Chen, Y., Liu, T., Liu, X., Zhang, X., Yi, M., Chu, Z., Han, X. A novel three-dimensional hierarchical CuAl layered double hydroxide with excellent catalytic activity for degradation of methyl orange. RSC Adv. 2017, 7, 29051-29057.
38. Zhang, S., Kano, N., Mishima, K., Okawa, H. Adsorption and desorption mechanism of rare earth elements (REEs) by layered double hydroxide (LDH) modified with chelating agents. Appl. Sci. 2019, 9, 4805-4821.
39. Chang, Z., Evan, D., Duan, X., Boutinoud, P., De Roy, M., Forano, C. Preparation and characterization of rare-earth containing layered double hydroxides. Journal of Physics and Chemistry of Solids 2006, 67, 1054-1057.

40. Wang, Z., Fongarland, P., Lu, G., Essayem, N. Reconstructed La-, Y-, Ce-modified MgAl-hydrotalcite as a solid base catalyst for aldol condensation: Investigation of water tolerance. Journal of Catalysis 2014, 318, 108-118.
41. Smalenskaite, A., Vieira, D.E.L., Salak, A.N., Ferreira, M.G.S., Katelnikovas, A., Kareiva, A. A comparative study of co-precipitation and sol-gel synthetic approaches to fabricate cerium-substituted Mg-Al layered double hydroxides with luminescence properties. Applied Clay Science 2017, 143, 175-183.
42. Shannon, R.D. Revised Effective Ionic radii, and systematic studies of interatomic distances in halides and chalcogenides. Acta ryst. 1976, 32, 751-767.
43. Zhang, Y., Li, Y., Ren, Y., Wang, H., Chen, F. Double-doped LDH films on aluminum alloys for active protection. Materials Letters 2017, 192, 33–35.
44. Ebitani, K., Motokura, K.,Mori, K., Mizugaki, T., Kaneda, K. Reconstructed Hydrotalcite as a Highly Active Heterogeneous Base Catalyst for Carbon-Carbon Bond Formations in the Presence of Water. J. Org. Chem. 2006, 71, 5440-5447.
45. Iqbal, M.A., Fedel, M. Protective Cerium-Based Layered Double Hydroxides Thin Films Developed on Anodized AA6082. Advances in Materials Science and Engineering. 2020, 1-12.
46. Birjega, R., Pavel, O.D., Costentin, G., Che, M., Angelescu, E. Rare-earth elements modified hydrotalcites and corresponding mesoporous mixed oxides as basic solid catalysts. Appl. Catal. A: General 2005, 288, 185-193.
47. Cota, I., Ramirez, E., Medina, F., Sueiras, J.E., Layrac, G., Tichit, D. Highly basic catalysts obtained by intercalation of La-containing anionic complexes in layered double hydroxides. Appl. Catal. A. 2010, 382, 272-276.
48. Carneiro, J., Caetano, A.F., Kuznetsova, A., Maia, F., Salak, A.N., Tedim, J., Scharnagl, N., Zheludkevich, M.L., Ferreira, M.G.S. Polyelectrolyte-modified layered double hydroxide nanocontainers as vehicles for combined inhibitors. RSC Advances 2015, 5, 39916–39929.
49. Gunawan, P., Xu, R. Lanthanide-Doped Layered Double Hydroxides Intercalated with Sensitizing Anions: Efficient Energy Transfer between Host and Guest Layers. J. Phys. Chem. C 2009, 113, 17206–17214.
50. Baskaran, T., Christopher, J., Sakthivel, A. Progress on layered hydrotalcite (HT) materials as potential support and catalytic materials. RSC Adv. 2015, 120, 98853-98875.
51. Ferencz, Z., PhD Thesis: Mechanochemical Preparation and Structural Characterization of Layered Double Hydroxides and their Amino Acid-Intercalated Derivatives, University of Szeged, 2016, Chapter 2. Literature review, pgs. 10-11.

52. Omwoma, S. Chen, W. Tsunashima, R. Song, Y.F. Recent Advances on Polyoxometalates Intercalated Layered Double Hydroxides: From Synthetic Approaches to Functional Material Applications. Coord. Chem. Rev. 2014, 258–259, 58–71.
53. Li, T., Miras, H.N., Song, Y.F. Polyoxometalate (POM)-Layered Double Hydroxides (LDH) Composite Materials: Design and Catalytic Applications. Catalysts 2017, 7, 260–277.
54. Izarova, N.V., Pope, M.T., Kortz, U. Noble Metals in Polyoxometalates. Angewandte Chemie International Edition 2012, 51, 9492–9510.
55. Knözinger, H.Infrared Spectroscopy for the characterization of Surface Acidity and Basicity. In Handbook of Heterogeneous Catalysis; Ertl, G., Knözinger, H., Schüth, F., Waitkamp, J., Eds.; Wiley-VCH Verlag GmbH &Co. KGaA: Weinheim, Germany, 2008, pp. 1155–1156.
56. Schoonheydt, R.A., Pinnavaia, T.J., Lagaly, G., Gangas, N. Pillared clays and pillared layered solids. Pure Appl. Chem. 1999, 71, 2367–2371.
57. Rives, V., Carriazo, D. Martín, C. Heterogeneous Catalysis by Polyoxometalate-Intercalated Layered Double Hydroxides. In Pillared Clays and Related Catalysts, 1st ed.; Gil, A., Korili, S.A., Trujillano, R.,Vicente, M.A., Eds.; Springer Science and Business Media: New York, NY, USA, 2010; pp. 319–393.
58. Muramatsu, K., Saber, O., Tagaya, H. Preparation of new layered double hydroxide, Zn-Mo LDH. J. Porous Mater. 2007, 14, 481–484.
59. Krishnan, C.V., Garnett, M.; Hsiao, B., Chu, B. Electrochemical Measurements of Isopolyoxomolybdates: 1.pH Dependent Behavior of Sodium Molybdate. Int. J. Electrochem. Sci. 2007, 2, 29–51.
60. Carriazo, D., Domingo, C., Martin, C., Rives, V. Structural and texture evolution with temperature of layered double hydroxides intercalated with paramolybdate anions. Inorg. Chem. 2006, 45, 1243–1251.
61. Soled, S., Levin, D., Miseo, S., Ying, J. Soft chemical synthesis of mixed metal molybdate oxidation catalysts and their structural relationship to hydrotalcite. In Studies in Surface Science and Catalysis; Delmon, B., Jacobs, P.A., Maggi, R., Martens, J.A., Grange, P., Poncelet, G., Eds.; Elsevier Science B.V.: Louvain-la-Neuve, Belgium, 1998; Volume 118, pp. 359–367.
62. Palmer, S.J., Frost, R.L., Nguyen, T. Thermal decomposition of hydrotalcite with molybdate and vanadate anions in the interlayer. J. Therm. Anal. Calorim. 2008, 92, 879–886.

63. Davantès. A., Lefèvre, G. In Situ Real Time Infrared Spectroscopy of Sorption of (Poly) molybdate Ions into Layered Double Hydroxides. J. Phys. Chem. A 2013, 117, 12922–12929.
64. Carriazo, D., Martin, C., Rives, V. An FT-IR study of the adsorption of isopropanol on calcined layered double hydroxides containing isopolymolybdate. Catal. Today 2007,126, 153–161.
65. Del Arco, M., Carriazo, D., Gutierrez, S., Martin, C., Rives, V. Synthesis and Characterization of New Mg2Al-Paratungstate Layered Double Hydroxides. Inorg. Chem. 2004, 43, 375–384.
66. Dobrea, I.D., Ciocan, C.E., Dumitriu, E., Popa, M.I., Petit, E., Hulea, V. Raman spectroscopy—Useful tool for studying the catalysts derived from Mo and V-oxyanion-intercalated layered double hydroxides. Appl. Clay Sci. 2015, 104, 205–210.
67. Marcu, I.C., Popescu, I., Urda, A., Hulea. V. Layered Double Hydroxides-Based Materials as Oxidation Catalysts. In Sustainable Nanosystems Development, Properties, and Applications, 1st ed.; Putz, M.V., Mirica, M.C., Eds.; IGI Global: Hershey, PA, USA, 2017; pp. 59–121.
68. Ciocan, C.E., Dumitriu, E., Cacciaguerra, T., Fajula, F., Hulea, V. New approach for synthesis of Mo-containing LDH based catalysts. Catal. Today 2012, 198, 239–245.
69. Yu, X., Wang, J., Zhang, M., Yang, P., Yang, L., Cao, D., Li, J. One-step synthesis of lamellar molybdate pillared hydrotalcite and its application for AZ31 Mg alloy protection. Solid State Sci. 2009, 11, 376–381.
70. Zavoianu, R., Birjega, R., Pavel, O.D., Cruceanu, A., Alifanti, M. Hydrotalcite like compounds with low Mo-loading active catalysts for selective oxidation of cyclohexene with hydrogen peroxide. Appl. Catal. A 2005, 286, 211–220.
71. Kwon, T., Pinnavaia, T.J. Synthesis and properties of anionic clays pillared by [XM12O40]n− Keggin ions. J. Mol. Catal. 1992, 74, 23–33.
72. Van Laar, F.M.P.R., de Vos, D.E., Pierard, F., Kirsch-de Mesmaeker, A., Fiermans, L., Jacobs, P.A. Generation of Singlet Molecular Oxygen from H2O2 with Molybdate-Exchanged Layered Double Hydroxides: Effects of Catalyst Composition and Reaction Conditions. J. Catal. 2001, 197, 139–150.
73. Zavoianu, R., Cruceanu, A., Pavel, O.D., Angelescu, E., Soares Dias, A.P., Birjega, R. Oxidation of tert-butanethiol with air using Mo containing hydrotalcite-like compounds and their derived mixed oxides as catalysts. React. Kinet. Mech. Catal. 2012, 105, 145–162.

74. Choudary, B.M., Someshwar, T., Lakshmi Kantam, M., Venkat Reddy, C.; Molybdate-exchanged Mg–Al–LDH catalyst: An eco-compatible route for the synthesis of β-bromostyrenes in aqueous medium. Catal. Commun. 2004, 5, 215–219.
75. Klemkaite-Ramanauske, K., Zilinskas, A., Taraskevicius, R., Khinsky, A., Kareiva, A. Preparation of Mg/Al layered double hydroxide (LDH) with structurally embedded molybdate ions and application as a catalyst for the synthesis of 2-adamantylidene(phenyl)amine Schiff base. Polyhedron 2014, 68, 340–345.
76. Han, N., Zhao, F., Li, L. Ultrathin Nickel-Iron Layered Double Hydroxide Nanosheets Intercalated with Molybdate Anions for Electrocatalytic Water Oxidation. J. Mater. Chem. A 2015, 3, 16348–16353.
77. Levin, D., Soled, S.L., Ying, J.Y. Chimie Douce Synthesis of a Layered Ammonium Zinc Molybdate. Chem. Mater. 1996, 8, 836–843.
78. Zeng, R.G., Liu, Z.G., Zhang, F., Li, S.Q., Cui, H.Z., Han, E.H. Corrosion of molybdate intercalated hydrotalcite coating on AZ31 Mg alloy. J. Mater. Chem. A 2014, 2, 13049–13057.
79. Brodie, B.C. XIII. On the atomic weight of graphite. Philos. Trans. R. Soc. London 1859, 149, 249–259.
80. Novoselov, K.S., Geim, A.K., Morozov, S.V., Jiang, D., Zhang, Y., Dubonos, S.V., Grigorieva, I.V., Firsov, A.A. Electric Field Effect in Atomically Thin Carbon Films. Science 2004, 306, 666-669.
81. Wimalasiri, Y., Fan, R., Zhao, X.S., Zou, L. Assembly of Ni-Al layered double hydroxide and graphene electrodes for supercapacitors. Electrochimica Acta 2014, 134, 127-135.
82. Geim, A.K., Novoselov, K.S. The rise of graphene. Nature Materials 2007, 6, 183-190.
83. Tararan, A., Zobelli, A., Benito, A.M., Maser, W.M., Stephan, O. Revisiting graphene oxide chemistry via spatially-resolved electron energy loss spectroscopy. Chem. Mater 2016, 28, 3741-3748.
84. Szabo, T., Berkesi, O., Forgo, P., Josepovits, K., Sanakis, Y., Petridis, D., Dekany, I. Evolution of surface functional groups in a series of progressively oxidized graphite oxides. Chem. Mater. 2006, 18. 2740-2749.
85. Hofmann, U., Holst, R. Über die Säurenatur und die Methylierung von Graphitoxyd. Ber. Dtsch. Chem. Ges. 1939, 72, 754–771.
86. Ruess, G. Über das Graphitoxyhydroxyd (Graphitoxyd). Monatshefte für Chemie 1947, 76, 381–417.

87. Clauss, A., Plass, R., Boehm, H. P., Hofmann, U. Z. Untersuchungen zur Struktur des Graphitoxyds. Anorg. Allg. Chem. 1957, 291, 205–220.
88. Scholz, W., Boehm, H.P. Untersuchungen am Graphitoxid. VI. Betrachtungen zur Struktur des Graphitoxids. Z. anorg. allg. Chem. 1967, 353, 236-340.
89. Nakajima, T., Mabuchi, A., Hagiwara, R. A new structure model of graphite oxide. Carbon 1988, 3, 357-361.
90. Kim, S., Zhou, S., Hu, Y., Acik, M., Chabal, Y. J., Berger, C., De Heer, W., Bongiorno, A., Riedo, E. Room-temperature metastability of multilayer graphene oxide films. Nat. Mater. 2012, 11, 544−549.
91. Zhou, S., Bongiorno, A. Origin of the Chemical and Kinetic Stability of Graphene Oxide. Sci. Rep. 2013, 3, 2484.
92. Eigler, S., Dotzer, C., Hirsch, A., Enzelberger, M., Müller, P. Formation and Decomposition of CO2 Intercalated Graphene Oxide. Chem. Mater. 2012, 24, 1276−1282.
93. Dimiev, A. M., Alemany, L. B., Tour, J. M. Graphene Oxide. Origin of Acidity, Its Instability in Water, and a New Dynamic Structural Model. ACS Nano 2013, 7, 576−588.
94. Smith, A.T., LaChance, A.N., Zeng, S., Liu, B., Sun, L. Synthesis, properties, and applications of graphene oxide/reduced graphene oxide and their nanocomposites. Nano Materials Science 2019, 1, 31-47.
95. Brodie, B.C. On the Atomic Weight of Graphite. The Royal Society 1859, 249–259.
96. Staudenmaier, L. Verfahren zur Darstellung der Graphitsaure. Ber. Dtsch. Chem.Ges. 1898, 31, 1481–1487.
97. Hummers, W.S., Offeman, R.E. Preparation of graphitic oxide. J. Am. Chem. Soc.1958, 80, 1339-1339
98. Eigler, S., Hirsch, A. Chemistry with Graphene and Graphene Oxide—Challenges for Synthetic Chemists. Angew. Chem. Int. Ed. 2014, 53, 7720 – 7738.
99. Cao, Y., Li, G., Li, X. Graphene/layered double hydroxide nanocomposite: Properties, synthesis, and applications. Chemical Engineering Journal 2016, 292, 207-223.
100. Lonkar, S.P., Raquez, J.M., Dubois, P. One-pot microwave-assisted synthesis of graphene/layered double hydroxide (LDH) nanohybrids. Nano-Micro Lett. 2015, 7, 332–340.
101. Pang, H., Wu, Y., Wang, X., Hu, B., Wang, X. Recent Advances in composites of graphene and layered double hydroxides for water remediation: A Review. Chem. Asian. J. 2019, 14, 2542-2552.

102. Huang, S., Zhu, G.N., Zhang, C., Tjiu, W.W., Xia, Y.Y., Liu, T.X. Immobilizaiton of CoAl-layered double hydroxides on graphene oxide nanosheets: growth mechanism and supercapacitor studies. ACS Appl. Mater. Interfaces 2012, 4, 2242–2249.
103. Huang, W., Zhong, H.H., Li, D.Q., Tang, P.G., Feng, Y.J. Reduced graphene oxide supported CoO/MnO2 electrocatalysts from layered double hydroxides for oxygen reduction reaction. Electrochim. Acta 2015, 173, 575–580.
104. Yang, Z., Ji, S.S., Gao, W., Zhang, C., Ren, R.R., Tjiu, W.W., Zhang, Z., Pan, J.S., Liu, T.X. Magnetic nanomaterial derived from graphene oxide/layered double hydroxide hybrid for efficient removal of methyl orange from aqueous solution. J. Colloid Interface Sci. 2013, 408, 25–32.
105. Huang, G.B., Chen, S.Q, Song, P.A., Lu, P.P., Wu, C.L., Liang, H.D. Combination effects of graphene and layered double hydroxides on intumescent flame retardant poly(methyl methacrylate) nanocomposites. Appl. Clay Sci. 2014, 88–89, 78–85.
106. Wang, Y., Zhang, D., Bao, Q., Wu, J.J, Wan, Y. Controlled drug release characteristics and enhanced antibacterial effect of graphene oxide-drug intercalated layered double hydroxide hybrid films. J. Mater. Chem. 2012, 22, 23106–23113.
107. Li, S.,Wang, D.,Wu, X., Chen, Y. Recent advance on VOCs oxidation over layered double hydroxides derived mixed metal oxides. Chinese J. Catal. 2020, 41, 550–560.
108. Xu, Z.P. Zhang, J., Adebajo, M.O., Zhang, H., Zhou, C. Catalytic applications of layered double hydroxides and derivatives. Appl. Clay Sci. 2011, 53, 139–150.
109. Lee, S.B., Ko, E.H., Park, J.Y., Oh, J.M. Mixed Metal Oxide by Calcination of Layered Double Hydroxide: Parameters Affecting Specific Surface Area. Nanomaterials 2021, 11, 1153.
110. Fan, G., Li, F., Evans, D.G., Duan, X. Catalytic applications of layered double hydroxides:
recent advances and perspectives. Chem. Soc. Rev. 2014, 43, 7040-7066.
111. Rives, V. Layered Double Hydroxides: Present and Future, Nova Science Publisher, Inc, New York, 2001.
112. Zhang, X., Li, X. Mechanochemical approach for synthesis of layered double hydroxides. Appl. Surf. Sci. 2013, 274, 158-163.
113. Bravo-Suárez, J.J., Páez-Mozo, E.A., Oyama, S.T. Review of the synthesis of layered double hydroxides: a thermodynamic approach. Quim. Nova 2004, 601-614.

114. Iwasaki, T., Shimizu, K., Nakamura, H., Watano, S. Novel mechanochemical process for facile and rapid synthesis of a Co–Fe layered double hydroxide. Mater. Lett. 2012, 68, 406-408.
115. Qu, J., Zhang, Q., Li, X., He, X., Song, S. Mechanochemical approaches to synthesize layered double hydroxides: a review. Appl. Clay Sci. 2016, 185-192.
116. Ertl, G., Knözinger, H.,Schüth, F., Waitkamp, J. Handbook Heterogeneous Catalysis, Volume 1, Wiley-VCH (2012), Edit. Kubias, B., Fait, M.J.G., Schlögl, R., Chapter 2.4.8. Mechanochemical methods, pgs. 571-577.
117. Wu, H., Li, Q., Application of mechanochemical synthesis of advanced materials. J. Adv. Ceram., 2012, 1, 130-137.
118. Mahapatra, D.K.; Bharti, S.K.; Asati, V. Anti-cancer Chalcones: Structural and Molecular Target Perspectives.Eur. J. Med. Chem.2015,101, 496–524.
119. Stamate, A.E., Pavel, O.D., Zavoianu, R., Marcu, I.C. Highlights on the Catalytic Properties of Polyoxometalate-Intercalated Layered Double Hydroxides: A Review. Catalysts 2020, 10, 57.
120. Velu, S., Swamy, C.S. Alkylation of phenol with 1-propanol and 2-propanol over catalysts derived from hydrotalcite-like anionic clays. Catal. Lett., 1996, 40, 265-272.
121. Ordónez, S., Díaz, E., León, M., Faba, L. Hydrotalcite-derived mixed oxides as catalysts for different C–C bond formation reactions from bioorganic materials. Catal. Today 2011, 167, 2011, 71-76.
122. Lutic, D. Heterogeneous Acid-Base Catalyzed Aldol Condensation: Acetaldehyde and Heptaldehyde on Hydrotalcites. Optimization of Operatory Conditions, Acta Chem. Iasi. 2010, 18, 31-46.
123. Zhu, K., Liu, C., Ye, X., Wu, Y. Catalysis of hydrotalcite-like compounds in liquid phase oxidation: (I) phenol hydroxylation. Appl. Catal., A 1998, 168, 365-372.
124. Antonyraj, C.A., Gandhi, M., Kannan, S. Phenol Hydroxylation over Cu-Containing LDHs and Their Calcined Forms: Profound Cobivalent Metal Influence. Ind. Eng. Chem. Res. 2010, 49, 6020-6026.
125. Cativiela, C., Figueras, F., Fraile, J.M., Garcia, J.I., Mayoral, J. A. Hydrotalcite-promoted epoxidation of electron-deficient alkenes with hydrogen peroxide. Tetrahedron Lett. 1995, 36, 4125-4128.
126. Kaneda, K., Yamashita, T., Matsushita, T., Ebitani, K., Heterogeneous Oxidation of Allylic and Benzylic Alcohols Catalyzed by Ru−Al−Mg Hydrotalcites in the Presence of Molecular Oxygen. J. Org. Chem. 1998, 63, 1750-1751.

127. Choudary, B. M., Kantam, M.L., Rahman, A., Reddy, C.H. Selective reduction of aldehydes to alcohols by calcined Ni-Al hydrotalcite. J. Mol. Catal. A:Chem. 2003, 206, 145-151.
128. Kishore, D., Kannan, S. Environmentally benign route for isomerization of safrole—hydrotalcite as solid base catalyst. J. Mol. Catal. A: Chem. 2004, 223, 225-230.

Chapter 2. MATERIALS CHARACTERIZATION

2.1. Powder X-ray diffraction (XRD) analysis

The history of XRD dates back to 1912 when Max von Laue and Co. found out that crystalline compounds can behave as 3D diffraction grids for monochromatic X-rays almost identical to the architecture of the planes present in the network of crystals [1]. The structure of crystalline materials and the space between the component atoms can be quickly determined using the XRD technique. Some of the XRD technique advantages and limitations are presented in Table 1.

The working principle of XRD is quite simple. The X-rays produced by a cathode ray tube are directed toward the solid and instantly scattered by the electrons of the constituent atoms. This interaction can lead to the formation of constructive or destructive interferences which appear in all directions because the scattered waves are produced by atoms localized differently [2]. It is essential to mention that constructive waves appear only if the atoms are organized orderly. The periodicity of the atomic arrangement strongly influences the diffraction patterns. The diffraction occurs at small angles when there are long reiterated distances between the atoms and at high angles when there are short, repeated intervals [2].

The information regarding the crystal structure can be determined by geometric interpretation of the diffraction patterns. Bragg's law, seen below, is used to find a connection between the geometry of the diffraction grids and the diffraction patterns [3].

$$n\lambda = 2d\sin\theta$$

Where n is an integer representing the diffraction order, λ is the X-ray wavelength, d is the interplanar distance, and θ represent the diffraction angle.

Table 1. Advantages and limitations of XRD [6].

Advantages	Limitations
Minimal sample preparation	Solids need to be in powder form
Non-destructive technique	The data base is required
Fast time of analysis	Homogenous and single-phase materials
Easy data interpretation	Peak overlays may occur
Wide range of application	

The diffraction peak position reveals information regarding the size and shape of the unit cell. In contrast, the intensity of the peak is used to establish the position of atoms in the cell and to determine the atomic number [2].

X-ray powder diffraction is mainly used to identify crystalline solids such as inorganic materials or minerals. When layered materials like cationic or anionic clays are analyzed, broad and asymmetric diffraction peaks are noticed, probably caused by structural defects or stacking errors [4]. The diffraction patterns of an ideal LDH are characteristic of solid layered materials because they present narrow, symmetrical, and higher intensity lines at small values of 2θ. In contrast, at enhanced 2θ values, the lines are lower in intensity and asymmetrical [4, 5].

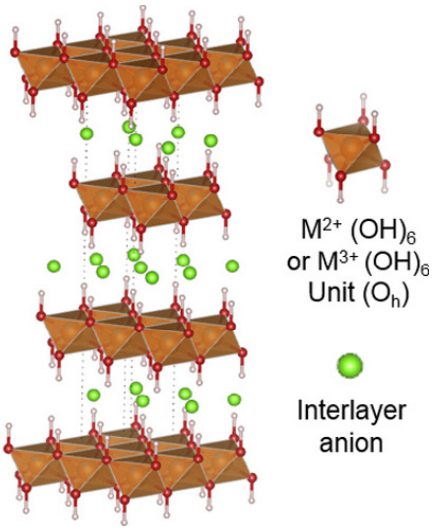

Figure 1. Crystalline structure of layered double hydroxides. Adapted from Ref. [4].

The ideal crystalline structure of LDH (Figure 1) is based mostly on the cations and the anions that are aimed to be included [4]. Difficulties in X-ray diffraction analysis of the hydrotalcites may occur due to insufficient crystallization or the non-stoichiometric nature of the LDH, which will cause asymmetry and broadness of the diffraction lines [5]. Despite these sources of imprecision, XRD analysis remains the primary analytical technique for the characterization of hydrotalcites in terms of structural order.

XRD powder patterns of the samples described in the thesis were recorded on a Panalytical X'Pert θ/2θ-diffractometer (from Panalytical Almelo, Netherlands) equipped with Xcelerator detector using automatic divergence slits and CuKα radiation (40 kV, 40 mA; λ=0.15418 nm). Cu beta-radiation was excluded using a nickel filter foil. The measurements were performed at 0.32°/min. Samples were mounted on silicon zero background holders. Obtained intensities were converted from automatic to fixed divergence slits (0.25°) for

further analysis. Peak positions and profiles were fitted with the Pseudo-Voigt function using the HighScore Plus software package (Panalytical). Phase identification was done by using the PDF-4+ database (2021) of the International Center of Diffraction Data (ICDD).

2.2. X-ray fluorescence (XRF) spectrometry

X-ray fluorescence (XRF) spectrometry is a well-established, non-destructive technique used to determine with good precision the elemental composition of materials [6]. The XRF analysis requires a miniumum effort for sample preparation and can be used for a large variety of materials both in solid or liquid form [6,7]. The working principle of XRF is quite simple. The X-rays produced by a synchroton or a radioactive material irradiate the samples [6]. At atomic level, a three step process ocurrs. First, the X-rays remove an electron from an orbital found near the atomic nucleus [6,7]. The electron removal produces further a hole in the orbital which lead to the formation of an unstable, high energy electronic configuration [6,7]. To reach an equilibrum, an electron from outer orbitals having a lower energy moves to fill the hole. Since there is a discrepancy between the energies, the excess is emitted in the form of fluorescent X-rays. Each element present in the sample will emit fluorescent X-rays with specific energies [6,7]. By measuring these energies and their intensities, it becomes posible to identify the element and its quantity [6,7].

X-ray fluorescence data for the samples described in the thesis have been collected using a Panalytical Epsilon 1 spectrometer (from Panalytical Almelo, Netherlands) operated with an Ag X-ray source.

2.3. X-ray photoelectron spectrometry (XPS)

X-ray photoelectron spectroscopy (XPS) is a surface sensitive, non-destructive analytical technique used for determining the composition and electronic structure of solid surfaces and interfaces of different materials [8,9]. Since most of the heterogenous catalytic reactions occur at the surface of the catalyst, obtaining information regarding the elemental atomic surface composition using XPS has become vital. XPS is based on the photoelectric effect discovered in 1887 by the German physicist Heinrich Hertz [10]. The solid is first irradiated with soft X-rays (photons) under ultra-high vacuum conditions. The absorption of the incident X-rays by the electrons results in their ejections from the sample with a certain kinetic energy [8,9]. These electrons with different energies are further analyzed by a detector and plotted related to the number of electrons.

In the present thesis, X-ray photoelectron spectroscopy (XPS) was employed to determine the chemical state of the elements present on the surface of the catalyst.

An Escalab Xi+ system, Thermo Scientific (Waltham, MA, USA) was used for X-ray photoelectron spectroscopy (XPS) survey and high-resolution XPS spectra acquisition. The survey scans were acquired using an Al Kα gun with a spot size of 900 μm, pass energy of 10.0 eV and an energy step size of 1.00 eV (5 scans). 20 scans were accumulated for Ce3d high-resolution XPS spectra, the pass energy was set to 10.0 eV, and the energy step size was 0.10 eV.

2.4. DRIFT spectroscopy

Diffuse reflectance infrared Fourier transformed (DRIFT) spectroscopy is a well-known technique since it can reveal the structural information and the chemical one for different solid materials [11]. Compared to the conventional transmission (or reflection) FTIR methods, DRIFT is a fast and non-destructive technique since the sample can be directly analyzed, both as it is or in its powdered form, also it is better suited to characterize strongly absorbing materials, whose main characteristic are very low signals and sloping baselines when analyzed in transmission [11]. Diffuse reflectance has been used extensively in the mid-IR and NIR regions of the electromagnetic spectrum to characterize solids [12,13]. The working principle of DRIFT spectroscopy is quite simple. When the spectrometer beam is focused on the sample, the light can be reflected, called specular reflection (Figure 2) [12,13]. Specular reflectance appears at the interface of two materials having different refractive indices while the angle of reflection is equal to incidence. Besides being reflected, the light can also pass through the sample. It can be partly absorbed, reflected, and refracted inside the material and diffused back to the surface, leading to diffuse reflection (Figure 2) [12,13].

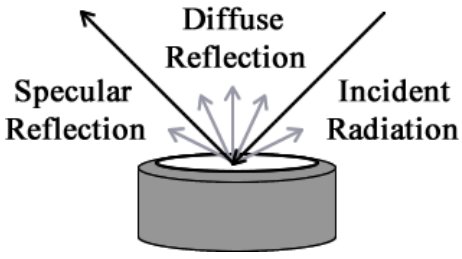

Figure 2. Working principle of DRIFT [8]

If the material has the right thickness, the intensity of the light penetrating the solid is equal to zero. When the specular reflection is negligible, the intensity of diffused light will supply all the information related to the light adsorbed by the material [12,13]. Exclusively the

segment of the light beam that scatters a material and turns back to the surface is recognized as diffuse reflection [13]. Although the diffuse reflectance technique can evaluate some solids as such, most of the samples need to be diluted with a non-absorbing matrix (KBr) to guarantee a deeper penetration of the incident beam into the solid which will lead to a decrease of the reflection component [12,13]. The spectrum obtained is very different compared to the one recorded in transmission mode, it appears to be of higher intensity than anticipated absorption from weak IR bands practically the quantitative laws are not similar [12,13]. Several models have been applied, leading to different expressions connecting the resulting diffuse reflectance to concentration [12]. The model complexity is characterized by the variety of empirical variables that need to be considered for each expression's development [12].

The resulted signals strongly rely on the light diffusion coefficient of the solid. This coefficient is influenced by particle size and the ratio between particle size and wavelength [14, 15]. When the particle size is of the same proportion level as the wavelength, the band intensities are directly proportional to the wavelength [15].

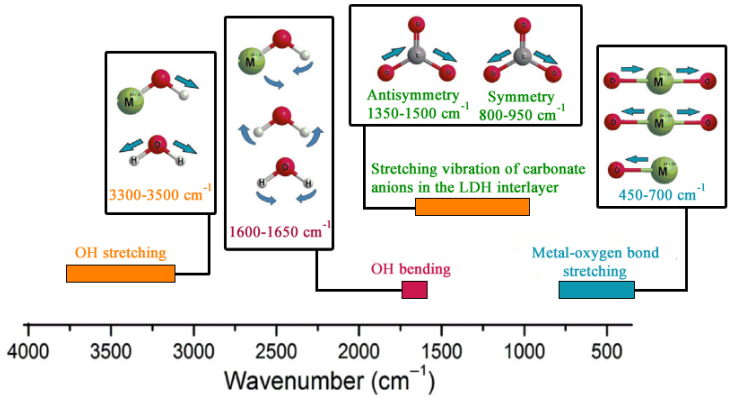

Figure 3. The approximate region of absorption bands for typical LDH [14]

When the particles are small, the bands are narrower, while the bands become broader at large particles. Temperature is another crucial factor that affects the intensity of the bands because it strongly influences the diffusion coefficient of the samples [15].

Diffuse reflectance infrared Fourier transformed (DRIFT) spectroscopy is one of the best techniques to identify the structure of layered double hydroxides and their intercalated anions. The structure of layered double hydroxides can be determined based on the specific absorption bands that appear in the DRIFT spectrum, as shown in Figure 3.

These bands are assigned as follows:

- The hydroxyl group stretching vibration related to the water molecules present in the interlamellar space of LDH and metal hydroxide layers, appearing often around 3300-3500 cm^{-1}. The combination of lattice or vibrational modes will lead to the appearance of a strong and broad absorption band corresponding to the brucite-type hydroxides [14,15].
- The absorption band around 1600-1650 cm^{-1} is attributed to the OH bending vibration [14,15].
- The absorption bands in the 450-700 cm^{-1} are related to the metal-oxygen and oxygen-metal-oxygen bands [14,15].
- The absorption bands corresponding to the anions found in the interlayer zone of the LDH appear in the range of 800-1700 cm^{-1} [14,15].

Based on the literature [14,15], the approximate region of the absorption bands attributed to some conventional anions that can be intercalated in the interlamellar space of the hydrotalcite is represented in Figure 4.

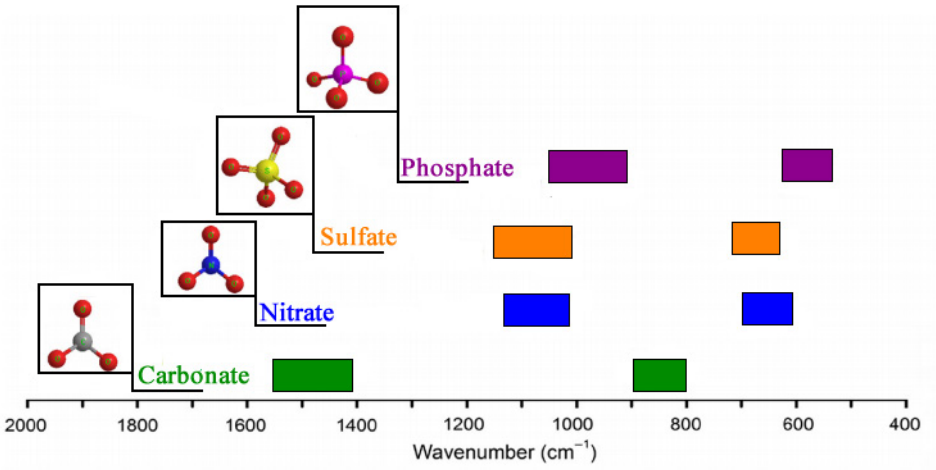

Figure 4. The approximate region of absorption bands attributed to common interlayer anions [14].

As shown in Figure 4, the absorption bands corresponding to typical anions intercalated in the LDH matrix, such as carbonate, nitrate, sulfate, phosphate, can be located in two regions [14]. The DRIFT spectra of the solids synthesized for the thesis were recorded with JASCO FT/IR-4700 spectrometer having a PIKE accessory for diffuse reflectance were collected in the spectral range 4000-400 cm^{-1}, with a scanning speed of 128 scans/min and a resolution of 4 cm^{-1} using KBr as background.

2.5. Diffuse reflectance UV-VIS spectroscopy (DR-UV-Vis)

Diffuse reflectance UV-VIS spectroscopy is based on the reflection of light in the ultraviolet (10–420 nm), visible (420–700 nm) and near-infrared (700–2500 nm) regions by a sample [16]. This technique is used for measuring the IR spectrum of materials that can be solid, powder or liquid [17,18]. When the incident infrared beam hits the sample, different situations can occur. The light can be reflected and the phenomen is called specular reflection, or it can penetrate the material and be absorbed or transmitted [17,18]. When the beam is travelling thorugh the material, it can also suffer absorbtion, reflection or refraction inside the sample, and can even be diffused back to the surface leading to the obtaining of diffuse reflection [17,18]. The relation between the diffuse reflectance of the sample (R_∞), absorption (K) and scattering (S) coefficients are related by the Schuster–Kubelka–Munk (SKM) remission function [16]:

$$F_{SKM}(R_\infty)=\frac{(1-R_\infty)^2}{2R_\infty}=\frac{K}{S}$$

The SKM remission function relates the experimentally determined diffuse reflectance of a thick sample to K and S [16]. In the current thesis, the diffuse reflectance UV-VIS-NIR spectra were recorded using UV3600 UV-VIS Shimadzu spectrometer and extra pure barium sulfate ($BaSO_4$) as white reference. The data were collected with 0.5 nm step and 8 nm slit width in the UV-Vis region and 2 nm step at 32 nm slit width in the NIR region.

2.6. Raman spectroscopy

The most used spectroscopies for identifying different types of molecular vibrations rely on infrared absorption and Raman scattering [19]. These techniques are used to calculate the quantity of a specific compound in material or even to determine an unknown sample. Also, they can offer information regarding the chemical structure [19]. Compared to infrared absorption, Raman scattering is exploited to a smaller extent, probably because it still has some unsolved issues regarding the deterioration of the sample material and the presence of fluorescence [19]. Nevertheless, these issues are soon to be clarified due to current technology. In 1923, Smekel introduced the idea of inelastic scattering of light, which was later, in 1928, determined empirically by Raman and Krishnan [19]. Consequently, the phenomenon became known as Raman spectroscopy.

When monochromatic light interacts with a material, there are three possibilities: the light will be absorbed, scattered, or it may just pass through the material. If a part of the light is scattered at the same frequency, the phenomenon is referred to as elastic or Rayleigh

scattering [20]. An even smaller segment of the light will shift the frequency attributed to the synergy among the vibration of the molecules and the photonic particles [20]. The Raman effect produces both positive and negative shifts of the initial wavelength known as Stokes and anti-Stokes lines [20]. Hence, Raman scattering is strongly influenced by the structure of the materials and is quite suitable to establish the molecular vibrations of symmetric molecules [20]. Raman is often combined with infrared spectroscopy due to its complementarity. Raman spectroscopy differs from the infrared one only because the polarizability changes of the molecules influence it. In contrast, infrared spectroscopy is affected by the changes in the molecules' dipole moment [20]. The two spectroscopic methods, Raman and infrared, are suitable for the characterization of layered double hydroxides and their derivatives since both can offer valuable information regarding all the vibrational species [20]. An essential key in the structural development of layered double hydroxides is attributed to water which is connected through hydrogen bonds to both anions and the hydroxyl groups present on the surface of the solid [20,21]. In infrared spectroscopy, the bands attributed to water molecules and those of the hydroxyl bounded to the metal sites are overlapping and cannot be distinguished. However, water is a very poor Raman scatterer, so the water is not observed in a Raman analysis leading to an efficient determination of hydroxyl absorption bands of the metal hydroxides [21]. So, the combination of Raman and Infrared spectroscopy is beneficial for studying layered double hydroxides. A high-resolution confocal Raman microscope (Renishaw system, Renishaw UK Ltd) equipped with two laser lines (514 nm and 785 nm, respectively) and a Leica DM2500 microscope was utilized for recording the Raman spectra of the solid samples present in the current paper, in extended mode using the 514 nm laser line, monitoring the shifts in the Raman band position narrower than 0.5 cm^{-1}, and measuring the Raman bands in the range 100 - 3100 cm^{-1}.

2.7. Scanning electron microscopy

In 1953, the German physicist Max Knoll proposed the notion of a scanning electron microscope. He believed that an image is obtained when an electron beam is focused on the surface of a material [22]. Manfred von Ardenne, another German physicist, developed further the concept and introduced the working principles of the technique [22].

The main elements of a scanning electron microscope are the electron column, specimen chamber, and computer control system, as shown in Figure 5. Their purposes are to implement different functions of microscopy and microchemical analysis [22]. The scanning electron microscope may also contain secondary and backscattered electron detectors,

energy-dispersive x-ray spectrometer (EDS), low vacuum detector etc. [22]. Scanning electron microscopy (SEM) can offer 3D-like images of the surface of different organic and inorganic heterogenous solid materials from a nanometer to a micrometre range [22]. The working principle of SEM is quite simple. Practically, the sample is irradiated with a focused electron beam, which can either glide on the surface of the solid resulting images or it can be static, leading to an analysis occurring in a particular position [22]. Different signals are generated during the interaction between the beam and the solid, namely secondary electrons, backscattered electrons, specific X-rays, and photons having different energies [22]. These signals provide valuable information regarding the surface topography, composition or crystallography [22]. The most important signals from the list mentioned above are the secondary and backscattered electrons which can influence the surface topology [22]. Moreover, the secondary electrons allow the formation of images with a resolution almost similar to the size of the electron beam [22]. The 3D aspect of the image is attributed to the increased depth of the microscope field and the shadow relief effect created by the secondary and backscattered electrons [22]. In scanning electron microscopy, signals corresponding to specific X-rays are also generated, which can be used to identify and quantify the elements present in the sample [22]. Scanning electron microscopy can be considered one of the most adjustable techniques suitable for investigating the microstructural features of solid materials. The many advantageous features, such as those presented in Table 2, have made scanning electron microscopy one of the most used analysis methods, providing valuable information regarding the morphology and composition of different materials. To overcome the limitations present in Table 2 and to obtain a complete analysis of a solid, it is essential to combine SEM with other analytical tools depending on the type of material [22]. Scanning electron microscopy has been successfully used to determine the shape and size of the layered double hydroxides (LDHs) [23]. Layered double hydroxides often have a hexagonal platelet morphology [23], but there are cases like takovite when fibrous particles have been noticed [23].

The diameter of the particles, thickness, and porosity can also be investigated using SEM. They are influenced mainly by the ageing treatment during synthesis [23]. All samples prepared in the current thesis were analyzed by scanning electron microscopy using a Philips XL 30 ESEM microscope (3.5 nm resolution) at 25 kV acceleration voltage. To emphasize the interesting aspects, the secondary electrons signal was mixed with the backscattered electrons signal in equal ratios.

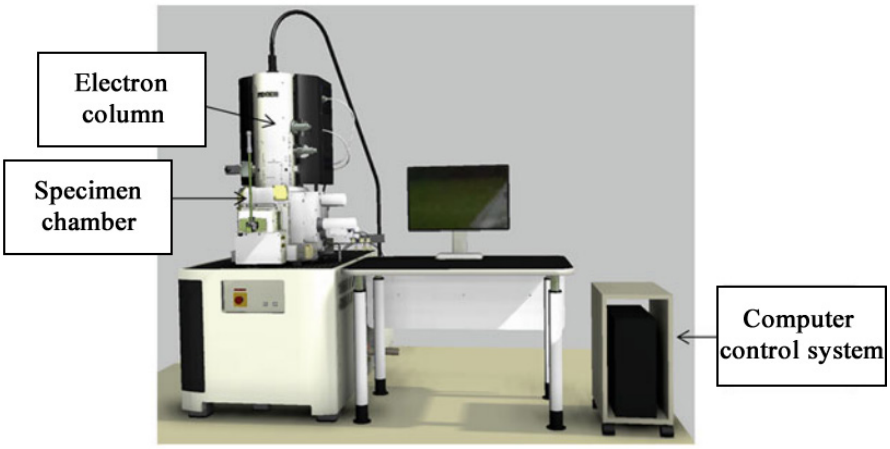

Figure 5. Three major components of a scanning electron microscope: electron column, specimen chamber, and computer control system [22].

Table 2. Advantages and limitations of SEM [22].

Advantages	Limitations
A wide variety of materials can be analyzed	The instrument needs ample space for installation
Non-destructive technique	A specific sample size
Easy and fast sample preparation	Use vacuum
Facile to handle the equipment	EDS detector cannot determine H, He or Li
Samples can be dried or wet	Samples need to be solid
High spatial resolution	
Capable of more types of imaging	

2.8. Determination of acid-base sites distribution

The metallic oxides that resulted after the calcination of the layered double hydroxides are versatile base catalysts that have been studied with considerable interest over the years. The nature of the base sites in heterogeneous catalysis is not yet fully understood because of the rare usage of solid base catalysts in organic reactions. The acidity of a solid is determined by the electronegativity of the compound and depends on how well ions are coordinated. So, low-coordinated anions and cations can form strong acidic sites [24]. Acidic Lewis sites from an oxide surface are low-coordinated metallic atoms obtained after the dehydration of the weak Brønsted sites [24]. Surface anions represent the base centres existing on the surface of the oxides: OH^- and O^{2-} [25]. The basicity is affected by the calcination procedure, around 400-500 °C and by structural and compositional parameters. Cations like Zn or Ni give less

basicity than Mg; fewer base catalysts are also obtained from Cl^- or SO_4^{2-} precursors than from CO_3^{2-} or OH^- containing materials [26].

The basicity also depends on the Mg/Al ratio. It has been reported that the total number of base sites increases by decreasing the Mg/Al ratio, but the portion of strong base sites decreases [26]. However, the correlation of the HT basic properties with the Mg/Al ratio is not always accurate [27]. The methods to determine the base surfaces are not as laborious as those for discovering the acidic sites, which are harder to find [26]. Weak acids containing an X-H bond can be connected to the basic sites from the surface through hydrogen bonds [26]. The most facile method used to determine the base sites distribution consists of the irreversible adsorption of organic acids with different values of pKa followed by quantitative determination of the adsorbed acid using a UV-VIS spectrometer. With pKa = 4.2, acrylic acid is used to determine the total number of basic sites, while phenol, pKa = 9.9, is used to determine the strong basic sites [26]. The number of low strength base sites is obtained from the difference between the total number of base sites and the number of high base sites. Before basicity measurement, the solids prepared in the current study were thoroughly calcined under static air condition in an oven. The materials were further weighed (0.05 g) and added to different volumetric flasks. Over the solids, 10 ml of freshly prepared solution of phenol/acrylic acid in cyclohexane was pipetted out and were shaken for two hours keeping the flasks closed. It was assumed that the interaction of the catalysts with atmospheric CO_2 and water was very negligible since the exposure of the samples to the atmosphere was for a brief period (during weighing only). The substrate concentration in solution in equilibrium with the adsorbed substrate was determined spectrophotometrically [27]. Sorption experiments were developed at the wavelength of maximum adsorption (λmax, nm) corresponding to phenol (λmax=271 nm) and respectively acrylic acid (λmax=225 nm) in the concentration range of the adsorbate where the Beer-Lambert Law holds well.

Pyridine adsorption was used for the determination of the total number of acid sites. The freshly calcined solids (0.05 grams) were wetted with pyridine aliquots (0.2 µl each) and maintained under inert flow at 90 °C for the removal of physisorbed pyridine. The procedure was repeated until the weight of each solid was constant after two consecutive additions of pyridine. The amount of adsorbed pyridine was divided by its molar weight to obtain the number of mmoles of adsorbed pyridine which is equal to the total number of acid sites determined by this method. To discern between the Brønsted and Lewis type acid sites, FT/IR-4700 Jasco spectrometer (Tokyo, Japan) was used to record the DRIFT spectra of the

solids with adsorbed pyridine considering the DRIFT spectra of the freshly dried materials as background. According to literature data, the bands corresponding to pyridine adsorbed on Lewis acid sites appear in the ranges of 1435-1455 cm^{-1} and 1570-1615 cm^{-1} while those corresponding to pyridine adsorbed on Brønsted acid sites appear in the range of 1520-1555 cm^{-1} and at 1630 cm^{-1} [28-30]. The areas of the peaks appearing in each of these regions were integrated and their total was calculated. Afterwards, the percentage distribution of the peaks corresponding to each type of acid site was calculated.

Real and bulk densities of the prepared catalysts were also determined. The real density of the LDHs was experimentally established using the pycnometer method. The bulk density was determined by averaging the results of 3 consecutive weightings of known volumes of the solid samples. The available volumes of solid were measured using a graduated cylinder where the solid sample was poured in. The filled cylinder was mechanically tapped until no further volume change was observed, and then it was weighted.

2.9. Textural measurements

The textural properties of the layered double hydroxides, such as surface area, pore size or total porous volume, play a significant role in understanding the catalytic activity of the materials. Usually, an inert gas is used for their determination, namely nitrogen [31,32]. The adsorption phenomenon occurs when the gas molecules stick to the surface of the solids. The analysis is performed at the temperature of liquid nitrogen, and it is used to determine the amount of nitrogen that is adsorbed or desorbed from the sample surface [31,32]. An adsorption-desorption isotherm is then plotted, giving valuable information about the solid porosity.

There are different types of adsorption-desorption isotherms classified by Braunauer and then by IUPAC [31]. This classification correlates the form of the isotherm with the dimensions of the pores and the intensity of the interaction between the gas and the solid surface [31,32]. The isotherm type I is attributed to the microporous solids; the type II isotherm is observed in the sample with no porosity or macropores. The isotherm type IV is specific to the solids with mesopores. Finally, type VI isotherm is attributed to groups of adsorption sites that are homogenous in energy [31,32]. These isotherms can be seen in Figure 6. Different methods were created to describe the isotherms. The most notorious is the one created by three different professors, namely Braunauer, Emmett and Teller, known as the BET model, which is used to extract information about the surface is from type II isotherms and also from type IV isotherms if there is a constant increased of the gas adsorbed on the surface [31,32].

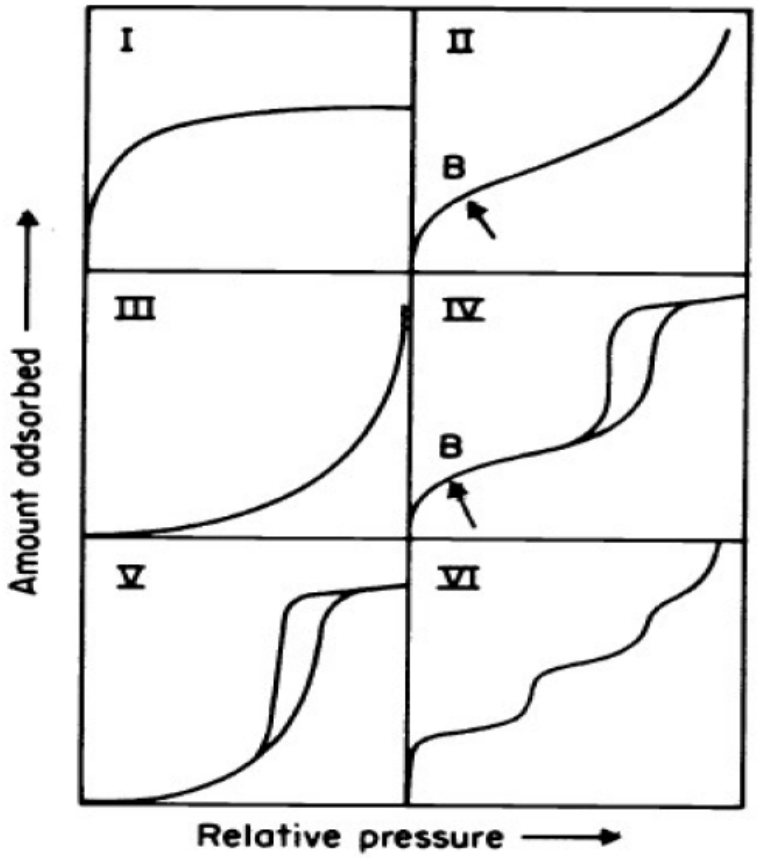

Figure 6. Adsorption-desorption isotherms classified by IUPAC [31]

References

1. Bunaciu, A.A., Udriştioiu, E.G., Aboul-Enein, H.Y. X-Ray Diffraction: Instrumentation and Applications. Critical Reviews in Analytical Chemistry 2015, 45, 289-299.

2. Ameh, E.S. A review of basic crystallography and x-ray diffraction applications. The International Journal of Advanced Manufacturing Technology 2019, 105, 3289–3302.

3. Bragg, W. H., Bragg, W. L. The Reflexion of X-rays by Crystals. Proc. R. Soc. Lond. A. 1913, 88, 428–438.

4. Park, D.H., Yang, J.H., Vinu, A., Elzatahry, A., Choy, J.H. X-ray diffraction and X-ray absorption spectroscopic analyses for intercalative nanohybrids with low crystallinity. Arabian Journal of Chemistry 2006, 9, 190-205.

5. Corma, A., Martin-Aranda, R.M. Application of solid base catalysts in the preparation of prepolymers by condensation of ketones and malononitrile. Appl. Catal. A: General 1993, 105, 271-279.

6. Brouwer, P. Theory of XRF. Getting acquainted with the principles. PANalytical BV, Almeo, The Netherlands, 2010, pages 10-11.

7. Tsuji, K., Matsuno, T., Takimoto, Y., Yamanashi, M., Kometani, N., Sasaki, Y.C., Hasegawa, T., Kato, S., Yamada, T., Shoji, T., Kawahara, N. New developments of X-ray fluorescence imaging techniques in laboratory. Spectrochimica Acta Part B 2015, 113, 43–53.
8. Stevie, F.A., Donley, C.L. Introduction to x-ray photoelectron spectroscopy. J. Vac. Sci. Technol. A 2020, 38, 063204.
9. Corcoran, C.J., Tavassol, H., Rigsby, M.A., Bagus, P.S., Wieckowski, A. Application of XPS to study electrocatalysts for fuel cells. Journal of Power Sources 2010, 195, 7856-7879.
10. Hertz, H. Uber einen Einfluss des ultravioletten Lichtes auf die electrische Entladung. Annalen der Physik 1887, 267, 983.
11. Accardo, G., Cioffi, R., Colangelo, F., D'Angelo, F., De Stefano, L., Paglietti, F. Diffuse Reflectance Infrared Fourier Transform Spectroscopy for the Determination of Asbestos Species in Bulk Building Materials. Materials 2014, 7, 457-470.
12. Khoshhesab, Z.M. Reflectance IR spectroscopy. Infrared Spectroscopy-Materials Science, Engineering and Technology. IntechOpen, 2012.
13. https://www.piketech.com/files/pdfs/PIKE_Diffuse-Reflectance-Theory-Applications.pdf
14. Mitchell, M.B. Fundamentals and Applications of Diffuse Reflectance Infrared Fourier Transform (DRIFT) Spectroscopy, In Structure-Property Relations in Polymers; Urban, M., et al.; Advances in Chemistry; American Chemical Society: Washington, DC, 1993.
15. Shabanian, M., Hajibeygi, M., Raeisi, A. FTIR characterization of layered double hydroxides and modified layered double hydroxides, Layered Double Hydroxide Polymer Nanocomposites Woodhead Publishing Series in Composites Science and Engineering 2020, 77-101.
16. Ranga, G., Ranjan, H. XRD and UV-Vis diffuse reflectance analysis of CeO_2–ZrO_2 solid solutions synthesized by combustion method. Proc. Indian Acad. Sci. 2001, 113, 651-658.
17. Leng, Y. Materials Characterization. Introduction to Microscopic and Spectroscopic Methods, Second edition, Chapter 9. Vibrational Spectroscopy for Molecular Analysis. Wiley-VCH Verlag GmbH & Co. KGaA, Boschstr. 12,69469 Weinheim, Germany, 2013, pgs. 283-305.
18. Thibault-Starzyk, F., Maugé, F. Characterization of Solid Materials and Heterogeneous. Catalysts. Chapter 1: Infrared Spectroscopy. Eds: Che, M., Vedrine, J.C., Wiley-VCH Verlag & Co. KGaA, Boschstr. 12, 69469 Weinheim, Germany, 2012, pg. 9.
19. Adar, F., Chapter 2. Evolution and Revolution of Raman Instrumentation-Application of Available Technologies to spectroscopy and microscopy, Ed.Lewis, I.R., Edwards, H.G.M.,

Handbook of Raman Spectroscopy From the research laboratory to the process line, 2001, Marcel Dekker,Inc..
20. Hess, C. New advances in using Raman spectroscopy for the characterization of catalysts and catalytic reactions, Chem. Soc. Rev. 2021, 50, 3519-3564.
21. Frost, R.L., Scholz, R., López, A., Theiss, F.L. Vibrational spectroscopic study of the natural layered double hydroxide manasseite now defined as hydrotalcite-2H – $Mg_6Al_2(OH)_{16}[CO_3]_4{\cdot}H_2O$. Spectrochimica Acta Part A: Molecular and Biomolecular Spectroscopy 2014, 118, 187–191.
22. Ul-Hamid A. Introduction. In: A Beginners' Guide to Scanning Electron Microscopy. Springer, Cham. 2018.
23. Kuang, Y., Zhao, L., Zhang, S., Zhang, F., Dong, M., Xu, S. Morphologies, Preparations and Applications of Layered Double Hydroxide Micro-/Nanostructures. Materials (Basel) 2010, 3, 5220–5235.
24. Sugunan, S., Chernparathy, G.V, Paul, A. MgAl hydrotalcites: preparation, characterization and ketonisation of acetic acid. Indian J. Eng. Mater. Sci. 1996, 3, 45-47.
25. Ertl, G., Knözinger, H.,Schüth, F., Waitkamp, J. Heterogeneous Catalysis of Alkene Epoxidation, Wiley-VCH, 2012, Chapter 3.2.4.3. Infrared Spectroscopy for the characterization of Surface Acidity and Basicity, 1155-1156.
26. Debecker, D.P., Gaigneaux, E.M., Busca, G., Exploring, Tuning, and Exploiting the Basicity of Hydrotalcites forApplications in Heterogeneous Catalysis, Chem. Eur. J., 2009,15, 3920 – 3935.
27. Ferencz, Z., PhD Thesis: Mechanochemical Preparation and Structural Characterization of Layered Double Hydroxides and their Amino Acid-Intercalated Derivatives, University of Szeged, 2016, Chapter 2. Literature review, pgs. 10-11.
28. Eimer, G. A., Casuscelli, S. G., Chanquia, C. M., Elías, V., Crivello, M. E., Herrero, E. R. The influence of Ti-loading on the acid behavior and on the catalytic efficiency of mesoporous Ti-MCM-41 molecular sieves. Catal. Today 2008, 133–135, 639-646.
29. Song, H.; Wang, J.; Wang, Z.; Song, H.; Li, F., Jin, Z. Effect of titanium content on dibenzothiophene HDS performance over Ni2P/Ti-MCM-41 catalyst, J. Catal. 2014, 311, 257–265.
30. Emeis, C.A. Determination of Integrated Molar Extinction Coefficients for Infrared Absorption Bands of Pyridine Adsorbed on Solid Acid Catalysts. J. Catal. 1993, 141, 347–354.

31. Sing, K. S. W. Reporting Physisorption Data for Gas/Solid Systems with Special Reference to the Determination of Surface Area and Porosity (Recommendations 1984). Pure and Applied Chemistry 1985, 4, 57.
32. Brunauer, S., Emmett, P. H., Teller, E. Adsorption of Gases in Multimolecular Layers. Journal of the American Chemical Society 1938, 60, 309–319.

Chapter 3. Ce-modified LDH structures as catalysts in condensation reactions: the effect of the preparation method

3.1. Overview

Recently, a new synthesis method based on mechanochemical treatment yielding related intercalates has been developed [1-3]. Besides the evident advantage of easy operation, this approach shows great potential to overcome the difficulties associated with solution operation, such as the different precipitation rates with pH adjustment [4]. To our knowledge, several studies have already been devoted to the synthesis of LDHs modified with different rare-earth elements through mechanochemical techniques [5,6]. Still, none of them has reported a LDH catalyst modified with cerium.

An interesting chemical transformation where the base catalytic properties of the LDHs/mixed oxides can be widely explored is the condensation reaction through which many types of compounds of vital interest for different kinds of industries can be synthesized. For instance, the self-condensation reaction of cyclohexanone which can be catalyzed by acidic or basic catalysts [7], has an essential role in caprolactam and adipic acid production processes and the production of 2-phenylphenol. In the cyclohexanone self-condensation, the adduct 1′-hydroxy-[1,1′-bicyclohexyl]-2-one is first generated, being subsequently transformed into a mixture of 2-(1-cyclohexen-1-yl)cyclohexanone and 2-cyclohexylidencyclohexanone by dehydration. The presence of another cyclohexanone molecule in the reaction medium can push the transformation to the di-condensation product or even further to dodecahydrotriphenylene or trihydroxyperhydrotriphenylene. Nowadays, although some catalytic materials have been highlighted for this transformation, namely: Mg-Al mixed oxide and reconstructed hydrotalcite [8], zirconia [9], MOF-encapsulating phosphotungstic acid [10], amberlyst 15 [7,11], silica chloride [12], keggin-type lanthanum phosphotungstate [13], ion exchange resin [14] etc., a lack of data involving the use of Ce-modified LDH catalysts can be noticed in the literature. Besides the self-condensation process, another interesting condensation reaction is the Claisen-Schmidt condensation, where compounds belonging to the flavonoid class, namely chalcone and flavone, are synthesized. Chalcone (CH) is an aromatic ketone and an enone that forms the central core for various important compounds, having various biological activities such as anti-diabetic, anti-neoplastic, anti-hypertensive, anti-retroviral, anti-inflammatory, anti-parasitic, anti-histaminic, anti-malarial, antioxidant, anti-fungal, etc. [15-17]. Similarly, flavone (FL) is considered the ”backbone” of many compounds used to treat numerous diseases. The

literature on this topic indicates that various LDH compositions were tested as catalysts for chalcone and flavone synthesis via Claisen-Schmidt condensation reaction [18-20]. Still, no studies were referring to the usage of LDH-type compounds modified with cerium until now.

In light of the aspects mentioned above, the current chapter intends to present the influence of the preparation method (co-precipitation and mechanochemical) on the physico-chemical properties and the catalytic activity of Ce-modified LDH structures and their corresponding mixed oxides in the above-mentioned condensation reactions.

3.2. Materials synthesis

3.2.1. Reagents and laboratory tools

The reagents and the materials used for both the preparation of the hydrotalcites-like compounds by using the co-precipitation, respectively the mecanochemical method are presented in Table 1.

Table 1: Reagents and materials for the synthesis of hydrotalcite-like catalysts: $[M(II)_{1-x}M(III)_x(OH)_2]A^{n-}_{x/n}\cdot mH2O$; $M(II):Mg^{2+}$; $M(III):Al^{3+},Ce^{3+}$.

Preparation method	Catalysts	Precursors	Reagents	Laboratory tools
Co-precipitation	HTCe-PP	$Mg(NO_3)_2\cdot 6H_2O$ $Al(NO_3)_3\cdot 9H_2O$ $Ce(NO_3)_3\cdot 6H_2O$	NaOH Na_2CO_3 Distilled water	-beakers -magnetic stirrer -Büchner funnel -pH-meter -conductometer
Mechanochemical	HTCe-MC			-mortar and pestle -Büchner funnel -pH-meter -conductometer

3.2.2. The preparation of the hydrotalcites

The compounds were synthesized by two different preparation routes: co-precipitation, respectively mechanochemical method.

3.2.2.1 The co-precipitation method

The co-precipitation method of the hydrotalcite-like catalysts implies the mixing of precursors (divalent and trivalent metal salts solutions, in well-defined proportions) with an alkaline solution containing the precipitating agent (Na_2CO_3, NaOH), which has the role of

maintaining a constant pH value (e.g. 10 pH units) to enable the co-precipitation of the mixed hydroxide [21]. The preparation steps of this method were identical for all the catalysts, the only difference in their synthesis is the initial solution of precursor salts used.In order to obtain the solid hydrotalcite type compounds, two solutions were needed (A and B). The solution A was prepared by dissolving 0.0343 moles $Ce(NO_3)_3 \cdot 6H_2O$, 0.5209 moles $Mg(NO_3)_2 \cdot 6H_2O$ and 0.1395 moles $Al(NO_3)_3 \cdot 9H_2O$ in 469 mL distilled water;

The solution B was prepared by dissolving 1.1575 moles NaOH and 0.4632 moles Na_2CO_3 in 387 mL distilled water.

The two solutions, A and B were mixed in a round-bottomed flask under continuous stirring and kept for aging for 18 hours.

a)  **b)**  

Figure 1. Synthesis (a) and purification (b) of the catalysts prepared by co-precipitation

The washing of the gel was carried out with distilled water until the pH reached 7. Filtering was performed using a Büchner funnel connected to a vacuum pump (Figure 1b). Drying was carried out in an oven at a temperature of 90°-100° C for 24 hours under air atmosphere. The solid obtained by co-precipitation was noted as HTCe-PP.

3.2.2.2. The mechanochemical method

A good method for preparing hydrotalcite-like catalysts is the mechanochemical route eliminating the need for feed pumps, magnetic stirrer with heating, and the aging step involved in the case of co-precipitation method. Practically the solid was prepared by dry grinding their precursor's nitrates salts with sodium hydroxide and sodium carbonate in a mortar. In order to obtain the compounds, the amounts of nitrates respecting the required molar ratios were mixed with sodium hydroxide and carbonate for one hour yielding a white paste (Figure 2a) which was further washed until the pH of the water was 7 (Figure 2b) and then dried in an oven at a temperature of 90-100°C for 24 hours under air atmosphere. The compound prepared using the mechanochemical method is called here HTCe-MC.

The corresponding mixed oxides were obtained by calcination at 460°C, for 18h and they were noted as Ce-PP (resulting from HTCe-PP) and Ce-MC (resulting from HTCe-MC).

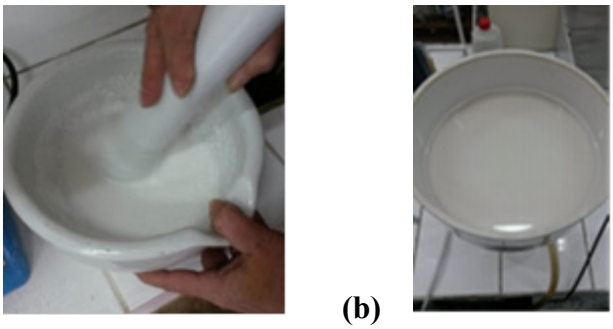

(a) **(b)**

Figure 2. Synthesis (a) and purification (b) of catalysts obtained by mechanochemical method

3.3. Catalysts characterization

The obtained solids were characterized using XRD, X-ray photoelectron spectroscopy (XPS), scanning electron microscopy (SEM), DRIFT, Raman spectroscopy, Diffuse reflectance UV-VIS-NIR spectroscopy. The base and acidic sites distribution of the cerium modified compounds along with the real and bulk densities were also determined. N_2 adsorption-desorption isotherms were also registred.

The XRD patterns (Figure 3a) show that both the dried form of the precipitated (HTCe-PP) and the mechanochemical (HTCe-MC) synthesized samples containing Ce expose the typical reflections of a layered double hydroxide-hydrotalcite type-phase (HT) ($Mg_6Al_2(CO_3)(OH)_{16}\cdot 4H_2O$, ICDD card 054-1030) as the dominant phase and small lines corresponding to CeO_2-phase (ICDD card 034-0394) as a minor phase. They are Miller indexed on Figure 3a. Reflections corresponding to cerium oxycarbonate side phase ($Ce_2(CO_3)_2O\cdot H_2O$, ICDD card 044-0617) denoted with (*) on Figure 3a were noticed only in the diffraction pattern of HTCe-PP.

The XRD patterns of the calcined form of the cerium-modified samples presented in Figure 3b display the reflections of both the mixed oxide Mg(Al)O periclase-type phase and CeO_2-cerianite phase. The structural data for the dried and calcined materials are gathered in Tables 2 and 3, respectively. For the hydrotalcite-type phase, two crystallite dimensions were calculated: the crystallite size perpendicular to the brucite-like layers (D003) and the crystallite size parallel to the brucite layers (D110). For the oxides phases, the most intense peaks from each phase were used. From the data presented in Table 2, a slight increase of the

a-parameter related to the minimum cation - cation distance in the brucite-like layer is evidenced. This is most likely due to an increase of the Mg/Al ratio, in comparison with Mg/Al = 3 for the standard ICDD card, because Ce^{3+} having a very large 6-coordinated ionic radius (1.01 Å) compared to Mg^{2+} (0.72 Å) and Al^{3+} (0.535 Å) almost certainly fails to enter in the brucite-like layer.

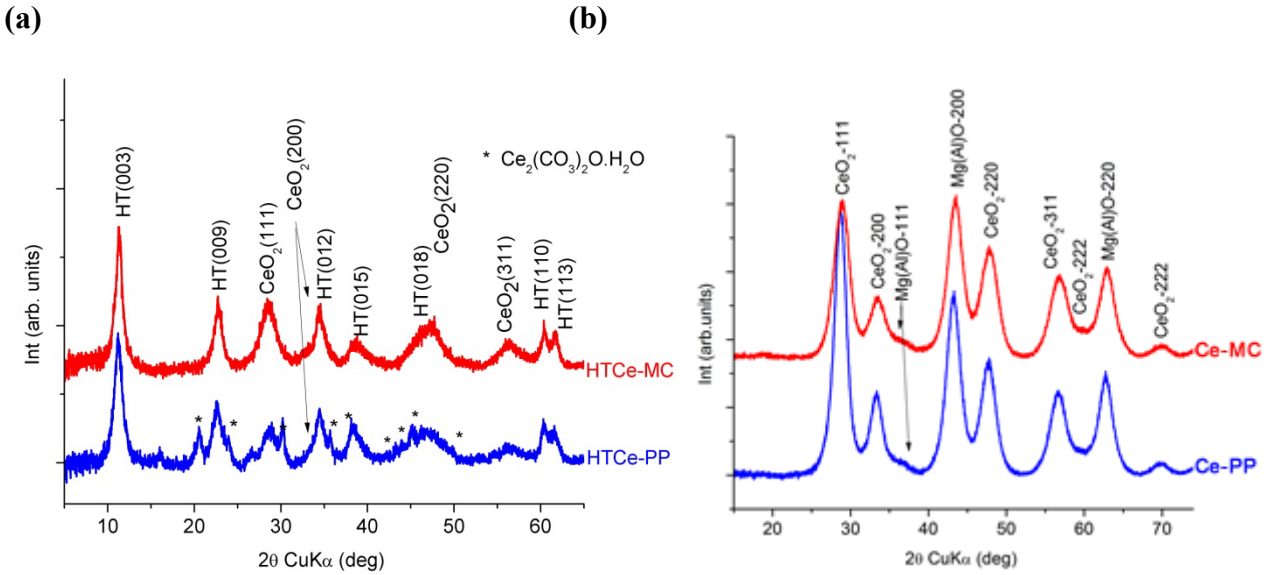

Figure 3. Diffraction patterns of the layered double hydroxides modified with cerium prepared by co-precipitation and mechanochemically under: (a) dried form (HTCe-PP and HTCe-MC); (b) calcined form (Ce-PP and Ce-MC).

In balance, a fluorite-type CeO_2 phase having unit cell parameter values almost identical with the standard cerianite (ICDD card 034-0394) occurred in both HTCe-PP and HTCe-MC samples, along with an oxycarbonate phase for the HTCe-PP.

The crystallite sizes related to the brucite-layer and the CeO_2 phases are smaller for HTCe-MC than for HTCe-PP indicating that the mechanochemical synthesis induces a slight degree of structural disorder. The slightly smaller dimensions of the crystalline phases of the mechanochemical prepared sample compared to the sample prepared via co-precipitation are preserved in the calcinated form of the materials (Table 3).

As expected, the a-parameter values of the Mg(Al)O phases are smaller than the standard periclase MgO due to the presence of Al^{3+} substituting cations.

The proportion of cerianite phase in the calcined form of the samples is higher and their unit cell parameters are smaller, which might be due to the substituting insertion of Mg^{2+} or Al^{3+}

generating defective and probably, more active ceria phases in comparison with the as-prepared samples they are originating from.

Table 2. The structural data for the dried form of the Ce-containing samples.

Samples	Crystalline phases								
	LDH				CeO_2		$Ce_2(CO_3)_2O{\cdot}H_2O$		
	a (Å)	c (Å)	D_{003}(nm)	D_{110}(nm)	a (Å)	D_{111}(nm)	a (Å)	b (Å)	c (Å)
ICDD-references	$Mg_6Al_2(CO_3)(OH)_{16}\cdot 4\,H_2O$ (ICCD card 054-1030)				CeO_2-cerianite (ICDD card 034-0394)		$Ce_2(CO_3)_2O{\cdot}H_2O$ (ICDD card 044-0617)		
	3.052	22.446			5.411	-	7.322	8.568	5.019
HTCe-PP	3.066	23.756	6.3	11.7	5.415	4.6	7.358	8.576	5.030
HTCe-MC	3.063	23.525	8.0	8.9	5.417	3.4	-	-	-

Table 3. The structural data for the calcined form of Ce-containing samples.

Samples	Crystalline phases			
	Mixed oxide Mg(Al)O		CeO_2	
	a (Å)	D_{200}(nm)	a (Å)	D_{111}(nm)
ICDD references	MgO-periclase ICDD card 045-0946		CeO_2-cerianite ICDD card 034-0394	
	4.2112	-	5.411	-
Ce-PP	4.187	3.8	5.386	3.9
Ce-MC	4.171	3.6	5.365	3.4

The SEM morphology (Figure 4) of the powders reveals a hierarchical structure with different aspects for the as-prepared samples compared to their corresponding calcined forms. For the as-synthesized samples assemblies of nanoplates nearly perpendicular to the outer surfaces of microspheres, characteristic of LDHs structures appeared, while for the calcined samples, the plate shape turned into a cloud-like form, suggesting that the hydrotalcite-like structure of the LDH precursor was destroyed during the thermal treatment. The SEM images of HTCe-MC and Ce-MC showed agglomerations of smaller particles compared to the samples obtained by precipitation method. This fact may be related to the absence of the ageing step in the mechanochemical preparation which shortened the crystal growth duration and hence the size of the crystallites.

The chemical compositions of the samples were determined via two different spectral techniques: energy-dispersive X-ray spectroscopy (EDS) and X-ray photoelectron spectroscopy (XPS), respectively. The difference between the two techniques is, in a concise description, related to their relative "depth of analysis". For EDS, the depth is around µm, giving the "bulk" concentration of chemical elements similar to other bulk sampling techniques, such as XRF or AAS.

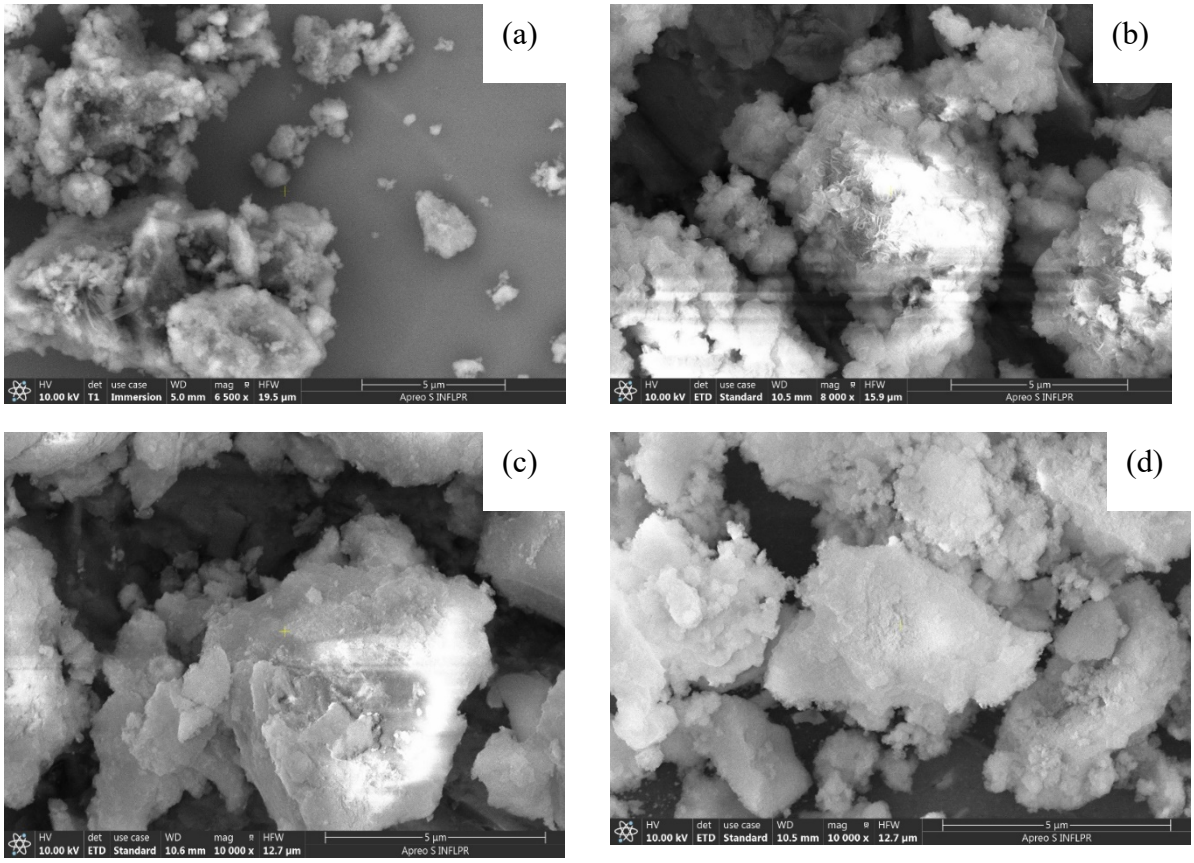

Figure 4. The SEM images of the LDHs modified with cerium: (a) HTCe-PP; (b) HTCe-MC; (c) Ce-PP; (d) Ce-MC.

On the other hand, the depth penetration of the signal for XPS is coming from the near-surface around 2-3 nm and, hence, it gives information on the elements present on the surface of the samples, including their oxidation state which is useful in heterogeneous catalysis, adsorption, corrosion or adhesion studies. The high-resolution XPS Ce3d spectra between 870 and 930 eV of the four samples (Figure 5) could be deconvoluted into ten bands, divided into two multiplets, labelled as υ and u, corresponding to the spin-orbit coupling of 3d 5/2 and 3d 3/2, respectively. The bands denoted as υ (u), υ'' (u'') and υ''' (u''') are ascribed to the photoemissions from the Ce^{4+} 3d core levels respectively, while the signals υ0 (u0) and υ' (u') are assigned to photoemissions from Ce^{3+} cations [22,23]. The proportion of Ce^{3+} was

calculated by comparing the integrated intensities of the peaks of υ, υ", υ"', u, u" and u"' of Ce^{4+} and υ0, υ', u0 and u' of Ce^{3+} in the XPS spectrum [24].

The chemical data are presented in Table 4. The data examination shows a decrease of the Mg/Al ratio on the external near-surface of the samples in comparison with the "bulk" values for all four catalysts. The Ce/Al ratio values are quite dispersed, probably due to a certain degree of the inhomogeneity of the samples. The proportion of surface Ce^{3+} ions is high for all the samples, being much higher than that of commercial ceria powders, such as a 4 N nanopowder (Ce^{3+}/Ce^{4+} = 0.45) and an abrasive powder (Ce^{3+}/Ce^{4+} = 0.34) [24]. These mixed Ce^{3+} and Ce^{4+} valence state of the fluorite structure of CeO_2 is considered to be responsible for many properties of ceria in various fields [24].

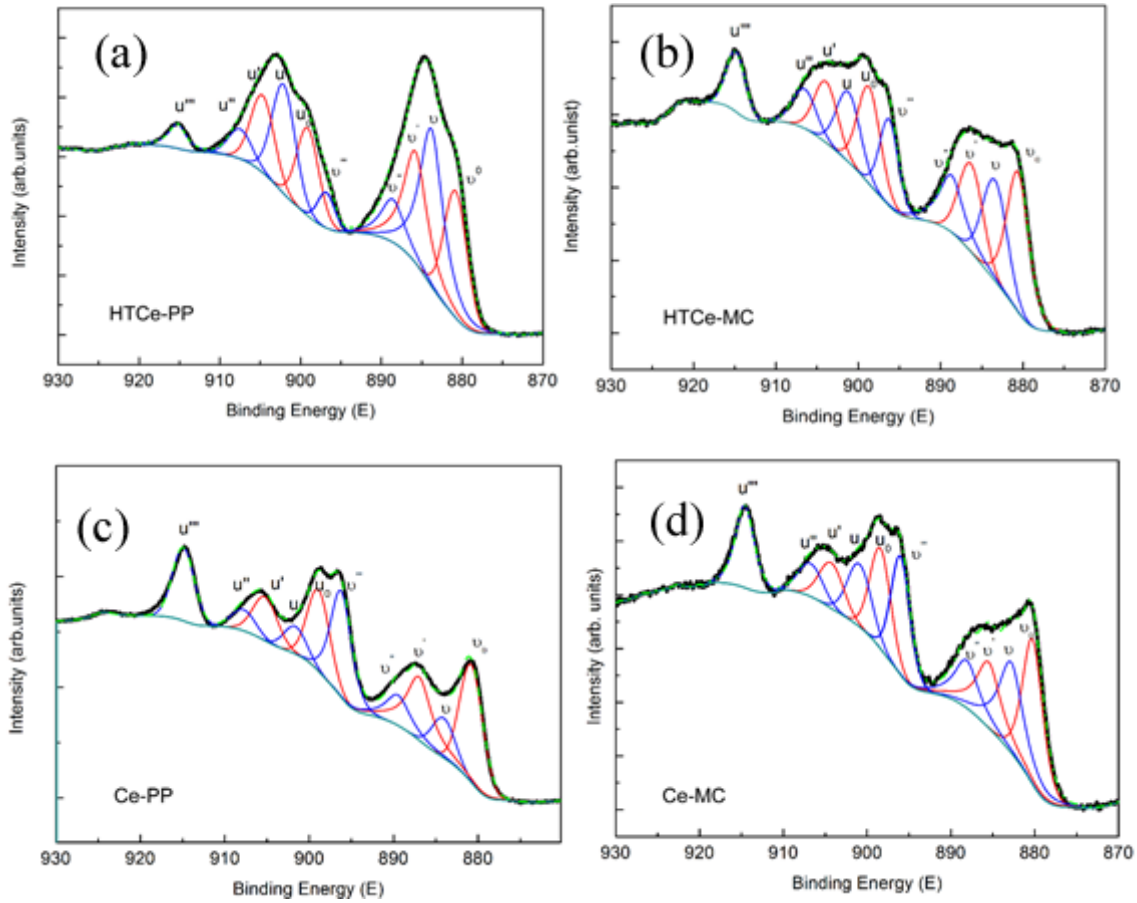

Figure 5. XPS analysis for a) HTCe-PP, b) HTCe-MC, c) Ce-PP, d) Ce-MC

It is noteworthy that the surface Mg/Al ratio decreases for both LDH samples during their thermal decomposition into the corresponding oxides. This suggests that the thermal decomposition of both LDH materials leads to mixed oxides whose surface is enriched in Al.

On the other hand, the surface Ce/Al ratio decreases while the surface Ce^{3+}/Ce^{4+} ratio increases during thermal decomposition of the coprecipitated LDH. Conversely, the surface Ce/Al ratio increases while the surface Ce^{3+}/Ce^{4+} ratio decreases for the mechanochemically

prepared oxide. This suggests the existence of some differences in the surface properties of Ce-PP and Ce-MC mixed oxides.

Table 4. Chemical composition of the prepared solids and their corresponding mixed oxides

Samples	Chemical compositions (atomic ratios)				
	EDS		XPS		
	Mg/Al	Ce/Al	Mg/Al	Ce/Al	Ce^{3+}/Ce^{4+}
HTCe-PP	3.09	0.11	2.07	0.25	0.98
HTCe-MC	3.24	0.29	2.85	0.13	1.07
Ce-PP	3.17	0.20	1.63	0.22	1.11
Ce-MC	3.03	0.31	2.19	0.19	0.80

The DRIFT spectra of the solids obtained by two different preparation methods, co-precipitation (HTCe-PP) and mechanochemical (HTCe-MC) and their corresponding mixed oxides are represented in Figure 6. The dried and calcined samples prepared by mechanochemical mixing present the same absorption bands as those of the corresponding samples obtained by the co-precipitation method.

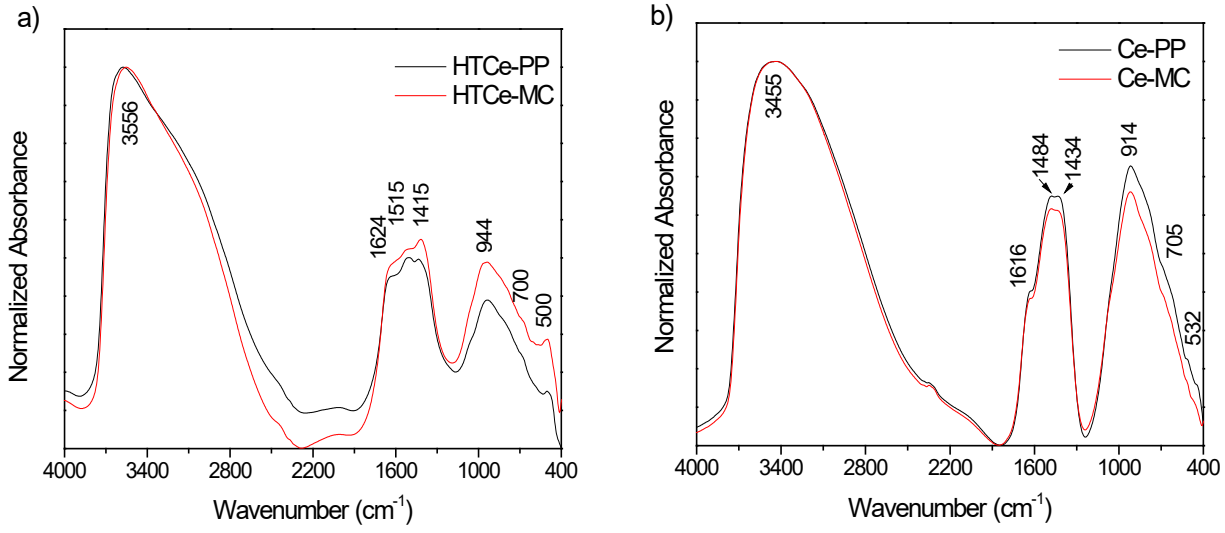

Figure 6. DRIFT spectra of the LDHs modified with cerium: (a) dried forms (HTCe-PP and HTCe-MC); (b) calcined forms (Ce-PP and Ce-MC).

The DRIFT spectra of the reference samples HTCe-PP and HTCe-MC, Figure 6a, show at around 3556 cm^{-1} an intense band that corresponds to the OH group vibration, ν(O–H) in the hydrotalcite structure and a shoulder at ca 3100 cm^{-1} suggesting the presence of a second type of –OH stretching vibration due to hydrogen bonding with the carbonate from the interlayer

space. The band at 1624 cm^{-1} is characteristic of the H_2O bending vibration of interlayer water in the hydrotalcite structure. The bands at 1415 cm^{-1} and 700 cm^{-1} were assigned to the CO_3^{2-} group vibration, while those at 600−400 cm^{-1} correspond to M-O bonds. The presence of unidentate carbonate asymmetric vibration is highlighted at 1515 cm^{-1}, while the peak at 944 cm^{-1} corresponds to carbohydrates. During calcination treatments, a part of OH^- and CO_3^{2-} groups are removed from the structure as carbon dioxide and water leading to a decrease of the intensity of the bands at 3100 and at around 1600 cm^{-1}, the latter suffering at the same time a shift from 1624 cm^{-1} (in the dried state) to 1616 cm^{-1} (in mixed oxides state). Because the carbonate anion is more stable, it is not totally removed at temperatures below 700 °C and, hence, it is also present in the calcined samples. The structural change that appeared by calcination also generates shifting of the bands from 1515 cm^{-1} to 1484 cm^{-1}, 1415 cm^{-1} to 1434 cm^{-1} and 944 cm^{-1} to 914 cm^{-1}.

The Raman spectra of the dried samples (Figure 7) show, at 150-153 cm^{-1}, one band attributed to the lattice vibrations [25]. The bands around 463 and 553 cm^{-1}, attributed to the Mg-O-Mg and Al-O-Al symmetric stretching vibrations, are accentuated in the case of the dried samples. The band at 463 cm^{-1} overlaps with the band corresponding to pure CeO_2 in F_{2g} vibrational mode displaying a symmetric breathing mode of four O^{2-} ions around each Ce^{4+} cation [26].

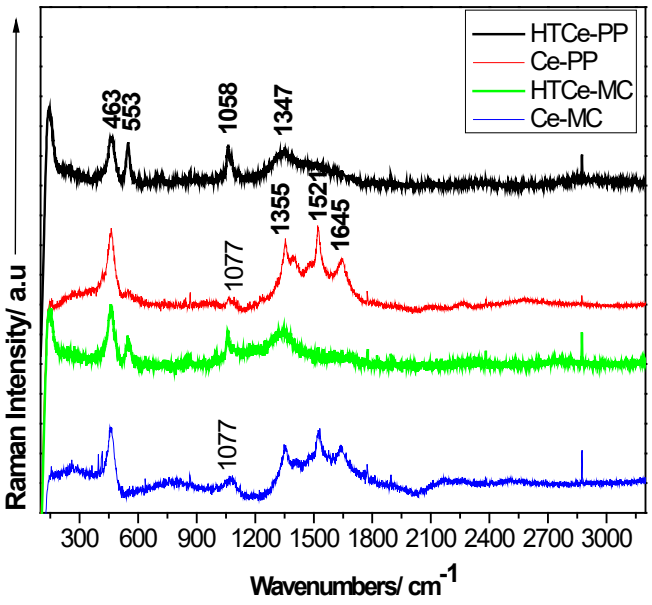

Figure 7. Raman spectra of the analyzed samples.

Moving further in the region of carbonate anions, there is a band at 1058 cm^{-1} which may be associated with the Mg_3OH unit [25] is shifted toward 1077 cm^{-1} in mixed oxides samples as

the ratio of the divalent to trivalent cations decreases [27]. The band at 1341 cm^{-1} is for the vibrations of CO_3^{2-} anions (v_3 symmetric stretching) [28]. In the carbonate vibrational region, there are at least four visible bands, especially in the case of the calcined samples which could not loose all the carbonate since the calcination temperature was below 700 °C. These bands occur at 1355 and 1395 cm^{-1} (due to the CO_3^{2-} antisymmetric stretching modes), at 1521 cm^{-1} (corresponding to the CO_3^{2-} ions [29]), and at 1645 cm^{-1} (attributed to the hydrogen bonds created by the water molecules [25]). Only a band at 2872 cm^{-1} appears in the hydroxyl stretching region due to the strong hydrogen bonds obtained between the carbonate anion and water.

The DRUV-VIS NIR spectra for the calcined compounds (Ce-PP and Ce-MC) are represented in Figure 8. The diffuse reflectance spectra of solids containing CeO_2 supported on alumina or silica present in the UV region intense bands at 250 and 297 nm, which are assigned to $Ce^{3+} \rightarrow O^{2-}$ and $Ce^{4+} \rightarrow O^{2-}$ charge transfer transitions, respectively [30,31]. In our case, for the calcined LDHs prepared by both methods, the $Ce^{4+} \rightarrow O^{2-}$ charge transfer transition peak is shifted with 17 nm to higher wavelengths (e.g. 314 nm), indicating a lower energy interaction. For both samples, there is also a peak at 290 nm, which is more intense for the sample Ce-MC indicating a stronger charge transfer for this sample.

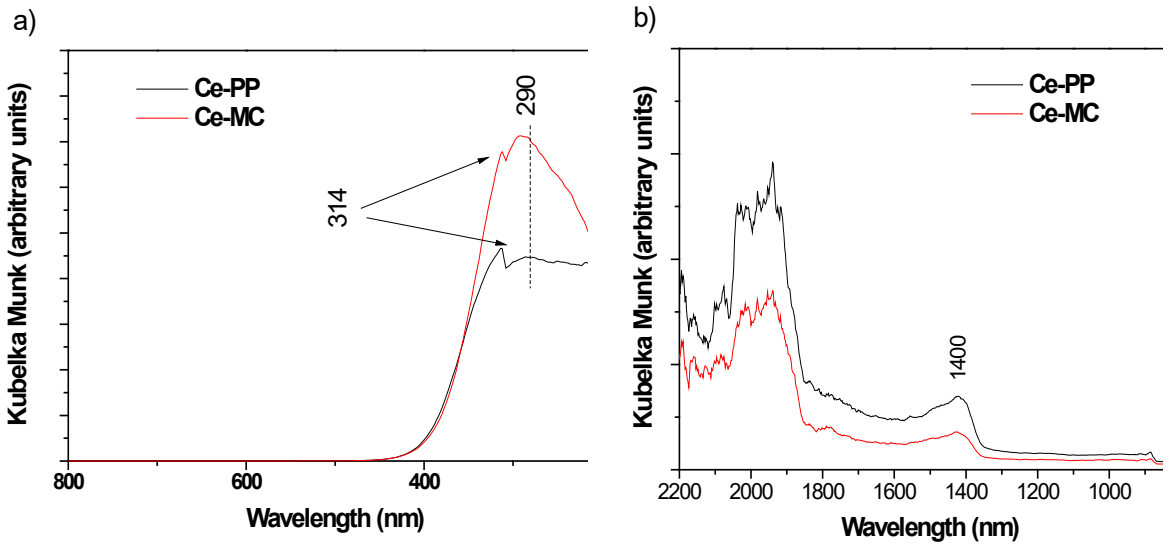

Figure 8. The DRUV-VIS NIR spectra of the calcined Mg3Al0.75Ce0.25 prepared by co-precipitation and mechanochemical methods in: (a) UV-Vis; (b) NIR.

Two absorption bands with similar intensities for the two samples were observed at higher wavelengths belonging to the NIR region, which can be ascribed to fundamental stretching frequencies of surface molecular groups such as H_2O and O–H [32].

The surface areas, bulk and real densities, acidities and basicities of the cerium-modified calcined hydrotalcite-like materials are tabulated in Table 5. It can be observed that the Ce-MC material has a total number of base sites two times higher compared with the Ce-PP sample. Moreover, while the Ce-MC sample show basic sites of all strengths, i.e. strong, medium and weak, the Ce-PP sample exposes almost only strong basic sites. responding LDH modified with rare earth cations [6]. This implies that the Ce-MC catalyst presents higher densities of OH^- and O^{2-} anions on its surface. This fact can be well related to the higher number of defects induced in the structure when using the mechanochemical method which does not include ageing. On the other hand, both mixed oxides possess a certain amount of surface acidity, in line with the XPS data showing that their surface is enriched in Al. At the same time, the Ce-PP sample shows a significantly higher number of acid sites compared to Ce-MC. In the former the Brønsted acid sites are dominant (76 %), while the latter mostly shows Lewis acid sites (95.6 %). Both real and bulk densities of the Ce-PP sample are about two times higher compared to those of the Ce-MC sample suggesting a significantly better packing of the former. Both samples show large surface areas as already noticed for mixed oxides obtained by calcination of the hydrotalcite samples.

Table 5. Surface area, density, acidity and basicity of the calcined Ce-modified LDHs.

Solid	Surface area ($m^2 \cdot g^{-1}$)	Total acid sites mmol Pyridine/g	% HB[1]	% Lewis acid sites	Total base sites (mmol acrylic acid/g)	Strong base sites (mmol phenol /g)	Weak and medium strength (mmol/g)	base /acid sites ratio	Density (kg/m^3)	
									Real	Bulk
Ce-MC	200	0.376	4.4	95.6	3.98	2.62	1.36	10.59	2224.7	539.0
Ce-PP	184	0.611	76	24	2.0	1.98	0.02	3.27	4632.4	981.6

[1] HB – Brønsted acid site

3.4. Catalytic studies

The catalytic activity of the prepared solids was tested first in the self-condensation reaction of cyclohexanone (Scheme 1), which requires 10 mmol of organic compound and 5 wt. % catalyst under batch and solvent-free conditions, at reflux (160 °C) and 5 h reaction time, with an agitation speed of 100 rpm.

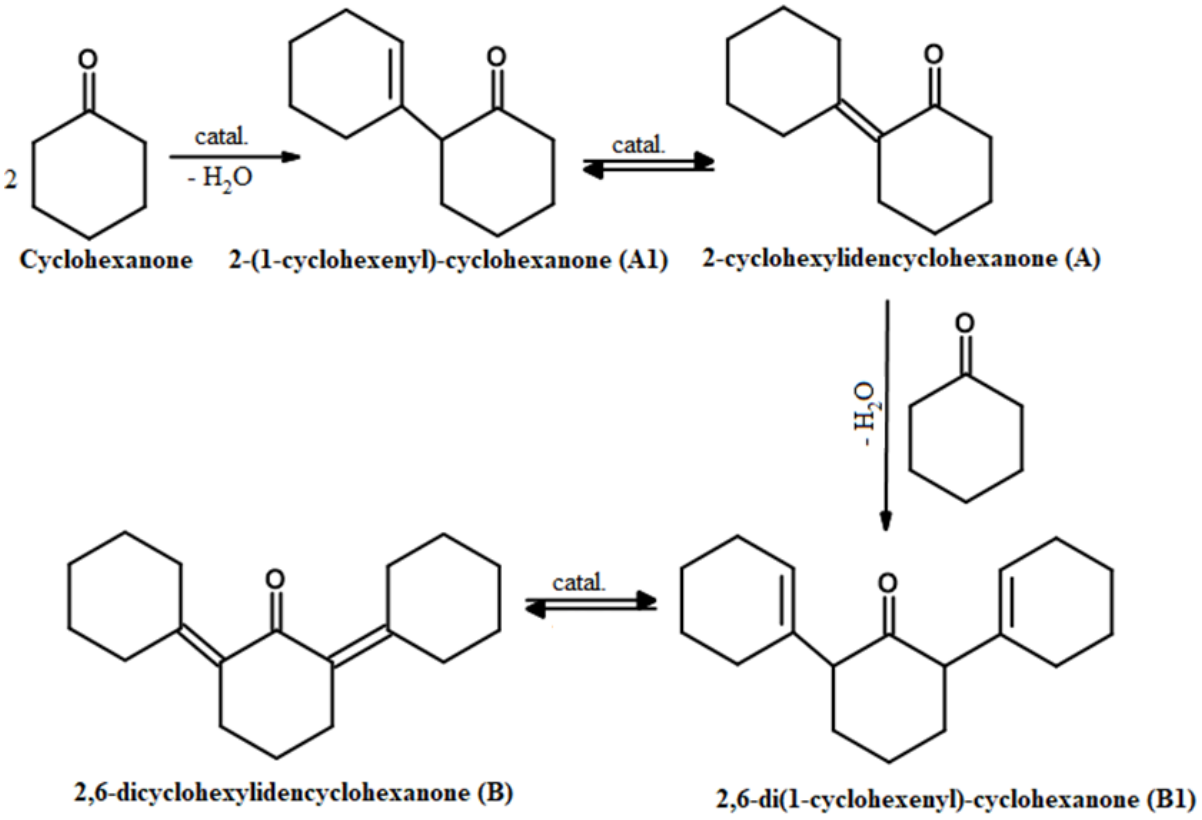

Scheme 1. Reaction route of cyclohexanone self-condensation.

They were also tested in two Claisen-Schmidt condensation reactions (Scheme 2 and 3), aiming the obtaining of compounds belonging to the flavonoid family, namely chalcone and flavone. For chalcone synthesis, benzaldehyde and acetophenone were used at different molar ratios, namely 1/1, 5/1, 10/1, while for flavone obtaining, acetophenone was replaced with its derivative compound 2'-hydroxyacetophenone, but the molar ratios benzaldehyde/ketone compound were kept the same. All the reagents were purchased from Merck. In all reactions, the catalyst concentration was 5% in the reaction admixture (w/w). The reactions were performed in a 50 mL stirred flask, under reflux conditions (e.g. 205 °C for chalcone synthesis and 300 °C for flavone synthesis), for 4 h reaction time, with an agitation speed of 100 rpm All the condensation products were analyzed with a Thermo Quest Chromatograph equipped with an FID detector and a capillary column of 30 m with DB5 stationary phase.

The reaction products were also identified by mass spectrometry-coupled chromatography, using a GC/MS/MS VARIAN SATURN 2100 T system equipped with a CP-SIL 8 C.B. Low Bleed/M.S. column of 30 m length and 0.25 mm diameter.

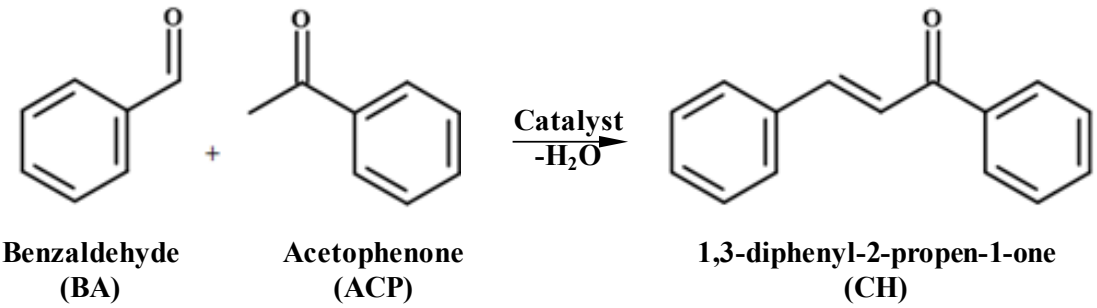

Scheme 2. Reaction route of chalcone synthesis

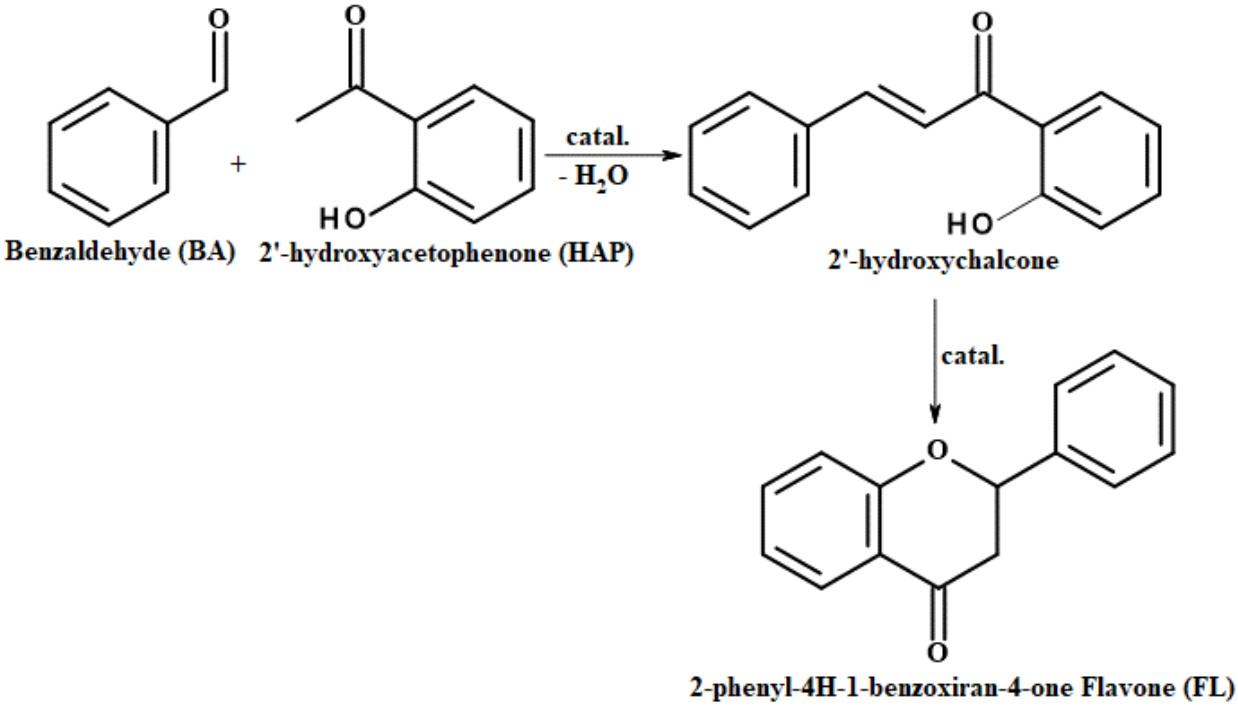

Scheme 3. Reaction route of flavone synthesis.

3.4.1. Self-condensation of cyclohexanone

Table 6 presents the values of cyclohexanone conversion after 5h under reflux conditions in cyclohexanone self-condensation reaction, the products observed being 2-cyclohexylidencyclohexanone (A), 2-(1-cyclohexenyl)-cyclohexanone (A1), 2,6-dicyclohexylidencyclohexanone (B) and 2,6-di(1-cyclohexenyl)-cyclohexanone (B1). The catalytic activity of the mixed oxides is superior to that of the dried samples regardless of the preparation method used. Notably, the mechanochemical method generates slightly more active catalytic materials, likely due to their higher basicity and larger specific surface area. In all cases, the selectivity to the mono-condensation product A is high, within the domain of 76-88%. It is worth noting that the mixed oxides catalysts gave only mono-condensation products A and A1, the selectivity towards di-condensation products being zero.

In the presence of cyclohexane (5 mL) as a solvent (Entry 6), the activity of Ce-MC catalyst is lowered without significant changes in the product distribution obviously due to the competition between reactant and solvent for the adsorption sites present onto the catalyst surface. By decreasing the reaction temperature from reflux conditions towards 100 °C, the conversion values for the reaction catalyzed by Ce-MC got lower by 25%. The stability of the Ce-MC catalyst was checked in four consecutive cyclohexanone self-condensation runs, the catalyst at the end of the reaction being separated by filtration and reused as such. After the four cycles, Entry 5, the conversion decreased by ca. 5 %, thus confirming the stability of this material in the reaction. However, there is a slight change in the ratio between mono- and di-condensation products.

Table 6. Conversion (Conv.) and selectivity (Sel.) obtained during the self-condensation reaction of cyclohexanone after 5 h under reflux conditions.

Entry	Catalysts	Conv. of cyclohexanone (%)	Sel. in (A) (%)	Sel. in (A1) (%)	Sel. in (B) (%)	Sel. in (B1) (%)
1	HTCe-PP	33.5	76.5	11.1	8.3	4.1
2	HTCe-MC	35.1	84.3	13.4	1.9	0.4
3	Ce-PP	53.2	86.3	13.7	0.00	0.00
4	Ce-MC	59.8	87.9	12.1	0.0	0.0
5	Ce-MC/recycled	54.2	83.4	11.8	2.4	2.4
6	Ce-MC/solvent	34.1	87.5	11.1	1.0	0.3

3.4.2. Claisen-Schmidt condensation

The conversions and selectivities obtained from one-pot synthesis of chalcone (CH) or flavone (FL) via Claisen-Schmidt condensation reactions between benzaldehyde (BA) and acetophenone (ACP) or benzaldehyde and 2'-hydroxyacetophenone (HAP), at different molar ratios (benzaldehyde/acetophenone or benzaldehyde/2'-hydroxyacetophenone = 1/1; 5/1; 10/1) are presented in Table 7. It can be observed that by increasing the molar ratios of the reagents, higher values of conversion but with lower selectivities are obtained. Moreover, the Ce-MC catalyst has proven to be more efficient than Ce-PP. The higher activity of the sample prepared by the mechanochemical method can be related to the fact that HTCe-MC and Ce-MC had smaller crystallite sizes as revealed by both the results of XRD analyses (Tables 3 & 4) and SEM micrographs since this preparation method did not imply the ageing step for the crystal growth. Its higher catalytic activity can also be well correlated to its higher number of base sites and larger surface area (see Table 5). Notably, the conversions of 2'-hydroxyacetophenone (HAP) are higher than those reached with acetophenone (ACP) on both catalysts and the selectivities to flavone are lower than those for chalcone. This fact can be a consequence of the higher reactivity of 2'-hydroxyacetophenone compared to acetophenone.

Table 7. Conversion (Conv.), selectivity (Sel.) and yields obtained on Ce-PP and Ce-MC mixed oxides catalysts operating at different molar ratios BA/ACP or BA/HAP under reflux conditions.

BA/ACP and BA/HAP molar ratios	**Conv. of ACP (%)**		**Sel. to CH (%)**		**Yield of CH (%)**		**Conv. of HAP (%)**		**Sel. to FL (%)**		**Yield of FL (%)**	
	Ce-PP	Ce-MC	Ce-PP	Ce-MC	Ce-PP	Ce-MC	Ce-PP	Ce-MC	Ce-PP	Ce-MC	Ce-PP	Ce-MC
1/1	37.1	42.3	100	100	37.1	42.3	57.2	79.1	77.7	78.8	44.4	62.3
5/1	77	78.2	94.5	96.2	72.8	75.2	84.3	85.2	70.5	75.9	59.4	64.7
10/1	93	97.1	92.5	95.4	86.0	92.6	94.1	96.2	67.3	69.7	63.3	67.1

3.5. Conclusions

The mechanochemical route of preparation has enabled the elimination of some steps, equipment and energetic consumption required in the co-precipitation method. The synthesized compounds exhibited the hydrotalcite structure, as indicated by the XRD measurements, whatever the preparation method used. However, apart from a ceria minor phase present in both of them, in the co-precipitated LDH material a supplementary side phase, i.e. cerium oxycarbonate, was identified.

The mixed oxide derived from the LDH prepared by the mechanochemical method show larger surface area, lower real and bulk densities, higher basicity and lower acidity compared with that obtained from the co-precipitated LDH material.

The LDH materials have comparable activities in cyclohexanone self-condensation but significantly lower compared to their corresponding mixed oxides. Among the latter, the mechanochemically prepared oxide was slightly more active than its co-precipitated counterpart. In all cases, the mono-condensation product 2-cyclohexylidencyclohexanone was the main reaction product, with selectivities of 76-84 % for the LDH catalysts, and 86-88 % for the LDH-derived mixed oxides. The mechanochemically prepared oxide showed a good stability during four reaction cycles.

In the Claisen-Schmidt condensation reactions, the mechanochemically prepared oxide catalyst was also shown to be more efficient than its co-precipitated counterpart, obviously due to its higher number of base sites. At the same time, both oxides show good selectivities to the desired product, the mechanochemically prepared oxide catalyst being slightly more selective to chalcone and flavone.

References

1. Li, Z., Chen, M., Hu, H., Zhang, Q. Tao, D. Mechanochemical synthesis of novel Pt modified ZnAl-LDH for effective ciprofloxacin photodegradation. J. Solid State Chem. 2020, 290, 121594.
2. Zhang, F., Hou, W. Mechano-hydrothermal preparation of Li-Al-OH layered double hydroxides. Sol. State Sci. 2018, 79, 93-98.
3. Jiang, Y., Yang, Z., Su, L., Chen, L., Wu, J., Meng, J. Preparation of Magnesium-Aluminum Hydrotalcite by Mechanochemical Method and Its Application as Heat Stabilizer in poly(vinyl chloride). Materials 2020, 13, 5223-5238.
4. Qu, J., Zhang, Q., Li, X., He, X., Song S. Mechanochemical approaches to synthesize layered double hydroxides: a review. Appl. Clay Sci. 2016, 119, 185-192.

5. Pavel, O.D., Zăvoianu, R., Bîrjega, R., Angelescu, E., Pârvulescu, V.I. Mechanochemical versus co-precipitated synthesized lanthanum-doped layered materials for olefin oxidation. Appl. Catal. A-Gen. 2017, 542, 10-20.
6. Pavel, O.D., Stamate, A.-E., Zăvoianu, R., Bucur, I.C., Bîrjega, R., Angelescu, E., Parvulescu, V.I. Mechano-chemical versus coprecipitation for the preparation of Y-modified LDHs for cyclohexene oxidation and Claisen-Schmidt condensations. Appl. Catal. A-Gen. 2020, 605, 117797.
7. Lorenzo, D., Santos, A., Simón, E., Romero, A., Kinetic of Alkali Catalyzed Self-Condensation of Cyclohexanone. Ind. Eng. Chem. Res. 2013, 52, 2257-2265.
8. Kikhtyanin, O., Kadlec, D., Velvarská, R., Kubička, D. Using Mg-Al Mixed Oxide and Reconstructed Hydrotalcite as Basic Catalysts for Aldol Condensation of Furfural and Cyclohexanone. ChemCatChem 2018, 10, 1464-1475.
9. Wan, M., Liang, D., Wang, L., Zhang, X., Yang, D., Li, G. Cycloketone condensation catalyzed by zirconia: Origin of reactant selectivity. J. Catal. 2018, 361, 186-192.
10. Deng, Q., Nie, G., Pan, L., Zou, J.-J., Zhang, X., Wang, L. Highly selective self-condensation of cyclic ketones using MOF-encapsulating phosphotungstic acid for renewable high-density fuel. Green Chem. 2015, 17, 4473-4481.
11. Kang, L., Wei, B. Synthesis of α,α′-bisbenzylidenecycloalkanones catalyzed by amberlyst 15. Chemistry Bulletin / Huaxue Tongbao 2007, 70, 801-804.
12. Hazarkhani, H., Kumar, P., Kondiram, K.S., Gadwal, I.M.S. Highly Selective Claisen–Schmidt Condensation Catalyzed by Silica Chloride Under Solvent-Free Reaction Conditions. Synth. Commun. 2010, 40, 2887-2896.
13. Gu, Y., Gao, Q., Suo, J. Self-condensation of cyclohexanone over keggin type lanthanum phosphotungstate catalyst. Shiyou Huagong/Petrochem. Technol. 2009, 38, 759-762.
14. Mahajan, Y.S., Kamath, R.S., Kumbhar, P.S., Mahajani, S.M. Self-condensation of cyclohexanone over ion exchange resin catalysts: kinetics and selectivity aspects. Ind. & Eng. Chem. 2008, 47, 25-33.
15. Mahapatra, D.K., Bharti, S.K., Asati, V. Anti-cancer Chalcones: Structural and Molecular Target Perspectives. Euro. J. of Med. Chem., 2015, 101, 496-524.
16. Mahapatra, D.K., Bharti, S.K. Therapeutic potential of chalcones as cardiovascular agents. Life Sci. 2016, 148, 154-172.
17. Mahapatra, D.K., Asati, V., Bharti, S.K., Chalcones and their therapeutic targets for the management of diabetes: structural and pharmacological perspectives. Eur. J. Med. Chem. 2015, 92, 839-865

18. Álvarez, M.G., Crivoi, D.G., Medina, F., Tichit, D. Synthesis of Chalcone Using LDH/Graphene Nanocatalysts of Different Compositions. ChemEngineering 2019, 3, 1-17.
19. Yadav, G.D., Wagh, D.P. Claisen-Schmidt Condensation using Green Catalytic Processes: A Critical Review. ChemistrySelect. 2020, 5, 9059-9085.
20. Climent, M.J., Corma, A., Iborra, S., Velty, A. Activated hydrotalcites as catalysts for the synthesis of chalcones of pharmaceutical interest. J. Catal. 2004, 221, 474-482.
21. Cavani, F., Trifiro, F., Vaccari, A. Hydrotalcite-type anionic clays: Preparation, Properties, and applications. Catalysis Today 1991, 11, 173-301.
22. Wang, Y., Zhao, J., Wang, T., Li, Y., Li, X., Yin, J., Wang, C. CO_2 photoreduction with H2O vapor on highly dispersed CeO_2/TiO_2 catalysts: Surface species and their reactivity. J. Catal. 2016, 337, 293-302.
23. Gao, X., Jiang, Y., Zhong, Y., Luo, Z., Cen, K. The activity and characterization of CeO_2-TiO_2 catalysts prepared by the sol-gel method for selective catalytic reduction of NO with NH_3. Hazard. Mater. 2010, 174, 734-739.
24. Ma, W., Mashimo, T., Tamura, S., Tokuda, M., Yoda, S., Tsushida, M., Koinuma, M., Kubota, A., Isobe, H., Yoshiasa, A. Cerium oxide (CeO2-x) nanoparticles with high Ce^{3+} proportion synthesized by pulsed plasma in liquid. Ceram.Int. 2020, 46, 26502-26510.
25. Palmer, S.J., Nguyen, T., Frost, R.L. Synthesis and Raman spectroscopic characterization of hydrotalcite with CO_3^{2-} and VO_3^- anions in the interlayer. J. Raman Spectrosc. 2007, 38, 1602-1608.
26. Dronova, M., Lair, V., Vermaut, P., Ringuedé, A. An, V. Study of ceria thin films prepared via electrochemical deposition: Role of selected electrochemical parameters on growth kinetics. Thin Solid Films 2020, 693, 137674.
27. Palmer, S.J., Frost, R.L.; Spratt, H.J. Synthesis and Raman spectroscopic study of Mg/Al,Fe hydrotalcites with variable cationic ratios. J. Raman Spectrosc. 2009, 40, 1138-1143.
28. Li, X., Guo, M., Bandyopadhyay, P., Lan, Q., Xie, H., Liu, G., Liu, X., Cheng, X., Kim, N.H., Lee, J.H. Two-dimensional materials modified layered double hydroxides: A series of fillers for improving gas barrier and permselectivity of poly(vinyl alcohol). Compos. B. Eng. 2021, 207, 108568.

29. Iqbal, M.A., Fedel, M. Effect of Synthesis Conditions on the Controlled Growth of MgAl–LDH Corrosion Resistance Film: Structure and Corrosion Resistance Properties. Coatings 2019, 9, 30.
30. Rao, R. G., Sahu, R.H. XRD and UV-Vis diffuse reflectance analysis of CeO2–ZrO2 solid solutions synthesized by combustion method. Proc. Indian Acad. Sci. 2001, 113, 651-658.
31. Abbasi, Z., Haghighi, M., Fatehifar, E., Saedy, S. Synthesis and physicochemical characterizations of nanostructured Pt/Al2O3–CeO2 catalysts for total oxidation of VOCs. J. Hazard. Mater. 2011, 186, 1445-1454.
32. Bensalem, A., Bozon-Verduraz, F., Delamar, M., Bugli, G. Preparation and Characterization of Highly Dispersed Silica-Supported Ceria. Appl. Catal. A 1995, 121, 81-93.

Chapter 4. MgAl-layered double hydroxide-graphene oxide hybrid materials as multifunctional catalysts for organic transformations

4.1. Ce-containing MgAl layered double hydroxide-graphene oxide hybrid materials

4.1.1. Overview

Developing improved strategies for the manufacture of two-dimensional (2D) nano-hybrid multifunctional materials has attracted a lot of interest in advanced research and technology. The combination of various nanomaterials having different physical and chemical properties can lead to improved nanocomposites possessing the qualities of the parent building blocks [1]. Recently, hybrid materials have gained a lot of attention due to their usefulness in various applications, from industry to water treatments and catalysis [1,2]. Graphene oxide and layered double hydroxides are among the various compounds that can be combined [2].

The combination of layered double hydroxides (LDH) with components such as graphene oxide (GO), a 2D honeycomb material with oxidizing properties [3,5], can lead to the formation of nanohybrids with improved properties that can be valorized in many applications, including catalysis [1,2]. Despite its advantageous properties such as increased optical, electronic, and thermal stability [4,6], graphene oxide tends to agglomerate and restack [1,4]. Thus, to overcome this problem, it is necessary to embed GO into other materials, like layered double hydroxides. Graphene oxide and LDH present different chemical and physical properties which complement each other up to a certain point offering hybrid materials that have layered structure, large surface area, multiple functional groups coming from GO and the anionic exchangeability of the hydrotalcites [6]. Although tremendous progress has been made, numerous hurdles still need to be overcome before hybrid materials containing GO and LDH can be used to their full potential. Although the present synthetic approaches seem promising, the materials must be generated on an industrial level to achieve large-scale production. The carbon-carbon bond formation has been considered as the fundamental key of the entire organic chemistry [7]. One of the most efficient ways to obtain the desired covalent bond has proven to be the aldol condensation which is generally catalyzed by bases, acids, or catalysts presenting both basic and acidic sites [8]. The base-catalyzed aldol condensation, known as the Knoevenagel condensation, has been widely exploited to produce various specialty chemicals, intermediates with biological applications, or valuable products such as calcium antagonists drugs, and other pharmaceuticals, polymers, coumarin derivatives and even for the beauty industry (cosmetics, perfumes) [7]. In the Knoevenagel condensation reaction, an aldehyde or a ketone condenses

with active methylene-containing compounds (acyclic 1,3-dicarbonyls and derivatives such as malonates, acetoacetates, acetonitriles, acetylacetone, malononitrile, or cyclic CH-acidic compounds like 1,3-cyclohexanediones, Meldrum's acid, barbituric acids, oxazepanediones, 4-hydroxycoumarin, etc.) usually in the presence of alkali metal hydroxides, organic bases (primary, secondary and tertiary amines) or their corresponding ammonium salts, urea, pyridine, as well as different Lewis basic/acidic materials [8-12]. However, the condensation process, conventionally performed under homogenous conditions, has some disadvantages associated to the inability of the homogeneous catalysts to be recovered and recycled or to the excess of the solvent used during the reaction, which may generate increased volumes of toxic waste affecting the environment [8,10]. To overcome these drawbacks, a large variety of solid catalysts has been exploited over the past years such as polystyrene-supported poly(amidoamine) dendrimers [13], polystyrene immobilized DABCO [14], various amine/diamine-functionalized materials [15-18], chitosan hydrogel [19], acrylic resin-immobilized lipase [20], zeolites [21-23], metal-organic frameworks [24], diethylenetriamine-functionalized graphene oxide with Fe_3O_4 nanoparticles [25], and many others. Nevertheless, these catalytic systems still present some inconveniences, such as the leaching of the basic fragment of the catalyst, the active site blocking and the redundant use of organic solvents and additives [12]. Considering these limitations, the development of an environmentally friendly, efficient, and selective heterogeneous catalytic system that presents a high activity for the Knoevenagel reaction under mild conditions continues to be a challenging research domain. One-pot cascade reactions, also called tandem reactions, represent an ingenious solution that can drastically simplify and improve intricate synthetic pathways, also reducing the production of wastes and energy consumption [26]. One-pot cascade reactions must be carefully planned to ensure that the correct sequence of reactions is followed in the correct order to get the target product. Designing a suitable multifunctional catalyst having various, spatially isolated active sites is essential for a successful tandem reaction. It is critical to select an appropriate material for the development of a multi-functional catalyst that has some catalytic activity of its own and that also possesses the ability to integrate some extra catalytic features. To date, a wide variety of catalytic systems have been proposed for cascade reactions, however, many of these have been based on homogeneous catalysts [26,27]. Compared to homogeneous catalysts, the heterogeneous ones present important advantages, such as easy recovery and recyclability, less contamination of the reaction medium, and increased stability [26,27]. The heterogeneous solids that have been reported in the literature as catalysts for the alcohol oxidation/Knoevenagel condensation

cascade reactions, such as Pd-nanoparticle-supported Nano-ZSM-5 [28], Pd/LS-AT-OH@catalyst [29], Pd0@UiO-68-AP [30], porphyrin-based microporous organic polymer Fe-POP-1 [31], polyoxometalate-intercalated LDH [26], Pd1-Au1/LDH [32], NiGa LDHs [33], and copper complexes [34] presented some drawbacks which referred to high costs of the synthesis, high-temperature regimes and the use of basic additives during the tandem reactions. Considering the already published data, a potential class of catalysts that exhibits the necessary requirements to obtain promising results not only in Knoevenagel condensations but also in oxidation/Knoevenagel condensation cascade reactions is represented by the layered double hydroxides. Developing a high-efficiency catalytic system for the aerobic oxidation of alcohols to the corresponding carbonyl compounds without any additives is particularly attractive in synthetic and industrial organic chemistry [26]. Recently, layered double hydroxides modified/doped with rare-earth elements have received increasing attention due to their enhanced basicity which led to improved catalytic performance [35]. However, the beneficial catalytic, electric and magnetic properties generated by the insertion of rare-earth metals cannot be exploited to their full potential due to the challenging incorporation of large rare-earth cations into the brucite structure, as in the case of cerium ions which possess a higher ionic radius compared to the main cations involved in the construction of the layers [36]. Also, according to the literature, the synthesis of single-phase Ce-modified LDHs is quite difficult since cerium (III) is easily oxidized in aqueous solutions [36]. Therefore, most of the samples contain supplementary phases such as $CeCO_3OH$ or CeO_2 [36]. The current study focuses on the synthesis, structural and catalytic properties of Ce-containing MgAl LDH-GO composites bearing different concentrations of GO in the range of 5-25 wt. % abbreviated as HT3Ce-xGO where *x* stands for the concentration of GO (*x* = 5, 10, 15, 15, 20, 25 wt. %). The solids were tested as catalysts in two different types of organo-chemical transformations: i) Knoevenagel condensation reaction (Scheme 1) and ii) one-pot cascade oxidation-Knoevenagel condensation (Scheme 2). Notably, by reviewing the literature, only two articles containing LDH-GO hybrids, with the layered double hydroxide modified with a lanthanide (La [37], and Gd [38], respectively) stood out. Moreover, these hybrids had no catalytic purpose, being only used as flame-retardant [37] and nano-carriers for magnetic resonance imaging and drug delivery [38].

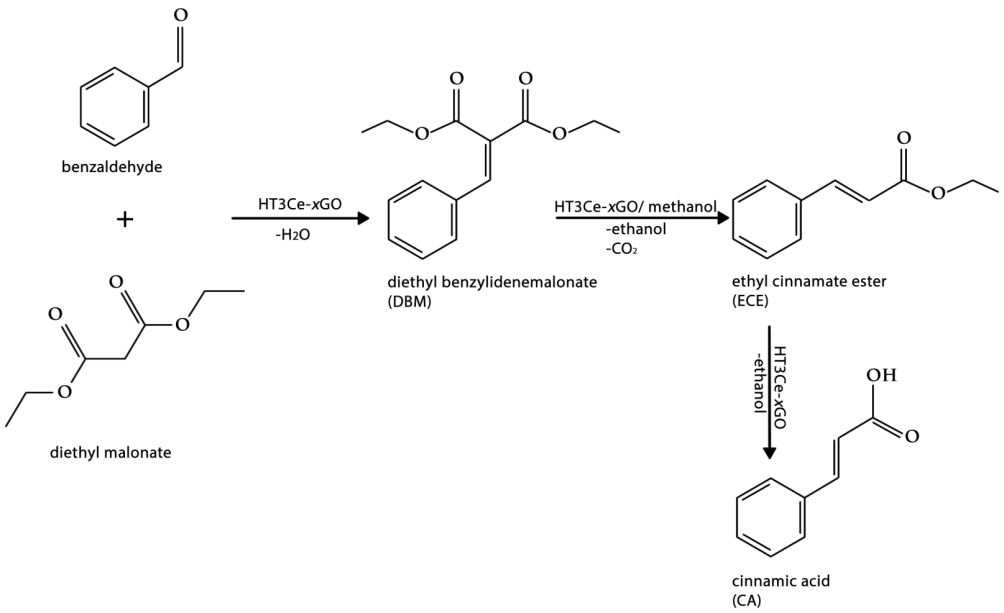

Scheme 1. Reaction route of Knoevenagel condensation

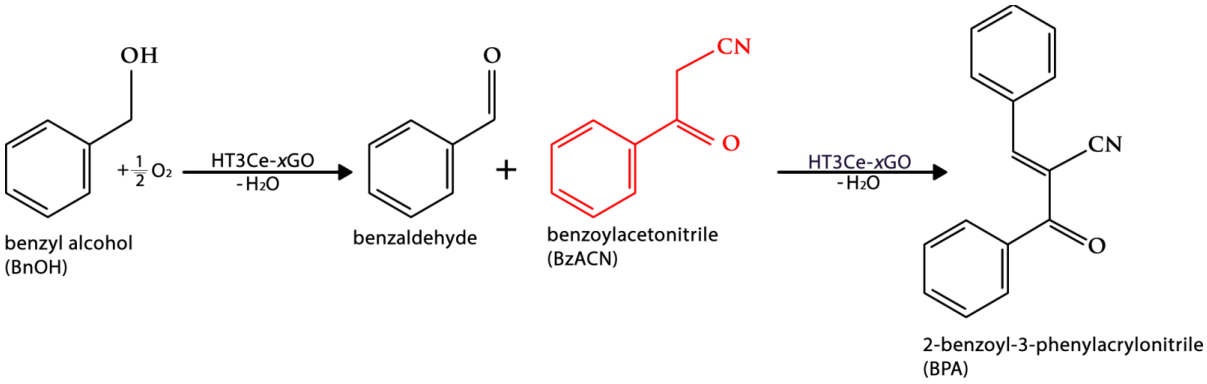

Scheme 2. Reaction route for one-pot cascade oxidation-Knoevenagel condensation reactions

4.1.2. Materials synthesis

4.1.2.1. Reagents and laboratory tools

The reagents and the materials used for the synthesis of graphene oxide (GO), the preparation of the hydrotalcites-like compounds intercalated with GO, using the co-precipitation method are presented in Tables 1 and 2.

Table 1. Reagents and materials used for the graphene oxide synthesis.

Preparation method	Reagents	Laboratory tools
Hummers' method	Graphite $KMnO_4$ $NaNO_3$ H_2O HCl	-beaker -magnetic stirrer -thermostat -Büchner funnel -pH-meter

Table 2. Reagents and materials used for the synthesis of hydrotalcite-like catalysts intercalated with GO: $[M(II)_{1-x}M(III)_x(OH)_2]A^{n-}_{x/n}\cdot mH_2O$; M(II):$Mg^{2+}$; M(III):$Al^{3+}$,$Ce^{3+}$.

Preparation method	Catalysts	Precursors	Reagents	Laboratory tools
Co-precipitation	$Mg_3Al_{0.75}Ce_{0.25}$-5% GO (HT3Ce-5GO)	$Mg(NO_3)_2\cdot 6H_2O$ $Al(NO_3)_3\cdot 9H_2O$ $Ce(NO_3)_3\cdot 6H_2O$ Graphene Oxide (GO)	NaOH Na_2CO_3 Distilled water	-beakers -magnetic stirrer -Büchner funnel -pH-meter -conductometer
	$Mg_3Al_{0.75}Ce_{0.25}$-10% GO (HT3Ce-10GO)			
	$Mg_3Al_{0.75}Ce_{0.25}$-15% GO (HT3Ce-15GO)			
	$Mg_3Al_{0.75}Ce_{0.25}$-20% GO (HT3Ce-20GO)			
	$Mg_3Al_{0.75}Ce_{0.25}$-25% GO (HT3Ce-25GO)			

4.1.2.2. The synthesis of the graphene oxide (GO)

The method applied for the preparation of graphene oxide is based on the technique developed by Hummers in 1952 [39] and its schematic representation can be seen in Figure 1. For the preparation of the GO phase, graphite powder 325 mesh from Aldrich, sodium nitrate $NaNO_3$ and potassium permanganate $KMnO_4$ (chemical purity from Merck), H_2SO_4 (98%) and hydrochloric acid HCl 37% (from Merck) and hydrogen peroxide H_2O_2 30% (from ChimReactiv) were utilized. In brief, 23 mL concentrated sulfuric acid (H_2SO_4, 98%) and 1 g of graphite were mixed in an Erlenmeyer flask maintained in an ice bath at 0 ºC. Then, 0.5 g of sodium nitrate ($NaNO_3$) and 3 g of potassium permanganate ($KMnO_4$) have been slowly added to the formed solution which was kept under continuous stirring for 30 minutes. Next, the conical flask was maintained for another 30 minutes in the thermostat at 30-40 °C. As the reaction progressed, the mixture gradually thickened turning into a green paste. Further, the paste was diluted with 46 mL distilled water causing strong effervescence and stirred for one hour at the 90°C. Moreover, to remove de residual permanganate, the whole solution was mixed with 71 ml warm distilled water and 5 ml H_2O_2 and kept for one hour under stirring. For the removal of the remaining metal ions, 125 mL HCl 0.1N is added and the solution is

stirred for another hour. The resulting mixture was centrifuged and washed with warm distilled water until the conductivity was below 100 µS/cm.

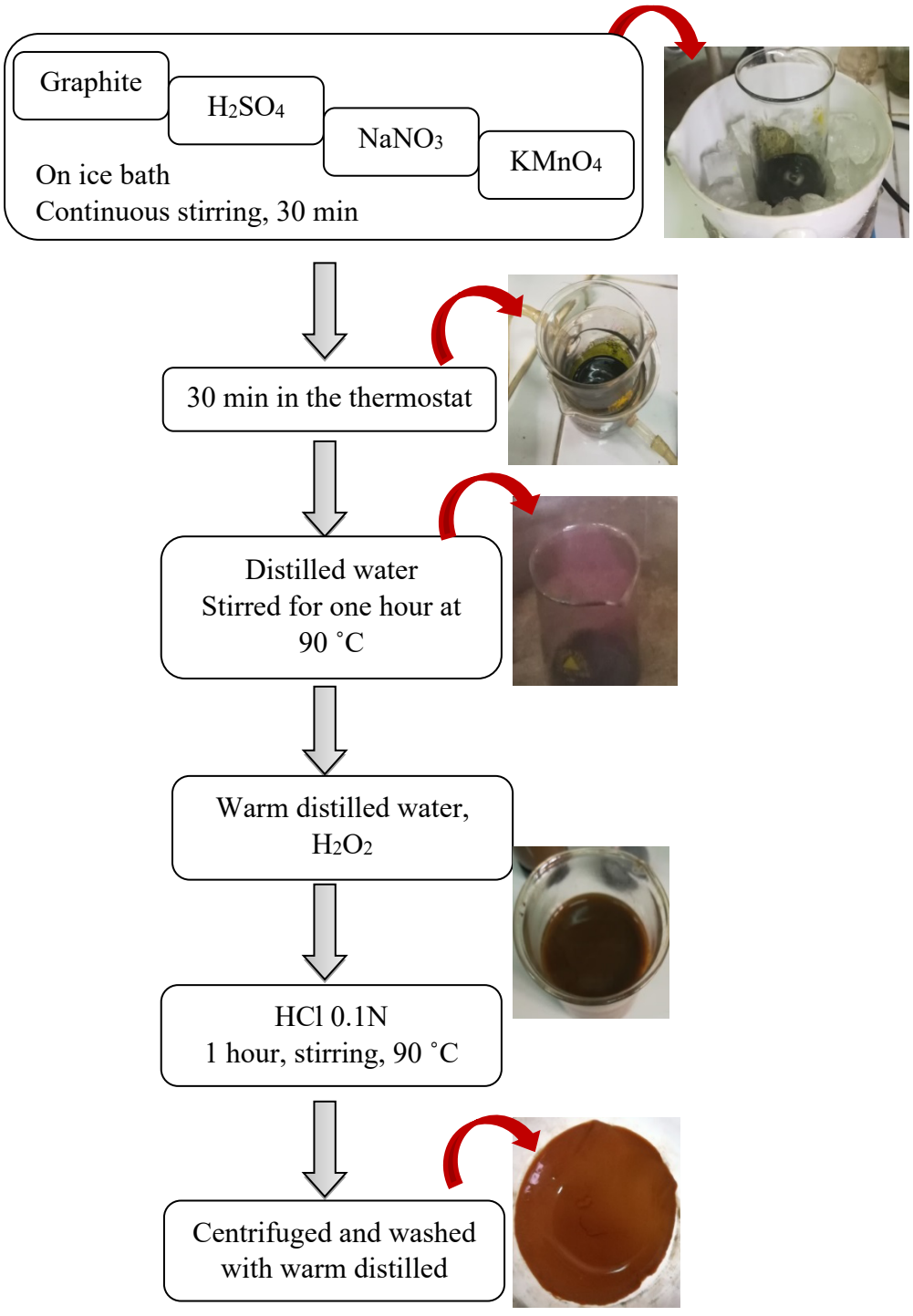

Figure 1. Experimental strategy for graphene oxide synthesis.

The concentration of GO in the suspension was determined using the gravimetric method, by weighing in Petri dishes 3 liquid samples of 100 mL before and after the evaporation of water under vacuum at 60°C for 24 h. The amount of solid recovered from the 3 samples was

0.4001 g, 0.4005 g, and 0.3998 g which gave an average value of the GO concentration in the suspension of 4 g/L.

4.1.2.3. The preparation of the hydrotalcite-GO composites

$Mg_3Al_{0.75}Ce_{0.25}$ LDH-GO composites bearing different concentrations of graphene oxide GO in the range of 5-25 wt.% labelled HT3Ce-*x*GO where *x* stands for the concentration of GO (*x* = 5,10,15,20,25 wt. %) were synthesized by co-precipitating the LDH phase in the presence of GO. Co-precipitation is the method used for the preparation of the hydrotalcite-like compounds and it implies the mixing of precursors (divalent and trivalent metal salts solutions, in well-defined proportions) with an alkaline solution containing the precipitating agent (Na_2CO_3, NaOH).The preparation steps of this method were identical for all the composites, the only difference in their synthesis being the amounts of precursor salts used (respecting the molar ratios Mg:Al:Ce of 3:0.75:0.25), which varied depending on the concentration of graphene oxide aimed to be included in the resulting solid (e.g. 5%, 10%, 15%, 20%, 25%, respectively). In order to obtain the solid hydrotalcite-type compounds, two solutions were necessary (A and B), as follows:

- **For HT3Ce-5GO**: The solution A was prepared by dissolving 3.8 mmol $Ce(NO_3)_3 \cdot 6H_2O$, 58.1 mmol $Mg(NO_3)_2 \cdot 6H_2O$ and 15.2 mmol $Al(NO_3)_3 \cdot 9H_2O$ in 472 mL distilled water and 70 mL of graphene oxide suspension. The solution B was obtained by dissolving 126.5 mmol NaOH and 50.6 mmol Na_2CO_3 in 551 mL distilled water.
- **For HT3Ce-10GO**: The solution A was prepared by dissolving 3.4 mmol $Ce(NO_3)_3 \cdot 6H_2O$, 53.3 mol $Mg(NO_3)_2 \cdot 6H_2O$ and 13.9 mol $Al(NO_3)_3 \cdot 9H_2O$ in 360 mL distilled water and 140 mL of graphene oxide suspension. The solution B was obtained by dissolving 115.8 mmol NaOH and 46.3 mmol Na_2CO_3 in 500 mL distilled water.
- **For HT3Ce-15GO**: The solution A was prepared by dissolving 3.3 mmol $Ce(NO_3)_3 \cdot 6H_2O$, 51 mol $Mg(NO_3)_2 \cdot 6H_2O$ and 13.3 mol $Al(NO_3)_3 \cdot 9H_2O$ in 280 mL distilled water and 205 mL of graphene oxide suspension. The solution B was obtained by dissolving 111 mmol NaOH and 44.3 mmol Na_2CO_3 in 485 mL distilled water.
- **For HT3Ce-20GO**: The solution A was prepared by dissolving 3.4 mmol $Ce(NO_3)_3 \cdot 6H_2O$, 53 mol $Mg(NO_3)_2 \cdot 6H_2O$ and 13.9 mol $Al(NO_3)_3 \cdot 9H_2O$ in 170 mL distilled water and 365 mL of graphene oxide suspension. The solution B was obtained by dissolving 116 mmol NaOH and 46.13 mmol Na_2CO_3 in 534 mL distilled water.
- **For HT3Ce-25GO**: The solution A was prepared by dissolving 3.4 mmol $Ce(NO_3)_3 \cdot 6H_2O$, 53 mol $Mg(NO_3)_2 \cdot 6H_2O$ and 13.9 mol $Al(NO_3)_3 \cdot 9H_2O$ in 170 mL

distilled water and 365 mL of graphene oxide suspension. The solution B was obtained by dissolving 116 mmol NaOH and 46.13 mmol Na_2CO_3 in 534 mL distilled water.

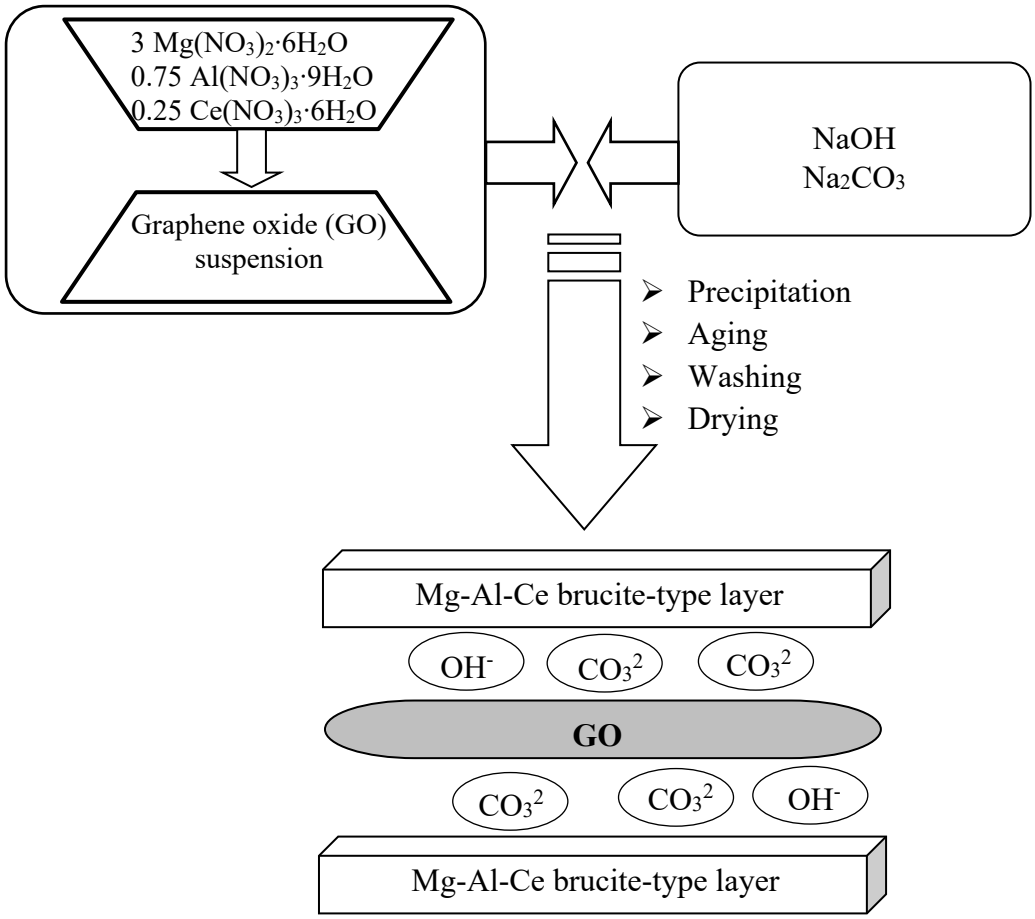

Figure 2. Experimental strategy for HT3Ce-xGO synthesis.

The two solutions, A and B were mixed in a round-bottomed flask under continuous stirring and kept for aging for 18 hours. The washing of the gel was carried out with distilled water until the conductivity was below 100 µS/cm. Drying was carried out in an oven at a temperature of 90°C for 24 hours under air atmosphere.

A Ce-containing hydrotalcite unmodified with graphene oxide was also prepared by co-precipitation under the same above-described conditions, but in this case the solution A was obtained with distilled water instead of GO suspension. The resulting compound was abbreviated as HT3Ce.

4.1.3. Materials characterization

The obtained solids were characterized using powder XRD, XRF, DRIFT, Raman spectroscopy, scanning electron microscopy (SEM). The base and acidic sites distribution of the cerium modified compounds were also determined. N_2 adsorption-desorption isotherms

were also registered. The theoretical cationic composition of the Ce-containing hydrotalcite-type solid is described by the Mg/(Al+Ce) and Ce/Al atomic ratios which were fixed at 3 and 1/3, respectively. The obtained XRF results (Table 1) indicated that the Mg/(Al+Ce) ratio was lower than the theoretical value, in the range 2.63-2.92, while the Ce/Al ratio was close to the theoretical value, for all the materials, suggesting that the precipitation of magnesium was incomplete. At the same time, the cationic content of the materials continuously decreases with increasing the GO theoretical content (Figure 3), confirming the insertion of graphene oxide. The results of the acidity and basicity measurements can also be seen in Table 3.

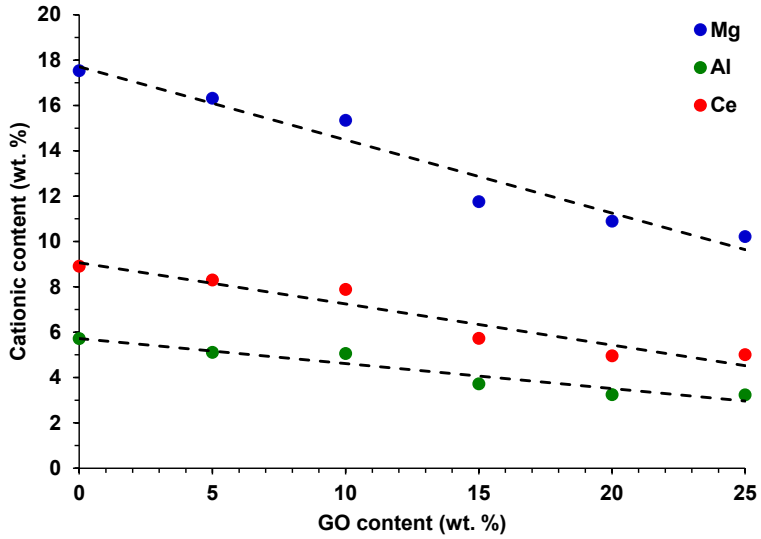

Figure 3. Evolution of the cationic content vs. GO content in the HT3Ce-*x*GO hybrid samples.

Table 3. Chemical composition determined by XRF and the results of acidity-basicity measurements.

Catalyst	Chemical composition					Acidity and basicity measurements			
	Mg^{2+} [wt.%]	Al^{3+} [wt.%]	Ce^{3+} [wt.%]	Mg/ (Al+Ce) atomic ratio	Ce/Al atomic ratio	Total acidic sites [mmol pyridine/g]	% HB[1]	Total basic sites [mmol acrylic acid/g]	Basic /acidic sites ratio
HT3Ce	17.53	5.71	8.91	2.65	0.30	0.03	63.4	0.78	26.00
HT3Ce-5GO	16.31	5.10	8.30	2.74	0.31	0.20	6.7	0.91	4.55
HT3Ce-10GO	15.34	5.05	7.88	2.63	0.30	0.32	18.8	0.89	2.78
HT3Ce-15GO	11.75	3.72	5.72	2.74	0.30	0.46	20.0	2.98	6.48
HT3Ce-20GO	10.89	3.24	4.95	2.92	0.29	0.29	25.4	1.80	6.21
HT3Ce-25GO	10.21	3.23	5.00	2.74	0.30	0.20	43.2	1.22	6.10
GO	-	-	-	-	-	0.77	31.2	0.06	0.08

[1]Brønsted acid sites

It can be observed that the HT3Ce solid is mainly basic, while the GO is mainly acidic. The hybrid materials show, as expected, both basic and acidic sites, which enable them to act as bifunctional catalysts. The amount of acidic sites passes through a maximum for the HT3Ce-15GO sample, but remains lower than that corresponding to GO. On the other hand, the amount of basic sites also passes through a maximum for HT3Ce-15GO, but it is higher than that corresponding to the HT3Ce solid for all the hybrids. This suggests a synergistic interaction between the Ce-containing MgAl-LDH and the graphene oxide rather than a simple additive effect in the hybrid materials. Notably, among the hybrids, the solid HT3Ce-15GO not only contains the highest values of both total acidic and basic sites, but also shows the highest basic-to-acidic sites ratio.

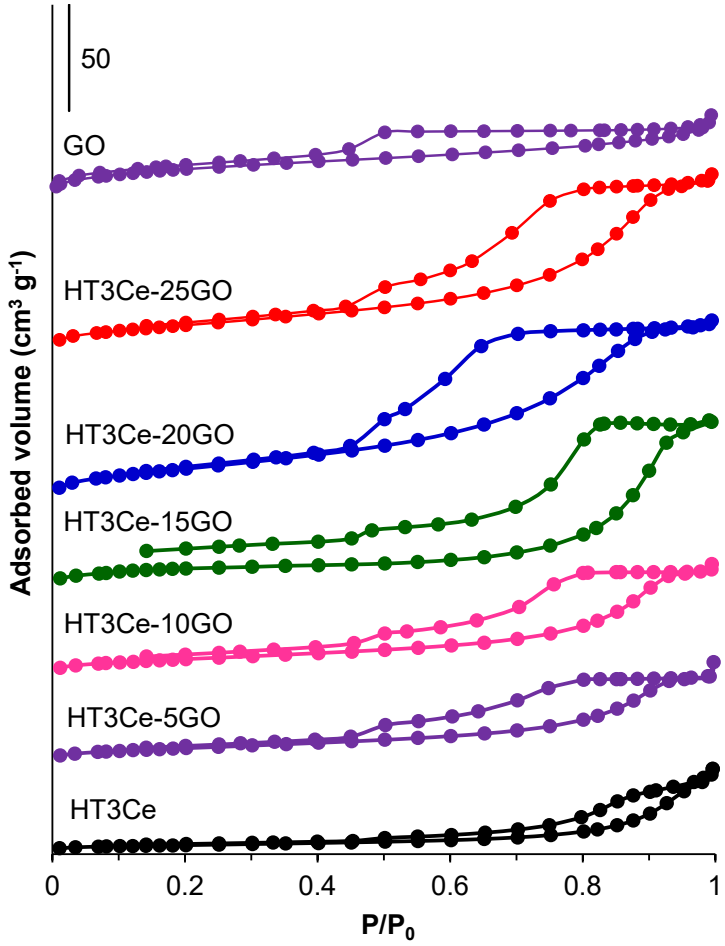

Figure 4. Nitrogen adsorption-desorption isotherms for HT3Ce-LDH, GO and HT3Ce-*x*GO samples.

This is expected to be correlated with the catalytic results in the Knoevenagel condensation reactions.The specific surface area, the pore volume and the pore size of the HT3Ce LDH, GO and HT3Ce-xGO hybrids are tabulated in Table 4, and their corresponding adsorption-desorption isotherms and pore size distributions are shown in Figures 4 and 5, respectively.

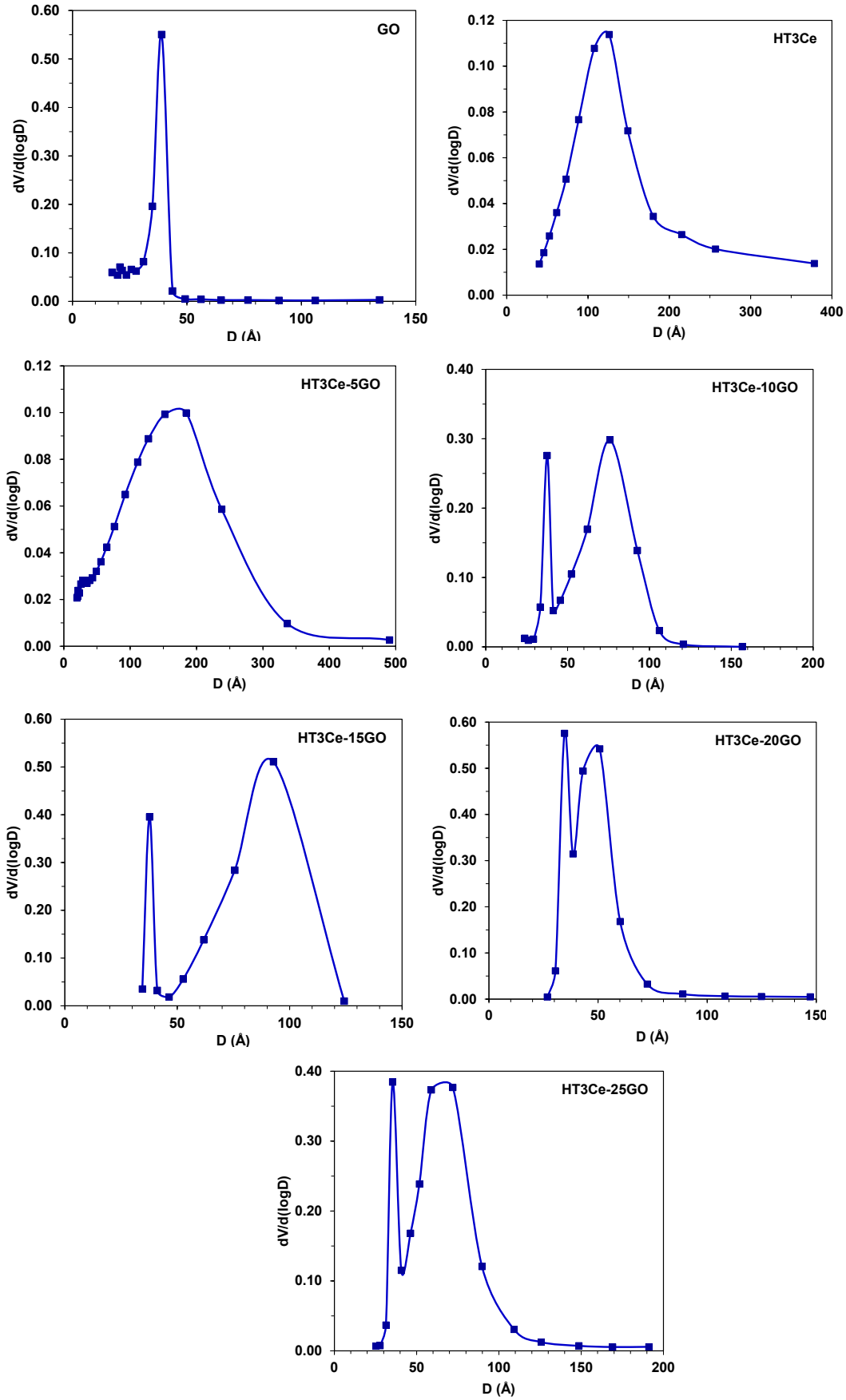

Figure 5. Pore size distributions of the GO, HT3Ce and HT3Ce-*x*GO samples.

All the samples reveal type IV isotherms according to the IUPAC classification, characteristic of mesoporous materials. However, the neat HT3Ce LDH shows a H3-type hysteresis loop attributed to aggregates of plate-like particles giving rise to slit-shaped pores, while the neat GO shows a H4-type hysteresis loop associated with narrow slit-like pores, including some microporosity [40]. At the same time, for the LDH-GO composites the hysteresis loop moves towards H2b-type, which corresponds to more complex pore structures [41]. The data in Table 4 show that LDH has the lowest (15 m^2/g), while GO has the highest (ca. 80 m^2/g) surface area in this series, and, as expected, it increases by adding GO to the LDH and by increasing its content suggesting alternative LDH-GO stacking interactions in the LDH-GO hybrids [42]. However, the surface area reaches a maximum of ca. 78 m^2/g for the HT3Ce-20GO hybrid, and, then, it decreases with ca. 10 m^2/g for the HT3Ce-25GO hybrid obviously due to the GO restacking after a certain GO content in the hybrid. The pore volume of both LDH and GO samples are lower than that of the hybrids, and, for the latter, it increases by increasing the GO content. The pore size distributions of the samples (Figure 5), obtained from the desorption branch of isotherms, indicate narrow and unimodal pore structures for GO (maximum at 38.9 Å), and broad and unimodal pore structures for the neat HT3Ce LDH and HT3Ce-5GO hybrid, with maxima at 126 and 186 Å, respectively. For the hybrid samples with higher GO content, narrower and bimodal pore size distributions are observed with maxima at 35-38 Å and 51-93 Å, respectively. The maxima of the large pores vary irrespective of the GO content in the LDH-GO composite materials.

Table 4. Textural properties of the synthesized samples.

Samples	Surface area (m^2/g)	Pore volume (cm^3/g)	Pore size[a] (Å)
HT3Ce	15.0	0.063	126.1
HT3Ce-5GO	35.5	0.079	185.6
HT3Ce-10GO	42.0	0.089	37.5 and 75.9
HT3Ce-15GO	51.7	0.117	37.8 and 92.8
HT3Ce-20GO	77.6	0.144	34.7 and 50.8
HT3Ce-25GO	68.3	0.142	35.5 and 72.1
GO	79.8	0.071	38.9

[a] Maxima of pore size distribution.

The diffraction patterns of the solid samples, namely hydrotalcites obtained in the presence of different amounts of GO, pure GO and HT3Ce are illustrated in Figure 6. The XRD pattern of

the HT3Ce displays a mixture of characteristic reflections of a hexagonal LDH phase with rhombohedral 3R symmetry (ICDD card no. 054-1030), and of a cubic cerianite CeO_2–phase (ICDD card no.034-0394). They are Miller indexed consequently in Figure 6a. Additionally, diffraction lines assigned to cerium oxycarbonate ($Ce_2(CO_3)_2O{\cdot}H_2O$, ICDD card 044-0617), labeled (*) in Figure 2a, can be observed. The GO pattern shows the structure of a nano-graphene oxide (ICDD card no. 065-1528). The XRD patterns of all HT3Ce-*x*GO nanocomposites (Figure 6b) expose the same mixture of characteristic reflections of LDH and cubic cerianite CeO_2 phases, with no additional impurity lines. The typical strong (001) basal diffraction peak of GO was not observed in all the nanocomposites. This could be attributed to the superimposed reflection with the (003) basal LDH peak and is also indicative of an exfoliation of the graphene sheets [43]. Apparently, the restacking of graphene sheets was inhibited by deposition of the LDH crystallites on the graphene sheets [44,45].

The structural data, the lattice parameters of the two phases and their crystallite sizes are provided in Table 5. For the LDH phase the crystallite sizes were calculated along two directions: perpendicular (D_{003}) and parallel (D_{110}) to the brucite-like layers, respectively. The data gathered in Table 3 show similar structural characteristics for all the samples.

The CeO_2 phase is structurally identical in all the samples, while the LDH-phase is more likely affected by the electrostatic interactions between GO and LDH during the synthesis [46,42]. As it can be observed, the crystallite sizes, in particular the coherence lengths in the layer-stacking direction (D_{003}), were affected by the presence of GO.

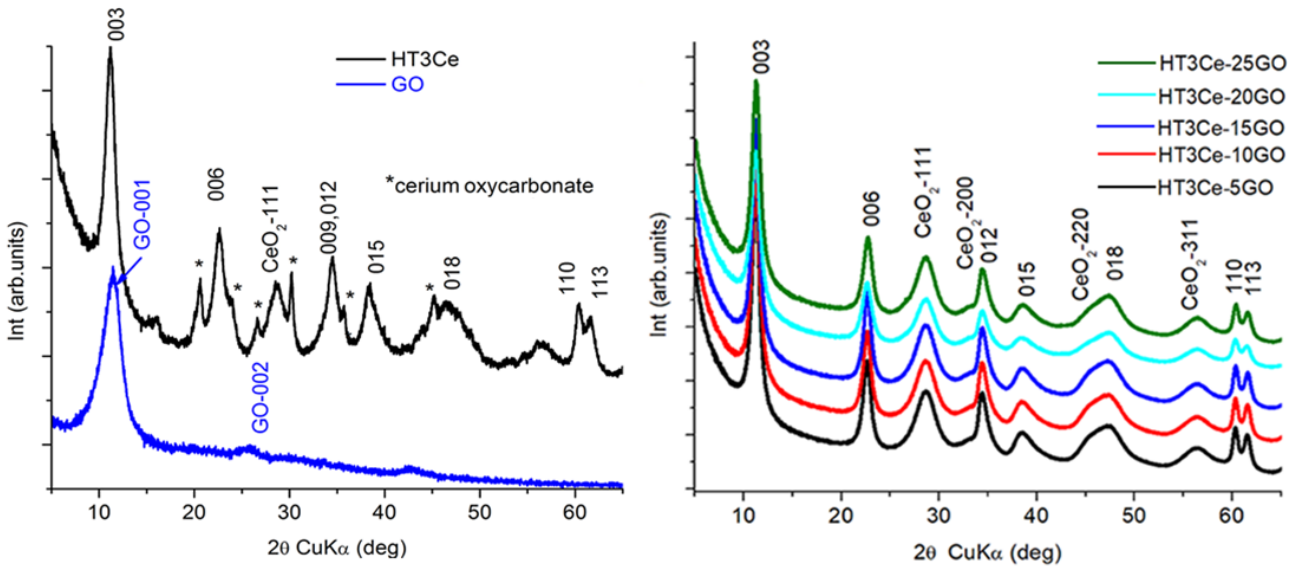

(a) **(b)**

Figure 6. XRD patterns of: (a) HT3Ce and GO; (b) the composite samples.

Indeed, the incorporation of GO led to the formation of larger LDH particles suggesting the involvement of the GO sheets as nucleating agents for the LDH phase formation [47]. The evolution, in the HT3Ce-xGO series, of the absolute intensities of the (110) line, exclusively related to the brucite-like layer, should go along with the decrease of the proportion of the LDH phase in the nanocomposites.

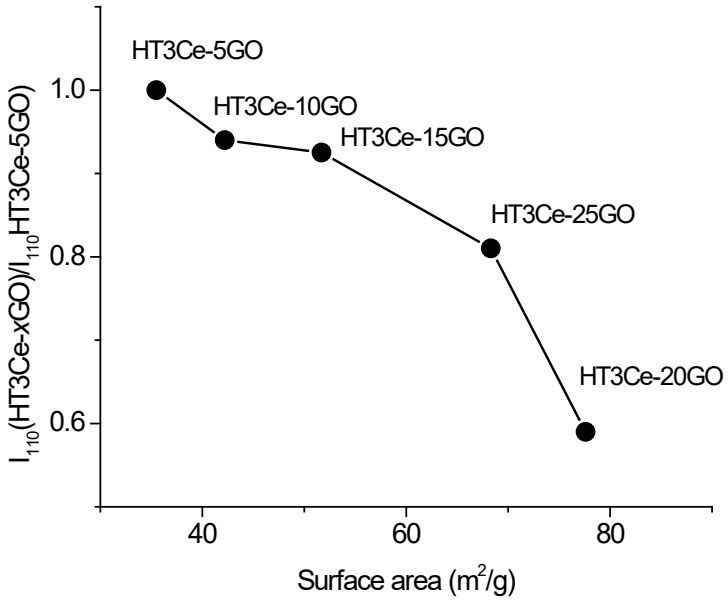

Figure 7. Evolution of the I_{110}(HT3Ce-*x*GO)/I_{110}(HT3Ce-5GO) ratio vs. surface area in the HT3Ce-*x*GO series.

This is the case, except for the inversion between the HT3Ce-20GO and HT3Ce-25GO samples, in line with the result obtained through textural measurements. Indeed, there is an obvious inverse correlation between the surface area and the I_{110}(HT3Ce-xGO)/I_{110}(HT3Ce-5GO) ratio (Figure 7), evidencing HT3Ce-5GO as the most "ordered" material, and HT3Ce-20GO as the most disordered one in this series. This order-disorder could be associated to the dispersion of HT3Ce on the GO sheets. HT3Ce-25GO appears to be more "ordered", i.e. less dispersed, than HT3Ce-20GO likely due to GO restacking.

A decrease of the *c*-lattice parameter value accompanied by an increase of the I_{003}/I_{110} ratio for all the HT3Ce-*x*GO nanocomposites in comparison with the HT3Ce sample is observed (Table 5). The result suggests a slight modification of the interlayer anionic composition, probably a higher degree of hydration with a different compaction of the anionic species, due to mutual electrostatic interaction between LDH and GO phases. These observations are consistent with the DRIFT data presented afterward. The DRIFT spectra of all the synthesized solids can be seen in Figure 8. The characteristics of the composites modified

with GO were close to the HT3Ce structure, depicting the main layered phase. As the GO concentration increased in the hybrid solids, the stretching vibrations bands attributed to the OH groups present in the hydroxide layer of HT3Ce at 3587 cm^{-1} shifted towards larger values, namely 3612, 3623, 3623, 3651, 3631 cm^{-1}, and their intensity also decreased. The same proportionality related to the GO concentration was observed influencing the shoulder displayed in the region at 3000-3200 cm^{-1} (probably due to the formation of hydrogen bonds between the water molecules).

Table 5. Crystal unit cell parameters of the synthesized samples.

Samples	LDH					CeO_2	
	a (Å)	c (Å)	I_{003}/I_{110}	D_{110}(nm)	D_{003}(nm)	a (Å)	D_{111}(nm)
HT3Ce-5GO	3.068	23.658	5.07	12.9	8.4	5.394	3.2
HT3Ce-10GO	3.067	23.660	5.41	15.4	8.2	5.395	3.2
HT3Ce-15GO	3.066	23.629	5.62	15.1	8.8	5.398	3.2
HT3Ce-20GO	3.068	23.681	5.96	12.0	7.3	5.405	3.3
HT3Ce-25GO	3.065	23.572	5.65	14.0	7.7	5.401	3.2
HT3Ce	3.066	23.756	4.85	11.7	6.3	5.415	4.6

Also, at 1645 cm^{-1}, the absorption of the hydroxyl groups of the water molecules in the HT3Ce interlayer space was perturbed in the GO-containing composites and shifted towards 1597 (for HT3Ce-5GO), 1655 (for HT3Ce-10GO), 1613 (also wider, for HT3Ce-15GO), 1658 (for HT3Ce-20GO), and 1636 cm^{-1} (for HT3Ce-25GO). This aspect can be explained by the different confinement of the LDH particles on the larger GO layers, in good correlation with the already observed perturbation by the "turbostratic" effect [48].

The perturbation of the interlayer region appeared due to the favorable interactions between LDH and GO, mediated by ceria ions, which could be observed further. The asymmetric stretching vibrations of CO_3^{2-} from HT3Ce were found at 1430 cm^{-1}. The same peak (in the composites containing 5, 10, 15 wt.% GO) was shifted towards a lower absolute value (1415, 1425, 1418 cm^{-1}), indicating a weaker interaction when GO was used. Also, the other CO_3^{2-} vibration modes were affected in the same manner (in the 1495-1528 cm^{-1} region).

At the same time, all the metal-oxygen vibrations in the 600-900 cm^{-1} region were shifted towards lower values indicating weaker energy states for the bending modes when GO was used. This aspect should be also viewed concerning the interlayer and edge interactions between LDH and GO. Other evidence on the perturbation of the interlayer region and the

decrease in size of LDH elementary particles (as observed in the SEM section) were found in the case of HT3Ce-15GO, for which new absorptions were detected at 1270 and 1026 cm^{-1} (bands for the edge OH groups found in GO layers), also in HT3Ce-20GO (1232 cm^{-1}, 1058 cm^{-1}) and HT3Ce-25GO (1269 cm^{-1}, 1028 cm^{-1}).

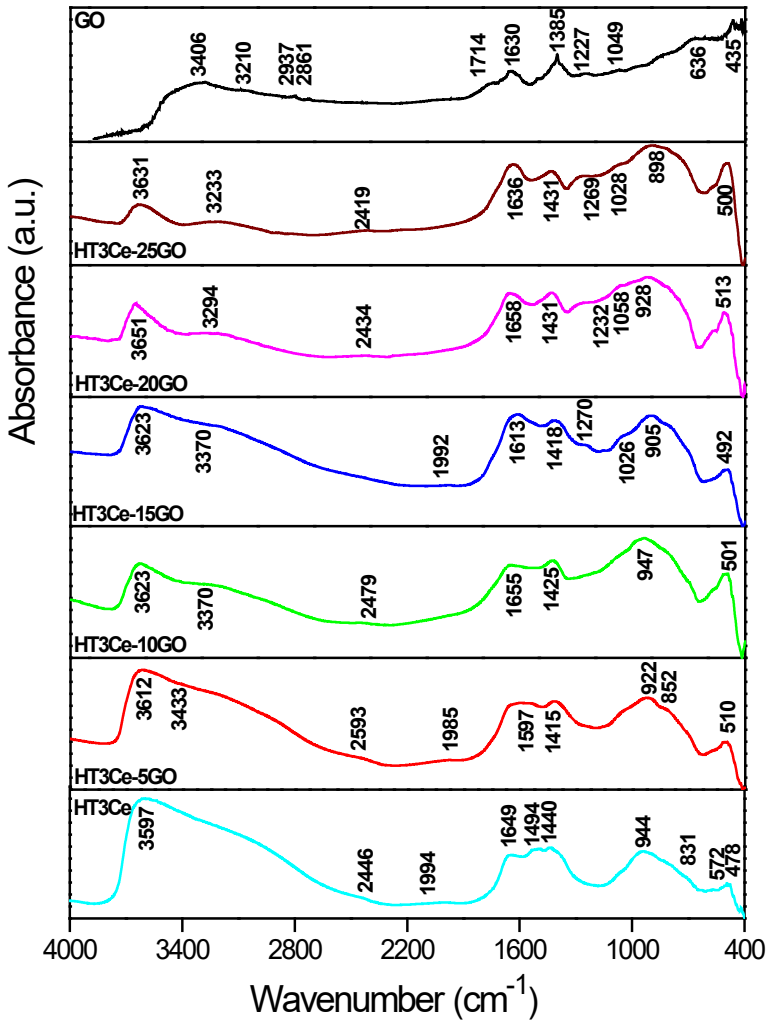

Figure 8. DRIFT spectra of the solids: HT3Ce-*x*GO composites, neat HT3Ce and GO.

The presence of GO in all the HT3Ce-xGO composites was clearly evidenced by Raman spectra of the samples which are displayed in Figure 9. The spectrum of HT3Ce presented different bands, some specific to the LDH structure, namely a broad band characteristic to the lattice vibrations of the hydrotalcites at 140 cm^{-1}, another one at 550 cm^{-1} attributed to stretching vibrations of the hydrogen bonds formed between the interlayer water and carbonate anions, and a band assigned to the symmetric stretching of the carbonate anion found at 1066 cm^{-1} [49]. Also, a band was observed at 461 cm^{-1}, characteristic to

nanocrystalline CeO_2 and some bands between 800-900 cm^{-1} specific for the stretching vibrations of peroxide groups and defective ceria surfaces [50].

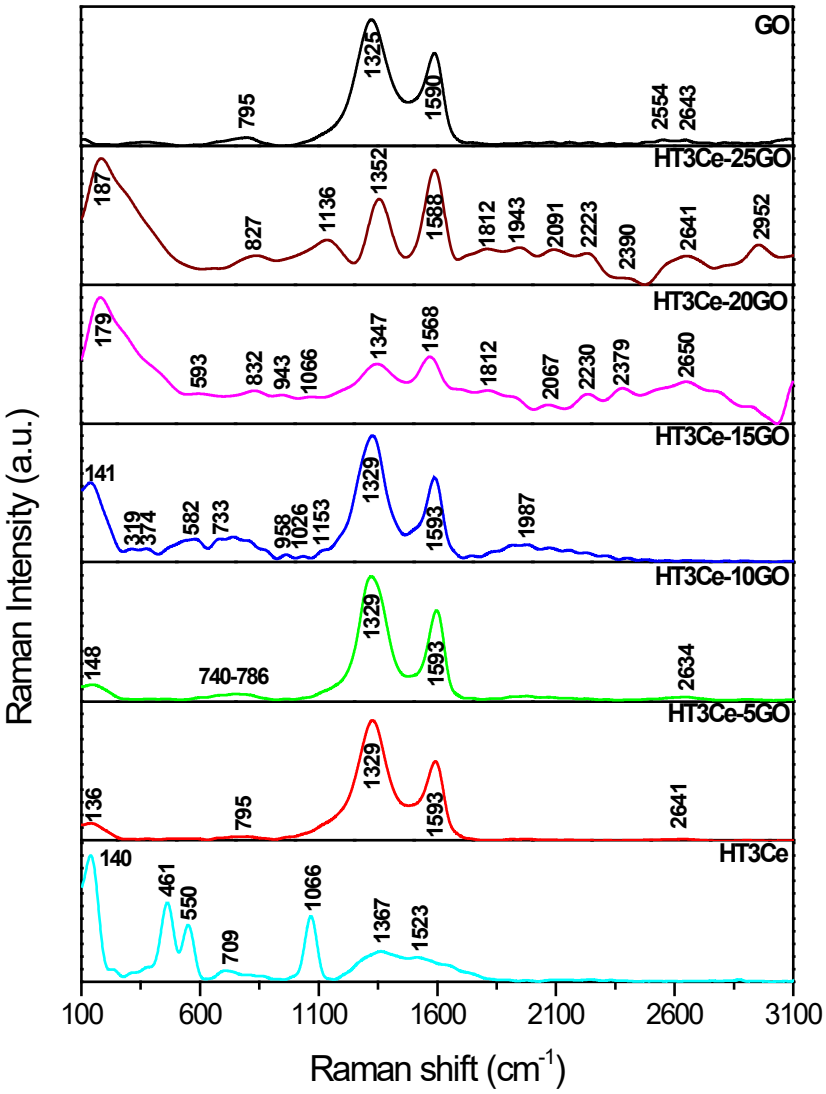

Figure 9. Raman spectra of the solids: HT3Ce-*x*GO composites, neat HT3Ce and GO.

The Raman spectrum of GO showed the D band at 1326 cm^{-1} and the G band at 1590 cm^{-1}, while the ratio between the intensities of the two bands, which is associated to the surface defect and the degree of lattice distortion of a graphite layer within the carbon material [51], was I_D/I_G = 1.38. Besides the band at 137 cm^{-1} specific to LDH lattice vibrations in the Raman spectra of the HT3Ce-*x*GO composites, the GO component overlapped the bands characteristic for the LDH component. In the spectra of all the composites, the positions of the GO bands D and G were slightly shifted to higher values, precisely to 1329 and 1593 cm^{-1} for the samples containing 5, 10 and 15 wt.% GO, and 1347 and 1590 cm^{-1} for the samples containing 20 and 25 wt.% GO, while the I_D/I_G ratio increased with the GO content in the

sample to 1.5, 1.43, and 1.53 for 5, 10 and 15 wt.%, respectively, indicating an increased disturbance of the GO layer. The situation changed for the samples containing 20 and 25 wt.% GO, the I_D/I_G ratio decreased with the GO content in the sample to 0.89 and 0.92 cm^{-1}, respectively. This could be due to GO restacking at high GO contents, as also suggested by the evolution of the surface area of the samples. Another interesting aspect noticed in the Raman spectra was the presence of the G' band, which appeared at around 2600 cm^{-1}. This band increases with the concentration of graphene oxide inserted in the composites. Apparently, with the increase of the GO concentration, the hydrotalcite crystallized on the surface of the graphene oxide, an observation also supported by the SEM images.

The composite structures, analyzed in powder form by SEM, highlighted different surface morphologies of the HT3Ce-xGO samples (Figure 10). A closer inspection of the grain surface revealed the presence of microparticles grouped either in polymorphic structures with sharp edges, "ovoidal" particles or cubic agglomerates (Figure 5). It is noteworthy that the morphology of the neat Ce-containing MgAl LDH sample was shown to be quite different [52], being described as assemblies of nanoplates nearly perpendicular to the outer surfaces of microspheres.

The number (frequency) of "ovoidal" particles on the grain surface increased with GO concentration, but their dimension decreased. This fact also determined a slight twist of the surface layers beyond the 15% GO concentration.

A possible explanation of the overall mechanism for the occurrence of the "ovoidal" composite particles and their positioning on the surface could also be related to the complex role played by Ce ions.

HT3Ce-5GO

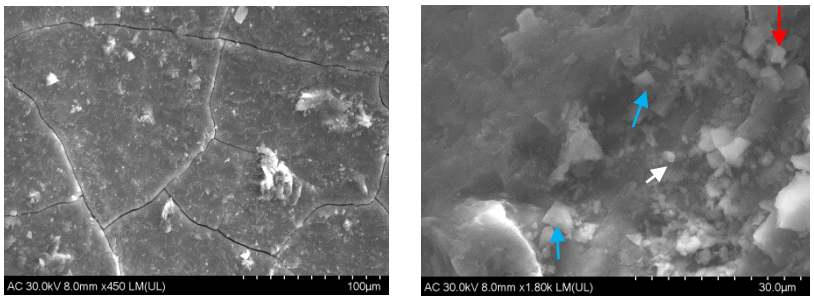

Figure 10. SEM images of the HT3Ce-*x*GO composites (left: low magnification; right: high magnification.), with different aspects of the grain surfaces indicating polymorphic (blue arrows), irregular "ovoidal" (white arrows) or cubic (red arrows) structures.

Figure 10. (continued)

HT3Ce-10GO

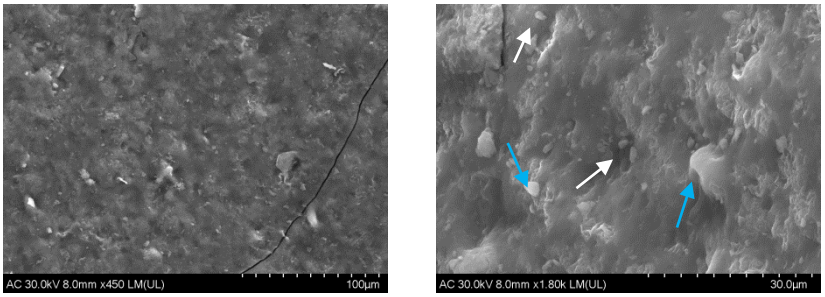

HT3Ce-15GO

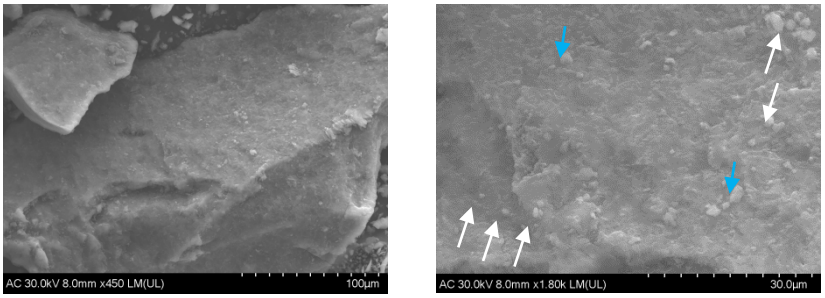

HT3Ce-20GO

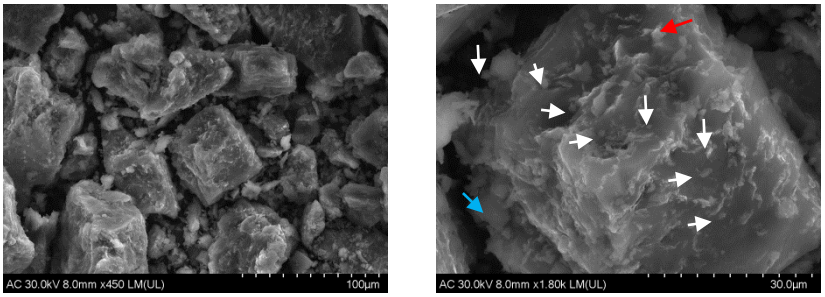

HT3Ce-25GO

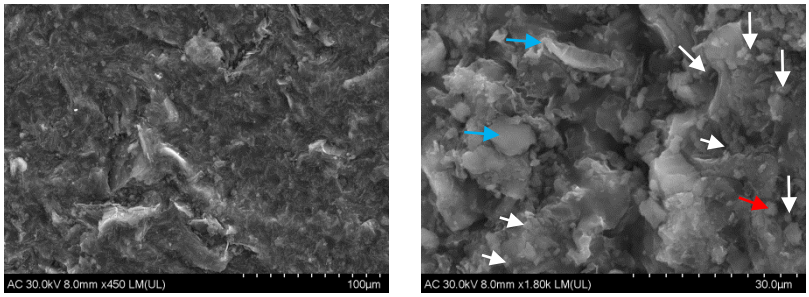

On one hand, they can influence the oxidative-reductive equilibrium and act on (not fully oxidized) GO sites, and, on the other hand, they could induce a basic character in the LDH reaction sites, leading to a spherical association of the hexagonal LDH platelets [53].

The "sensitivity" of the isoelectric point (IEP) for LDH during synthesis was broadly described in the literature [53,54]. Over the IEP, a spherical association of hexagonal LDH

platelets occurs. The formation of “ovoidal” composite particles was possible, in a larger context, due to pH conditions and GO availability for offering a large surface area (useful for both LDH and ceria particles). Moreover, it was reported that the ceria phase could be attached to the GO surface preventing the formation of extrinsic vacancies in the oxygen sub-lattice [50]. By this mechanism, a larger specific area with a higher number of active centers could be obtained for the catalytic reactions [55].

4.1.4. Catalytic study

The LDH-GO composites bearing different concentrations of GO in the range of 5-25 wt. % were tested as catalysts in two different types of organo-chemical transformations: i) Knoevenagel condensation reaction (Scheme 1) and ii) one-pot cascade oxidation-Knoevenagel condensation (Scheme 2).

All the Knoevenagel reactions were performed in a 100 mL stirred flask, under reflux conditions, at a temperature of 160 °C, for two different reaction times, i.e., 5 h and 24 h, respectively. The catalytic activity of both GO and HT3Ce solids was also tested in the Knoevenagel condensation.

In a typical experiment, at a molar ratio of 2:3, benzaldehyde (10 mmol, 1.02 mL) and diethyl malonate (15 mmol, 2.88 mL) were stirred and heated in a silicon oil bath. All reagents were purchased from Merck. In all reactions, the catalyst concentration was 1 wt. % in the reaction admixture, namely 0.346 g. After 5 and 24 h of reaction under reflux, respectively, the reactor was cooled to room temperature and 50 mL methanol was added to keep all the organic compounds in solution (heated again under reflux for 10 min). The catalysts were removed by filtration, while the organic phase was concentrated under vacuum and analyzed by mass spectrometer-coupled chromatography, using a GC/MS/MS Varian Saturn 2100 T (Varian Palo Alto, California, US) equipped with a CP-SIL 8 CB Low Bleed/MS column of 30 m length and 0.25 mm diameter.

The same catalysts were investigated in one-pot cascade oxidation-Knoevenagel condensation reactions (Scheme 2). The tandem reactions were performed in a 100 mL Büchi miniclave low-pressure reactor (from Buchiglas (Büchi AG) Uster, Switzerland). The optimum temperature for both steps, oxidation and condensation, was 80 °C, and a further increase of temperature did not have any positive effect on the rate of the reaction. Regarding the reaction time, the ideal time for the oxidation step was 6 h, while the optimum for the condensation step was 19 h.

During the oxidation step, 1 mmol of benzyl alcohol (BnOH) was placed in the autoclave and mixed with 1 g of catalyst and 10 mL of solvent (toluene, benzene or mesitylene). Then the mixture was stirred under 1 atm of O_2 and heated using a glycerin bath. After 6 h, the miniclave was opened and 1.2 mmol of benzoyl acetonitrile (BzACN) dissolved in 3 mL of solvent (toluene, benzene or mesitylene) was added to the existing mixture to enable the condensation step and the formation of 2-benzoyl-3-phenylacrylonitrile (BPA). The miniclave was closed, purged with argon, and the combined mixture was stirred under 1 atm of argon for a further 19 h.

At the end of the reaction, the reactor was cooled to room temperature, the catalyst was removed by filtration and washed with acetonitrile, while the organic phase was analyzed by GC-MS using a SHIMADZU GCMS-QP2010 SE instrument (Shimadzu, Kyoto, Japan) equipped with an HP-5MS capillary column (30 m x 0.25 mm x 0.25 μm) from Agilent. Highly pure He (99.999%) was used as a carrier gas.

First, the Knoevenagel condensation of benzaldehyde with diethyl malonate catalyzed by various $Mg_3Al_{0.75}Ce_{0.25}$ LDH-GO composites containing different concentrations of GO in the range of 5-25 wt.% resulted in diethyl benzylidene malonate (DBM). It was immediately converted to a certain extent in the presence of the basic catalyst according to a Doebner-like modification of the Knoevenagel reaction to cinnamyl ethyl ester (ECE), which was finally cleaved to cinnamic acid (CA) as a second main reaction product (Scheme 1).

Table 6. Catalytic results of the HT3Ce-*x*GO composites containing five different concentrations of GO (*x* = 5, 10, 15, 20, 25 wt. % GO) at 5 and 24 h reaction time.

Catalyst	**Conversion of aldehyde (%)**		**Selectivity (%) after 5 h**			**Selectivity (%) after 24 h**		
	5h	**24 h**	**DBM**	**ECE**	**CA**	**DBM**	**ECE**	**CA**
HT3Ce-5GO	14	56	54	7	39	53	-	47
HT3Ce-10GO	19	67	51	-	49	51	-	49
HT3Ce-15GO	24	76	56	-	44	38	3	59
HT3Ce-20GO	21	70	59	-	41	46	3	51
HT3Ce-25GO	18	69	62	-	38	47	5	48
HT3Ce	8	9	57	37	6	58	34	8
GO	5	7	-	1	99	-	5	95

The values of conversions and selectivities after 5 and 24 h reaction time, respectively, are presented in Table 6. As it can be observed in Table 6, the catalytic activity in the Knoevenagel condensation passes through a maximum for the system containing 15 % GO. This may be due to the fact that HT3Ce-15GO is the most basic system in the HT3Ce-*x*GO series, with the highest basic/acidic sites ratio (Table 1). At the same time, for neat HT3Ce and GO alone, the conversions obtained were rather small compared to the hybrid composites. This suggests a synergistic effect between the parent materials (GO and LDH) present in the HT3Ce-*x*GO composites leading to improved catalytic activity. The higher activities of the hybrid HT3Ce-*x*GO systems compared to the neat HT3Ce catalyst, could be due to their strong affinity for the organic substrate since graphene oxide presents a similar planar structure with the phenyl group.

Moreover, the association of composite platelets in "ovoidal" particles in the hybrid materials, as evidenced in the SEM images (Figure 10), could also be correlated with their enhanced activity compared to neat HT3Ce that shows no evident "ovoidal" particles [52]. Notably, a longer reaction time led to higher conversions of the substrate, with a conversion increase larger for the hybrid HT3Ce-*x*GO systems compared to pure HT3Ce and GO, in line with the higher activity of the former.

The yields of CA, a product of high interest, obtained with the investigated catalysts are illustrated in Figure 11.

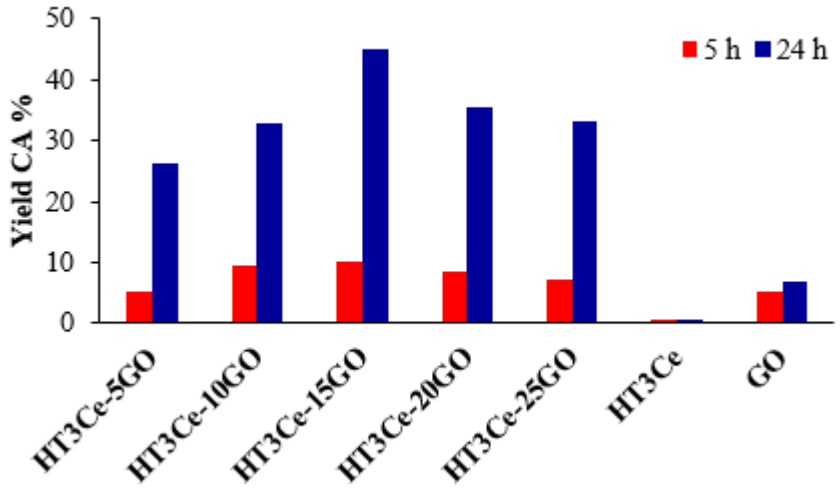

Figure 11. The yields of CA obtained with the investigated catalysts, namely: HT3Ce-5GO, HT3Ce-10GO, HT3Ce-15GO, HT3Ce-20GO, HT3Ce-25GO, HT3Ce, GO.

It can be observed that the yield passes through a maximum for the HT3Ce-15GO catalyst. The basicity of the catalyst should determine not only the activity but also the selectivity to

diethyl benzylidene malonate (DBM), as the basic sites are involved in the proton abstraction from the α-position of diethyl malonate and, then, the resulting anion undergoes nucleophilic addition to the carbonyl group of the benzaldehyde thus yielding to diethyl benzylidene malonate. However, surprisingly, the selectivity to DBM decreases with increasing the basicity of the catalyst (Figure 12a).

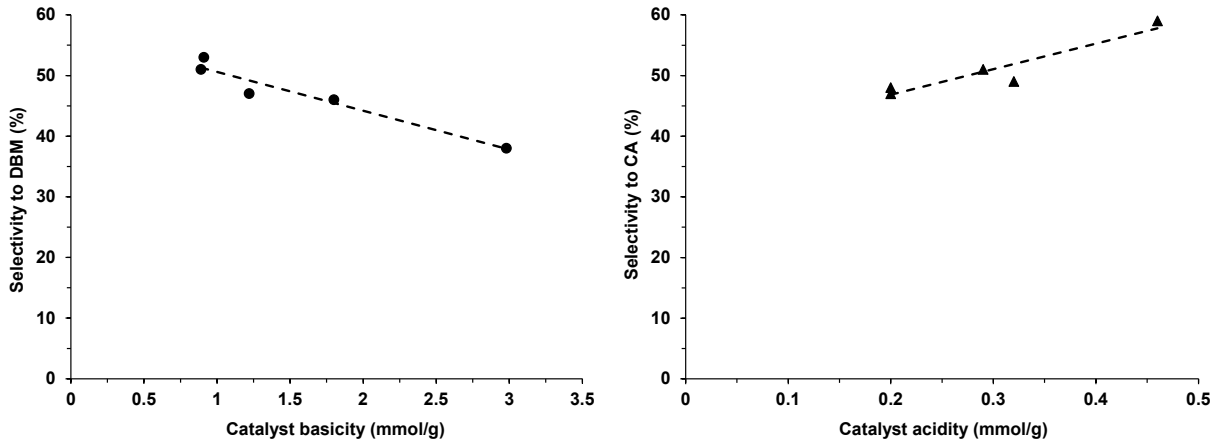

(**a**) (**b**)

Figure 12. Selectivity to DBM after 24 h reaction time vs. catalyst basicity (**a**) and selectivity to CA after 24 h reaction time vs. catalyst acidity (**b**) for the HT3Ce-*x*GO composites in the Knoevenagel condensation of benzaldehyde with diethylmalonate.

This could be explained by the fact that the decarbethoxylation of DBM in the solvent phase, first leading to the ethyl cinnamate ester intermediate, is also favored by the basicity of the catalyst. At the same time, the conversion of the latter into cinnamic acid (CA) seems to be favored by the acid sites of the catalytic material, as suggested by the linear correlation observed between the selectivity to CA and the acidity of the catalyst (Figure 7b).

Moreover, judging by the high selectivities for CA of pure GO phase (Table 4), the latter plays a key role in the cinnamic acid production obviously through the acid sites created in the hybrid materials. These data suggest that the ratio between the acid and basic sites in the hybrids is a key factor determining the product distribution. However, the fact that solids like HT3Ce-10GO and HT3Ce-25GO, which have quite different basic-to-acidic sites ratios (Table 3) show similar selectivities to CA for the reaction after 24 h, although quite different after only 5 h (Table 6), suggests that the strength of the acidic and basic sites also plays an important role. The conversion values for the one-pot oxidation – Knoevenagel condensation cascade reaction and the yields to 2-benzoyl-3-phenylacrylonitrile (BPA) can be seen in Table 7 and Figure 13, respectively.

Table 7. Catalytic results of the HT3Ce-*x*GO composites containing different concentrations of GO (*x* = 5, 10, 15, 20, 25 wt. % GO) in the one-pot oxidation – Knoevenagel condensation cascade reaction performed in different solvents: toluene, mesitylene and benzene.

Catalyst	Conversion of benzyl alcohol [%] in the following solvents:		
	Toluene	**Mesitylene**	**Benzene**
HT3Ce-25GO	14	17	38
HT3Ce-20GO	24	38	45
HT3Ce-15GO	25	38	49
HT3Ce-10GO	40	42	52
HT3Ce-5GO	40	45	53
HT3Ce	11	22	30
GO	0	0	0

HT3Ce-xGO composites exhibited a bifunctional catalytic behavior and could promote aromatic alcohol oxidation/Knoevenagel condensation in a stepwise way. From the already existing information in the open literature [56], low yields of oxidation products were obtained when polar solvents, such as acetonitrile, methanol and ethanol, were utilized. Therefore, three different non-polar solvents were used for the current reactions, namely toluene, benzene and mesitylene. According to the data presented in Table 7, the best conversion values were obtained when benzene was used as a solvent. Although it is a hazardous and carcinogenic compound, benzene is still a solvent appropriate for manifold reactions because it is inert and stable since its π electrons are maximally spread out evenly. Mesitylene and toluene were also suitable solvents, but their use led to the formation of a larger number of by-products.

Irrespective of the solvent used, the conversion of benzyl alcohol increased with the decrease of the graphene oxide concentration in the hybrid composite. This is not surprising if one takes into consideration that from the two pure materials, HT3Ce and GO, only the LDH is active, the GO being completely inactive. However, a synergistic effect between the two phases in the hybrid HT3Ce-xGO materials can be noticed, which is diminished, in this case, by a dilution effect with increasing the GO content. Taking into consideration that both redox (associated to cerium species) and basic active sites involved in the studied cascade reaction are contained by the LDH phase, the addition of GO to obtain the composites likely increases the accessibility to the catalytic sites by separating the LDH particles.

Further increase of the GO content results in a decrease of the number of redox active sites involved in the first step of the cascade reaction, in line with the observed decrease of Ce content (Table 3) with negative consequences on the overall activity. Thus, practically, HT3Ce-5GO catalyst gave the highest conversion of benzyl alcohol in the series studied. Also, the highest yield of 2-benzoyl-3-phenylacrylonitrile was achieved at the end of the cascade reaction with this catalytic system, as seen in Figure 13.

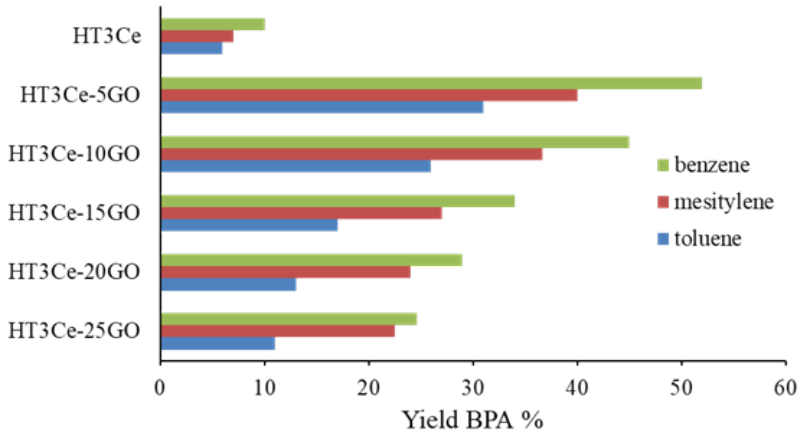

Figure 13. The yields of 2-benzoyl-3-phenylacrylonitrile (BPA) obtained at the end of the cascade reaction, for each cerium-modified LDH-GO composite catalyst.

Nevertheless, it is noteworthy that the conversion of benzyl alcohol is significantly lower for HT3Ce-25GO catalyst compared to HT3Ce-20GO, although they have similar Ce content. This could be attributed to the lower surface area of the former associated to the GO restacking at higher GO content in the hybrid thus limiting the accessibility to the redox sites.

4.1.5. Conclusions

The co-precipitation of $Mg_3Al_{0.75}Ce_{0.25}$ LDH in the presence of a GO suspension led to HT3Ce-*x*GO composites with increased crystallinity as indicated by the XRD analysis. The diffractograms of the composites also showed that no other impurities could be found besides the CeO_2 phase. Raman spectroscopy clearly highlighted the existence of GO in the HT3Ce-xGO composites, while the SEM images demonstrated that the elementary particles were grouped either in layered polymorphic particles with edges, “ovoidal” composite particles or cubic agglomerates, and the amount of ovoidal particles increased with GO content.

The catalytic activity of the obtained LDH-GO composites was tested in two reactions, namely the Knoevenagel condensation between benzaldehyde and diethyl malonate and the

tandem aerobic oxidation of benzyl alcohol followed by Knoevenagel condensation with benzoyl acetonitrile.

The following observations were established for the Knoevenagel condensation reaction:

- Using the unmodified solids HT3Ce and GO, the conversions obtained were rather low compared to the hybrid composites. A synergistic effect between the LDH and GO parent materials present in the HT3Ce-*x*GO composites, leading to improved catalytic activity, was noticed.
- The catalytic activity of the hybrids increased with the GO content in the composite catalysts up to an optimum for HT3Ce-15GO system, then it decreased for higher GO contents. This follows the evolution of the number of basic sites in the catalytic material.
- The ratio between the basic and acid sites in the hybrids, associated to the LDH and GO phases, respectively, is a key factor determining the product distribution.
- A longer reaction time led to higher conversions of the substrate, with a conversion increase larger for the hybrid HT3Ce-*x*GO systems compared to their pure constituents.

In the case of the tandem reaction, the conversion of benzyl alcohol was higher for the hybrid HT3Ce-*x*GO systems compared to the LDH and GO materials alone, the latter being completely inactive, but it decreased with the increase of the GO concentration. This behavior was attributed to the fact that the addition of GO to LDH to obtain the composites increases the accessibility to the redox sites needed in the first sequence of the tandem reaction located in the LDH material by separating its particles. Then, further increasing the GO content results in a decrease of the number of redox active sites and, thus, of both conversion and product yield. At high GO content, the GO restacking takes place, the accessibility to the catalytic sites being unfavorably affected. Notably, the conversion of benzyl alcohol depended on the solvent used, the most suitable solvent being benzene.

4.2. Molybdate-containing MgAl layered double hydroxide-graphene oxide hybrid materials

4.2.1. Overview

The emergence of nanomaterials with different properties can obtain new, improved noncompounds that can surmount the starting precursors from every point of view [57]. It is highly desirable to create new bi-functional catalysts that can promote cascade reactions without any other additives and under mild conditions. The use of a polyoxometalate intercalated into the matrix of an LDH as a catalyst for a cascade reaction was reported only by Liu and his co-workers in 2016 [26]. They have prepared a series of Tris-LDH-$X_4(PW_9)_2$ by intercalating POM anions of $[X_4(H_2O)_2(PW_9O_{34})_2]^{10-}$ (X= Mn, Fe, Co, Ni, Cu and Zn) into a Tris-modified LDH for the oxidation of benzyl alcohol followed by Knoevenagel condensation with ethyl cyanoacetate, which led to benzylidene ethyl cyanoacetate. The previous subchapter described the catalytic properties of Ce-containing MgAl LDH-GO composites bearing different concentrations of GO in the range of 5-25 wt. % in the one-pot cascade oxidation-Knoevenagel condensation. In the current study, the neat Mg3Al-LDH was modified with molybdate anions (MoO_4^{2-}) and with graphene oxide in the range of 5-25 wt.% resulting in a series labelled HTMo-*x*GO, where *x* is the concentration of graphene oxide. The purpose is to observe noticeable differences between the catalytic results of hybrid GO and Mg_3Al layered double hydroxides when the brucite-like layers are modified by inserting another cation like cerium or when the interlayer space contains other anions, like molybdate.

4.2.2. Synthesis of the materials

$Mg_3Al(OH)_{8.8}(MoO_4)_{0.1}$ LDH-GO composites bearing different concentrations of graphene oxide (GO) in the range of 5-25 wt.% labelled HTMo-*x*GO were synthesized by co-precipitating the LDH phase in the presence of GO. The co-precipitation method was used again for the synthesis of the solids. The preparation steps of this method were identical for all the composites, the only difference in their synthesis being the amounts of precursor salts used (respecting the molar ratios Mg: Al of 3:1), which varied depending on the concentration of graphene oxide aimed to be included in the resulting solid (e.g. 5%, 10%, 15%, 20%, 25%, respectively). The method used to prepare the graphene oxide is the same as the one mentioned in the previous chapter and is based on Hummer's method. To obtain the solid hydrotalcite-type compounds, two solutions were necessary (A and B), as follows:

- **For HTMo-5GO**

Solution A was prepared by dissolving 48.6 mmol $Mg(NO_3)_2{\cdot}6H_2O$ and 16.2 mmol $Al(NO_3)_3{\cdot}9H_2O$ in a mixture containing 8 mL distilled water and 77 mL of graphene oxide suspension. The solution B was obtained by dissolving 142 mmol NaOH and 8.5 mmol $Na_2MoO_4x2H_2O$ in 84 mL of distilled water.

- **For HTMo-10GO**

  Solution A was prepared by dissolving 114 mmol $Mg(NO_3)_2{\cdot}6H_2O$ and 38.1 mmol $Al(NO_3)_3{\cdot}9H_2O$ in a mixture containing 58 mL distilled water and 340 mL of graphene oxide suspension. The solution B was obtained by dissolving 335 mmol NaOH and 20.5 mmol $Na_2MoO_4x2H_2O$ in 358 mL distilled water.

- **For HTMo-15GO**

  Solution A was prepared by dissolving 100 mmol $Mg(NO_3)_2{\cdot}6H_2O$ and 33.4 mmol $Al(NO_3)_3{\cdot}9H_2O$ in a mixture containing 51 mL distilled water and 472 mL of graphene oxide suspension. The solution B was obtained by dissolving 293 mmol NaOH and 17.7 mmol $Na_2MoO_4x2H_2O$ in 512 mL distilled water.

- **For HTMo-20GO**

  Solution A was prepared by dissolving 40.5 mmol $Mg(NO_3)_2{\cdot}6H_2O$ and 13.5 mmol $Al(NO_3)_3{\cdot}9H_2O$ in a mixture containing 7.9 mL distilled water and 305.8 mL of water graphene oxide suspension. The solution B was obtained by dissolving 118.8 mmol NaOH and 7.1 mmol $Na_2MoO_4x2H_2O$ in 312 mL distilled water.

- **For HTMo-25GO**

  Solution A was prepared by dissolving 48.6 mmol $Mg(NO_3)_2{\cdot}6H_2O$ and 16.2 mmol $Al(NO_3)_3{\cdot}9H_2O$ in mixture containing 8 mL distilled water and 489 mL of graphene oxide suspension. The solution B was obtained by dissolving 142.5 mmol NaOH and 8.5 mmol $Na_2MoO_4x2H_2O$ in 496 mL distilled water.

- **For HTMo**

  Solution A was prepared by dissolving 195 mmol $Mg(NO_3)_2{\cdot}6H_2O$ and 65.1 mmol $Al(NO_3)_3{\cdot}9H_2O$ in mixture containing 718 mL distilled. The solution B was obtained by dissolving 572 mmol NaOH and 34.5 mmol $Na_2MoO_4x2H_2O$ in 748 mL distilled water.

The two solutions, A and B were mixed in a round-bottomed flask under continuous stirring and kept for aging for 18 hours. The washing of the gel was carried out with distilled water until the conductivity was below 100 µS/cm. Drying was carried out in an oven at a temperature of 90°C for 24 hours under an air atmosphere.

4.2.3. Characterization of the materials

The obtained solids were characterized using powder XRD, XRF, DRIFT, Diffuse reflectance UV-VIS-NIR spectroscopy, Raman spectroscopy and scanning electron microscopy (SEM).

The XRD patterns of the synthesized molybdate-doped LDH modified with graphene oxide show the formation of single-phase layered double hydroxides without any impurities and confirm that the concentration of GO introduced during synthesis has a strong influence on the intensity of the peaks. Practically, the insertion of large amounts of graphene oxide during the synthesis of the materials led to obtaining higher-intensity peaks, as can be observed in Figure 14.

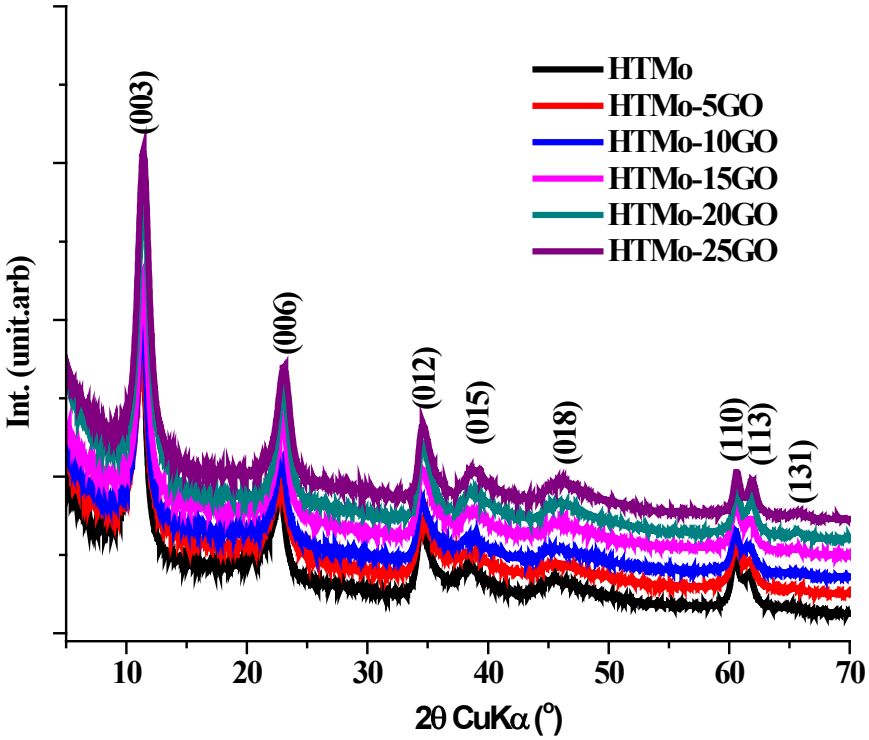

Figure 14. XRD analysis of the composite materials.

Moreover, the diffraction peaks of the samples are rather broad, indicating low crystallinity or the formation of nano-scaled LDH crystallites [58]. The lattice parameters and the crystallite sizes can be seen in Table 8. The crystallite sizes were calculated along two directions: perpendicular (D_{003}) and parallel (D_{110}) to the brucite-like layers, respectively**.** The data illustrated in Table 8 show similar structural characteristics for all the samples.

As it can be observed, the crystallite sizes, in particular the coherence lengths in the layer-stacking direction (D_{003}), were affected by the presence of GO. The insertion of GO led to the formation of larger LDH particles suggesting the involvement of the GO sheets as nucleating agents for the LDH phase formation [47]. The evolution, in the HTMo-xGO series, of the

absolute intensities of the (110) line, exclusively related to the brucite-like layer, should go along with the decrease of the proportion of the LDH phase in the nanocomposites.

A decrease of the *c*-lattice parameter value accompanied by an increase of the I_{003}/I_{110} ratio for all the HTMo-*x*GO nanocomposites in comparison with the HTMo sample is observed (Table 8).

Table 8. Structural data for the hydrotalcite-like compounds.

Sample	**Lattice parameters**		**Crystallite sizes**		**I_{003}/I_{110}**	**$I_{110(HTMO)}/I_{110(HTMo-xGO)}$**
	***a* (Å)**	***c* (Å)**	**D_{003} (nm)**	**D_{110} (nm)**		
HTMo-5GO	3.058	23.582	10.4	6.5	4.2	0.85
HTMo-10GO	3.059	23.509	12.4	8.3	5.2	0.84
HTMo-15GO	3.058	23.326	12.3	8.3	4.7	0.99
HTMo-20GO	3.055	23.232	13.7	7.2	6.4	0.94
HTMo-25GO	3.054	23.271	15.0	6.9	6.7	0.92
HTMo	3.061	23.814	12.7	6.8	4.4	1.00

The result suggests a slight modification of the interlayer anionic composition, probably a higher degree of hydration with a different compaction of the anionic species, due to mutual electrostatic interaction between LDH and GO phases.

The elemental composition determined by XRF analysis (Table 9) confirms that the ratio between the divalent and trivalent cations is close to the calculated one.

Table 9. Elemental composition determined by XRF analysis.

Catalyst	Elemental composition				
	Mg^{2+} [wt%]	Al^{3+} [wt%]	Mo [wt%]	Mg/Al Atomic ratio	Mo/Al Atomic ratio
HTMo-5GO	10.65	4.12	6.42	2.91	0.34
HTMo-10GO	11.36	4.46	6.03	2.86	0.28
HTMo-15GO	15.59	5.99	8.74	2.83	0.21
HTMo-20GO	13.01	5.33	3.64	2.75	0.19
HTMo-25GO	11.25	4.75	4.03	2.66	0.14
HTMo	15.04	5.74	7.44	2.95	0.36

Moreover, the insertion of molybdate anions was also validated through the XRF determination. The DRIFT spectrum of the hybrid solids is presented in Figure 15. As it can be noticed, growing the concentration of graphene oxide in the composite materials during the synthesis step shows no substantial changes in the DRIFT spectrum. The bands attributed to the composites containing graphene oxide are shifted to smaller wavenumbers than those corresponding to the neat HTMo. All the samples present a broad absorption band at around 879 cm^{-1} for the hybrids containing GO and at 996 cm^{-1} for the parent material HT-MO which is attributed to the antisymmetric mode of Mo–O–Mo characteristic for molybdate anions (MoO_4^{2-}) [58,59].

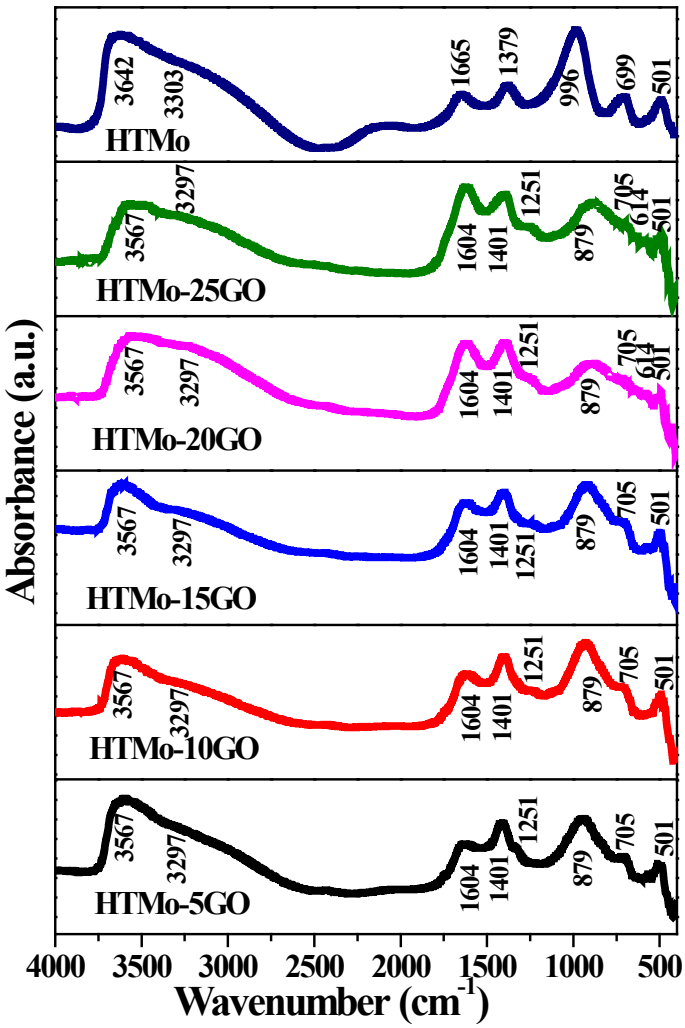

Figure 15. DRIFT spectra of the composite materials.

It can be observed that this band has lower intensities for the samples having higher GO concentration suggesting that the amount of molybdate anions decreases with the increase of graphene oxide concentration, as it can also be seen in the XRF results. The bands present at

1401-1251 cm^{-1} could be due to the stretching mode of carbonate anion (CO_3^{2-}), which suggests that the samples were contaminated with CO_2 from the atmosphere [58,59].

Strong absorption bands assigned to OH stretching vibrations and the interlayer water bending modes can be observed at 3567 and 1604 cm^{-1} for the HTMo-xGO samples and at 3642 and 1665 cm^{-1} for the neat HTMo. There is also a shoulder at 3297 and 3303 cm^{-1} which appeared probably due to the formation of hydrogen bonds between the water molecules [59]. All the solids containing GO present a distinct band at 705 cm^{-1} which decreases with the increase of GO concentration. Also, for the compound having only molybdate anions, this distinct band appears at a lower wavenumber, at 669 cm^{-1} and it has the highest intensity. Furthermore, the bands at 614 cm^{-1} and 501 cm^{-1} are specific to the vibrations mode of the oxygen atoms bonded to Mg and Al from the crystal lattice [58].

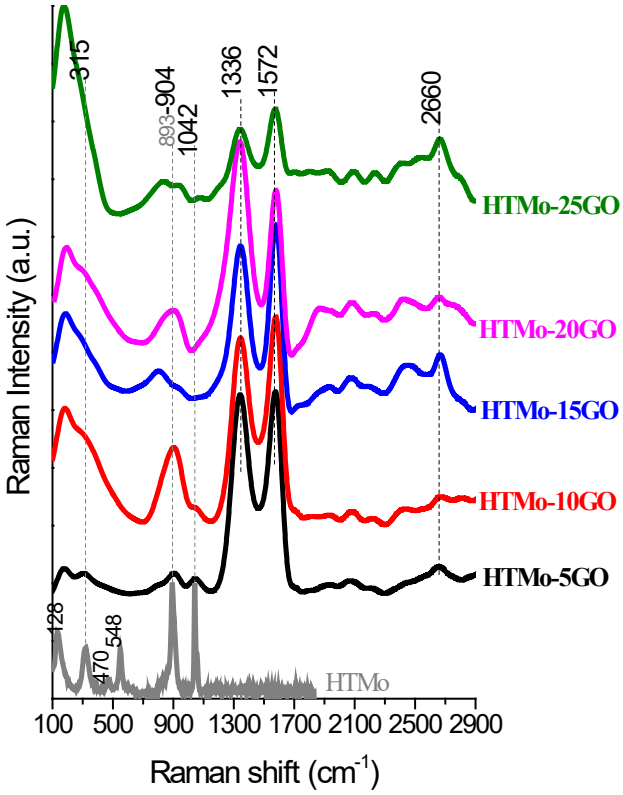

Figure 16. Raman spectra of the hybrid materials containing both molybdate anions and GO compared to the layered double hydroxide with molybdate anions.

In the Raman spectra presented in Figure 16, the most intense band is the one appearing at 893 cm^{-1} which can be attributed to the Mo–O symmetrical stretching vibration in MoO_4^{2-} (Mo in tetrahedral coordination), while the band at 315 cm^{-1} can be associated to the Mo=O bending vibrations [60]. The Raman spectrum of the HTMo (Figure 16) presents an intense band at 1038 cm^{-1} specific to the carbonate anions located in the interlayer region [60]. The

absorption bands present at 470 and 548 cm^{-1} are specific for the bending vibrations of Mg-OH, Al-OH. In the Raman spectrum of the hybrid materials, the signal coming from the graphene oxide component screens the bands emitted by the neat HTMo in the region 100-1100 cm^{-1}, even though the concentration of the parent solid was higher than the GO concentration.

The presence of GO in all the HTMo-*x*GO composites was evidenced by Raman spectra of the samples displayed in Figure 16. In the Raman spectrum the GO is highlighted by the presence of the D band, which is the dominant sp^2 Raman signature of disorder in nanocrystalline carbonic structures at 1336 cm^{-1} and the G band at 1572 cm^{-1} (characteristic of planar carbonic structures with sp^2 hybridized C atoms) [61], while the ratio between the intensities of the two bands is I_D/I_G = 1.43. The Raman spectrum of the composites containing GO (Figure 16 a) reveals the presence of Mo–O symmetrical stretching vibration in MoO_4^{2-} based on the absorption band at 904 cm^{-1}. For the HT-Mo (Figure 16 b), this absorption band appears at 893 cm^{-1}. The shift of the band from 893 to 904 cm^{-1} is attributed to the insertion of graphene oxide.

The Raman spectrum of the samples containing GO show a band characteristic to the LDH structure, namely the band related to the ν_1 symmetric stretch of A1' symmetry of carbonate anion at 1030 cm^{-1} [62]. Another exciting aspect noticed in the Raman spectra is the presence of the G' band, which appears around 2600 cm^{-1}. This band increases with the concentration of graphene oxide inserted in the composites. Apparently, with the increase of the GO concentration, a part of the hydrotalcite crystalizes on the graphene oxide's surface, observation also sustained by the SEM images.

Figure 17 shows SEM images of $Mg_3Al(OH)_{8.8}(MoO_4)_{0.1}$ LDH-GO composites bearing different concentrations of graphene oxide GO in the range of 5-25 wt.%. The hybrid materials exhibited the typical sheet-like morphology of hydrotalcites. By increasing the amount of graphene oxide, the composite HTMo-*x*GO (x=5-25 wt.%) particles were more separated with smaller layer thickness. This morphology change could be caused by the formation of hydrotalcites on the GO surface in the structure of the hybrid materials [63]. The SEM results agreed with the result of the XRD analysis.

HTMo 100µm

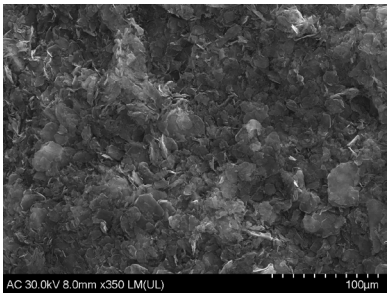

HTMo 30 µm

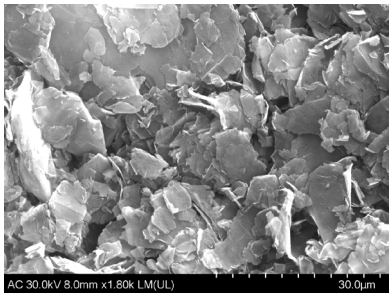

HTMo-5GO 100µm

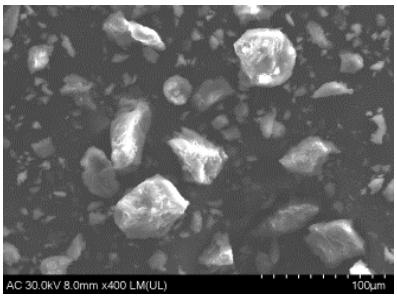

HTMo-5GO 30µm

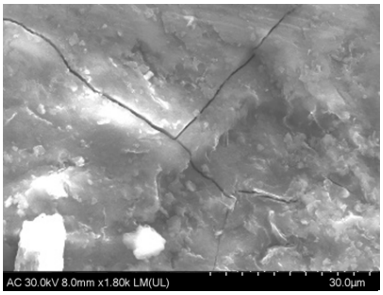

HTMo-10GO 100µm

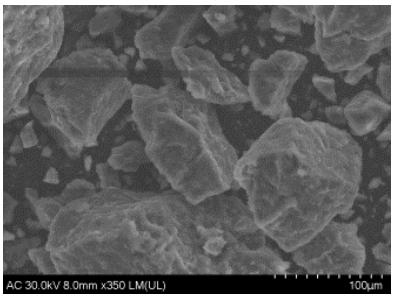

HTMo-10GO 30µm

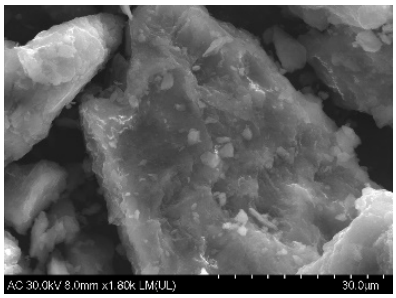

HTMo-15GO 100µm

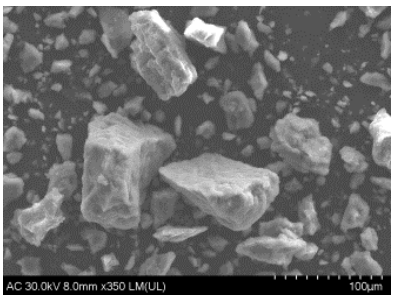

HTMo-15GO 30µm

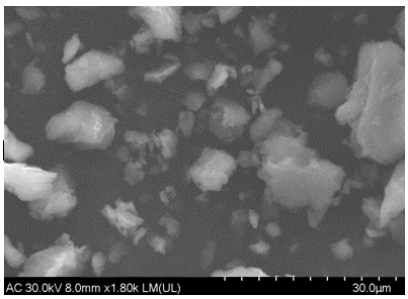

Figure 17. SEM analysis of the hybrid materials

Figure 17. (continued)

HTMo-20GO 100μm

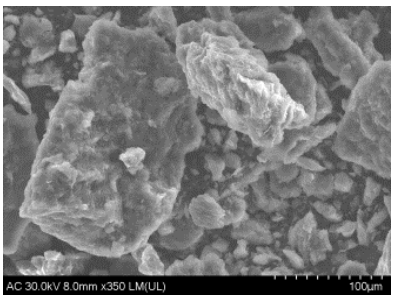

HTMo-20GO 30μm

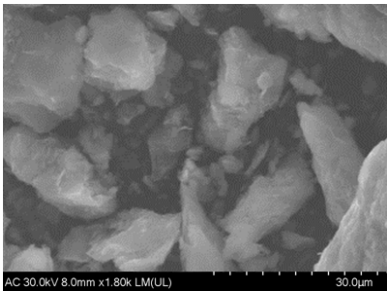

HTMo-25GO 100μm

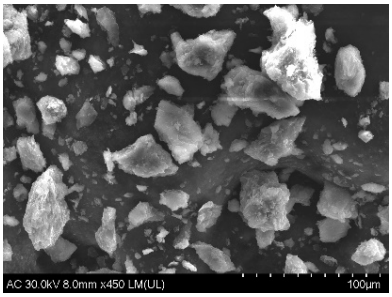

HTMo-25GO 30μm

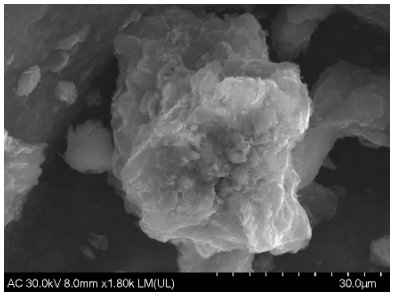

4.2.4. Catalytic study

The LDH-GO composites bearing different concentrations of GO in the range of 5-25 wt. % were tested as catalysts in the one-pot cascade oxidation-Knoevenagel condensation (Scheme 2).

Table 10. Catalytic results of Mg_3Al LDH-MoO_4, with different concentrations of GO (graphene oxides) in the range of 5-25 wt. %.

Catalyst	Yield to BPA (%) in the following solvents:			Conversion of BnOH (%) in the following solvents:		
	Toluene	Mesitylene	Benzene	Toluene	Mesitylene	Benzene
HTMo-5GO	4	4	9	8	9	11
HTMo-10GO	6	9	14	8	9	15
HTMo-15GO	9	10	16	11	14	25
HTMo-20GO	14	16	27	30	36	31
HTMo-25GO	27	29	36	34	43	51
HT-Mo	0.9	2	8	20	29	34

The reaction conditions are explained thoroughly in the first part of the current Chapter. 2-Benzoyl-3-phenylacrylonitrile (BPA) was synthesized by the aerobic oxidation of benzyl alcohol (BnOH) followed by the Knoevenagel condensation with benzoyl acetonitrile (BzACN) using three different non-polar solvents, i.e., toluene, benzene, and mesitylene.

The conversion results and the yields of 2-benzoyl-3-phenylacrylonitrile (BPA) can be seen in Table 10.

As in the HT3Ce-xGO case which was discussed in the previous chapter, benzene has proven to be the best solvent compared to mesitylene and toluene. Without considering the solvent, this time, the conversion of benzyl alcohol increased with the graphene oxide concentration. The insertion of graphene oxide led to higher surface areas and better accessibility to active sites, explaining the increased conversion.

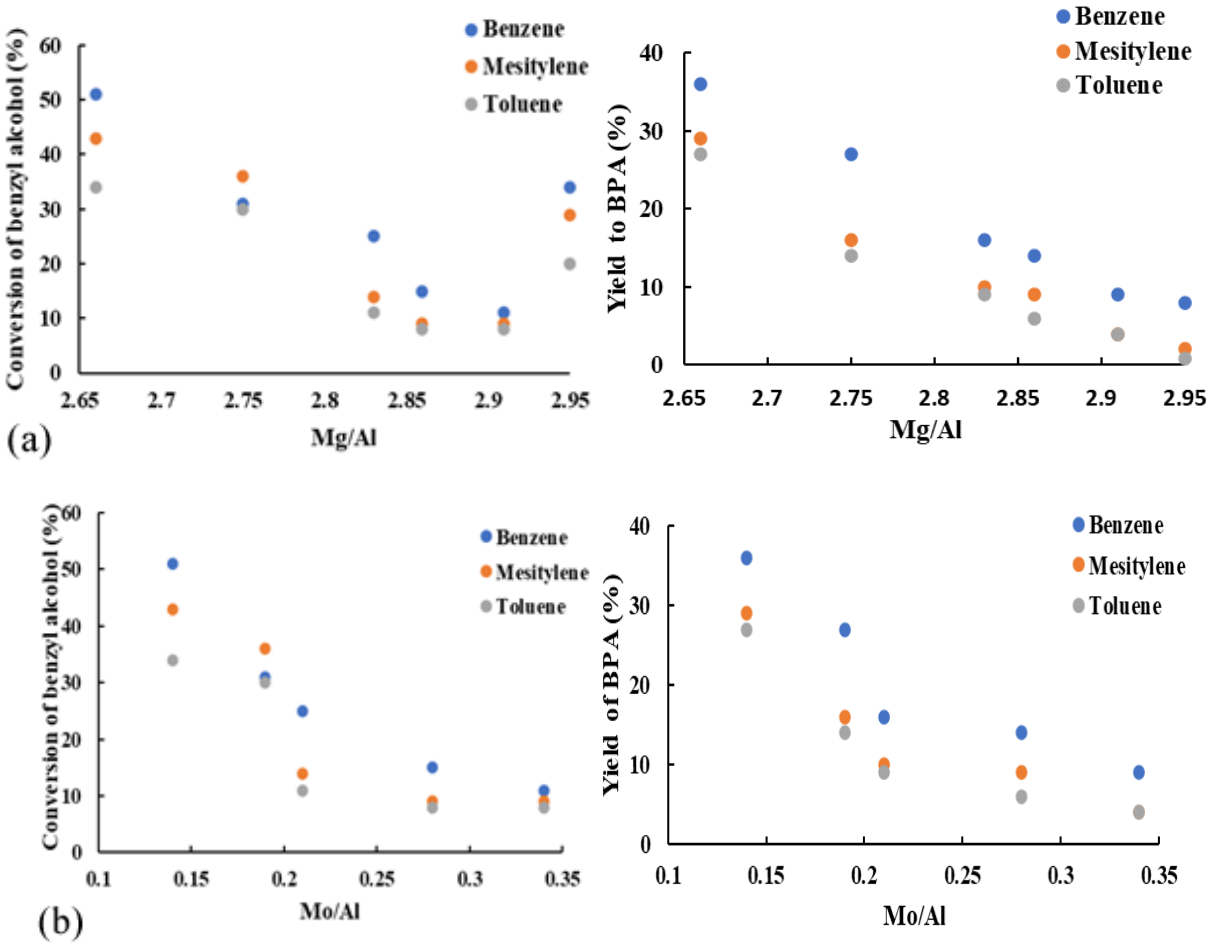

Figure 18. The variation of the conversion of benzyl alcohol and the yields to 2-benzoyl-3-phenylacrylonitrile (BPA) vs the Mg/Al ratio in the brucite type layer of the catalysts (a) and vs Mo/Al ratio (b).

In what concerns the obtaining of higher yield values (Figure 5) for the samples containing the GO phase compared to the neat solid Mg_3Al LDH-MoO_4 (HT-Mo), it can be reiterated that graphene oxide is needed in the LDH structure. Notably, higher catalytic activities were obtained when both the Mg/Al and Mo/Al atomic ratios were smaller (Figure 18 and b). The combinatorial effect of this family of composite materials was demonstrated by the fine-tuning of the oxidative activity of molybdate species and the basic character of the LDH layers which catalyse the Knoevenagel condensation.

4.2.5. Conclusion

The co-precipitation of Mg3Al-LDH modified with molybdate anions (MoO_4^{2-}) and with graphene oxide in the range of 5-25 wt.% has led to the obtaining of HTMo-*x*GO composites with increased crystallinity as indicated by the XRD analysis. The diffractograms of the composites also showed no other impurities. Raman spectroscopy clearly highlighted the existence of GO in the HTMo-xGO composites, while the SEM images demonstrated typical sheet-like morphology of hydrotalcite and suggested that with the increase of the graphene oxide amount, the space between the particles was more extensive, and they had a smaller layer thickness. In the case of the catalysts modified with GO, it was observed that when the brucite-type layer was modified with another cation like cerium, the conversion of benzyl alcohol increased with the decrease of the graphene oxide concentration. The situation changed when the interlayer of the LDH was modified with molybdate, namely, the conversion increased with the increase of the GO concentration.

References

1. Lonkar, S.P., Raquez, J.M., Dubois, P. One-pot microwave-assisted synthesis of graphene/layered double hydroxide (LDH) nanohybrids. Nano-Micro Lett. 2015, 7, 332–340.

2. Álvarez, M.G., Marcu, I.-C., Tichit, D. Recent Innovative Developments of Layered Double Hydroxide-Based Hybrids and Nanocomposite Catalysts. In Progress in Layered Double Hydroxides – From Synthesis to New Applications, Nocchetti, M., Costantino, U., Eds., World Scientific Publishing Ltd.: Singapore, 2022, Ch. 4, pp. 189–362, in press.

3. Newman, S.P., Jones, W. Synthesis, characterization, and applications of layered double hydroxides containing organic guests.New J. Chem. 1998, 22, 105–115.

4. Brisebois, P.P., Siaj, M. Harvesting graphene oxide – years 1859 to 2019: A review of its structure, synthesis, properties and exfoliation. J. Mater. Chem. C 2020, 8, 1517–1547.

5. Dreyer, D.R., Jia, H.P., Bielawski, C.W. Graphene Oxide: A Convenient Carbocatalyst for Facilitating Oxidation and Hydration Reactions. Angew. Chem. Int. Ed. 2010, 49, 6813–6816.
6. Pang, H., Wu, Y., Wang, X., Hu, B.,Wang, X. Recent Advances in composites of graphene and layered double hydroxides for water remediation: A Review. Chem. Asian. J. 2019, 14, 2542–2552.
7. Van Schijndel, J., Molendijk, D., Spakman, H., Knaven, E., Canalle, L.A., Meuldijk, J. Mechanistic consideration and characterization of ammonia-based catalytic active intermediates of the green Knoevenagel reaction of various benzaldehydes. Green Chem.Lett. Rev. 2019, 12, 323–331.
8. Dumbre, D.K., Mozammel, T., Selvakannan, P.R., Hamid, S.B.A., Choudhary, V.R., Bhargava, S.K. Thermally decomposed mesoporous nickel Iiron hydrotalcite: An active solid-base catalyst for solvent-free Knoevenagel condensation. J. Colloid Interface Sci. 2015, 441, 52–58.
9. Trost, B.M., Fleming, I. Chapter 1.11. The Knoevenagel Reaction. In Comprehensive organic synthesis: Selectivity, strategy and efficiency in modern organic chemistry, Tietze, L.F., Beifuss, U., Eds., Elsevier Ltd.: Oxford, UK, 1991, Volume 2, pp. 341–388.
10. Bhattacharjee, S. Synthesis and application of layered double hydroxide-hosted 2-aminoterephthalate for the Knoevenagel condensation reaction. Inorg. Nano-Met. Chem 2019, 48, 340–346
11. Rana, S., Jonnalagadda, S.B. Synthesis and characterization of amine functionalized graphene oxide and scope as catalyst for Knoevenagel condensation reaction. Cat. Comm. 2016, 92, 31–34.
12. Li, T., Zhang, W., Chen, W., Miras, H.N., Song, Y.F. Layered double hydroxides anchored ionic liquids as amphiphilic heterogeneous catalysts for Knoevenagel condensation reaction. Dalton Trans. 2018, 47, 3059–3067.
13. Krishnan, G.R., Sreekumar, K. First Example of Organocatalysis by Polystyrene-Supported Pamam Dendrimers: Highly Efficient and Reusable Catalyst for Knoevenagel Condensations. Eur. J. Org. Chem. 2008, 2008, 4763–4768.
14. Xu, D.-Z., Shi, S., Wang, Y. Polystyrene-Immobilized DABCO as a Highly Efficient and Recyclable Organocatalyst for the Knoevenagel Condensation Reaction. RSC Adv. 2013, 3, 23075–23079.

15. Mondal, J., Modak, A., Bhaumik, A. Highly efficient mesoporous base catalyzed Knoevenagel condensation of different aromatic aldehydes with malononitrile and subsequent noncatalytic Diels–Alder reactions. J. Mol. Catal. 2011, 335, 236–241.
16. Xing, R., Wu, H., Li, X., Zhao, Z., Liu, Y., Chena, L., Wu, P. Mesopolymer solid base catalysts with variable basicity: Preparation and catalytic properties. J. Mater. Chem. 2009, 19, 4004–4011.
17. Parida, K.M., Mallick, S., Sahoo, P.C., Rana, S.K. A facile method for synthesis of amine-functionalized mesoporous zirconia and its catalytic evaluation in Knoevenagel condensation. Appl. Catal. A Gen. 2010, 381, 226–232.
18. Phan, N.T.S., Jones, C.W. Highly accessible catalytic sites on recyclable organosilane-functionalized magnetic nanoparticles: An alternative to functionalized porous silica catalysts. J. Mol. Catal. 2006, 253, 123–131.
19. Reddy, K.R., Rajgopal, K., Maheswaria, C.U., Kantama, M.L. Chitosan hydrogel: A green and recyclable biopolymer catalyst for aldol and Knoevenagel reactions. New J. Chem. 2006, 30, 1549–1552.
20. Feng, X.W., Li, C., Wang, N., Li, K., Zhang, W.W., Wanga, Z., Yu, X.Q. Lipase-catalysed decarboxylative aldol reaction and decarboxylative Knoevenagel reaction. Green Chem. 2009, 11, 1933–1936.
21. Cho, H.-Y., Kim, J., Kim, S.-N., Ahn, W.-S. High Yield 1-L Scale Synthesis of ZIF-8 via a Sonochemical Route. Micropor. Mesopor. Mater. 2013, 169, 180–184.
22. Bhattacharjee, S., Jang, M.-S., Kwon, H.-J., Ahn, W.-S. Zeolitic Imidazolate Frameworks: Synthesis, Functionalization, and Catalytic/Adsorption Applications. Catal. Surv. Asia 2014, 18, 101–127.
23. Reddy, T.I., Varma, R.S. Rare-earth (RE) exchanged NaY zeolite promoted knoevenagel condensation. Tetrahedron Lett. 1997, 38, 1721–1724.
24. Gascon, J., Aktay, U., Hernandez-Alonso, M.D., Van Klink, G.P.M., Kapteijn, F. Amino-based metal-organic frameworks as stable, highly active basic catalysts. J. Catal. 2009, 261, 75–87.
25. Hassan, H.M.A., Elshaarawy, R.F.M., Dey, S.K., Simon, I., Janiak, C. Microwave-Assisted Hydrothermal Fabrication of Magnetic Amino-Grafted Graphene Oxide Nanocomposite as a Heterogeneous Knoevenagel Catalyst. Catal. Lett. 2017, 147, 1998–2005.

26. Liu, K., Xu, Y., Yao, Z., Miras, H.N., Song, S.F. Polyoxometalate-Intercalated Layered Double Hydroxides as Efficient and Recyclable Bifunctional Catalysts for Cascade Reactions. Chem. Cat. Chem. 2016, 8, 929–937

27. Aryanejad, S., Bagherzade, G., Farrokhi, A. Efficient and recyclable novel Ni-based metal–organic framework nanostructure as the catalyst for the cascade reaction of alcohol oxidation – Knoevenagel condensation. Appl. Organometal. Chem. 2018, 32, 1–11.

28. Srivastava, R., Sarmah, B., Satpati, B. Nanocrystalline ZSM-5 based bi-functional catalyst for two-step and three step tandem reactions. RSC Adv. 2015, 5, 25998–26006.

29. Xu, L., Li, C.G., Zhang, K., Wu, P. Bifunctional tandem catalysis on multilamellar organic–inorganic hybrid zeolites. ACS Catal.2014, 4, 2959–2968.

30. Li, Y.A., Yang, S., Liu, Q.K., Chen, G.J., Ma, J.P., Dong, Y.B. Pd(0)@UiO-68-AP: Chelation-directed bifunctional heterogeneous catalyst for stepwise organic transformations. Chem. Commun. 2016, 52, 6517–6520.

31. Modak, A., Mondal, J., Bhaumik, A. Porphyrin based porous organic polymer as bi-functional catalyst for selective oxidation and Knoevenagel condensation reactions. Appl. Catal. A 2013, 459, 41–51.

32. Chen, C., Yang, H.M., Chen, J.Z., Zhang, R., Guo, L., Gan, H.M., Song, B.N., Zhu, W.W., Hua, L., Hou, Z.S. One-pot tandem catalytic synthesis of α, β-unsaturated nitriles from alcohol with nitriles in aqueous phase. Catal. Commun. 2014, 47, 49–53.

33. Zhou, W., Zhai, S., Pan, J., Cui, A., Qian, J., He, M., Xu, Z., Chen, Q. Bifunctional NiGa Layered Double Hydroxide for the Aerobic Oxidation/ Condensation Tandem Reaction between Aromatic Alcohols and Active Methylene Compounds. Asian J. Org. Chem. 2017, 6, 1536–1541.

34. Ang, W.J., Chng, Y.S., Lam, Y.L. Fluorous bispidine: A bifunctional reagent for copper-catalyzed oxidation and Knoevenagel condensation reactions in water. RSC Adv. 2015, 5, 81415–81428.

35. Cao, Y., Li, H., Zhang, J., Shi, L., Zhang, D. Promotional effects of rare earth elements (Sc, Y, Ce, and Pr) on NiMgAl catalysts for dry reforming of methane. RSC Adv. 2016, 6, 112215–112225.

36. Golovin, S.N., Yapryntsev, M.N., Ryltsova, I.G., Veligzhanin, A.A., Lebedeva, O.E. Novel cerium-containing layered double hydroxide. Chem. Pap. 2020, 74, 367–370.

37. Qian, Y., Qiao, P., Li, L., Han, H., Zhang, H., Chang, G. Hydrothermal Synthesis of Lanthanum-Doped MgAl-Layered Double Hydroxide/Graphene Oxide Hybrid and Its

Application as Flame Retardant for Thermoplastic Polyurethane. Adv. Polym. Technol. 2020, 2020, 1–10.
38. Usman, M.S., Hussein, M.Z., Fakurazi, S., Saad, F.F.A. Gadolinium-based layered double hydroxide and graphene oxide nano-carriers for magnetic resonance imaging and drug delivery. Chem. Cent. J. 2017, 47, 1–10.
39. Hummers, W., Offeman, R. Preparation of Graphitic Oxide. J. Am. Chem. Soc. 1958, 80, 1339.
40. Sing, K.S.W., Everett, D.H., Haul, R.A.W., Moscou, L., Pierotti, R.A., Rouquerol, J., Siemieniewska, T. Reporting Physisorption Data for Gas/Solid Systems with Special Reference to the Determination of Surface Area and Porosity. Pure Appl. Chem. 1985, 57,603–619.
41. Thommes, M., Kaneko, K., Neimark, A.V., Olivier, J.P., Rodriguez-Reinoso, F., Rouquerol, J., Sing, K.S.W. Physisorption of gases, with special reference to the evaluation of surface area and pore size distribution (IUPAC Technical Report). Pure Appl. Chem. 2015, 87, 1051–1069.
42. Garcia-Gallastegui, A., Iruretagoyena, D., Gouvea, V., Mokhtar, M., Asiri, A.M., Basahel, S.N., Al-Thabaiti, S.A., Alyoubi, A.O., Chadwick, D., Shaffer, M.S.P. Graphene Oxide as Support for Layered Double Hydroxides: Enhancing the CO2 Adsorption Capacity. Chem. Mater. 2012, 24, 4531–4539.
43. Zhao, X., Zhang, Q., Chen, D. Enhanced Mechanical Properties of Graphene-Based Poly(vinyl alcohol) Composites. Macromolecules 2010, 43, 2357–2363.
44. Yuan, X., Wang, Y., Wang, J., Zhou, C., Tang, Q. Calcined graphene/MgAl-layered double hydroxides for enhanced Cr(VI) removal. Chem. Eng. J. 2013, 221, 204–213.
45. Wang, J., Mei, X., Huang, L., Zheng, Q., Qiao, Y., Zang, K., Mao, S., Yang, R., Zhang, Z., Gao, Y., et al. Synthesis of layereddouble hydroxides/graphene oxide nanocomposite as a novel high-temperature CO2 adsorbent. Energy Chem. 2015, 24, 127–137.
46. Yang, Z., Ji, S., Gao, W., Zhang, C., Ren, L., Tjiu, W.W., Zhang, Z., Pan, J., Liu, T. Magnetic nanomaterial derived from graphene oxide/layered double hydroxide hybrid for efficient removal of methyl orange from aqueous solution. J. Colloid Interface Sci.2013, 408, 25–32.
47. Álvarez, M.G., Dana, G., Crivoi, D.G., Medina, F., Tichit, D. Synthesis of Chalcone Using LDH/Graphene Nanocatalysts of Different Compositions. ChemEngineering 2019, 3, 29.

48. Negishi, R., Wei, C., Yao, Y., Ogawa, Y., Akabori, M., Kanai, Y., Matsumoto, K., Taniyasu, Y., Kobayashi, Y. Turbostratic Stacking Effect in Multilayer Graphene on the Electrical Transport Properties. Phys. Status Solidi B 2019, 257, 1900437.
49. Frost, R.L., Scholz, R., López, A., Theiss, F.L. Vibrational spectroscopic study of the natural layered double hydroxide manasseite now defined as hydrotalcite-2H–Mg6Al2(OH)16[CO3] • 4H2O. Spectrochim. Acta A 2014, 118, 187–191.
50. Schilling, C., Hofmann, A., Hess, C., Ganduglia-Pirovano, M.V. Raman Spectra of Polycrystalline CeO2: A Density Functional Theory Study. J. Phys. Chem. C 2017, 121, 20834–20849.
51. Abedi, H., Mehrpooya, M. Synthesis of three-metal layered double hydroxide and dual doped graphene oxide composite as a novel electrocatalyst for oxygen reduction reaction. J. Alloys Compd. 2021, 875, 160047.
52. Stamate, A.-E., Zăvoianu, R., Pavel, O.D., Birjega, R., Matei, A., Dumitru, M., Brezestean, I., Osiac, M., Marcu, I.-C. The influence of the preparation method on the physico-chemical properties and catalytic activities of Ce-modified LDH structures used as catalysts in condensation reactions. Molecules 2021, 26, 6191.
53. Wang, Q., Gao, Y., Luo, J., Zhong, Z., Borgna, A., Guo, Z., O'Hare, D. Synthesis of nano-sized spherical Mg3Al–CO3 layered double hydroxide as a high-temperature CO2 adsorbent. RSC Adv. 2013, 3, 3414–3420.
54. Abdellattif, M.H., Mokhtar, M. MgAl-Layered Double Hydroxide Solid Base Catalysts for Henry Reaction: A Green Protocol. Catalysts 2018, 8, 133.
55. Channei, D., Nakaruk, A., Phanichphant, S. Influence of Graphene Oxide on Photocatalytic Enhancement of Cerium Dioxide.Mater. Lett. 2017, 209, 43–47
56. Choudary, B.M., Kantam, M.L., Rahman, A., Reddy, C.V., Rao, K.K. The First Example of Activation of Molecular Oxygen by Nickel in Ni-Al Hydrotalcite: A Novel Protocol for the Selective Oxidation of Alcohols. Angew. Chem. Int. Ed. 2001, 40, 763–766.
57. Cao, Y., Li, G., Li, X., Graphene/layered double hydroxide nanocomposite: Properties, synthesis, and applications, Chemical Engineering Journal, 2016, 292, 207-223.
58. Klemkaite-Ramanauske, K., Zilinskas, A., Taraskevcius, R.,Khinsky, A., Kareiva, A. Preparation of Mg/Al layered double hydroxide (LDH) with structurally embedded molybdate ions and application as a catalyst for the synthesis of 2-adamantylidene(phenyl)amine Schiff base. Polyhedron 2014, 68, 340–345.

59. Yu, X., Wang, J., Zhang, M., Yang, P., Yang, L., Cao, L., Li, J. One-step synthesis of lamellar molybdate pillared hydrotalcite and its application for AZ31 Mg alloy protection. Solid State Sciences 2009, 11, 376–381.
60. Zavoianu, R., Birjega, R., Pavel, O.D., Cruceanu, A., Alifanti, M. Hydrotalcite like compounds with low Mo-loading active catalysts for selective oxidation of cyclohexene with hydrogen peroxide. Applied Catalysis A: General 2005, 286, 211–220.
61. Claramunt, S., Varea, A., López-Díaz, D., Velázquez, M.M., Cornet, A., Cirera, A., The Importance of Interbands on the Interpretation of the Raman Spectrum of Graphene Oxide, J. Phys. Chem. C, 2015, 119, 10123-10129.
62. Frost, R.L. , Scholz, R., López, A., Theiss, F.L., Vibrational spectroscopic study of the natural layered double hydroxide manasseite now defined as hydrotalcite-2H – Mg6Al2(OH)16[CO3]▪4H2O, Spectrochim. Acta A, 118, 2014, 187–191.
63. Nguyena, T.D., Nguyena, A.S., Tran, B.A., Vu, K.O., Tran, D.L., Phan, T.T., Scharnagl, N., Zheludkevich, M.L., Toa, T.X.H. Molybdate intercalated hydrotalcite/graphene oxide composite as corrosion inhibitor for carbon steel. Surface & Coatings Technology 2020, 399, 126165.

Chapter 5. Multicationic MgNiMAl LDH (M = Cu or Co) – bifunctional catalysts for organic synthesis

5.1. Overview

The current chapter aims to open up new perspectives in the rational design of efficient bifunctional catalytic systems for organic synthesis. The discussion will be focused on the synthesis of MgNiMAl (M = Cu or Co)-layered double hydroxides having different cationic molar ratios using the co-precipitation method and the study of their catalytic properties. All the catalysts were tested in the one-pot cascade oxidation-Knoevenagel condensation reaction. The target product, 2-Benzoyl-3-phenylacrylonitrile (BPA) was synthesized through the aerobic oxidation of benzyl alcohol (BnOH) followed by Knoevenagel condensation with benzoyl acetonitrile (BzACN). The reactions were performed in three different solvents, namely, toluene, benzene and mesitylene. 2-Benzoyl-3-phenylacrylonitrile and their derivatives, (E)-2-benzoyl-3-(substituted phenyl)acrylonitriles, which possess a linear β-phenyl-α,β-unsaturated carbonyl scaffold have been intensively used for anti-tyrosinase activity and melanogenesis and do not display cytotoxic effects [1]. Two of the copper-containing series, namely $Mg_{1.2}Ni_aCu_bAl(OH)_6(CO_3)_{0.5}$ (a+b=0.8) and $A_2Al(OH)_6(CO_3)_{0.5}$ (where A is Ni or Cu) were calcined and transformed in their coresponding mixed oxides which were further used as catalysts for Payne oxidation reactions which combine an environmentally friendly oxidation agent (H_2O_2) with a nitrile co-reagent in order to obtain a selective conversion of cyclohexene to cyclohexene epoxide, a versatile intermediate used for the preparation of a variety of chemical products, such as pharmaceuticals and fragrances [2]. Selective oxidation faces many challenges, especially regarding the control of the selectivity to the desired product but it compensates with the many opportunities that it brings to chemical manufacturing [3,4]. The oxidative conversions of olefines to their corresponding epoxides or diols are intensively studied both at the laboratory and industrial level, respectively due to economic reasons and the versatile structure with double functionality of alkenes [4]. Due to its high efficiency and green character, hydrogen peroxide can successfully be used as the oxidation agent in such reactions. Payne has demonstrated that olefines combined with hydrogen peroxide, a cyano compound and a suitable basic catalyst can lead to epoxides [3]. The novelty of this work consists in the fact that there are no records in the literature about any NiCu layered double hydroxides used as catayst in tandem reactions or as catalyst precursor for the Payne oxidation of cyclohexene to cyclohexene epoxide. There are not many studies that talk about the catalytic activity of MgNi(Co)Al

compounds either. Most of them are used for electrochemical studies. However, Zhou and his co-workers [1] have prepared Ni_2Co-LDH and tested it in the aerobic oxidation/condensation tandem reaction between alcohols and active methylene compounds. They have tried different solvents and chose toluene as the best one. Between the solvents used, benzene was not on the list. The results obtained revealed a maximum conversion of benzyl alcohol of 90%, using toluene as a solvent.

5.2. Synthesis of the MgNiCuAl LDH materials

5.2.1. Synthesis of $Mg_{1.2}Ni_aCu_bAl(OH)_6(CO_3)_{0.5}$ (a+b=0.8)

Three solids modified with different Ni: Cu ratios but with the M^{2+}/M^{3+} = 2 as in the following formula $Mg_{1.2}Ni_aCu_bAl(OH)_6(CO_3)_{0.5}$ (a+b=0.8) were prepared via the co-precipitation method which implies the mixing of two different solutions at a constant value of pH=10. The first solution contains the precursor metallic salts, namely $Ni(NO_3)_2{\cdot}6H_2O$, $Cu(NO_3)_2{\cdot}6H_2O$, $Mg(NO_3)_2{\cdot}6H_2O$, $Al(NO_3)_3{\cdot}9H2O$ (all of the chemical purity grade, purchased from Merck), having a concentration of the cations of 1 M, respecting the molar ratios. The second solution was obtained by dissolving 205 mmol NaOH and 155.7 mmol Na_2CO_3 in 170 mL distilled water (NaOH and Na_2CO_3 purchased from Merck).

The exact amounts of the reagents used for each prepared solid are the following:

- For **$Mg_{1.2}Ni_{0.6}Cu_{0.2}Al(OH)_6(CO_3)_{0.5}$** (denoted as **HT-$Mg_{1.2}Ni_{0.6}Cu_{0.2}Al$**):

The first solution was prepared by dissolving 34.4 mmol $Ni(NO_3)_2{\cdot}6H_2O$, 12.4 mmol, $Cu(NO_3)_2{\cdot}6H_2O$, 70.2 mmol $Mg(NO_3)_2{\cdot}6H_2O$ and 58.7 mmol $Al(NO_3)_3{\cdot}9H_2O$ in 148.5 mL distilled water.

- For **$Mg_{1.2}Ni_{0.4}Cu_{0.4}Al(OH)_6(CO_3)_{0.5}$** (denoted as **HT-$Mg_{1.2}Ni_{0.4}Cu_{0.4}Al$**):

The first solution was prepared by dissolving 20.6 mmol $Ni(NO_3)_2{\cdot}6H_2O$, 24.8 mmol, $Cu(NO_3)_2{\cdot}6H_2O$, 70.2 mmol $Mg(NO_3)_2{\cdot}6H_2O$ and 58.7 mmol $Al(NO_3)_3{\cdot}9H_2O$ in 149.3 mL distilled water.

- For **$Mg_{1.2}Ni_{0.2}Cu_{0.6}Al(OH)_6(CO_3)_{0.5}$** (denoted as **HT-$Mg_{1.2}Ni_{0.2}Cu_{0.6}Al$**).

The first solution was prepared by dissolving 13.8 mmol $Ni(NO_3)_2{\cdot}6H_2O$, 33.1 mmol, $Cu(NO_3)_2{\cdot}6H_2O$, 70.2 mmol $Mg(NO_3)_2{\cdot}6H_2O$ and 58.7 mmol $Al(NO_3)_3{\cdot}9H_2O$ in 149.6 mL distilled water.

The precipitation reactor placed on the stirring plate was first filled with 100 mL of distilled water. After the pH is adjusted to 10 using the base solution, the two solutions are added dropwise simultaneously under intense stirring, at room temperature. Once the two solutions are mixed, the precipitation reactor is transferred on a heating stirring plate letting the

obtained gel age at 75º C for 18 h. The gel is then filtrated and washed with distilled water until the conductivity of the washing water is below 100 μS/cm. The next step consists in drying the solids in an oven at 90ºC for 24h. The compounds obtained were further calcined for 18h at 460ºC resulting the next solids CHT-Mg1.2Ni0.6Cu0.2, CHT-Mg1.2Ni0.4Cu0.4, and CHT-Mg1.2Ni0.2Cu0.6, respectively.

5.2.2. Synthesis of $Mg_{0.8}Ni_cCu_dAl(OH)_6(CO_3)_{0.5}$ (c+d=1.2)

Three solids modified with different Ni: Cu ratios but with the M^{2+}/M^{3+} = 2 as in the following formula $Mg_{0.8}Ni_cCu_dAl(OH)_6(CO_3)_{0.5}$ (c+d=1.2) were also prepared using the co-precipitation method, which was thoroughly described above. The second solution, B, for every preparation was obtained by dissolving 205 mmol NaOH and 155.7 mmol Na_2CO_3 in 170 mL of distilled water.

The exact amounts of the reagents used for each prepared solid are the following:

- For **$Mg_{0.8}Ni_{0.8}Cu_{0.4}Al(OH)_6(CO_3)_{0.5}$** (denoted as **HT-$Mg_{0.8}Ni_{0.8}Cu_{0.4}Al$**):

The first solution was prepared by dissolving 48.2 mmol $Ni(NO_3)_2{\cdot}6H_2O$, 24.8 mmol, $Cu(NO_3)_2{\cdot}6H_2O$, 46.8 mmol $Mg(NO_3)_2{\cdot}6H_2O$ and 58.7 mmol $Al(NO_3)_3{\cdot}9H_2O$ in 148.9 mL distilled water.

- For **$Mg_{0.8}Ni_{0.6}Cu_{0.6}Al(OH)_6(CO_3)_{0.5}$** (denoted as **HT-$Mg_{0.8}Ni_{0.6}Cu_{0.6}Al$**):

The first solution was prepared by dissolving 34.4 mmol $Ni(NO_3)_2{\cdot}6H_2O$, 37.3 mmol, $Cu(NO_3)_2{\cdot}6H_2O$, 46.8 mmol $Mg(NO_3)_2{\cdot}6H_2O$ and 58.7 mmol $Al(NO_3)_3{\cdot}9H_2O$ in 149.7 mL distilled water.

- For **$Mg_{0.8}Ni_{0.4}Cu_{0.8}Al(OH)_6(CO_3)_{0.5}$** (denoted as **HT-$Mg_{0.8}Ni_{0.4}Cu_{0.8}Al$**):

The first solution was prepared by dissolving 20.6 mmol $Ni(NO_3)_2{\cdot}6H_2O$, 49.7 mmol, $Cu(NO_3)_2{\cdot}6H_2O$, 46.8 mmol $Mg(NO_3)_2{\cdot}6H_2O$ and 58.7 mmol $Al(NO_3)_3{\cdot}9H_2O$ in 150.5 mL distilled water. The solutions were mixed and the obtained gel was further washed, filtered and dried as described in the previous case.

5.3. Synthesis of the MgNiCoAl LDH materials

5.3.1. Synthesis of $Mg_{1.2}Ni_aCo_bAl(OH)_6(CO_3)_{0.5}$ (a + b = 0.8)

Three solids with different Ni:Co ratios but with the M^{2+}/M^{3+} ratio fixed to 2, as in the following formula $Mg_{1.2}Ni_aCo_bAl(OH)_6(CO_3)_{0.5}$ (a+b = 0.8), were prepared by the co-precipitation method which implies the mixing of two different solutions at a constant value of pH = 10. The first solution contains the precursor metallic salts, namely $Ni(NO_3)_2{\cdot}6H_2O$, $Co(NO_3)_2{\cdot}6H_2O$, $Mg(NO_3)_2{\cdot}6H_2O$ and $Al(NO_3)_3{\cdot}9H_2O$ (all of the chemical purity grade, purchased from Merck), having a concentration of the cations of 1 M, respecting the desired

molar ratio. The second one is prepared by dissolving NaOH and Na_2CO_3 (chemical purity grade, purchased from Merck), in distilled water.

The exact amounts of the reagents used for each prepared solid are the following:

- For $Mg_{1.2}Ni_{0.6}Co_{0.2}Al(OH)_6(CO_3)_{0.5}$ (denoted as HT-$Mg_{1.2}Ni_{0.6}Co_{0.2}Al$):

The first solution was prepared by dissolving 34.4 mmol $Ni(NO_3)_2{\cdot}6H_2O$, 13.7 mmol $Co(NO_3)_2{\cdot}6H_2O$, 70.2 mmol $Mg(NO_3)_2{\cdot}6H_2O$ and 58.7 mmol $Al(NO_3)_3{\cdot}9H_2O$ in 147.7 mL distilled water.

- For $Mg_{1.2}Ni_{0.4}Co_{0.4}Al(OH)_6(CO_3)_{0.5}$ (denoted as $Mg_{1.2}Ni_{0.4}Co_{0.4}Al$):

The first solution was prepared by dissolving 20.6 mmol $Ni(NO_3)_2{\cdot}6H_2O$, 20.6 mmol $Co(NO_3)_2{\cdot}6H_2O$, 70.2 mmol $Mg(NO_3)_2{\cdot}6H_2O$ and 58.7 mmol $Al(NO_3)_3{\cdot}9H_2O$ in 148.5 mL distilled water.

- For $Mg_{1.2}Ni_{0.2}Co_{0.6}Al(OH)_6(CO_3)_{0.5}$ (denoted as $Mg_{1.2}Ni_{0.2}Co_{0.6}Al$):

The first solution was prepared by dissolving 13.8 mmol $Ni(NO_3)_2{\cdot}6H_2O$, 34.4 mmol $Co(NO_3)_2{\cdot}6H_2O$, 70.2 mmol $Mg(NO_3)_2{\cdot}6H_2O$ and 58.7 mmol $Al(NO_3)_3{\cdot}9H_2O$ in 147.7 mL distilled water.

The second solution for every preparation was obtained by dissolving 305 mmol NaOH and 155.7 mmol Na_2CO_3 in 170 mL distilled water.

The precipitation reactor placed on the stirring plate was first filled with 100 mL of distilled water. The two solutions are added dropwise simultaneously under vigorous stirring at room temperature. Once the two solutions are mixed, the precipitation reactor is transferred on a heating stirring plate, letting the obtained precipitate age at 75 ºC for 18 h. The solid is then filtrated and washed with distilled water until the conductivity of the washing water is below 100 µS/cm. The next step consists in drying the solids in an oven at 90ºC for 24h.

5.3.2. Synthesis of $Mg_{0.8}Ni_cCo_dAl(OH)_6(CO_3)_{0.5}$ (c + d = 1.2)

Three solids with different Ni:Co ratios but with the M^{2+}/M^{3+} ratio fixed to 2, as in the following formula $Mg_{0.8}Ni_cCo_dAl(OH)_6(CO_3)_{0.5}$ (c + d = 1.2), were also prepared using the co-precipitation method, which was thoroughly described above.

The exact amounts of the reagents used for each prepared solid are the following:

- For $Mg_{0.8}Ni_{0.8}Co_{0.4}Al(OH)_6(CO_3)_{0.5}$ (denoted as $Mg_{0.8}Ni_{0.8}Co_{0.4}Al$):

The first solution was prepared by dissolving 48.2 mmol $Ni(NO_3)_2{\cdot}6H_2O$, 20.6 mmol $Co(NO_3)_2{\cdot}6H_2O$, 46.8 mmol $Mg(NO_3)_2{\cdot}6H_2O$ and 58.7 mmol $Al(NO_3)_3{\cdot}9H_2O$ in 148 mL distilled water.

- For $Mg_{0.8}Ni_{0.6}Co_{0.6}Al(OH)_6(CO_3)_{0.5}$ (denoted as $Mg_{0.8}Ni_{0.6}Co_{0.6}Al$):

The first solution was prepared by dissolving 34.4 mmol $Ni(NO_3)_2 \cdot 6H_2O$, 34.4 mmol $Co(NO_3)_2 \cdot 6H_2O$, 46.8 mmol $Mg(NO_3)_2 \cdot 6H_2O$ and 58.7 mmol $Al(NO_3)_3 \cdot 9H_2O$ in 148 mL distilled water.

- For $Mg_{0.8}Ni_{0.4}Co_{0.8}Al(OH)_6(CO_3)_{0.5}$ (denoted as $Mg_{0.8}Ni_{0.4}Co_{0.8}Al$):

The first solution was prepared by dissolving 20.6 mmol $Ni(NO_3)_2 \cdot 6H_2O$, 48.1 mmol $Co(NO_3)_2 \cdot 6H_2O$, 46.8 mmol $Mg(NO_3)_2 \cdot 6H_2O$ and 58.7 mmol $Al(NO_3)_3 \cdot 9H_2O$ in 148 mL distilled water. The second solution for every sample was obtained by dissolving 305 mmol NaOH and 155.7 mmol Na_2CO_3 in 170 mL distilled water.

The solutions were mixed, and the obtained precipitate was further washed, filtered and dried as described in the previous case.

5.4. Synthesis of the solids containing one of the bivalent cations, namely HT-Ni_2Al, HT-Cu_2Al and HT-Co_2Al

To check the existence of a synergetic effect between the nickel and copper or cobalt cations, different solids with the same M^{2+}/Al^{3+} ratio but containing only one of the divalent cations (Ni or Cu or Co), namely HT-Ni_2Al, HT-Cu_2Al and HT-Co_2Al were synthesized using again the co-precipitation method described above,

The exact amounts of the reagents used for each prepared solid are the following:

- For **HT-Ni_2Al**:

The first solution was prepared by dissolving 103.2 mmol $Ni(NO_3)_2 \cdot 6H_2O$ and 50.7 mmol $Al(NO_3)_3 \cdot 9H_2O$ in 130.6 mL distilled water. The second solution was obtained by dissolving 177.5 mmol NaOH and 134.9 mmol Na_2CO_3 in 150 mL distilled water.

- For **HT-Cu_2Al**:

The first solution was prepared by dissolving 115.9 mmol, $Cu(NO_3)_2 \cdot 6H_2O$ and 58.7 mmol $Al(NO_3)_3 \cdot 9H_2O$ in 154.2 mL distilled water.

- For **HT-Co_2Al**:

The first solution was prepared by dissolving 110 mmol $Co(NO_3)_2 \cdot 6H_2O$ and 54.4 mmol $Al(NO_3)_3 \cdot 9H_2O$ in 139.3 mL distilled water. The second solution was obtained by dissolving 190 mmol NaOH and 145 mmol Na_2CO_3 in 160 mL distilled water.

The two solutions were treated as described above. The compounds HT-Ni_2Al, HT-Cu_2Al were further calcined for 18h at 460ºC resulting the next solids CHT-Ni_2Al and CHT-Cu_2Al.

5.5. Characterization of the materials

5.5.1. Characterization of the MgNiCuAl LDH solids

The characterization of the hydrotalcite-type solids included X-Ray diffraction of powders (XRD), scanning electron microscopy (SEM), XRF, BET, basicity and acidity measurements, diffuse reflectance infrared Fourier-transform spectroscopy (DRIFT) and DR-UV-VIS. The cationic composition of the LDH solids determined by XRF together with the M/Al atomic ratios (M = Mg, Ni and/or Cu) can be seen in Table 1. First, these results confirm the chemical modification of the layered double hydroxides with Ni and Cu cations. The obtained values indicate that the Mg/Al ratio is slightly smaller than expected, probably due to the incomplete precipitation of magnesium during the synthesis step. This effect is more discernable for the samples with a smaller amount of Mg and greater amount of Cu, i.e., HT-$Mg_{0.8}Ni_{0.6}Cu_{0.6}Al$ and HT-$Mg_{0.8}Ni_{0.4}Cu_{0.8}Al$. For the latter and for HT-Cu_2Al, the Cu/Al atomic ratios are slightly higher than the theoretical values, while they are close to the calculated values for the other samples. At the same time, the Ni/Al atomic ratios are close to the theoretical values for all the Mg-containing samples, being slightly higher for HT-Ni_2Al sample.

Table 1: Elemental composition determined by XRF.

Catalyst	Elemental composition				Mg/Al atomic ratio	Ni/Al atomic ratio	Cu/Al atomic ratio
	Mg^{2+} [wt%]	Al^{3+} [wt%]	Ni^{2+} [wt%]	Cu^{2+} [wt%]			
HT-$Mg_{1.2}Ni_{0.6}Cu_{0.2}Al$	7.39	7.64	9.96	4.07	1.09	0.60	0.23
HT-$Mg_{1.2}Ni_{0.4}Cu_{0.4}Al$	7.26	7.49	5.97	7.62	1.09	0.36	0.43
HT-$Mg_{1.2}Ni_{0.2}Cu_{0.6}Al$	7.84	7.84	4.01	10.39	1.13	0.23	0.56
HT-$Mg_{0.8}Ni_{0.8}Cu_{0.4}Al$	5.35	7.64	13.78	7.72	0.79	0.83	0.43
HT-$Mg_{0.8}Ni_{0.6}Cu_{0.6}Al$	4.32	6.93	9.74	11.24	0.70	0.64	0.69
HT-$Mg_{0.8}Ni_{0.4}Cu_{0.8}Al$	4.03	7.17	6.03	15.63	0.63	0.39	0.93
HT-Ni_2Al	-	6.93	33.16	-	-	2.2	-
HT-Cu_2Al	-	5.99	-	33.77	-	-	2.39

The results of the acidity and basicity measurements are tabulated in Table 2. It can be observed that all the samples present both acidic and basic sites, but as expected, the number of acid sites is sensibly lower than that of base sites. In both Mg-containing series, i.e., HT-$Mg_{1.2}Ni_aCu_bAl$ and HT-$Mg_{0.8}Ni_cCu_dAl$, the total number of base sites increases, while that of acid sites decreases with increasing the Cu content at the expense of Ni. The unexpectedly high basicity found in the HT-Cu_2Al sample is thought to be caused by the XRD-detected $Cu_2(CO_3)(OH)_2$-malachite side-phase impurities. Since Ni^{2+} (1.91) and Cu^{2+} (1.91) on the

Pauling scale have identical electronegativity values [5], the so-called Jahn-Teller effect, which copper cations exhibit, is crucial to catalytic activity [6]. This action leads to distortion of the octahedral coordination structure of the LDH, which raises surface energy. As a result, there is a small increase in catalytic activity.

Table 2. Acidity, basicity and textural properties of the hydrotalcite-like samples.

Sample	Total acidity (mmol Py g^{-1})	Total basicity (mmol acrylic acid g^{-1})	Base sites/acid sites ratio	Surface area ($m^2 g^{-1}$)	Pore volume ($cm^3 g^{-1}$)	Pore size (nm)
HT-$Mg_{1.2}Ni_{0.6}Cu_{0.2}Al$	0.055	2.3	41.8	160	0.41	7.79
HT-$Mg_{1.2}Ni_{0.4}Cu_{0.4}Al$	0.051	2.6	51.0	163	0.42	6.19
HT-$Mg_{1.2}Ni_{0.2}Cu_{0.6}Al$	0.049	2.8	57.1	149	0.33	8.72
HT-$Mg_{0.8}Ni_{0.8}Cu_{0.4}Al$	0.070	0.9	12.9	130	0.18	3.86
HT-$Mg_{0.8}Ni_{0.6}Cu_{0.6}Al$	0.065	1.9	29.2	169	0.39	7.21
HT-$Mg_{0.8}Ni_{0.4}Cu_{0.8}Al$	0.060	2.1	35.0	132	0.27	0.86
HT-Ni_2Al	0.073	1.9	26.0	144	0.66	0.89
HT-Cu_2Al	0.025	7.2	288.0	57	0.19	0.84

Additionally, the isomorphic substitution in the brucite-like layer octahedral locations, which is influenced by the ionic radius of Cu^{2+} (0.73), which is close to that of Mg^{2+} (0.72) and larger than that of Ni^{2+} (0.69), should be taken into consideration [7]. The specific surface area, the pore volume, and the pore size of the prepared samples are presented in Table 2. Their corresponding pore size distributions and adsorption-desorption isotherms are shown in Figure 1 and Figure 2, respectively. According to the IUPAC classification, the solids reveal type IV isotherms specific to mesoporous materials. All the MgNiCuAl-type compounds present an H2b-type hysteresis loop characteristic for narrow slit-like mesopores which can present a fine bottleneck with one side almost closed or double side open [8,9]. Additionally, these samples frequently combine cylinder-shaped pores with parallel plate-shaped pores [9]. This resemblance can be associated to the similar aspect of the SEM images corresponding to the samples with quaternary composition. The HT-Ni_2Al exhibit an H1-type hysteresis loop specific to a narrow range of uniform mesopore [8]. The type H1 loop is also associated with materials that agglomerate, forming spheres spread in an uniform array [10]. This information is confirmed by the SEM image (Figure 10) of the solid HT-Ni_2Al. The HT-Cu_2Al presents an H3-type loop given by aggregates of plate-like particles, as confirmed by the SEM images.

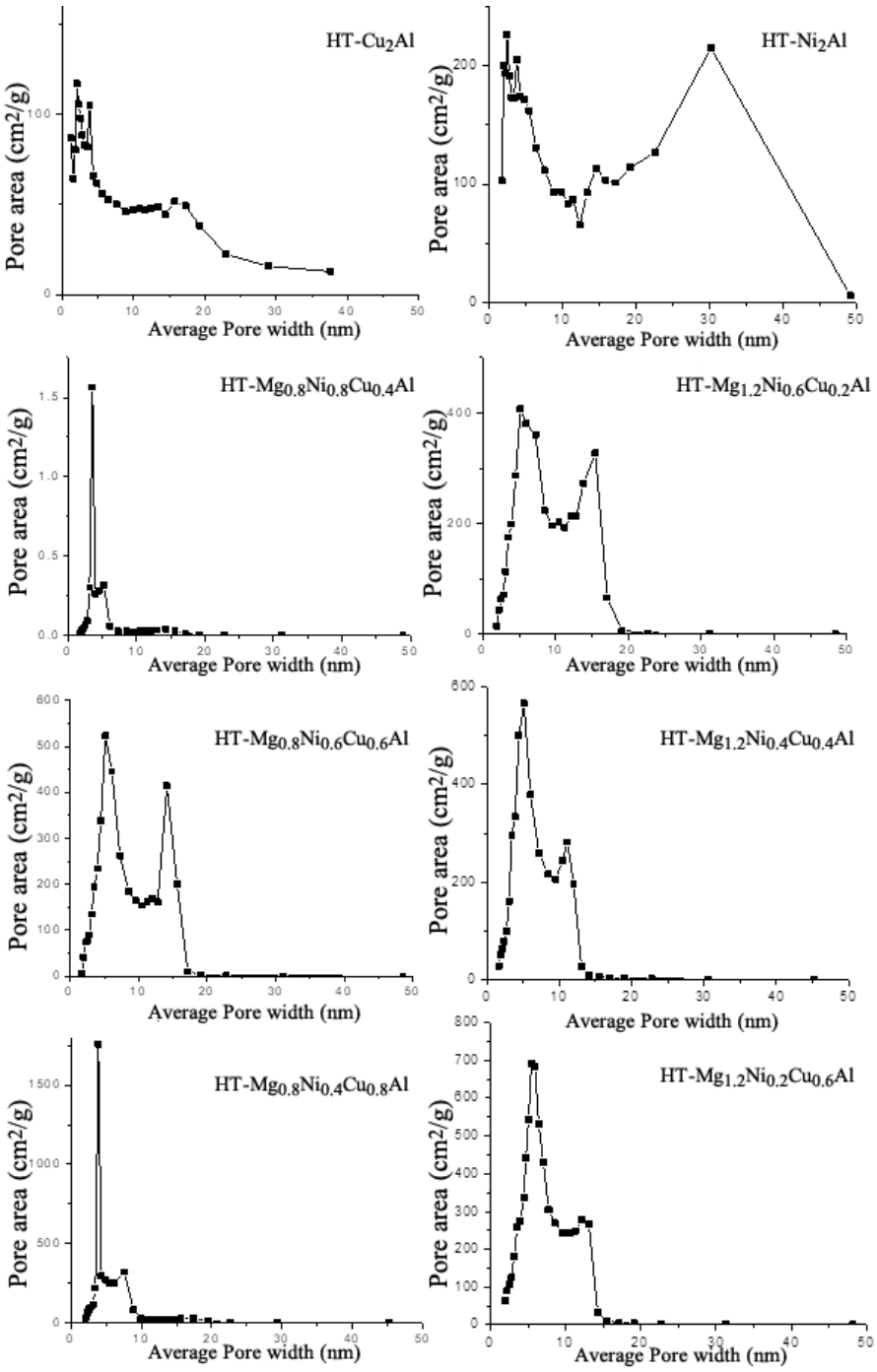

Figure 1. Pore area distributions of the samples.

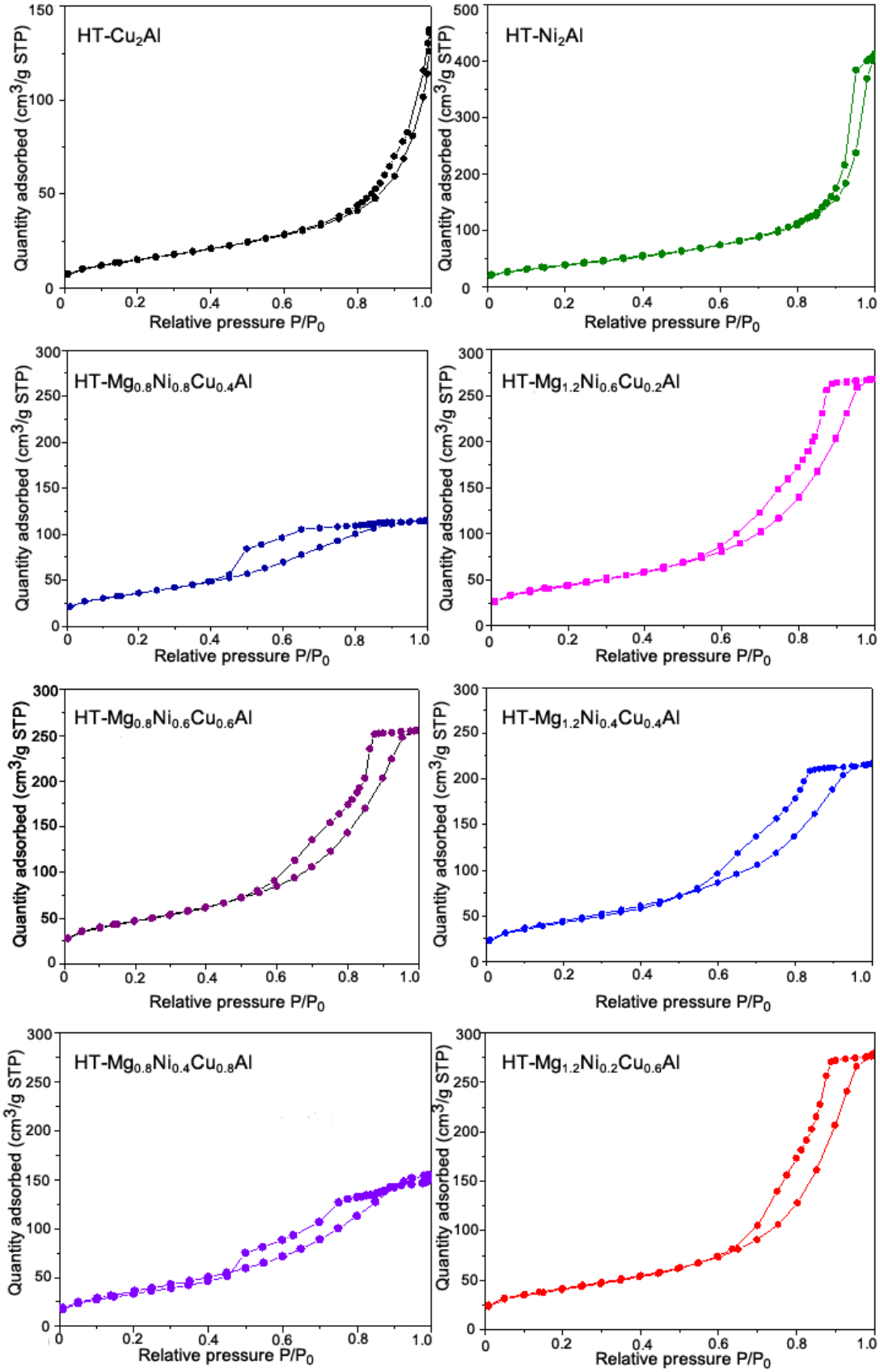

Figure 2. Nitrogen adsorption-desorption isotherms of the prepared samples.

The XRD patterns of the Mg-containing materials, i.e., HT-$Mg_{1.2}Ni_aCu_bAl$ and HT-$Mg_{0.8}Ni_cCu_dAl$, (Figure 3) have the characteristics of a typical well crystallized single hydrotalcite-like phase, with sharp, symmetric and intense diffraction lines at low 2θ angular values and less intense, asymmetric lines, at higher 2θ angular values (ICDD card no.01-089-5434). HT-Ni_2Al pattern matches the Ni,Al-LDH phase (ICDD card no. 04-018-1341), while in the HT-Cu_2Al pattern, besides the Cu,Al-LDH phase (ICDD card no.00-037-0630), lines corresponding to a monoclinic $Cu_2(CO_3)(OH)_2$-malachite side-phase (ICDD card no. 00-056-0001) can be identified. All the layered phase reflections were indexed to a hexagonal lattice with an *R3m* rhombohedral symmetry. Lattice parameters *a* (average distance between two cations in the layers, $a = 2d_{110}$) and *c* (three times the distance between two layers, $c = 3d_{003}$) were calculated from their (110) and (003) diffraction lines and were gathered in Table 3.

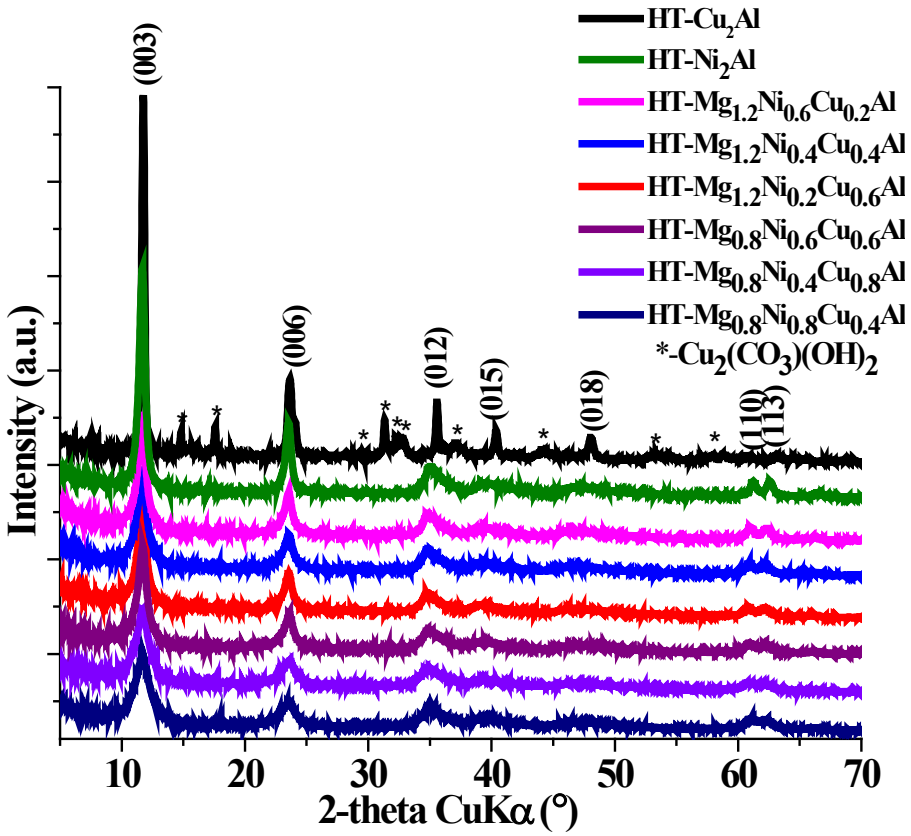

Figure 3. The XRD spectra of the HT-$Mg_{1.2}Ni_aCu_bAl$, HT-$Mg_{0.8}Ni_cCu_dAl$, HT-Ni_2Al and HT-Cu_2Al materials.

The sensitivity of parameter *a* to the nature of layer cations is exposed in Figure 4. Based on the proportion of the metal components, as revealed by XRF measurements (Table 1), and on their Shannon ionic radii: 0.72, 0.73, 0.69 and 0.535 Å for Mg^{2+}, Cu^{2+}, Ni^{2+} and Al^{3+}, respectively, an average ionic radius of the layer cations, r(Me,Al), was determined for each

solid (Table 3). Indeed, as shown in Figure 4, the *a* lattice parameter values are proportional to the cationic composition of the solids, except for the HT-Cu_2Al solid, which contains a side-phase (malachite). The correlation of the *a*-parameter value with the apparent composition of the ternary LDH emphasizes the effective substitution of the Mg^{2+} by Ni^{2+} and Cu^{2+} and is an indication that other non-LDH phases are absent.

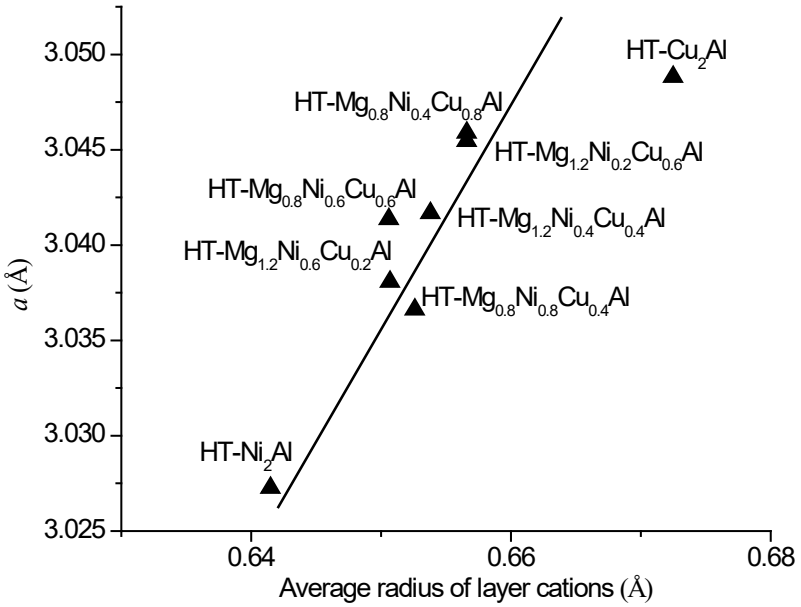

Figure 4. The linear relationship between the cationic composition of the brucite-like layers (average cations radius) and the lattice parameter *a*.

The *c* lattice parameter values, determined by the nature and orientation of the interlayer anions, are nearly identical for all materials, except for HT-Cu_2Al. This can be explained taking into consideration that, on the one hand, the Me/Al atomic ratios are roughly the same for all the solids and, on the other hand, as the DRIFT spectra indicate only carbonates, OH groups and water are present in the interlayer spaces. Due to the presence of the malachite impurity phase, the smaller Cu/Al atomic ratio of the Cu,Al-LDH phase in the HT-Cu_2Al solid leads to stronger electrostatic interactions of the layers with the interlayer anions and stronger hydrogen bonding with the interlayer water molecules and, hence, to a smaller *c* parameter value.

Crystallite sizes along the normal to the layers, D_{003}, and in the plane of the layers, D_{110}, were calculated with the Scherrer formula using the full width at half maximum (FWHM) of the (003) and (110) diffraction lines, respectively, the values obtained being tabulated in Table 3. As expected, the largest crystalline domain sizes of the brucite-like layer are attained in the solids with only one divalent transition-metal cation, i.e., HT-Ni_2Al and HT-Cu_2Al, respectively. For the quaternary hydrotalcite-like materials, there is an evident disorder effect

due to the isomorphous substitution of Mg^{2+} by Ni^{2+} and Cu^{2+}, in particular for the HT-$Mg_{0.8}Ni_cCu_dAl$ series characterized by a higher degree of substitution [11-13]. The brucite-like sheet disorder induces a smaller long-range order along the *c*-axis due mainly to the presence of stacking faults, reflected in the D_{003} values, and to turbostratic distortions, reflected by the large and asymmetric broadness of the (0*kl*) reflections in the medium 2-theta angular domain. Table 3 shows the values of FWHM of the (015) reflection as a marker of turbostraticity effect. Linear relationships between the crystalline domain sizes, i.e., D_{003} vs D_{001}, on one hand, and between the turbostraticity ($FWHM_{015}$) and the crystalline domain size inside the brucite-like layer (D_{110}), on the other hand, can be observed (Figures 5 and 6).

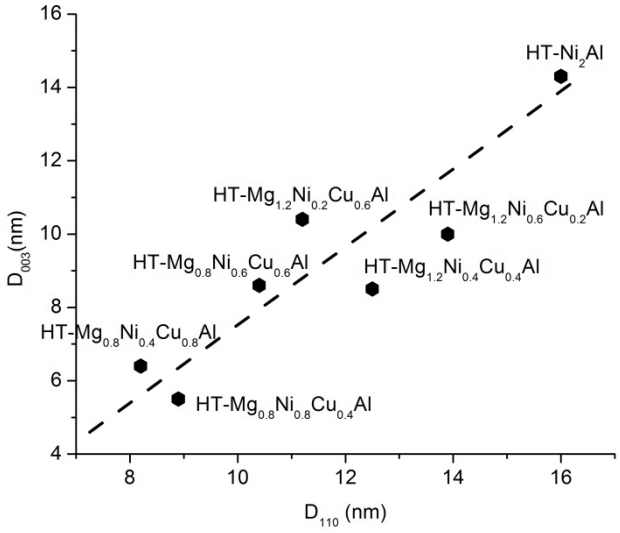

Figure 5. Correlation between the crystalline domain sizes: inside brucite-like layer (D_{110}) and along the layers stacking direction, *c* (D_{003}).

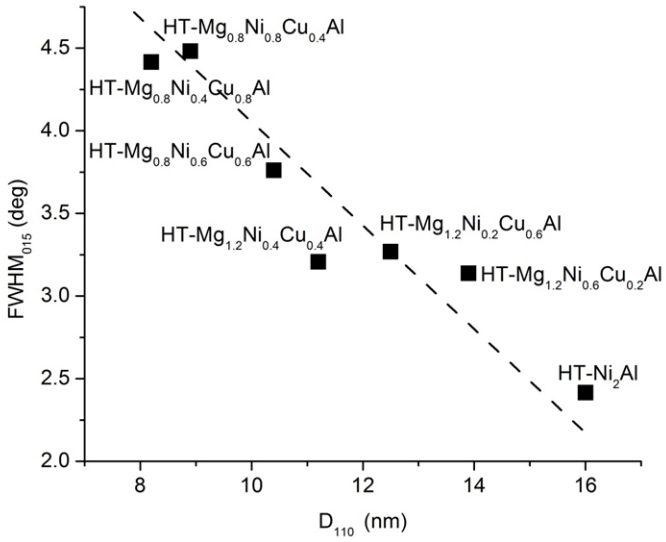

Figure 6. Correlation between the crystalline domain size inside the brucite-like layer (D_{110}) and turbostraticity ($FWHM_{015}$).

Stacking faults and turbostratic distortion have been associated with a mismatch in the geometries of layers and interlayer anions, which prevents an ideal packing of the layers or local distortions within slabs due to the microstrain arising from the distribution of electrostatic charges [14,15]. This is likely the case of the quaternary hydrotalcite-like solids. These results are to be correlated with the textural properties of the as-prepared materials: relative large surface areas (Table 2) and the proportionality of the D_{003} values, indicative of the long-range order along layers stacking direction, with the pore volumes (Figure 7).

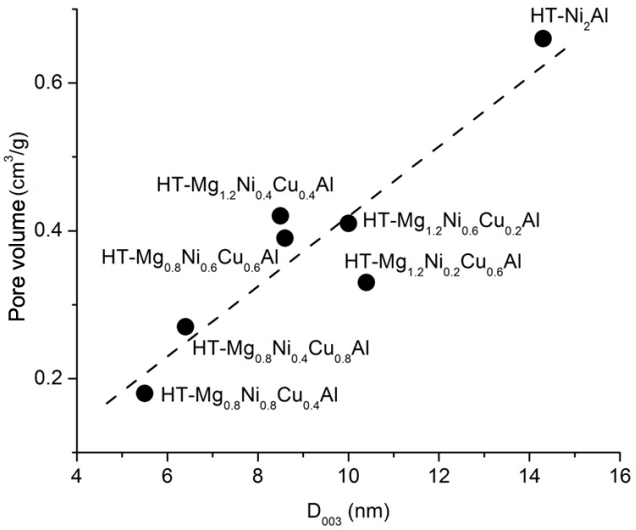

Figure 7. Correlation between the crystalline domain size along the layers stacking direction (D_{003}) and the pore volume.

Notably, as previously mentioned, the HT-Cu_2Al material is apart due to the Jahn-Teller distortion effect of copper, which is responsible for the presence of a side-phase and a different LDH-phase pattern shape with preferred orientation in the *c*-direction. This is consistent with the acicular forms observed in the SEM image (Figure 10).

Table 3. Structural data of the hydrotalcite-like compounds.

LDH material	**r(Me,Al) (Å)**	***a* (Å)**	***c* (Å)**	**D_{003} (nm)**	**D_{110} (nm)**	**$FWHM_{015}$ (deg)**
HT-$Mg_{1.2}Ni_{0.6}Cu_{0.2}Al$	0.651	3.038	22.749	10.0	13.9	3.138
HT-$Mg_{1.2}Ni_{0.4}Cu_{0.4}Al$	0.654	3.042	22.749	8.5	12.5	3.269
HT-$Mg_{1.2}Ni_{0.2}Cu_{0.6}Al$	0.657	3.046	22.747	10.4	11.2	3.207
HT-$Mg_{0.8}Ni_{0.8}Cu_{0.4}Al$	0.653	3.037	22.767	5.5	8.9	4.481
HT-$Mg_{0.8}Ni_{0.6}Cu_{0.6}Al$	0.651	3.041	22.716	8.6	10.4	3.761
HT-$Mg_{0.8}Ni_{0.4}Cu_{0.8}Al$	0.657	3.046	22.716	6.4	8.2	4.415
HT-Ni_2Al	0.642	3.027	22.734	14.3	16.0	2.415
HT-Cu_2Al[a]	0.673	3.049	22.599	29.0	11.5	0.340

[a] Also contains a $Cu_2(CO_3)(OH)_2$-malachite side-phase.

On the other hand, it is noteworthy that the presence of some amorphous phase could not be completely ruled out. The intensity of (110) reflection, related only to the brucite-like layer, is an indicative of the amount of LDH crystalline phase, which includes ordered stacked layers as well as delaminated layers. The amount of amorphous material is expected to affect the textural properties by its deposition inside the pores. Indeed, a linear correlation has been found between the intensity of the (110) reflection and the pore volume: the HT-Ni_2Al material, which contains the least amorphous phase exhibits the highest pore volume (Figure 7).

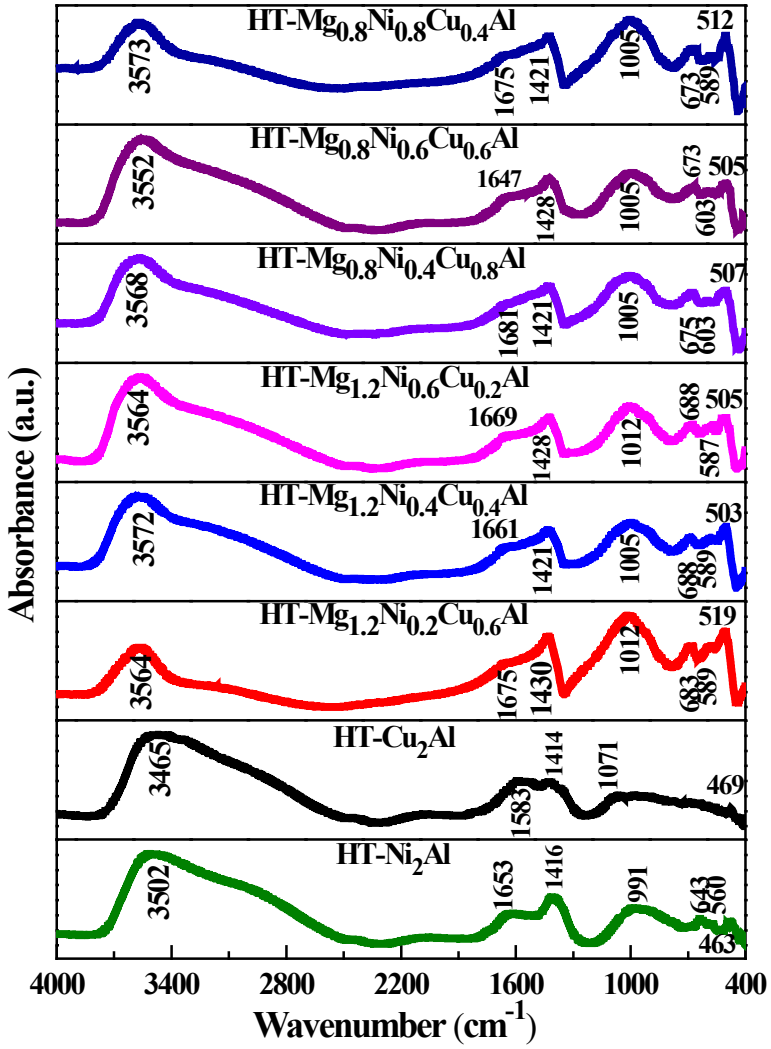

Figure 8. DRIFT spectra of the LDH solids.

To determine the nature and the symmetry of the anions present in the interlayer space and the existence of any impurity phases, the DRIFT spectra shown in Figure 8 were recorded. All the hydrotalcite-like samples showed an intense broad band between ca. 3800 and 3000 cm^{-1} attributed to the hydroxyl stretching mode characteristic for the layer OH groups and interlayered water molecules. A weak shoulder around 3000 cm^{-1} appeared in all the cases

ascribed to the OH stretching mode resulting from the interaction through hydrogen bonds between the water molecules and carbonate anions present in the interlayer region [16]. The weak band at around 1600 cm^{-1} is specific for the bending mode of water molecules. The relatively sharp, intense band at about 1000 cm^{-1} is attributed to mode ν_3 antisymmetric stretching of interlayer carbonate. The results confirm the presence of carbonate and the absence of nitrate in the interlayer space of the hydrotalcite-like samples. At lower wavenumber values, i.e., 1000-400 cm^{-1}, there are bands characteristic to O-Metal-O vibrations overlapping [16].

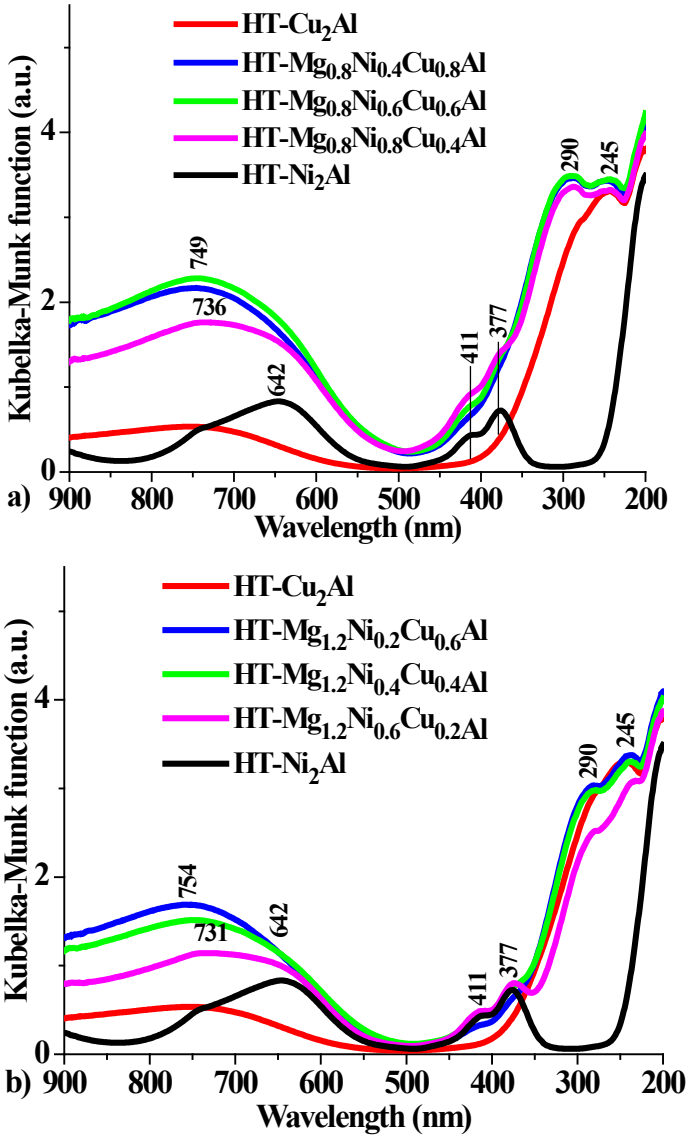

Figure 9. DR-UV-VIS spectra of the LDH samples.

To obtain information about the oxidation states and the stereochemistry of the metallic cations, the LDH samples were analyzed by DR-UV-VIS spectroscopy (Figure 9). The spectra present bands attributed to O^{2-}-M^{2+} charge transfer and d-d transitions characteristic

to the octahedral geometry of the transition-metal divalent cations, Ni^{2+} and Cu^{2+}. For the Ni^{2+} cations, two spin-allowed transitions, namely: $^3A_{2g}(F) \rightarrow {}^3T_{1g}(F)$ and $^3A_{2g}(F) \rightarrow {}^3T_{1g}(P)$, were observed. The band specific for $^3A_{2g}(F) \rightarrow {}^3T_{1g}(F)$ transition splits due to the spin-orbit coupling [17] and it can be found at 750 nm [17], while the band for $^3A_{2g}(F) \rightarrow {}^3T_{1g}(P)$ transition is located at 377 nm. Both bands correspond to Ni^{2+} in octahedral coordination. For all the samples containing Ni cations, some spin-forbidden transitions $^3A_{2g}(F) \rightarrow {}^1E_g(D)$ and $^3A_{2g}(F) \rightarrow {}^1T_{2g}(D)$ (bands at ca. 642 and 411 nm, respectively) were also recorded [17].

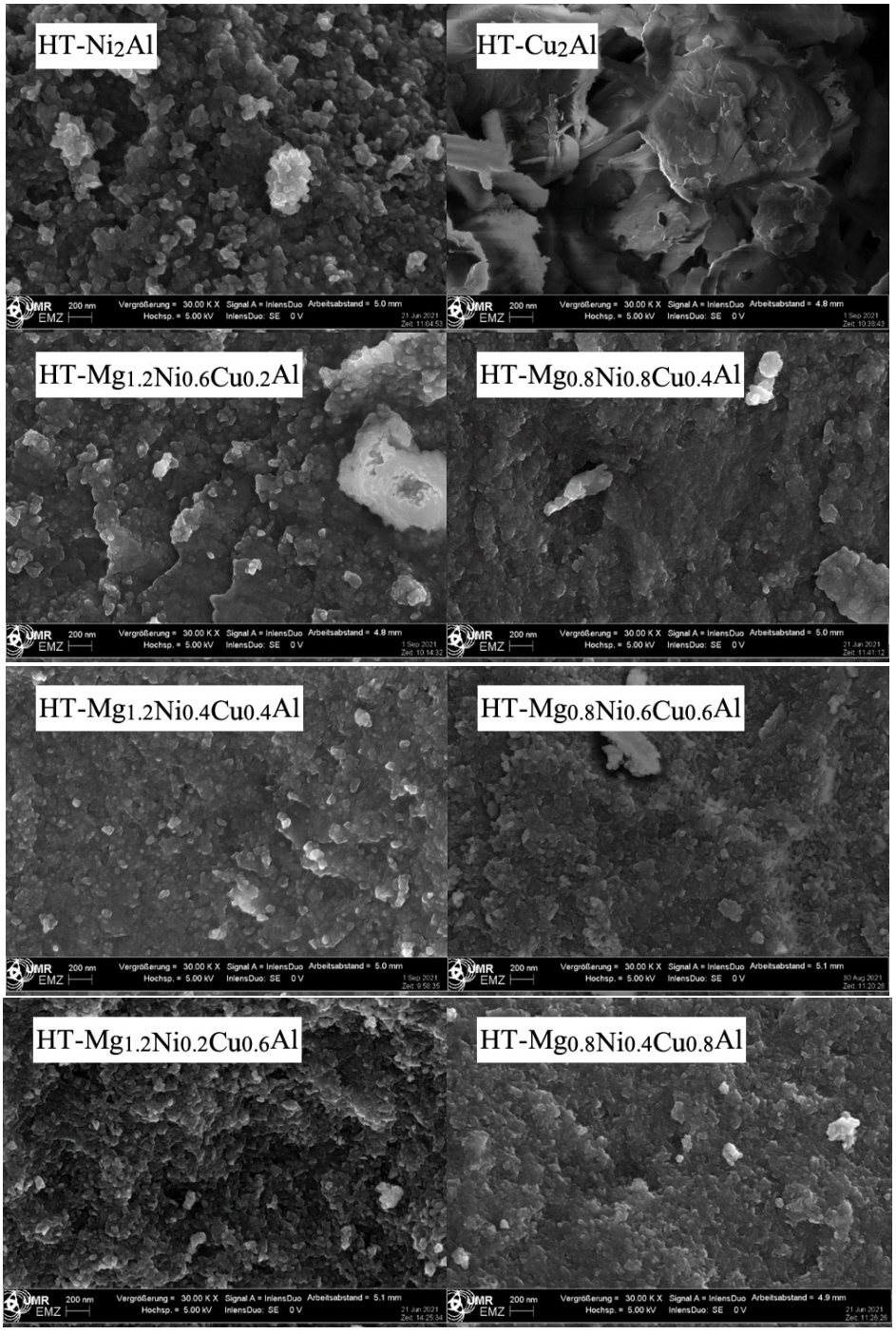

Figure 10. SEM images of the hydrotalcite-like compounds.

In contrast with the Ni-rich solids, the Cu^{2+}-rich LDH samples show wider UV-VIS bands due to an increased structural disorder in line with the XRD measurements. In the spectrum of HT-Cu_2Al sample, only one spin-allowed, Laporte-forbidden transition is observed $^2E_g(D) \rightarrow {}^2T_{2g}(D)$, as expected, which indicates the presence of Cu^{2+} in the octahedral symmetry [18]. The intensity and width of this band, centered at ca. 770 cm^{-1}, are attributed to the distortion of the octahedral coordination of Cu^{2+} due to the Jahn-Teller effect. The bands noticed in the UV region for the samples containing both Ni and Cu cations are ascribed to $O^{2-} \rightarrow M^{n+}$ charge transfer transitions [18]. The SEM images (Figure 10) indicated that the samples are not entirely homogenous. Moreover, it seems like small particles are formed and distributed among larger ones. The increase of the nickel content enables the formation of round particles uniformly distributed. It appears that the ovoidal aspect of the particles is more pronounced in the HT-$Mg_{1.2}Ni_aCu_bAl$ samples compared to the HT-$Mg_{0.8}Ni_cCu_dAl$. In the SEM image of HT-Cu_2Al sample, one can see hexagonal platelets and some rod-like particles that are not recurrent in the samples containing nickel and copper.

5.5.2. Characterization of the MgNiCoAl LDH solids

The characterization of the hydrotalcite-type solids included X-Ray diffraction of powders (XRD), XRF, diffuse reflectance infrared Fourier-transform spectroscopy (DRIFT), acidity measuremnts and DR-UV-VIS.

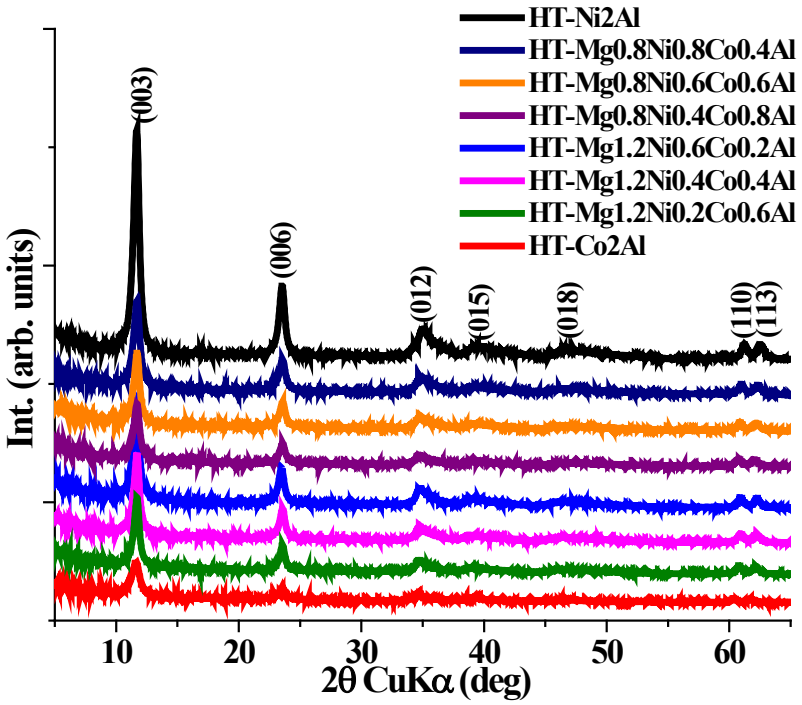

Figure 11. XRD analysis of the different MgNiCoAl LDH samples.

The XRD was used for phase confirmation and for revealing the crystalline structure. The diffraction patterns of the materials exhibit common characteristics and can be seen in Figure 11. For the sample containing only Co and Al, namely HT-Co_2Al, the XRD pattern illustrate the typical hydrotalcite-like structure of Co_6Al_2-$CO_3(OH)_{16}{\cdot}H_2O$ (JCPDS: 51-0045) [19]. Indeed, it shows diffraction lines which can be attributed to the planes (003), (006), (012), (015), (018), (110) and (113), respectively. The XRD pattern of the LDH sample containing only Ni and Al, i.e. HT-Ni_2Al, is assigned to the hydrotalcite-like structure of $Ni_6Al_2(OH)_{16}(CO_3,OH)\cdot 4H_2O$ (JCPDS: 15-0087) [19].

Table 4. Structural data for the different MgNiCoAl LDH compounds.

Sample	Lattice parameters		Crystallite Sizes		I_{003}/I_{110}
	a **(Å)**	***c*** **(Å)**	D_{003} **(nm)**	D_{110} **(nm)**	
HT-$Mg_{1.2}Ni_{0.2}Co_{0.6}Al$	3.047	22.741	15.5	23.9	7.4
HT-$Mg_{1.2}Ni_{0.4}Co_{0.4}Al$	3.042	22.751	14.4	20.0	8.1
HT-$Mg_{1.2}Ni_{0.6}Co_{0.2}Al$	3.041	22.837	14.0	21.8	8.7
HT-$Mg_{0.8}Ni_{0.4}Co_{0.8}Al$	3.049	22.735	14.1	22.0	7.2
HT-$Mg_{0.8}Ni_{0.6}Co_{0.6}Al$	3.043	22.736	14.1	20.0	8.1
HT-$Mg_{0.8}Ni_{0.8}Co_{0.4}Al$	3.039	22.747	12.9	19.9	7.8
HT-Ni_2Al	3.027	22.793	13.9	18.5	13.9
HT-Co_2Al	3.066	22.893	10.4	20.7	8.1

In what concerns the other samples containing different Co/Ni molar ratios, their diffractograms show a similar feature to the diffractions of HT-Co_2Al or HT-Ni_2Al. In addition, the sharp diffraction patterns indicate the high crystallinity of the materials. Interestingly, the (00l) diffraction intensities roughly increase with the increase of Ni-loading correlated with the enhanced crystallinity of the samples. The lattice parameters and the crystallite sizes can be seen in Table 4. The crystallite sizes were calculated along two directions: perpendicular (D_{003}) and parallel (D_{110}) to the brucite-like layers, respectively. The data illustrated in Table 4 show similar structural characteristics for all the samples.

The XRF results in Table 5 show a slight difference between the Mg/Al atomic ratio calculated and that experimentally determined. A possible explanation for this situation is that a part of the magnesium content was lost during the preparation step. The other atomic ratios, namely Ni/Al and Co/Al, are close to the theoretical values. However, for the HT-Ni_2Al and HTCo_2Al samples, the M/Al ratios (M = Ni or Co) are higher than in the solution suggesting the loss of aluminum during the preparation. Regarding the basicity measurement, it can be observed that the samples containing a higher quantity of nickel (HT-

$Mg_{1.2}Ni_{0.6}Co_{0.2}$, HT-$Mg_{0.8}Ni_{0.8}Co_{0.4}$, HT-Ni_2Al) show an increased number of the total basic sites.

Table 5. Elemental composition determined by XRF analysis and basicity measurement.

Catalyst	Elemental composition							Total basic sites mmol acrylic acid/g
	Mg^{2+} [wt%]	Al^{3+} [wt%]	Ni^{2+} [wt%]	Co^{2+} [wt%]	Mg/Al Atomic ratio	Ni/Al Atomic ratio	Co/Al Atomic ratio	
HT-$Mg_{1.2}Ni_{0.6}Co_{0.2}$	7.90	8.20	11.11	4.74	1.08	0.60	0.26	1.51
HT-$Mg_{1.2}Ni_{0.4}Co_{0.4}$	7.91	8.24	6.99	7.77	1.08	0.39	0.43	1.03
HT-$Mg_{1.2}Ni_{0.2}Co_{0.6}$	7.52	8.49	4.81	13.27	1.00	0.26	0.72	0.77
HT-$Mg_{0.8}Ni_{0.8}Co_{0.4}$	4.79	8.05	15.51	7.63	0.67	0.89	0.43	1.50
HT-$Mg_{0.8}Ni_{0.6}Co_{0.6}$	4.73	8.22	10.85	12.08	0.65	0.61	0.67	0.68
HT-$Mg_{0.8}Ni_{0.4}Co_{0.8}$	4.92	8.47	7.28	18.95	0.65	0.4	1.03	0.62
HT-Ni_2Al	-	6.93	33.16	-	-	2.2	-	1.96
HT-Co_2Al	-	9.36	-	51.47	-	-	2.52	1.55

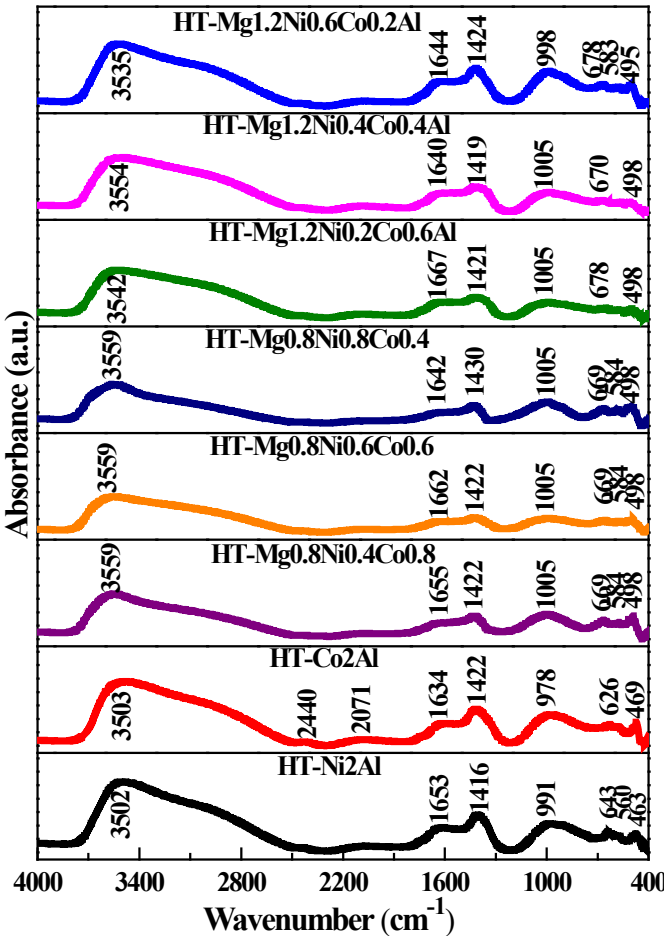

Figure 12. DRIFT spectra of the LDH solids.

The DRIFT spectra of the prepared solids can be seen in Figure 12. All the samples present an absorption band at around 3500 cm^{-1} which can be attributed to the O-H stretching vibrations in the interlayer and then in the hydroxyl group of water molecules [20]. The absorption bands appearing at around 1424 cm^{-1} and between 998-1005 cm^{-1} are due to the ν_3 vibration and bending modes of carbonate, respectively [19]. The band at about 1640-1667 cm^{-1} corresponds to the bending vibration of water molecules. The peaks below 800 cm^{-1} are attributed to the stretching and bending vibration mode of MO, and MOH (M=Co, Ni, Al) in the brucite like structure.

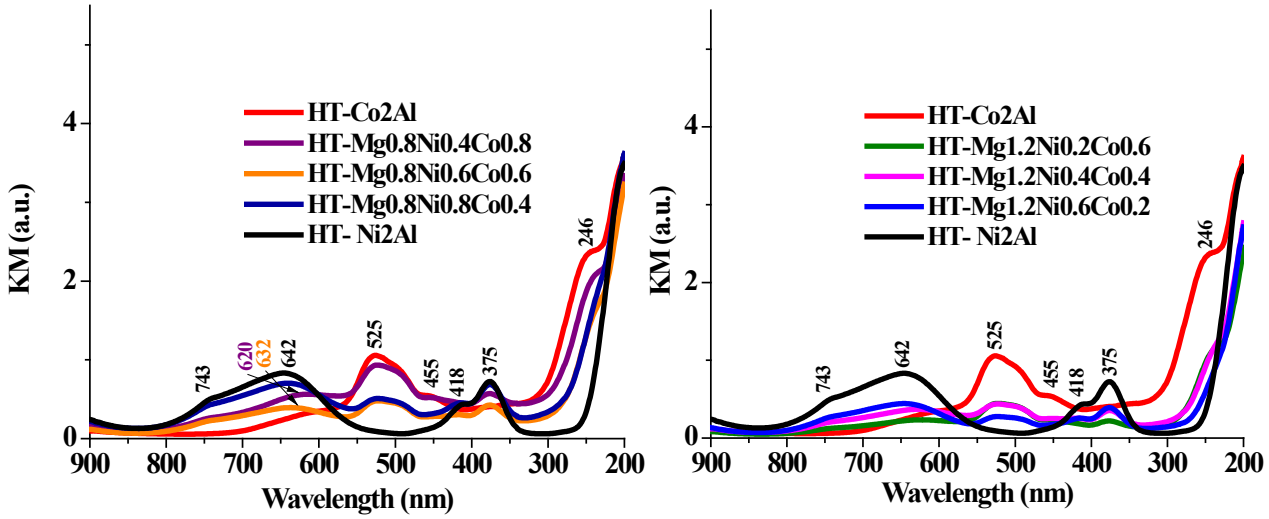

Figure 13. DR-UV-VIS spectra of the prepared samples.

Figure 13 shows the results of the DR-UV-VIS analysis done for all the prepared samples. The spectra of the materials present bands attributed to O^{2-}-M^{2+} charge transfer and d-d transitions characteristic to the octahedral geometry of the divalent cations, Ni^{2+} and Co^{2+}. For the Ni^{2+} cations, two spin-allowed transitions were attributed to the bands present around 743 and 375 nm, namely: $^3A_{2g}(F) \rightarrow {}^3T_{1g}(F)$ and $^3A_{2g}(F) \rightarrow {}^3T_{1g}(P)$ [21].

Both bands correspond to Ni^{2+} in octahedral coordination. Some spin-forbidden transitions $^3A_{2g}(F) \rightarrow {}^1E_g(D)$ and $^3A_{2g}(F) \rightarrow {}^1T_{2g}(D)$ (bands around 642 and 418 nm, respectively) were also recorded [21]. All the samples present characteristic bands of cobalt(II) in both octahedral and tetrahedral coordination [22]. The bands at 525 and 246 nm correspond to octahedral sites of cobalt (II) [22,23]. No bands around 700 nm corresponding to octahedrally coordinated Co^{3+} can be observed [23].

5.5.3. Characterization of the ex-LDH mixed oxide samples

The characterization of the calcined samples belonging tothe series $Mg_{1.2}Ni_aCu_bAl(OH)_6(CO_3)_{0.5}$ (a+b=0.8) and $M_2Al(OH)_6(CO_3)_{0.5}$ (where M is Ni or Cu) included only X-Ray diffraction of powders (XRD), basicity and acidity measurements, diffuse reflectance infrared Fourier-transform spectroscopy (DRIFT) and DR-UV-VIS.

The diffraction patterns for the calcined LDH samples (Figure 14) indicate, as expected, the destruction of the lamellar structure and the appearance of the mixed oxides with the periclase-like structure. No other diffraction lines corresponding to alumina or spinel-type phases were detected, except for the CHT-Cu_2Al sample where Cu is clearly present as CuO (tenorite), in a monoclinic crystal arrangement [24].

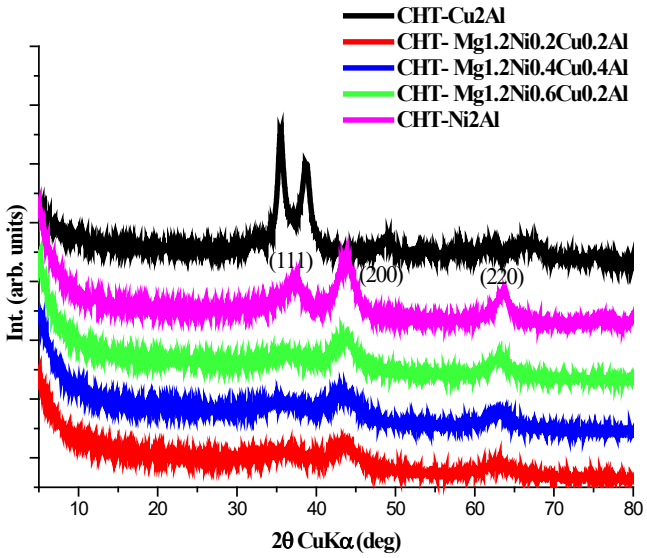

Figure 14. The XRD spectra of the calcined LDH samples.

Table 6. Acidity and basicity measurements.

Sample	Total acidity mmoles Py/g	Brønsted acidity %	Lewis acidity %	Total basicity mmoles acrylic acid/g	Base sites/ acid sites ratio	S_{BET} m^2/g	V_p cm^3/g
CHT-Ni_2Al	0.174	18.4	85.6	1.20	6.88	-	-
CHT-Cu_2Al	0.376	100	0	0.78	2.075	-	-
CHT-$Mg_{1.2}Ni_{0.6}Cu_{0.2}Al$	0.373	14.2	85.8	3.61	9.669	260	0.51
CHT-$Mg_{1.2}Ni_{0.4}Cu_{0.4}Al$	0.408	1.8	98.2	3.58	8.772	263	0.52
CHT-$Mg_{1.2}Ni_{0.2}Cu_{0.6}Al$	0.608	0	100	3.71	6.104	249	0.43

The data in Table 6 show that the total number of base sites in the MgNiAlCuAl mixed oxides increases with the increase of the number of Cu cations and the decrease of Ni cations.

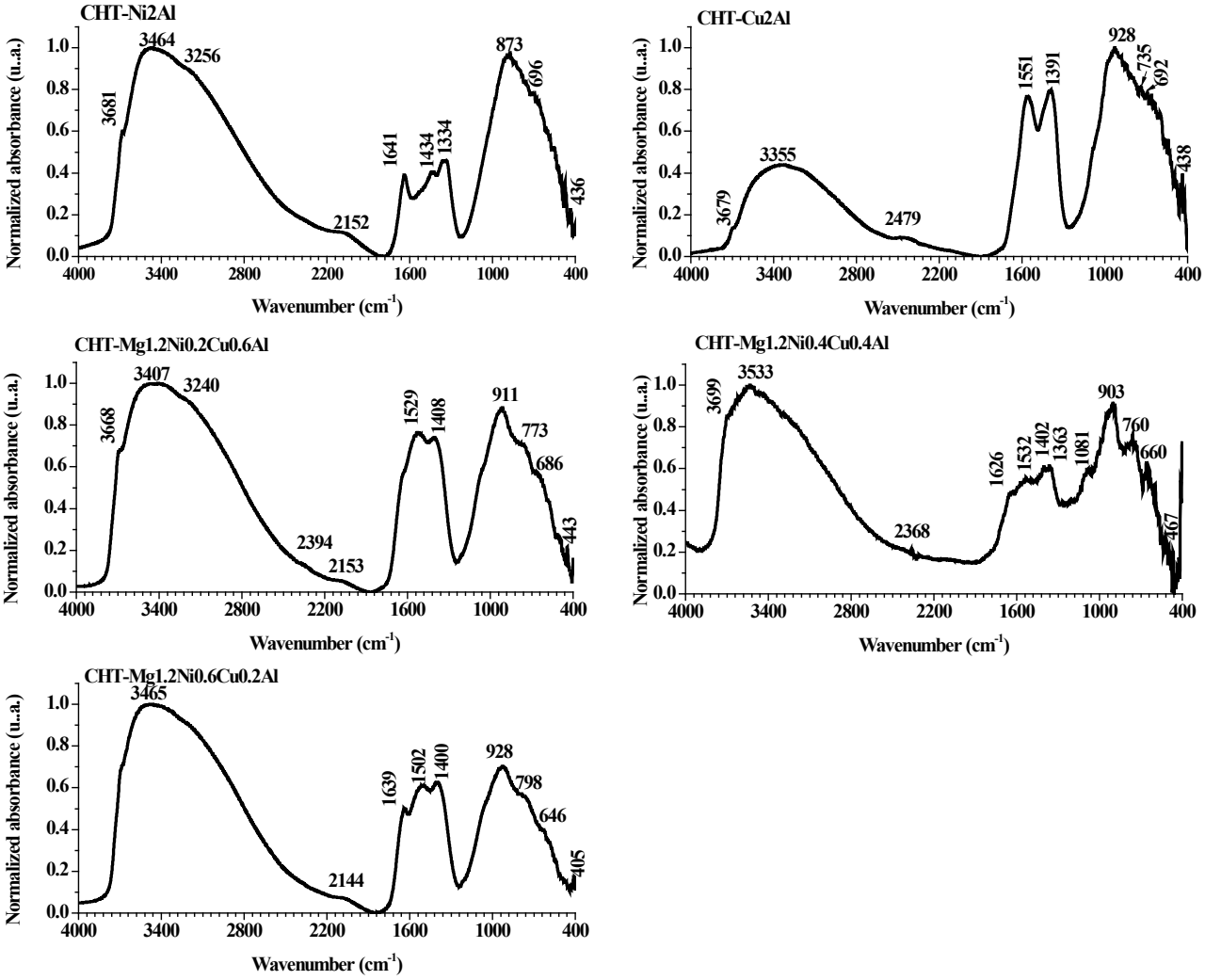

Figure 15. DRIFT spectra of the calcined LDH solids.

The DRIFT spectra of the calcined samples can be found in Figure 15. CHT-Cu_2Al loses the highest amount of H_2O during its calcination since the bands corresponding to hydroxyl groups at ca 3400 cm^{-1} as well as the band at ca 1620 cm^{-1} corresponding to the deformation vibration of interlayer H_2O disappears. Meanwhile, CHT-Ni_2Al solid still preserve significant amounts of hydroxylic groups even after the calcination. The spectra of the solids containing both Ni and Cu show increased intensity of the bands corresponding to symmetric stretching of hydroxyl groups and water bending and the decrease of the Cu content from 0.6 to 0.2. At lower values of wavelengths, 1000-400 cm^{-2}, there is a series of bands characteristic of O-Metal-O vibrations which are overlapping.

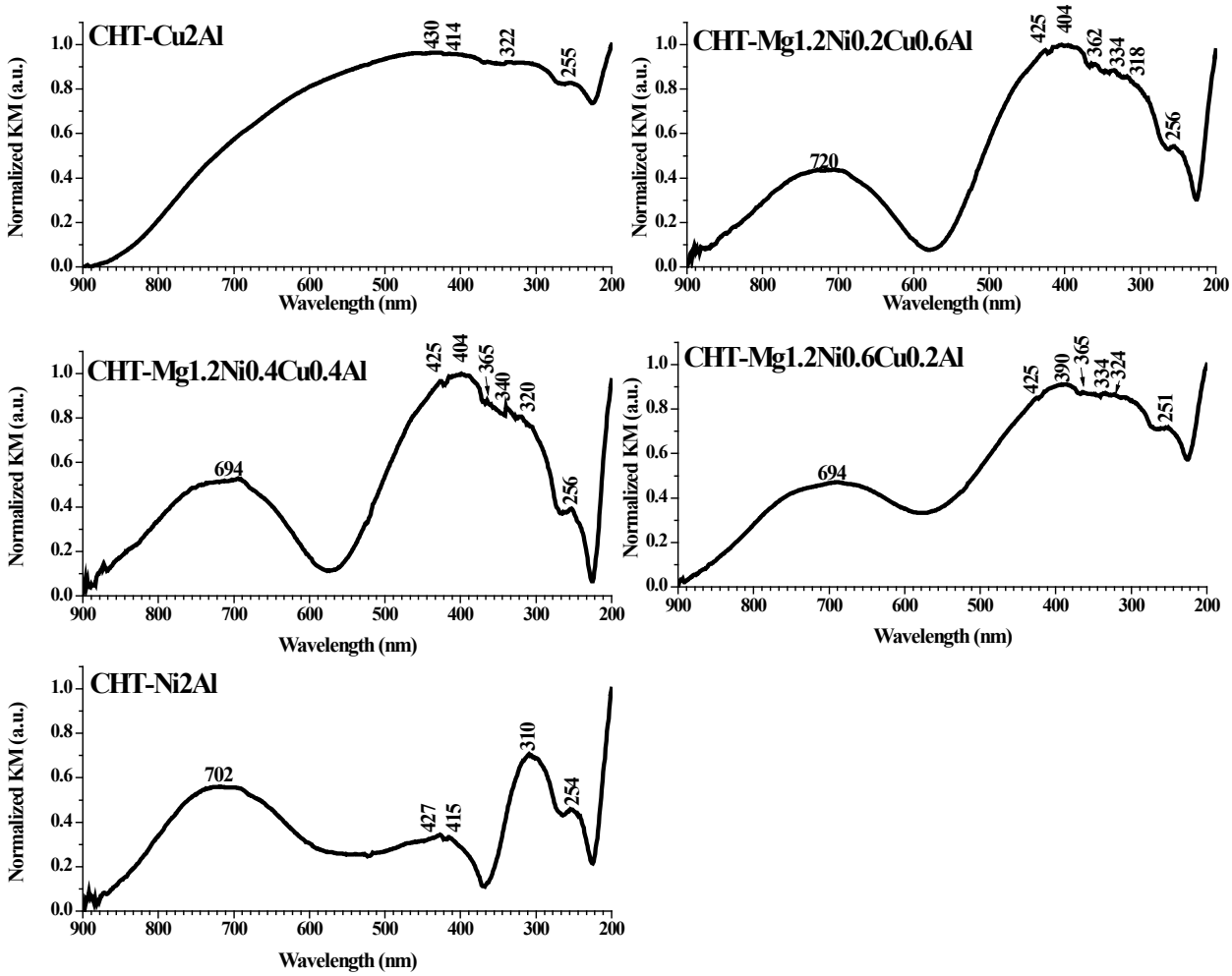

Figure 16. DR-UV-VIS of the calcined samples.

The poor resolution of these bands suggests a lower crystallinity of the calcined solids [18]. The higher concentration of hydroxyl groups in CHT-$Mg_{1.2}Ni_{0.6}Cu_{0.2}Al$ may be responsible for its higher catalytic activity.

To obtain information about the oxidation states and the stereochemistry of the metallic cations, the calcined samples were analyzed by DR-UV-VIS spectroscopy (Figure 16). According to the results, the DR-UV–VIS spectra of samples containing Ni show the presence of Ni^{2+} cations with octahedral coordination (band around 425 nm), with the appearance of the band around 700 nm, attributed to the bulk NiO [25]. The samples containing copper presents a band around 250 nm that is characteristic to Cu-Al samples and has been attributed to the $^{2}E_g$-$^{2}T_{2g}$ spin-allowed transition of Cu^{2+} ions in the distorted octahedral environment with a spinel-type structure [26]. There are also bands at around 300 and 350 nm attributed to the charge transfer involving Cu^{2+}–O^{2-}–Cu^{2+} species, possibly cluster-like or bulk-like species [26].

5.6. Catalytic results

5.6.1. The aerobic oxidation/condensation tandem reaction

5.6.1.1. MgNiCuAl LDH catalysts

The LDH catalysts were tested in the aerobic oxidation/condensation tandem reaction using benzene, toluene and mesitylene as solvents. Toluene and mesitylene have shown to be effective solvents in the tandem reactions explored by Zhou et al. [1]. They, together with benzene, served as adequate solvents in our investigation as well. The alcohol conversion was calculated using the following formula:

$$Conv.(\%) = \frac{n^0_{BnOH} - n_{BnOH}}{n^0_{BnOH}} \times 100$$

where n^0_{BnOH} and n_{BnOH} are the initial and final (unreacted) number of moles of benzyl alcohol, respectively.

Because, according to the overall reaction, one mol of alcohol leads to one mol of desired product, *i.e.*, 2-benzoyl-3-phenylacrylonitrile, the yield was calculated as follows:

$$Yield\ to\ BPA\ (\%) = \frac{n_{BPA}}{n^0_{BnOH}} \times 100$$

where n_{BPA} is the number of moles of BPA formed in the tandem reaction.

The alcohol conversions and yields to BPA are displayed in Table 7. First, we noticed that, compared to the Ce-containing MgAl LDH-graphene oxide composite catalysts used in our previous study [27], the current LDH materials have proven to be more efficient.

Table 7. Catalytic results of the HT-$Mg_{1.2}Ni_aCu_bAl$, HT-$Mg_{0.8}Ni_cCu_dAl$, HT-Ni_2Al and HT-Cu_2Al systems in the aerobic oxidation/condensation tandem reaction.

Catalyst	Conversion of Benzyl Alcohol (%) in the following solvents:			Yield to BPA[a] (%) in the following solvents:		
	Toluene	Mesitylene	Benzene	Toluene	Mesitylene	Benzene
HT-$Mg_{1.2}Ni_{0.6}Cu_{0.2}Al$	58	73	75	34	70	70
HT-$Mg_{1.2}Ni_{0.4}Cu_{0.4}Al$	54	60	70	32	58	69
HT-$Mg_{1.2}Ni_{0.2}Cu_{0.6}Al$	52	55	68	25	51	63
HT-$Mg_{0.8}Ni_{0.8}Cu_{0.4}Al$	84	90	96	67	89	92
HT-$Mg_{0.8}Ni_{0.6}Cu_{0.6}Al$	83	84	88	46	82	82
HT-$Mg_{0.8}Ni_{0.4}Cu_{0.8}Al$	70	78	81	41	55	78
HT-Ni_2Al	96	98	100	76	97	98
HT-Cu_2Al	41	48	57	32	30	33

[a] 2-benzoyl-3-phenylacrylonitrile

All the prepared LDH samples exhibited a bifunctional catalytic behavior involving both redox sites, represented by transition metal cations, and acid-base sites, being, thus, able to

promote both the alcohol oxidation and the Knoevenagel condensation in a stepwise way. Except for HT-Cu_2Al, the catalysts with higher content of transition metal cations presented higher activity for the oxidation step of the tandem reaction.

The low activity of HT-Cu_2Al could be related to the sensibly lower value of its specific surface area and to the presence of the malachite impurity. However, it can be observed that for a given LDH series, i.e., HT-$Mg_{1.2}Ni_aCu_bAl$ or HT-$Mg_{0.8}Ni_cCu_dAl$, the catalytic performance decreases with increasing the Cu content at the expense of Ni, whatever the solvent used, suggesting a simple additive effect [28].

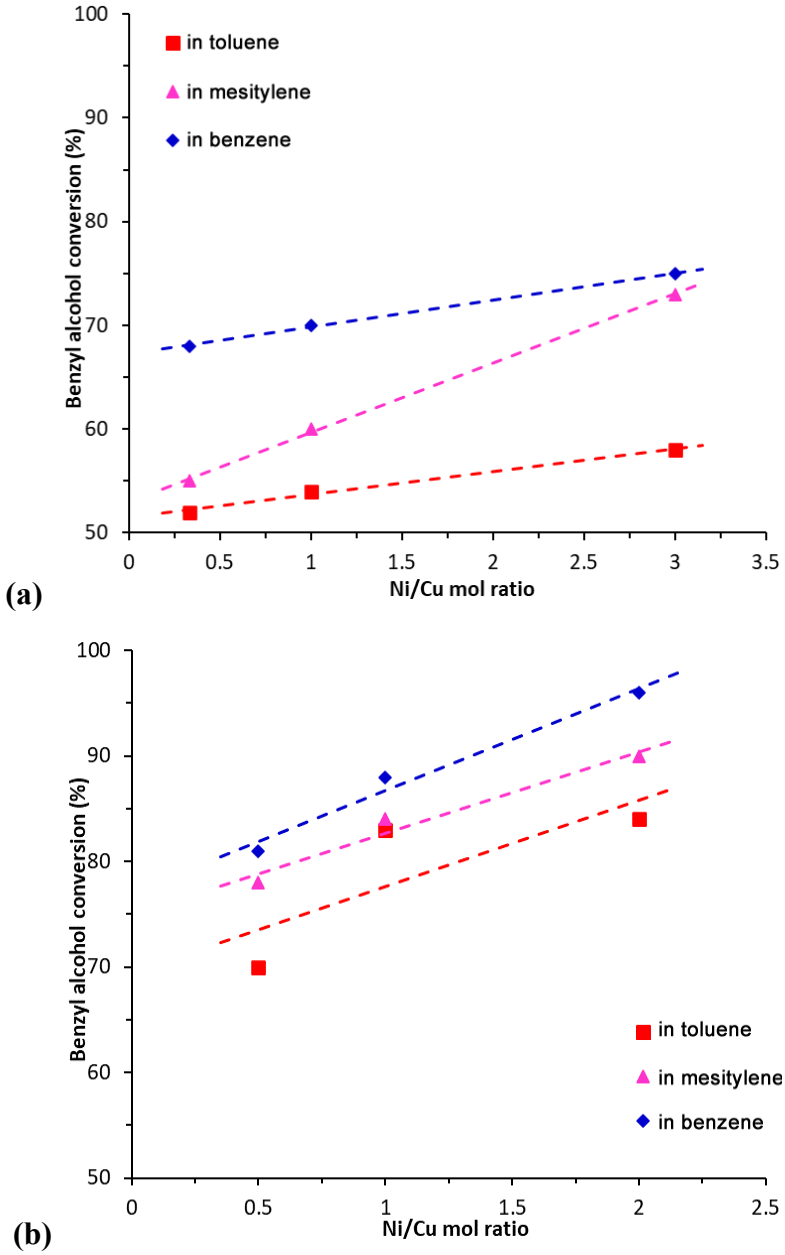

Figure 17. Alcohol conversion vs Ni/Cu mol ratio in the HT-$Mg_{1.2}Ni_aCu_bAl$ (a) and HT-$Mg_{0.8}Ni_cCu_dAl$ (b) series.

Indeed, the catalytic activity in terms of alcohol conversion increases linearly, within the limits of the experimental error, with increasing the Ni/Cu mol ratio in the MgNiCuAl LDH catalysts as seen in Figure 17.

Moreover, the BPA yield follows the same trend (Figure 18). The decrease of activity with the increase of Cu content in the catalyst is likely due to the fact that this cation is already in its superior oxidation state and, hence, it is less prone to activate the molecular oxygen in the first step of the process.

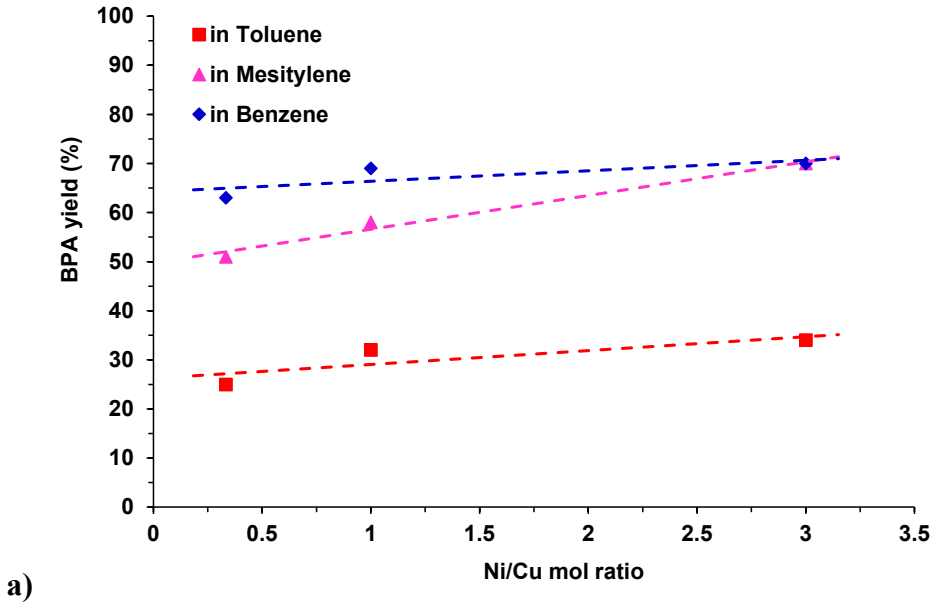

a)

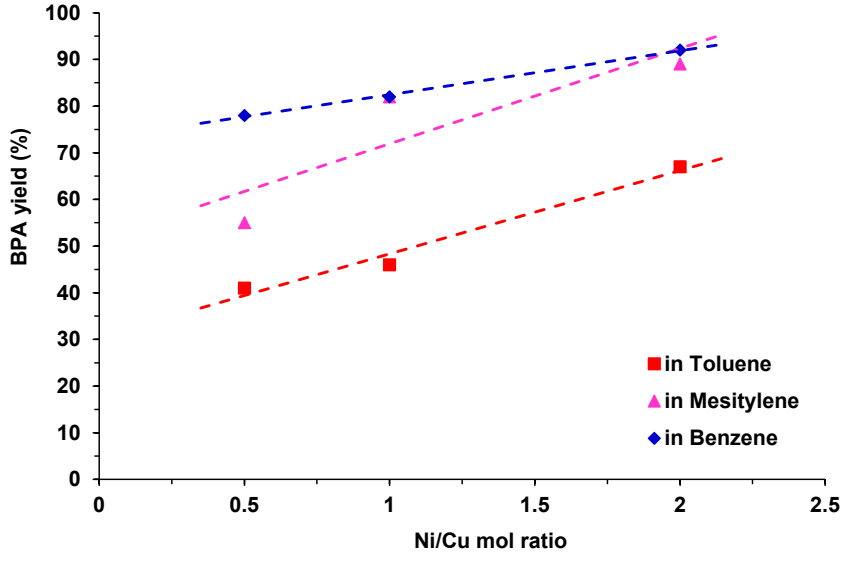

(b)

Figure 18. BPA yield vs Ni/Cu mol ratio in the HT-$Mg_{1.2}Ni_aCu_bAl$ (a) and HT-$Mg_{0.8}Ni_cCu_dAl$ (b) series.

The highest values of alcohol conversion and BPA yield were obtained with the solid containing only one of the divalent cations, namely HT-Ni_2Al, probably due to its ability to

activate the molecular oxygen, which is chemisorbed on Ni^{2+} sites yielding a peroxide type structure.

Meanwhile the benzyl alcohol is transformed into an aluminum alkoxide intermediate, which suffers a hydride abstraction by the neighboring peroxide on the nickel cation being further converted to benzaldehyde according to the mechanism described by Choudary et al. [29]. Notably, this solid also shows the tendency to form spherical aggregates, uniformly distributed, as indicated by the SEM results. The results in Table 7 also show that the catalytic performance of the MgNiCuAl LDH systems is higher for the samples containing lower amounts of Mg and Cu and higher amounts of Ni. Since there are only slight differences between their specific surface areas, this property cannot explain the evolution of their catalytic performance.

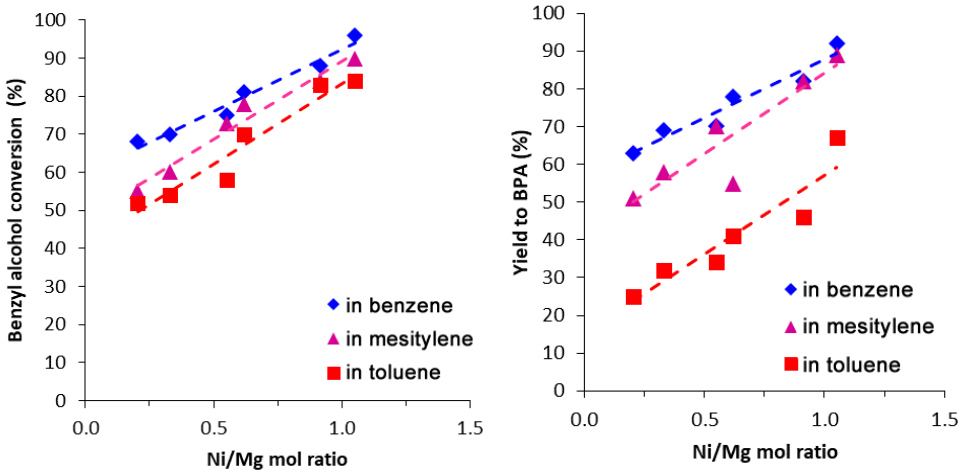

Figure 19. The variation of the conversion of benzyl alcohol and the yields of 2-benzoyl-3-phenylacrylonitrile (BPA) in different solvents vs the Ni/Mg ratio in the MgNiCuAl LDH catalysts.

However, good correlations between, on the one hand, the conversion of benzyl alcohol and, on the other hand, the yield of BPA, and the Ni/Mg ratio in the MgNiCuAl LDH catalysts have been observed (Figure 19): the higher the Ni/Mg ratio, the higher the catalytic performance. On the other hand, the second step of the tandem reaction, i.e., the Knoevenagel condensation, is expected to be more affected by the acid-base properties of the solid catalysts [30]. Indeed, the yield of the target product (BPA) was shown to decrease with increasing the base-to-acid sites mol ratio for the MgNiCuAl LDH catalysts (Figure 20). The best BPA yield was observed for the HT-$Mg_{0.8}Ni_{0.8}Cu_{0.4}Al$ system which shows the lowest base-to-acid sites mol ratio. As reported by Corma et al. [30], there is a cooperation between the acid and the base sites in the Knoevenagel condensation reactions of carbonyl compounds

with active methylene groups via an ion-pair mechanism, which consists of the deprotonation of the active methylene group by the base sites of the catalyst, forming a carbanion. Meanwhile, the carbonyl of the benzaldehyde is activated by the acidic sites a carbocation is being generated. When the carbanion attacks the carbocation, the dehydration reaction takes place and the BPA product is formed.

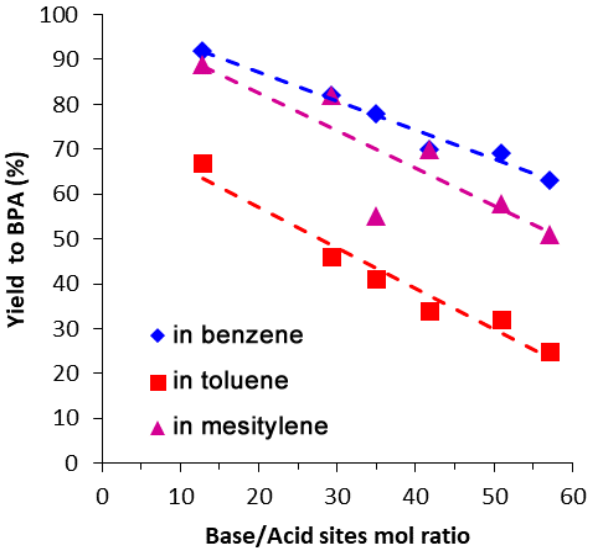

Figure 20. The variation of the yield to 2-benzoyl-3-phenylacrylonitrile (BPA) in different solvents vs the base/acid sites mol ratio of the MgNiCuAl LDH catalysts.

5.6.1.2. MgNiCoAl LDH catalysts

The hydrotalcite-type solids were tested as catalysts in the one-pot cascade oxidation-Knoevenagel condensation. The reaction conditions are identical to those described in previous chapter. 2-Benzoyl-3-phenylacrylonitrile (BPA) was synthesized by the aerobic oxidation of benzyl alcohol (BnOH) followed by the Knoevenagel condensation with benzoyl acetonitrile (BzACN) using three different non-polar solvents, i.e., toluene, benzene, and mesitylene. The conversions and yields are displayed in Table 8. First, we noticed that, the current LDH materials have proven to be less efficient compared to MgNiCuAl LDH-catalysts used in our previous study. However, all the prepared LDH samples exhibited a bifunctional catalytic behavior due to both redox sites, represented by transition metal cations, and acid-base sites, being, thus, able to promote both the alcohol oxidation and the Knoevenagel condensation in a stepwise manner. The catalytic activity in terms of alcohol conversion increases linearly, within the limits of the experimental error, with increasing of the Ni/Al mol ratio in the MgNiCoAl LDH catalysts as seen in Figure 21.

Table 8. Catalytic results of the MgNiCoAl-LDHs with different Ni:Co ratios.

Catalyst	Conversion of benzyl alcohol (%) in the following solvents:			Yield to BPA (%) in the following solvents:		
	Toluene	Mesitylene	Benzene	Toluene	Mesitylene	Benzene
HT-$Mg_{0.8}Ni_{0.8}Co_{0.4}Al$	32	47	51	30	46	50
HT-$Mg_{0.8}Ni_{0.6}Co_{0.6}Al$	32	44	50	7	31	45
HT-$Mg_{0.8}Ni_{0.4}Co_{0.8}Al$	24	36	41	6	23	38
HT-$Mg_{1.2}Ni_{0.6}Co_{0.2}Al$	38	48	54	4	21	34
HT-$Mg_{1.2}Ni_{0.4}Co_{0.4}Al$	35	37	50	2	15	26
HT-$Mg_{1.2}Ni_{0.2}Co_{0.6}Al$	28	32	49	1	5	9
HT-Ni_2Al	96	98	100	76	97	98
HT-Co_2Al	24	30	36	5	8	9

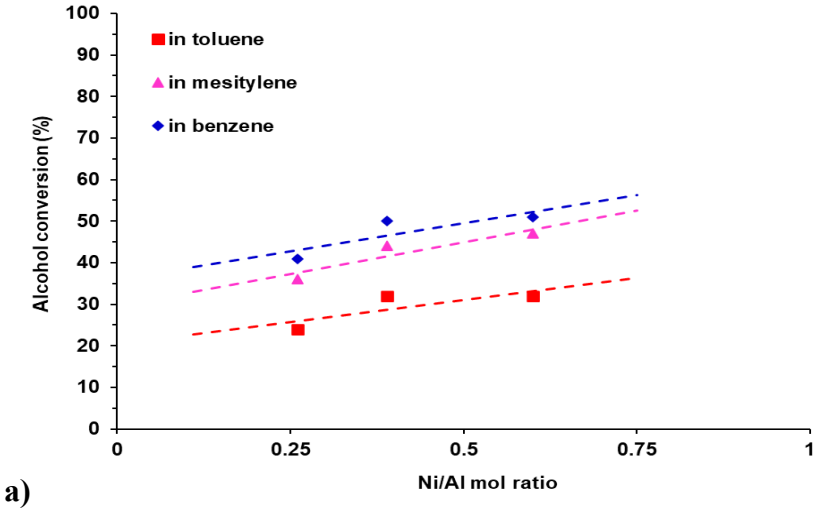

a)

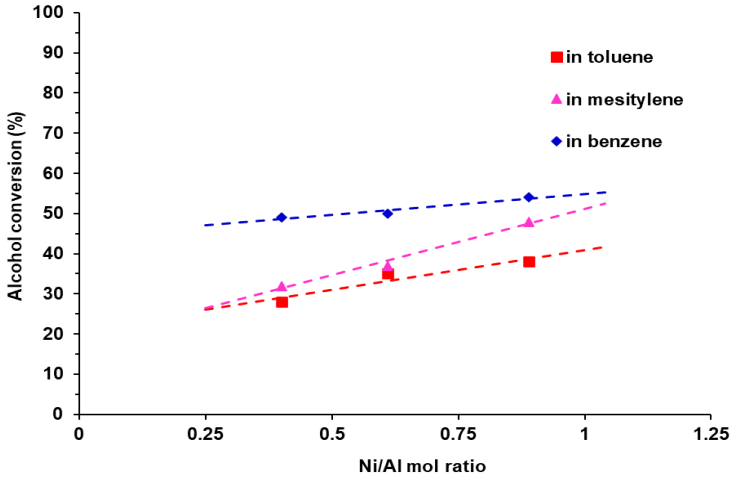

b)

Figure 21. Alcohol conversion vs Ni/Al mol ratio in the HT-$Mg_{0.8}Ni_cCo_dAl$ (a) and HT-$Mg_{1.2}Ni_aCo_bAl$ (b) series.

The highest values of alcohol conversion and BPA yield were obtained by the solid containing only one of the divalent cations, namely HT-Ni_2Al, probably due to its ability to

activate the molecular oxygen, which is chemisorbed on Ni^{2+} sites yielding a peroxide type structure. The results in Table 8 also show that the catalytic performance of the MgNiCoAl LDH systems is higher for the samples containing lower amounts of Mg and Co and higher amounts of Ni.

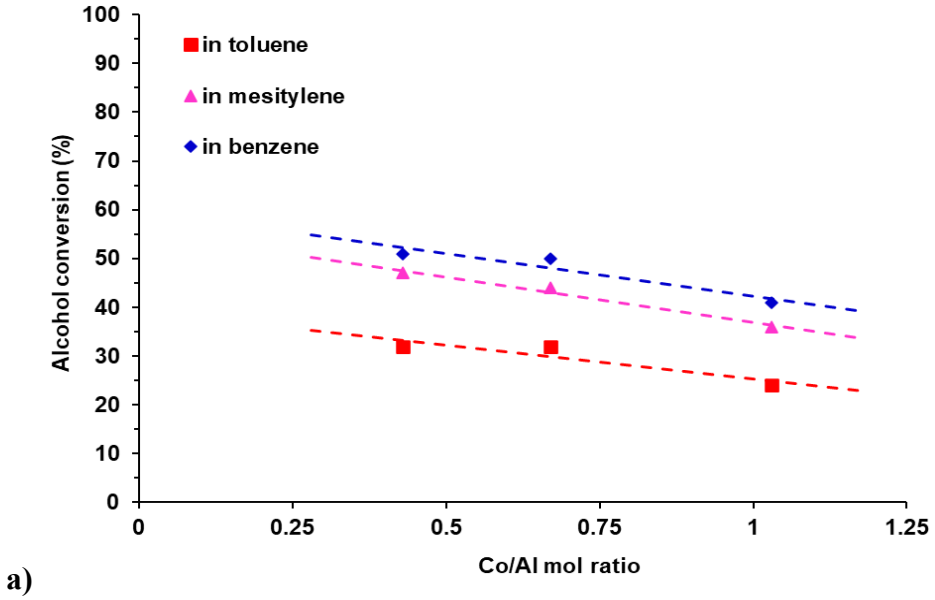

a)

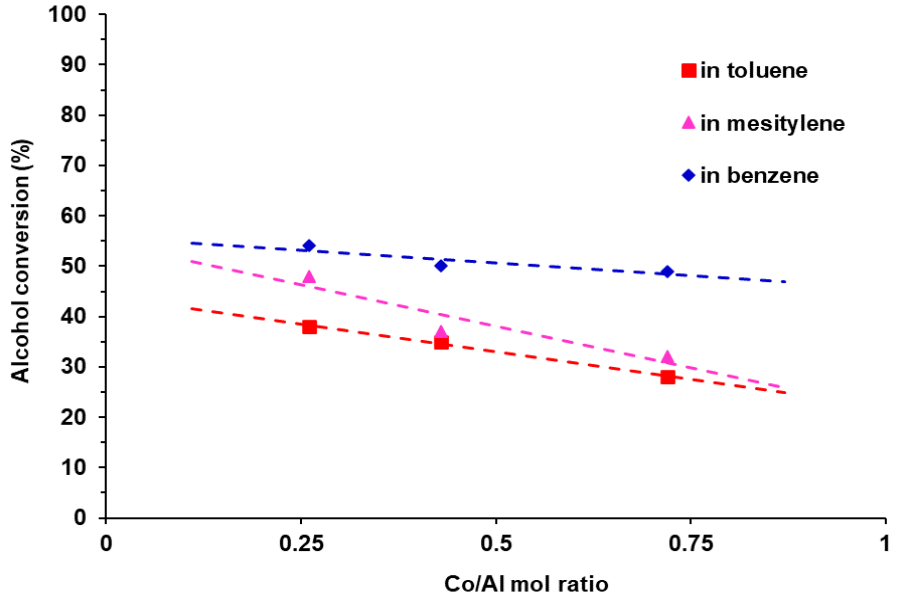

b)

Figure 22. Alcohol conversion vs Co/Al mol ratio in the HT-$Mg_{0.8}Ni_cCo_dAl$ (a) and HT-$Mg_{1.2}Ni_aCo_bAl$ (b) series.

Figure 22 shows that the activity decreases with the increase of the Co content in the catalysts. This is likely to happen due to the fact that this cation is already in its superior oxidation state and, hence, it is less prone to activate the molecular oxygen in the first step of the process, namely the oxidation. A similar trendline was also observed in the case of

MgNiCu.Al LDH catalysts. The catalysts tested work better with benzene as the solvent, followed by mesitylene and toluene.

5.6.2.The Payne oxidation reaction of cyclohexene over ex-LDH mixed oxide catalysts

The catalytic activity of the calcined LDH samples was tested in the Payne oxidation of cyclohexene with a solution of hydrogen peroxide and acetonitrile (Scheme 1). During the experiment 0.004 moles of cyclohexene and 0.032 moles of acetonitrile were added in a stirred flask. The reaction mixture was dissolved in 20 mL of solvent (10 mL water and 10 mL acetone). A quantity of 0.128 moles H_2O_2 (molar ratio cyclohexene/H_2O_2 = 1/32) was added in small equal ratios during the reaction (3 mL/60 min). The reactions were performed at 60 °C, for 5 h reaction time. In all reactions, the catalyst concentration was 3% wt. per volume of the reaction mixture. The reaction products were also identified by mass spectrometer-coupled chromatography, using a GC/MS/MS VARIAN SATURN 2100 T equipped with a CP-SIL 8 CB Low Bleed/MS column of 30 m length and 0.25 mm diameter.

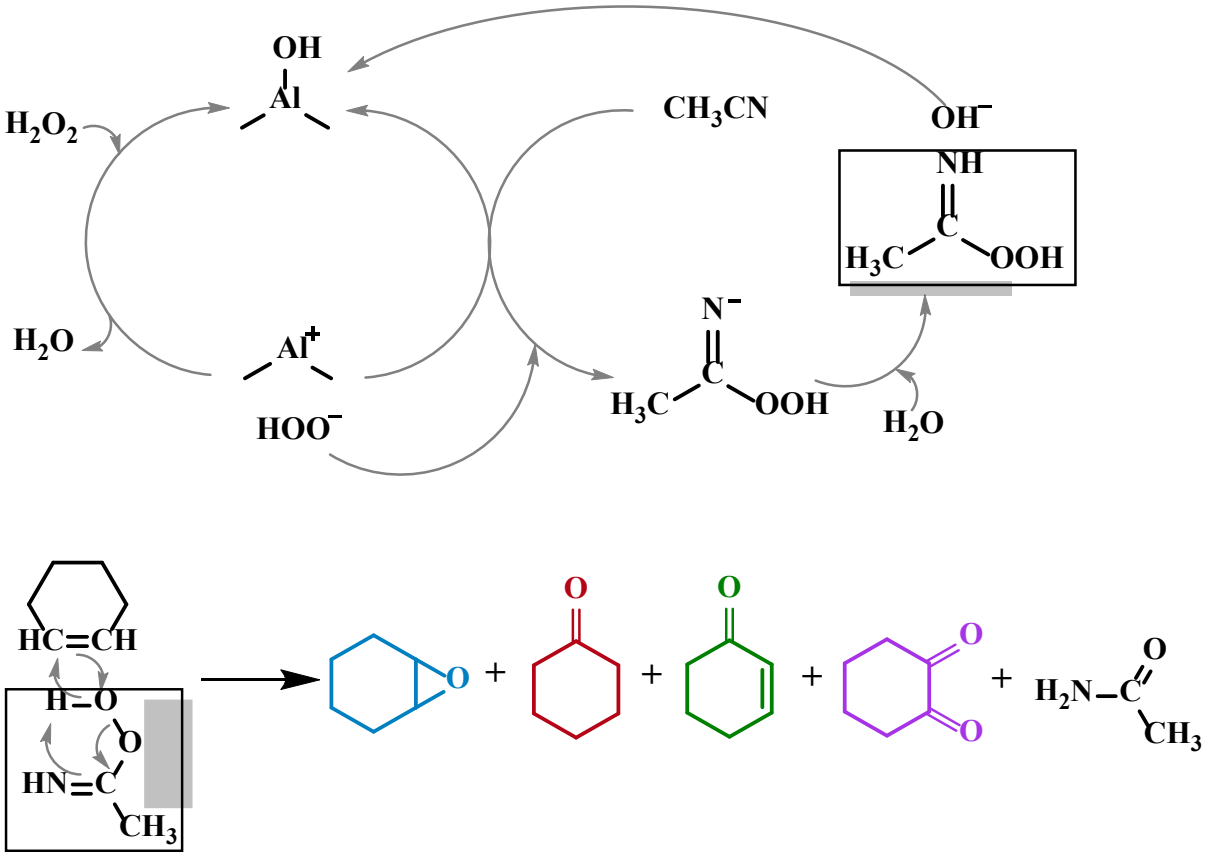

Scheme 1. Reaction route for Payne oxidation.

These reactions occur with the help of peroxycarboximidic acid, a reaction product obtained after the nucleophilic attack of the hydrogen peroxide on the C atom from the nitrile group (Scheme 1).The peroxicarboximidic acid starts the epoxidation reaction of the cyclohexene

by transferring the terminal oxygen to the C double bond. During the oxidation reaction, besides the main, desired product epoxy cyclohexane, other by-products may be obtained such as cyclohexanone (red), cyclohexenone (green) and cyclohexandione (purple), as shown in Scheme 1.

In the case of multicationic mixed oxides, the highest cyclohexene conversion (99.5%) was obtained for the CHT-$Mg_{1.2}Ni_{0.6}Cu_{0.2}Al$ composition, while the lowest conversion (40.9%) was obtained for the CHT-$Mg_{1.2}Ni_{0.2}Cu_{0.6}Al$ (Figure 23b). The compounds CHT-$Mg_{1.2}Ni_{0.6}Cu_{0.2}Al$ and CHT-$Mg_{1.2}Ni_{0.4}Cu_{0.4}Al$ present almost similar surface areas and pore volumes, but they show different acidity and basicity. CHT-$Mg_{1.2}Ni_{0.6}Cu_{0.2}Al$ presents increased Brønsted and Lewis acidity and also a higher total basicity value compared to CHT-$Mg_{1.2}Ni_{0.4}Cu_{0.4}Al$. The reactions catalyzed by the composites containing both Ni and Cu cations were significantly more selective, the only reaction product being the epoxide. Meanwhile, under the same reaction conditions, catalysts containing only one bivalent cation but the same M^{2+}/Al^{3+} ratio had lower catalytic activity than the most performant multicationic LDH and showed different selectivities for epoxide formation ranging from ca. 95% (at 85% conversion) for CHT-Ni_2Al, and 0% (at 39.2% conversion) for CHT-Cu_2Al.

a)

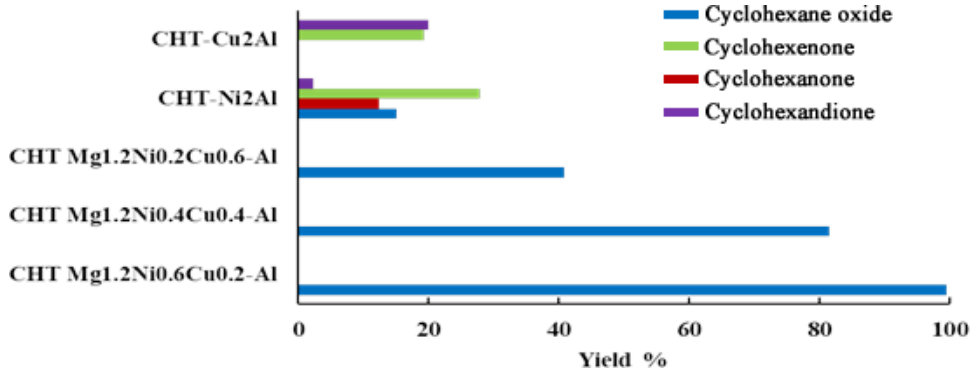

b)

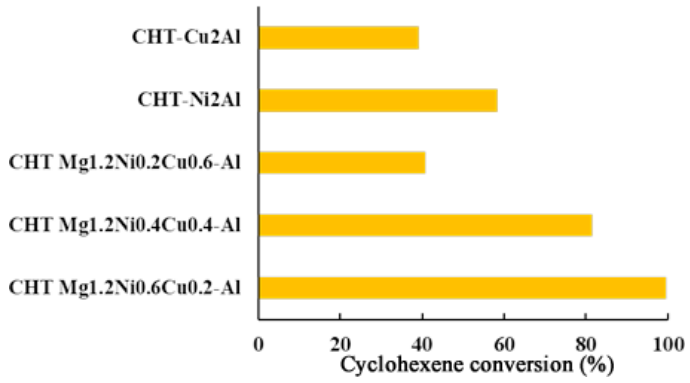

Figure 23. a) Yield of the reaction b) Conversion of the reaction.

These results suggest that both Cu and Ni cations, likely interacting synergistically, together with Mg are necessary in the mixed oxides to obtain almost complete conversion with total selectivity to epoxide.

5.7. Conclusions

Multicationic MgNiCuAl LDH materials were successfully prepared by simple coprecipitation. The XRD studies showed that all the LDH samples have increased crystallinity and confirmed no other impurities present in the solids, except for that containing only copper and aluminum. DR-UV-VIS spectroscopy clearly indicated the existence of the octahedral geometry of the transition-metal divalent cations, Ni^{2+} and Cu^{2+}. The SEM images demonstrated the samples are not entirely homogenous. For the multicationic LDH samples containing both nickel and copper, irrespective to the nature of solvent used, the benzyl alcohol conversion and the BPA yield increased linearly with the nickel loading, which corresponds to a simple additive effect. In line with this, the NiAl-LDH (HT-Ni_2Al) was the most active, while the CuAl LDH (HT-Cu_2Al) was the least active system. Notably, HT-Ni_2Al showed the largest crystalline domain sizes of the brucite-like layer. For the multicationic MgNiCuAl LDH catalysts, whatever the solvent used, the yield of the target product (BPA) decreased with increasing the base-to-acid sites mol ratio.

The multicationic MgNiCoAl LDH materials were prepared using the same method as in the case of MgNiCuAl LDH, namely the copreciptation. The XRD studies of the MgNiCoAl LDHshowed that all the samples have increased crystallinity and confirmed no other impurities present in the solids. DR-UV-VIS clearly highlighted the existence of the octahedral geometry of the Ni^{2+} cations, and the tetrahedral coordination of the Co^{2+}. Regarding their catalytic activity, for the LDH samples modified with nickel and cobalt, the conversion and the yields varied with the loading of nickel. A higher amount of Ni led to increased values of conversion and yield of BPA, which explain the good results obtained when HT-Ni_2Al was used.

Benzene has proven to be the best solvent used in all the catalytic reactions, no matter the catalyst used (MgNiCuAl LDH or MgNiCoAl LDH). Finally, it can unambiguously be sustained that all the studied LDH materials acted as bifunctional catalysts in the aerobic oxidation/condensation tandem reaction.

Regarding the mixed oxide solids derived from the hydrotalcites, the XRD studies showed that all the samples were succesfully converted into their oxidic form with the periclase-like structure. No impurities were identified, except for the sample CHT-Cu_2Al. The DRIFT

spectra revealed a lower crystallinity of the calcined solids. The catalytic results suggested that the highest cyclohexene conversion (99.5%) was obtained for the CHT-$Mg_{1.2}Ni_{0.6}Cu_{0.2}Al$ composition, while the lowest conversion (40.9%) was obtained for the CHT-$Mg_{1.2}Ni_{0.2}Cu_{0.6}Al$. CHT-$Mg_{1.2}Ni_{0.6}Cu_{0.2}Al$ presents increased Brønsted and Lewis acidity and also a higher total basicity value compared to the other catalysts. The reactions catalyzed by the composites containing both Ni and Cu cations were significantly more selective, the only reaction product being the epoxide. The results indicate that both Cu and Ni cations, likely interacting synergistically, together with Mg are necessary in the mixed oxides to obtain almost complete conversion with total selectivity to epoxide.

References

1. Zhou, W., Zhai, S., Pan, J., Cui, A., Qian, J., He, M., Xu, Z., Chen, Q. Bifunctional NiGa Layered Double Hydroxide for the Aerobic Oxidation/ Condensation Tandem Reaction between Aromatic Alcohols and Active Methylene Compounds. Asian J. Org. Chem. 2017, 6, 1536–1540.

2. Cavani, F. Catalytic selective oxidation: The forefront in the challenge for a more sustainable chemical industry, Catalysis Today, 2010, 157, 8-15.

3. Fan, G., Li, F., Evans, D.G., Duan, X. Catalytic applications of layered double hydroxides: recent advances and perspectives, Chemical Society Reviews, 2014, 43, 7040-7066.

4. Forano, C., Costantino, U., Prevota, V., Taviot Gueho, C. Layered Double Hydroxides (LDH) Developments in Clay Science 2013, 5, 745-782.

5. Pauling, L. The nature of the chemical bond. IV. The energy of single bonds and the relative electronegativity of atoms. J. Am. Chem. Soc. 1932, 54, 3570–3582.

6. Cavani, F., Trifiro, F., Vaccari, A. Hydrotalcite-type anionic clays: Preparation, Properties and applications. Catal. Today 1991, 11, 173-301.

7. Shannon, R.D. Revised effective ionic radii and systematic studies of interatomic distances in halides and chalcogenides. Acta Cryst. 1976, A32, 751-767.

8. Sing, K.S.W., Everett, D.H., Haul, R.A.W., Moscou, L., Pierotti, R.A., Rouquerol, J., Siemieniewska, T. Reporting Physisorption Data for Gas/Solid Systems with Special Reference to the Determination of Surface Area and Porosity. Pure Appl. Chem. 1985, 57, 603–619.

9. Wang, Z., Jiang, X., Pan, M., Shi, Y. Nano-Scale Pore Structure and Its Multi-Fractal Characteristics of Tight Sandstone by N2 Adsorption/Desorption Analyses: A Case Study of Shihezi Formation from the Sulige Gas Filed, Ordos Basin, China. Minerals 2020, 10, 377.

10. Thommes, M., Kaneko, K., Neimark, A.V., Olivier, J.P., Rodriguez-Reinoso, F., Rouquerol, J., Sing, K.S.W. Physisorption of gases,with special reference to the evaluation of surface area and pore size distribution (IUPAC Technical Report). Pure Appl. Chem. 2015, 87, 1051–1069.

11. Klemkaite, K., Prosyceva, I., Taraskevicius, R., Khinsky, A., Aivaras Kareiva, A. Synthesis and characterization of layered double hydroxides with different cations (Mg, Co, Ni, Al), decomposition and reformation of mixed metal oxides to layered structures. Cent. Eur. J. Chem. 2011, 9, 275-282.

12. Gevers, B.R., Naseem, S., Leuteritz, A., Labuschagne, F.J.W.J. Comparison of nano-structured transition metal modified tri-metal MgMAl–LDHs (M=Fe, Zn, Cu,Ni, Co) prepared using co-precipitation. RSC Adv. 2019, 9, 28262.

13. Stepanova, L. N., Belskaya, O.B., Leont'eva N.N.,Kobzar, E.O., Salanov, A.N., Gulyaeva, T.I., Trenikhin, M.V., Likholobov, V.A. Study of the properties of the catalysts based on Ni(Mg)Al-Layered Hydroxides for the reaction of furfural hydrogenation. Mat.Chem.Phys. 2021*, 263*, 124091.

14. Vaysse, C., Guerlou-Demourgues, L., Demourgues, A., Lazartigues, F., Fertier, D., Delmas,C., New (Ni, Co)-based layered double hydroxides with intercalated oxometalate (Mo, W) species, obtained by chimie douce reactions, J Mater. Chem, 2002, 12, 1035-1043.

15. Evans, D.G., Slade, R.C.T., Structural Aspects of Layered Double Hydroxides, Struc. Bond, 2006, 119, 1-87.

16. Alejandre, A., Medina, F., Rodriguez, X., Salagre, P., Cesteros, Y., Sueiras, J.E. Cu/Ni/Al layered double hydroxides as precursors of catalysts for the wet air oxidation of phenol aqueous solutions. Appl. Catal. B 2001, 30, 195–207.

17. Rives, V., Kannan, S. Layered double hydroxides with the hydrotalcite-type structure containing Cu2+, Ni2+ and Al3+. J. Mater. Chem. 2000, 10, 489-495.

18. Wang, J., Zhang, T., Li, K., Cao, Y., Zeng, Y. Dehydrogenation Catalysts for Synthesis of O-Phenylphenol via Cu/Ni/Mg/Al Hydrotalcite-Like Compounds as Precursors. Catalysts 2018, 8, 186.

19. Su, L., Ma, C., Hou, T., Han, W. Selective synthesis and capacitive characteristics of CoNiAl three-component layered double hydroxide platelets, RSC Adv., 2013, 3, 19807.

20. Abdel-Aziz, M.H., Zoromba, M. S., Bassyouni, M., Zwawi, M., Alshehri, A. A., Al-Hossainy, A. F. Synthesis and Characterization of Co-Al Mixed Oxide Nanoparticles via Thermal Decomposition Route of Layered Double Hydroxide, Journal of Molecular Structure 2020, 1206, 127679.

21. Wang, J., Zhang, T., Li, K., Cao, Y., Zeng, Y. Dehydrogenation Catalysts for Synthesis of O-Phenylphenol via Cu/Ni/Mg/Al Hydrotalcite-Like Compounds as Precursors. Catalysts 2018, 8, 186.
22. Taibi, M., Ammar, S., Jouini, N., Fievet, F. Layered nickel–cobalt hydroxyacetates and hydroxycarbonates: Chimie douce synthesis and structural features, Journal of Physics and Chemistry of Solids 2006, 67, 932–937.
23. Pourfaraj, R., Kazemi, S.Y., Fatemia, S.J., Biparva, P. Synthesis of α- and β-CoNi binary hydroxides nanostructures and luminol chemiluminescence study for H_2O_2 detection. Journal of Photochemistry & Photobiology A: Chemistry 2018, 364, 534–541.
24. Van Everbroeck, T, Ciocarlan, R.G., Van Hoey, W., Mertens, M., Cool, P. Copper-Containing Mixed Metal Oxides (Al, Fe, Mn)for Application in Three-Way Catalysis. Catalysts 2020, 10, 1344.
25. Kawabata, T., Shinozuka, Y., Ohishi, Y., Shishido, T.,Takaki, K.,Takehira, K. Nickel containing Mg-Al hydrotalcite-type anionic clay catalyst for the oxidation of alcohols with molecular oxygen. Journal of Molecular Catalysis A: Chemical 2005, 236, 206–215.
26. Crivello, M., Perez, C., Herrero, E., Ghione, G., Casuscelli, S., Rodriguez-Castellon, E. Characterization of Al–Cu and Al–Cu–Mg mixed oxides and theircatalytic activity in dehydrogenation of 2-octanol. Catal. Today 2005, 107–108, 215–222.
27. Stamate, A.-E., Pavel, O.D., Zavoianu, R., Brezestean, I., Ciorita, A.; Birjega, R.; Neubauer, K., Koeckritz, A., Marcu, I.-C. Ce-Containing MgAl-Layered Double Hydroxide-Graphene Oxide Hybrid Materials as Multifunctional Catalysts for Organic Transformations. Materials 2021, 14, 7457.
28. Mittasch, A., Frankenburg, W. Early Studies of Multicomponent Catalysts, Adv. Catal. 1950, 2, 81-104.
29. Choudary, B.M., Kantam, L.M., Rahman, A., Reddy, C.V., Rao, K.K. The First Example of Activation of Molecular Oxygen by Nickel in Ni-Al Hydrotalcite: A Novel Protocol for the Selective Oxidation of Alcohols. Angew. Chem. Int. Ed. Engl. 2001, 40, 763-766.
30. Corma, A., Fornés, V., Martín-Aranda, R. M., García, H., Primo, J. Zeolites as base catalysts: Condensation of aldehydes with derivatives of malonic esters. Appl.Catal. 1990, 59, 237-248.

General conclusions

The first chapter summarized all the information found in the literature regarding the subject, namely layered double catalysts used for fine organic synthesis, while Chapter 2 presents shortly the physiochemical methods used for the characterization of the catalytic materials.

In **Chapter 3**, two methods of synthesis were applied for the obtaining of the Ce-modified layered double hydroxides, namely co-precipitation and mechanochemical technique. The resulting layered double hydroxides and their corresponding mixed oxides were catalytically tested in different types of condensation reactions. First, in the self-condensation of cyclohexanone and then in the Claisen-Schmidt condensation, where compounds belonging to the flavonoid class, namely chalcone and flavone, are synthesized. The mixed oxide derived from the LDH prepared by the mechanochemical method show enlarger surface area, lower real and bulk densities, higher basicity and lower acidity compared with that obtained from the co-precipitated LDH material. The LDH materials have comparable activities in cyclohexanone self-condensation but significantly lower compared to their corresponding mixed oxides. Among the latter, the mechanochemically prepared oxide was slightly more active than its co-precipitated counterpart. In all cases, the mono-condensation product 2-cyclohexylidencyclohexanone was the main reaction product, with selectivities of 76-84 % for the LDH catalysts, and 86-88 % for the LDH-derived mixed oxides. The mechanochemically prepared oxide showed a good stability during four reaction cycles.

In the Claisen-Schmidt condensation reactions, the mechanochemically prepared oxide catalyst was also shown to be more efficient than its co-precipitated counterpart, obviously due to its higher number of base sites. At the same time, both oxides show good selectivities to the desired product, the mechanochemically prepared oxide catalyst being slightly more selective to chalcone and flavone.

In **Chapter 4,** the solids containing cerium prepared by coprecipitation in the previous chapter were modified with graphene oxide, resulting in sandwich-like compounds bearing different concentrations of GO in the range of 5-25 wt. %. The LDH-GO composites were tested as catalysts in two other organo-chemical transformations: i) Knoevenagel condensation reaction and ii) one-pot cascade oxidation-Knoevenagel condensation. The co-precipitation of Mg3Al0.75Ce0.25 LDH in the presence of a GO suspension led to HT3Ce-xGO composites with increased crystallinity.

Using the unmodified solids HT3Ce and GO, the conversions obtained were rather low compared to the hybrid composites. A synergistic effect between the LDH and GO parent

materials present in the HT3Ce-xGO composites, leading to improved catalytic activity, was noticed.

To observe if there are noticeable differences between the catalytic results of hybrid GO and Mg_3Al layered double hydroxides not only when the brucite-like layers are modified by inserting another cation like cerium, but also when the interlayer space contains other anions, like molybdate, the neat Mg3Al-LDH was modified with molybdate anions (MoO_4^{2-}) and with graphene oxide in the range of 5-25 wt.%. The solids were tested as in the previous case in one-pot cascade oxidation-Knoevenagel condensation. Ithe case of the catalysts modified with GO, it was observed that when the brucite-type layer was modified with another cation like cerium, the conversion of benzyl alcohol increased with the decrease of the graphene oxide concentration. The situation changed when the interlayer of the LDH was modified with molybdate, namely, the conversion increased with the increase of the GO concentration.

Chapter 5 presents new perspectives in the rational design of efficient bifunctional catalytic systems. Several LDH samples were prepared by inserting various metallic cations having different molar ratios in the brucite-like layers. The study involved synthesizing MgNi(Cu)Al-layered double hydroxides having different molar ratios using the co-precipitation method. All three series were tested catalytically in the one-pot cascade oxidation-Knoevenagel condensation reaction. The calcined forms of two of the series were also tested in Payne oxidation reaction of cyclohexene. Regarding their catalytic activity, for the LDH samples modified with nickel and copper, the conversion and the yields varied with the loading of nickel. A higher amount of Ni led to increased values of conversion and yield. It can be sustained that all the materials acted as bifunctional catalysts.

Regarding the mixed oxide solids derived from the hydrotalcites, the catalytic results suggested that the highest cyclohexene conversion was obtained for the compound containing both nickel and copper cations reiterating the idea that there is a synergetic relationship between the two divalent cations.

In the same chapter, the importance of the copper inserted in the brucite-type layers was checked by replacing it with cobalt cations. The samples were also tested as catalysts in the one-pot oxidation-Knoevenagel condensation reaction. The results were inferior compared to the solids containg copper.

Published scientific papers

i) Related to the PhD thesis

1. Alexandra-Elisabeta Stamate, Octavian Dumitru Pavel, Rodica Zavoianu, Ioan-Cezar Marcu, Highlights on the Catalytic Properties of Polyoxometalate-Intercalated Layered Double Hydroxides: A Review, Catalysts 2020, 10, 57.
https://doi.org/10.3390/catal10010057

2. Alexandra-Elisabeta Stamate, Octavian Dumitru Pavel, Rodica Zăvoianu, Ioana Brezeştean, Alexandra Ciorîță, Ruxandra Bîrjega, Katja Neubauer, Angela Koeckritz, Ioan-Cezar Marcu. Ce-Containing MgAl-Layered Double Hydroxide-Graphene Oxide Hybrid Materials as Multifunctional Catalysts for Organic Transformations, Materials 2021, 14(23), 7457. https://doi.org/10.3390/ma14237457

3. Alexandra-Elisabeta Stamate, Rodica Zăvoianu, Octavian Dumitru Pavel, Ruxandra Birjega, Andreea Matei, Marius Dumitru, Ioana Brezeștean, Mariana Osiac, Ioan-Cezar Marcu. The influence of the preparation method on the physico-chemical properties and catalytic activities of Ce-modified LDH structures used as catalysts in condensation reactions. Molecules 2021, 26(20), 6191. https://doi.org/10.3390/molecules26206191

ii) Unrelated to the PhD thesis

1. Pavel, O.D., Stamate, A.-E., Bacalum, E., Cojocaru, B., Zăvoianu, R., Pârvulescu, V.I, Catalytic behavior of Li-Al-LDH prepared via mechanochemical and co-precipitation routes for cyanoethylation reaction, Catalysis Today 2020.

2. Octavian Dumitru Pavel, Alexandra-Elisabeta Stamate, Rodica Zăvoianu, Ioana Cristina Bucur, Ruxandra Bîrjega, Emilian Angelescu, Vasile I. Pârvulescu, Mechano-chemical versus co-precipitation for the preparation of Y-modified LDHs for cyclohexene oxidation and Claisen-Schmidt condensations, Applied Catalysis A: General 2020.

3. Alexandra-Elisabeta Stamate, Octavian Dumitru Pavel, Anca Cruceanu, Mihai Cosmin Corobea, Mariana Osiac, Nicoleta Cioatera, LDH-GO composites as catalysts for the oxidative removal of indigo carmine dye from wastewater, Romanian Journal of Ecology & Environmental Chemistry 2020.

Scientific Communications

1. Synthesis, characterization and catalytic activity of $Mg_3Al_{0.75}Ce_{0.25}$-LDH-GO composite, Alexandra-Elisabeta Stamate, Rodica Zăvoianu, Octavian Dumitru Pavel, Ioan-Cezar Marcu, 16th Edition of Student Communications Session-Oral presentation.

2. Highlights on the catalytic properties of MgNi(Cu)Al LDH in the selective epoxidation of cyclohexene, Alexandra-Elisabeta Stamate, Octavian Dumitru Pavel, Ruxandra Birjega, Rodica Zavoianu, Ioan-Cezar Marcu, The third Edition of the Young Researchers' International Conference on Chemistry and Chemical Engineering (YRICCCE III)-Oral presentation.

Acknowledgements

At the end of my incredible journey as a PhD student, I would like to show my gratitude to all the people that have influenced my formation as a scientist and have helped me during my research. I was fortunate to be surrounded by people who cared for me and wanted to share their knowledge, experience, and time.

Firstly, I want to thank Conf. Dr. Rodica Zavoianu, Lect. Dr. Octavian-Dumitru Pavel, Lect. Dr. Alina Jurca, Conf. Dr. Bogdan Jurca and Lect. Dr. Anca Cruceanu for all the support, advice and kindness they have shown me.

I would also like to show my appreciation to Dr. Ruxandra Birjega from the National Institute for Laser, Plasma and Radiation Physics, Bucharest, for all the help regarding the physicochemical characterization of the catalysts prepared.

I want to thank Dr. Angela Köckritz and Dr. Katja Neubauer from the Leibniz Institute for Catalysis, Rostock, Germany, for enabling me to work in their laboratory and for all the support given during my accommodation in Germany.

I want to express my gratitude to Prof. Dr. Camelia Bala, director of the Doctoral School in Chemistry at the University of Bucharest and all the Department of Organic Chemistry, Biochemistry and Catalysis members from the University of Bucharest.

Last but not least, I want to show my deepest gratitude to my PhD supervisor, Prof. Dr. Habil Ioan-Cezar Marcu, for his valuable insights, constructive comments and constant support.

Finally, I want to acknowledge my parents and my boyfriend for being there for me every time and for their unconditional love.

Thank you, everyone!